

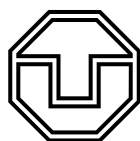
Institut für Angewandte Photophysik
Fachrichtung Physik
Fakultät Mathematik und Naturwissenschaften
Technische Universität Dresden

Photoelectron Spectroscopy on Doped Organic Semiconductors and Related Interfaces

Dissertation
zur Erlangung des akademischen Grades
Doktor der Naturwissenschaften
(Doctor rerum naturalium)

vorgelegt von
Selina Sandra Olthof
geboren am 15. Juni 1981 in Stuttgart

Dresden 2010



**TECHNISCHE
UNIVERSITÄT
DRESDEN**

Eingereicht am 15. März 2010

1. Gutachter: Prof. Dr. Karl Leo
2. Gutachter: Prof. Dr. Torsten Fritz

Verteidigt am 8. Juni 2010

Contents

Abstract / Kurzfassung	5
Publications	7
1 Introduction	11
2 The Basics of Organic Semiconductors	15
2.1 Properties of Organic Molecules	15
2.1.1 Structure of Organic Molecules	15
2.1.2 Molecular Solids	19
2.1.3 Optical Properties	22
2.2 Principles of Doping	25
2.2.1 Fundamentals of Doping	25
2.2.2 Existing Doping Methods	27
2.2.3 Investigation of the Doping Process in Organic Semiconductors	29
2.3 Interface Formation in Organic Semiconductors	31
2.3.1 Intrinsic Semiconductors	31
2.3.2 Doped Semiconductors	39
2.3.3 Level Bending vs. Alternative Explanations	43
2.3.4 Metal Layers on Organic Semiconductors	45
2.4 Optoelectronic Applications of Organic Semiconductors	49
2.4.1 Organic Light Emitting Diodes	49
2.4.2 Organic Solar Cells	50
3 Materials and Experimental Setups	53
3.1 Materials	53
3.2 Sample Preparation	59
3.3 Theory of Photoelectron Spectroscopy	60
3.4 Further Measurement Techniques	72
3.4.1 Electrical Measurements	72
3.4.2 Impedance Spectroscopy	72

4	Interface Formation at Metal Contacts	75
4.1	Injection Barriers between Metal Contacts and Doped Layers	75
4.1.1	Energy Level Alignment between Silver Bottom and Top Contacts with Doped MeO-TPD	76
4.1.2	Energy Level Alignment between Silver Bottom and Top Contacts with Doped BPhen	79
4.2	Formation of Ultra-Thin Metal Top Contacts	83
5	Investigation of the p-Doping Process in Organic Semiconductors	91
5.1	Current Status of the Field	91
5.2	Testing the Stability of the Matrix - Dopant System	92
5.3	Dependence of the Hole Injection Barrier on the Substrate Work Function	93
5.4	Systematic Variation of the Doping Concentration	95
5.4.1	Change in Fermi Level Position	95
5.4.2	Change in Depletion Layer Thickness	102
5.5	Interface Doping vs. Bulk Doping	107
5.6	Conclusion	108
6	Investigation of pn Junctions and Related Devices	111
6.1	Recombination Contacts in a MeO-TPD/C60 Tandem Solar Cell	111
6.2	PES Investigation of a Pentacene pin Homojunction	118
6.3	PES Investigation of a Zener Diode	128
7	Investigation of a Complete OLED Device	137
7.1	Photoelectron Spectroscopy Measurements	137
7.2	Comparison to IV Characteristics	144
8	Conclusion and Outlook	147
8.1	Conclusion	147
8.2	Outlook	149
	Appendix	153
	References	159
	Acknowledgments	177
	Erklärung	179

Abstract

Using photoelectron spectroscopy, we show measurements of energy level alignment of organic semiconducting layers. The main focus is on the properties and the influence of doped layers.

The investigations on the p-doping process in organic semiconductors show typical charge carrier concentrations up to $2 \cdot 10^{20} \text{ cm}^{-3}$. By a variation of the doping concentration, an over proportional influence on the position of the Fermi energy is observed. Comparing the number of charge carriers with the amount of dopants present in the layer, it is found that only 5% of the dopants undergo a full charge transfer. Furthermore, a detailed investigation of the density of states beyond the HOMO onset reveals that an exponentially decaying density of states reaches further into the band gap than commonly assumed. For an increasing amount of doping, the Fermi energy gets pinned on these states which suggests that a significant amount of charge carriers is present there.

The investigation of metal top and bottom contacts aims at understanding the asymmetric current-voltage characteristics found for some symmetrically built device stacks. It can be shown that a reaction between the atoms from the top contact with the molecules of the layer leads to a change in energy level alignment that produces a 1.16 eV lower electron injection barrier from the top. Further detailed investigations on such contacts show that the formation of a silver top contact is dominated by diffusion processes, leading to a broadened interface. However, upon insertion of a thin aluminum interlayer this diffusion can be stopped and an abrupt interface is achieved. Furthermore, in the case of a thick silver top contact, a monolayer of molecules is found to float on top of the metal layer, almost independent on the metal layer thickness.

Finally, several device stacks are investigated, regarding interface dipoles, formation of depletion regions, energy alignment in mixed layers, and the influence of the built-in voltage. We show schematic energy level alignments of *pn* junctions, *pin* homojunctions, more complex *pin* heterojunctions with Zener-diode characteristics, as well as a complete OLED stack. The results allow a deeper insight in the working principle of such devices.

Kurzfassung

Mit Hilfe der Photoelektronenspektroskopie werden in der vorliegenden Arbeit Energieniveaus an Grenzflächen von organischen Halbleitern untersucht, wobei ein Hauptaugenmerk auf dem Einfluss und den Eigenschaften dotierter Schichten liegt.

Bei der Untersuchung grundlegender Eigenschaften eines p-dotierten organischen Halbleiters können Ladungsträgerkonzentrationen bis zu $2 \cdot 10^{20} \text{ cm}^{-3}$ nachgewiesen werden. Eine Variation der Dotierkonzentration zeigt einen überproportionalen Einfluss der Ladungsträger auf die Position des Fermi-niveaus verglichen mit Experimenten an anorganischen Schichten. Durch den Vergleich mit der Anzahl Dotanden in der Schicht kann gezeigt werden, dass dabei nur etwa 5% der Dotanden einen vollständigen Ladungstransfer eingehen. Eine detaillierte Untersuchung der Zustandsdichte jenseits des HOMOs (Highest Occupied Molecular Orbital) zeigt, dass die exponentiell abfallende Flanke der Zustandsdichte weiter in die Bandlücke hineinreicht als üblicherweise angenommen. Das Fermi-niveau erfährt bei steigender Dotierung ein Pinning an diesen Zuständen, was für eine signifikante Ladungsträgerkonzentration spricht.

Weiterhin wurden Untersuchungen zu Metal Top- und Grundkontakten durchgeführt. Es kann gezeigt werden, dass die Ursache für die Entstehung unsymmetrischer Strom-Spannungskurven, trotz eines symmetrischen Probenaufbaus, an einer Reaktion zwischen dem Molekül und den Metallatomen liegt. Dadurch entsteht eine um 1.16 eV reduzierte Injektionsbarriere für Elektronen am Topkontakt. Weitere detaillierte Untersuchungen an diesen Topkontakten zeigen, dass im Falle von Silber als Metall diese Grenzfläche von Diffusionsprozessen dominiert ist. Im Gegensatz dazu zeigt das unedle Metall Aluminium keine Diffusion und führt zu abrupten Grenzflächen. Im ersten Fall kann zudem eine Monolage vom Molekül auf dem Metallkontakt nachgewiesen werden, die unabhängig von der Metalldicke aufschwimmt.

Zuletzt werden Bauelemente oder Teile solcher mit Photoelektronenspektroskopie vermessen. Hierbei werden die Grenzflächendipole, die Ausbildung von Verarmungszonen, die Energieangleichung in Mischschichten und der Einfluss der Eingebauten Spannung untersucht. Es können die Banddiagramme von *pn*-Übergängen, einfachen *pin* Homoübergängen, komplexeren *pin* Heteroübergängen mit Zener-Dioden Verhalten sowie eine gesamte OLED gezeigt werden. Die Ergebnisse erlauben einen tieferen Einblick in die Arbeitsweise solcher Bauelemente.

Publications

Articles

- A1** K. Fehse, S. Olthof, K. Walzer, K. Leo, R. L. Johnson, H. Glowatzki, B. Bröker, and N. Koch *Energy level alignment of electrically doped hole transport layers with transparent and conductive indium tin oxide and polymer anodes*. Journal of Applied Physics **102**, 073719 (2007).
- A2** C. Uhrich, D. Wynands, S. Olthof, M. Riede, K. Leo, S. Sonntag, B. Maennig, and M. Pfeiffer *Origin of open circuit voltage in planar and bulk heterojunction organic thin-film photovoltaics depending on doped transport layers*. Journal of Applied Physics **104**, 043107 (2008).
- A3** C. Falkenberg, C. Uhrich, S. Olthof, B. Maennig, M. K. Riede, and K. Leo *Efficient p-i-n type organic solar cells incorporating 1,4,5,8-naphthalenetetracarboxylic dianhydride as transparent electron transport material*. Journal of Applied Physics **104**, 034506 (2008).
- A4** S. Scholz, Q. Huang, M. Thomschke, S. Olthof, P. Sebastian, K. Walzer, K. Leo, S. Oswald, C. Corten, and D. Kuckling *Self-doping and partial oxidation of metal-on-organic interfaces for organic semiconductor devices studied by chemical analysis techniques*. Journal of Applied Physics **104**, 104502 (2008).
- A5** R. Meerheim, S. Scholz, S. Olthof, G. Schwartz, S. Reineke, K. Walzer, and K. Leo: *Influence of charge balance and exciton distribution on efficiency and lifetime of phosphorescent organic light-emitting devices*. Journal of Applied Physics **104**, 14510 (2008).
- A6** R. Meerheim, S. Scholz, G. Schwartz, S. Reineke, S. Olthof, K. Walzer, and K. Leo: *Efficiency and lifetime enhancement of phosphorescent organic devices*. Proc. of SPIE **6999**, 699917 (2008).
- A7** S. Olthof, R. Meerheim, M. Schober, and K. Leo: *Energy level alignment at the interfaces in a multilayer organic light-emitting diode structure*. Physical Review B **79**, 245308 (2009).

- A8** S. Olthof, W. Tress, R. Meerheim, B. Lüssem, and K. Leo: *Photoelectron spectroscopy study of systematic varied doping concentrations in an organic semiconductor layer using a molecular p-dopant*. Journal of Applied Physics **106**, 03711 (2009).
- A9** R. Timmreck, S. Olthof, M. K. Riede, and K. Leo: *Highly doped layers as efficient electron-hole conversion contacts for tandem organic solar cells*. Journal of Applied Physics. Accepted.
- A10** S. Olthof, J. Meiss, M. K. Riede, B. Lüssem, and K. Leo: *Photoelectron spectroscopy investigation of transparent metal top contacts for organic solar cells*. Thin Solid Films. Submitted.
- A11** S. Olthof, H. Kleemann, B. Lüssem, and K. Leo: *Built-in potential of a pentacene pin homojunction studied by ultraviolet photoemission spectroscopy*. 2010 MRS Spring Meeting Symposium II Proceedings. Accepted.
- A12** M. Schober, S. Olthof, M. Furno, B. Lüssem, and K. Leo: *A novel device concept for the characterization for charge carrier transport in organic semiconductor hetero-structures*. Applied Physics Letters. Submitted.
- A13** Th. C. Rosenow, S. Reineke, S. Olthof, M. Furno, B. Lüssem, and K. Leo: *Highly efficient white organic light-emitting diodes based on fluorescent blue emitters*. Nature Photonics. Submitted.
- A14** P. Freitag, S. Reineke, S. Olthof, M. Furno, B. Lüssem, and K. Leo: *White top-emitting organic light-emitting diodes with forward directed emission and high color quality*. Organic Electronics. Submitted.
- A15** R. Meerheim, S. Olthof, M. Hermenau, S. Scholz, A. Petrich, B. Lüssem, M. Riede, and K. Leo: *Investigation of C₆₀F₃₆ as non-volatile p-dopant for hole transport layers in small-molecule organic optoelectronic devices*. Nature Materials. Submitted.

Conference Contributions

- C1** S. Olthof, K. Fehse, K. Walzer, and K. Leo: *Photoelectron spectroscopy of organic semiconductor interfaces*. OLLA international Summer School, June 18th-25th 2007, Krutyn (Poster).
- C2** S. Olthof, R. Meerheim, K. Walzer, and K. Leo: *Measuring the energy level alignment at all interfaces in a complete OLED*. 72. Jahrestagung der DPG, February 25th-29th 2008, Berlin (Talk).
- C3** S. Olthof, R. Meerheim, K. Walzer, and K. Leo: *Measuring the energy level alignment at all interfaces in a complete OLED*. 7th International Conference on Electroluminescence of Molecular Materials and Related Phenomena, September 2nd-6th 2008, Dresden (Talk).
- C4** S. Olthof, R. Meerheim, and K. Leo: *Experimental determination of energy level alignment at all interfaces in a complete OLED structure*. Material Research Society Fall Meeting, December 1st-5th 2008, Boston (Poster).
- C5** S. Olthof, B. Lüssem, and K. Leo: *p-doping organic semiconductors: a study of varying doping concentration*. 427. WE-Heraeus-Seminar on Molecular and Organic Electronics: Bridging the Gaps, January 26th-29th 2009, Physikzentrum Bad Honnef (Poster).
- C6** S. Olthof, B. Lüssem, and K. Leo: *Investigation of the effects of doping concentration in a p-doped organic semiconductor*. 73. Jahrestagung der DPG, March 22th-27th 2009, Dresden (Poster).
- C7** S. Olthof, H. Kleemann, B. Lüssem, and K. Leo: *Built-in potential of a pentacene pin homojunction studied by ultraviolet photoelectron spectroscopy*. Material Research Society Spring Meeting, April 5th-9th 2010, San Fransisco (Poster).

1 Introduction

So far, mainly inorganic semiconducting materials such as silicon and gallium arsenide are employed to produce devices for optoelectronic applications like light emitting diodes or solar cells. However, it was already realized in the beginning of the 20th century that organic materials like Anthracene can show a semiconducting behavior as well [1]. These first experiments suffered from a lack of material purity and therefore showed little reproducibility. The interest in this field only started to grow in the 50s, when fundamental research had answered the basic questions on inorganic semiconductors and organic material of higher purity became available. By that time, the electroluminescence was first observed by Beranose [2] when applying a high AC voltage to crystalline films of Acridine Orange and Carbazole.

It took until the 80s for the first efficient optoelectronic devices to emerge that showed the promising possibilities of this new field. In 1985 the first efficient organic photovoltaic cell was presented at Eastman Kodak by Tang [3]. This device had a power conversion efficiency of 1% which was possible by the application of two different organic materials (Phthalocyanine and a Perylene derivative) in a heterojunction. Two years later, the same group published the first efficient two-layer organic light emitting diode device (OLED) [4] with an external quantum efficiency of about 1%, achieving a luminance of 100 cd/m⁻² at a driving voltage of 5.5 V.

Today, the research has split into two directions which either employ semiconducting polymers that are applied by a spin cast process or small molecules deposited by vacuum evaporation. In our group at the *Institut für Angewandte Photophysik* we focus on the second approach. These small molecule organic semiconductors are made of conjugated hydrocarbons combined with other low weight atoms and show an extended π -electron system. They are available in form of a powder that is usually stable under ambient conditions and is evaporated under UHV conditions to produce the semiconducting layers.

In comparison to inorganic semiconductors, this new class of material offers promising avenues for practical applications due to novel physical properties. For inorganic semiconductors, epitaxially grown single crystals are needed that are complicated and costly to produce and need clean-room conditions. Defects in the crystal structure or lattice mismatch between adjacent layers lead to dangling bonds that produce traps and optical recombination centers. In contrast, organic semiconductors have a low processing temperature and are produced by the evaporation of amorphous layers. There is no need for lattice match because of the close shelled conformation of mol-

ecules. A mass production is implementable with this technology as well. This is e.g. planned in the role-to-role production of OLEDs in the ROLLEX project by the BMBF¹. An advantage is furthermore the high absorption coefficient and at the same time the low reabsorption after emission due to strongly shifted absorption and emission bands. Devices can be made very thin, in the range of a few 100 nm which keeps material consumption low. For lighting applications, the possibility for the production of large illuminated areas is advantageous, as well as the possibility to produce devices on transparent and flexible substrates. Finally, the limitless diversity of organic molecules makes it possible to tailor suitable molecules that have desired properties regarding e.g. the energy level arrangement, emission spectra, mobility, solubility, or film morphology.

An important challenge in this field lies in the stability of the devices. An encapsulation is necessary to shield the organic layers from reactive oxygen and water. The longtime stability of some of the molecules, e.g. for blue emitter materials, has to be improved as well. Furthermore, the low orbital overlap between the weakly interacting molecules in a solid leads to low mobility and low conductivity. This last point can be overcome by the concept of doping. It is known from silicon technology that controllable doping was a turning point for efficient, stable, and reproducible devices and the same enhancement is true for organic devices employing doped layers [5, 6]. The doping for molecular semiconductors is achieved by co-evaporation of suitable atoms or molecules that have a high electron affinity (or low ionization potential) as acceptors (or donors). It was shown that doping works similar to the process in inorganic semiconductors, shifting the Fermi level position [7, 8], increasing the conductivity [9], and realizing ohmic injection through narrow depletion regions [10].

In the past thirty years, considerable efforts have been made to design, optimize, and understand organic semiconductors. Today, the research on organic semiconductors is a quickly growing field and a large number of products have already entered the market. Most noticeably, Sony introduced an 11 inch OLED TV in 2008. Displays for mp3-player, mobile phones, and radios have been used even longer by Sony, Samsung, LG, Nokia, and many more. Phillips and Osram are both selling large area white lighting panels. In the emerging field of organic solar cells made of small molecules, recent results show certified efficiencies of 6.1 % [11]. The application of this material class does not stop at the field of optoelectronic devices and promising research is done towards organic lasers [12, 13], transistors [14], memory devices [15, 16], and electronic components [17] as well.

Even though a wide range of applications has already been realized, it is still a challenge to understand and describe basic properties of organic semiconductors like charge carrier formation, carrier transport, or the doping process. This is due to fundamental physical differences compared to inorganic semiconductors like the low dielectric constant, the high exciton binding energy, and the transport via hopping between the molecules in a weakly interacting amorphous layer. Furthermore, devices

¹<http://www.rollex-projekt.de>

are usually built as multilayer structures containing 5 or more organic / organic heterojunctions in addition to the interfaces to the inorganic electrodes. Therefore, the investigation of surfaces and interfaces plays an important role both for understanding fundamental material properties as well as for the improvement of device designs and the development of new applications. Studies performed in the last 30 years have established that the energy level alignment between adjacent layers is not governed by common vacuum levels as previously believed. Instead, it depends on various interactions like charge transfer, chemical reactions, induced interface states, and intermixing processes. Understanding the properties of the single layers, the formation of interfaces, and the matching of energy levels is necessary for further advances in this field. In addition to structural optimization, another important topic is understanding the underlying concept of the doping process in organic layers. As mentioned before, a controllable and stable doping is important for the efficiency and existence of many organic devices.

This work deals with the formation of single interfaces as well as the alignment within multi-layer devices. Here, doped layers play an important role in determining the alignment and the built-in voltage. Therefore, this concept is investigated on the model system of the matrix molecule MeO-TPD doped by the acceptor molecule F4-TCNQ to test fundamental phenomena of the doping process. The main techniques used for these investigations are UV photoelectron spectroscopy as well as x-ray photoelectron spectroscopy. These are powerful tools to probe the occupied density of states and investigate material properties like the ionization potential and work function of a material and to look at the formation of interfaces and depletion regions. Furthermore, chemical reactions can be observed that change the density of states of a molecule.

The thesis is organized as follows. The basic physics needed for the later discussion are introduced in Chapter 2. The properties of the single molecule and the molecular solid are presented and the concept of doping is described. In particular the interface formation between metal / organic as well as organic / organic layers is discussed for intrinsic and doped semiconductors. Chapter 3 presents the properties of the molecules, the experimental details, and data evaluation of the photoelectron spectroscopy setup as well as further measurement techniques. The results are presented throughout the Chapters 4-7 and start with discussing the differences in formation of interfaces between a silver metal bottom and top contact with p- and n-doped organic semiconductors. This is followed in Chapter 5 by a detailed investigation of the p-doping process in MeO-TPD regarding the Fermi level alignment, change in Fermi level position, and the formation of a depletion region for varying concentrations of the dopant F4-TCNQ. Chapter 6 is dedicated to the investigation of novel organic device concepts employing p- and n-doped layers. These are either part of a device as it is the case for the *pn* recombination contact for organic tandem solar cells or a complete *pin* structure of a homojunction or Zener diode structure. In the last Chapter 7, the alignment throughout a OLED device is presented where each interface is investigated by incrementally building up the whole device.

2 The Basics of Organic Semiconductors

In this Chapter, small molecules are introduced as the building blocks of organic semiconductors. First, the formation of the molecular orbitals and their electronic properties are described, followed by the formation of organic solids with their transport and optical features. The focus of this Chapter is on the device relevant aspects of doping organic semiconductors, as well as the formation of interfaces between metal/organic and organic/organic layers, which are the main topics of this work. In the last Section, the utilization of these layers in optoelectronic devices is presented.

2.1 Properties of Organic Molecules

2.1.1 Structure of Organic Molecules

Calculation of Molecular Orbitals

In general, the properties of a molecule can be described by a quantum-mechanical approach. The allowed energy eigenstates E_i are given by the stationary Schrödinger Equation

$$\hat{H}\Psi_i = E_i\Psi_i \quad (2.1)$$

that is a function of the Hamiltonian \hat{H} and the eigenfunctions Ψ_i of the molecule. However, an exact solution to this many-particle problem is not possible and several approximations have to be made. The *Born Oppenheimer approximation*, for example, treats the nuclear and electron motion as independent. Thus, the overall wave function Ψ can be split into separate wave functions $\Psi_{electrical}$ and $\Psi_{nuclear}$ as given in Eq. 2.2. This is possible as the masses of nuclei and electron differ by several orders of magnitude and the nuclei move much slower than the electrons.

$$\Psi_i = \Psi_{electrical} \cdot \Psi_{nuclear} \quad (2.2)$$

As a further simplification, the electrons are considered to interact with an average potential created by the remaining electrons instead of treating every electron-electron interaction individually. Therefore, the electronic Hamiltonian can be separated into individual components for each electron

$$\hat{H} = \hat{H}_1 + \hat{H}_2 + \dots \quad (2.3)$$

Finally, the LCAO theory is applied. This *linear combination of atomic orbitals* assumes that the molecular orbitals Ψ_i can be constructed by a linear superposition of the individual atomic orbitals Φ_j , weighted by the LCAO coefficients c_i , so the molecular orbital is given by

$$\Psi_i = \sum_{j=1}^n c_{ij} \Phi_j. \quad (2.4)$$

This reduces the problem of finding the suitable function to the much simpler one of optimizing a set of coefficients c_i which may be determined numerically, e.g., by insertion of Eq. 2.4 into the Schrödinger Equation 2.1 and by applying a variational principle such as the *Hartree-Fock method* [18].

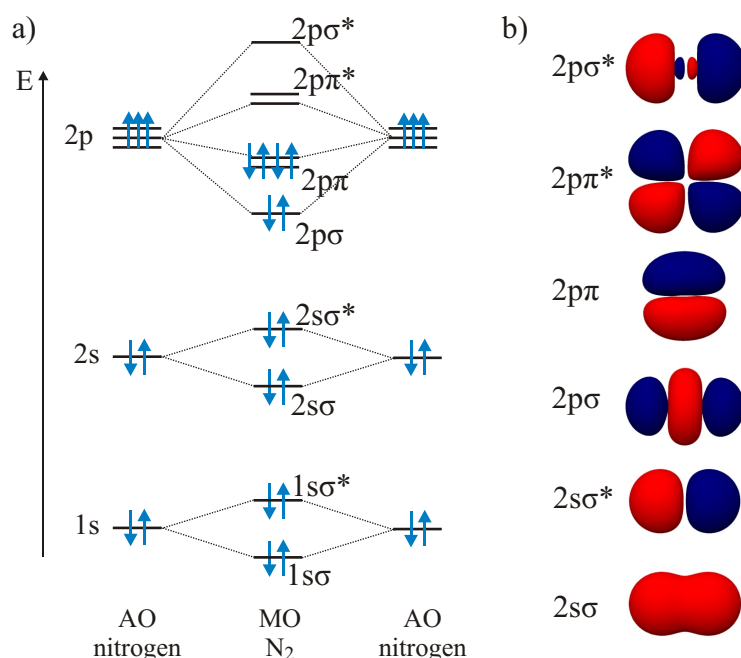


Figure 2.1: a) Illustration of the combination of the atomic orbitals of two nitrogen atoms to form the molecular orbitals of the N_2 molecule using the LCAO method (splitting is not to scale). b) Shape of the molecular orbitals formed by the combined atomic orbitals of the nitrogen atoms. Here, it is visualized that antibonding states have a node between the atoms, and σ orbitals are symmetric concerning rotations around the bond axis while π orbitals are not.

The calculations result in two sets of solutions, i.e. symmetric and antisymmetric wave functions, and yield as many molecular orbitals (MOs) as there are atomic orbitals (AO) on the individual atoms. The symmetric ones are bonding orbitals and are denoted by σ or π (depending whether they are invariant under rotation around the axis of the bond or not), while the antisymmetric orbitals are antibonding and named σ^* and π^* . Due to the energy splitting, the bonding orbitals are always lower in energy than the AO whereas the antibonding orbitals are higher in energy

compared to the AO. The amount of the splitting depends on the overlap of the atomic orbitals; in general, σ orbitals show a stronger splitting compared to π orbitals due to a stronger overlap.

In Fig. 2.1a an example is shown for the formation of these molecular orbitals in the case of the N_2 molecule. Each nitrogen contributes 7 electrons from the AOs resulting in 7 occupied MOs. The MOs are successively filled, each with 2 electrons, except for the $2p\pi$ orbital that is twofold degenerate and can host 4 electrons. The corresponding orbital shapes are given in Fig. 2.1b.

Extended π Systems

An extended electron system created by overlapping orbitals is necessary to introduce semiconducting properties in a layer. This cannot be achieved by the strongly localized σ bonds that only give an insulating property. Instead, π bonds are needed.

We will focus on the bonds of the carbon atom as it is the basis for organic molecules. Carbon atoms have 6 electrons, two are located in the $1s$ orbital and two in the $2s$ orbital. The final two are distributed among the degenerate $2p_x$, $2p_y$, and $2p_z$ orbitals. However, the splitting between the $2s$ and $2p$ orbitals is not very large, so that in the presence of an external potential, like an adjacent hydrogen atom, the energetic difference between $2s$ and $2p$ vanishes. This results in a degeneracy of 4 electrons that can all participate in a bond; the effect is called *hybridization*.

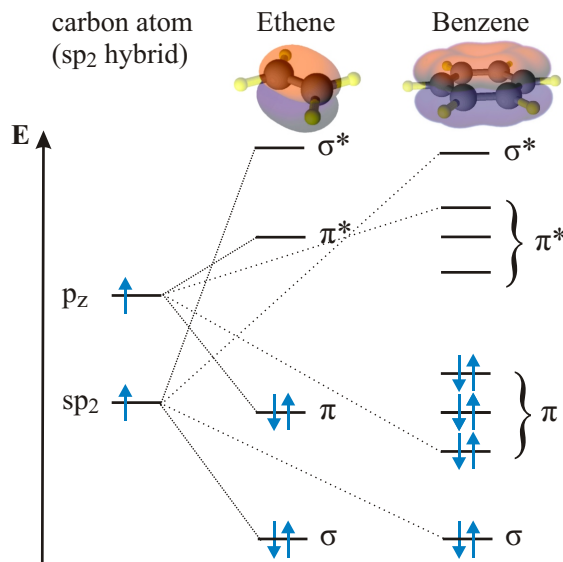


Figure 2.2: Schematic energy states of a hybridized carbon atom, and their level splitting (not to scale) in an Ethene and Benzene molecule. The p_z orbitals split into n orbitals in a molecule with n carbon atoms while the σ bonds are not affected. The insets show the structure of the two molecules with the localized σ bonds given as lines and delocalized π orbitals indicated by clouds.

Two examples of carbon molecules are schematically shown at the top of Fig. 2.2. The simplest example with a delocalized π system is Ethene (C_2H_4) where the hy-

bridized sp_2 orbitals form the strong σ double bond between the two carbon atoms while the p_z orbital gives rise to an additional carbon-carbon bond perpendicular to the σ bond. A further well known carbon molecule is the Benzene ring. Here, 6 carbon atoms are aligned in a circle held together by σ bonds while the p_z orbitals are delocalized over the whole molecule, forming the π system. In addition to the molecule structure, the schematic energy states of a hybridized carbon atom, the Ethene molecule and the Benzene molecule are plotted in Fig. 2.2 as well. It is indicated in these two examples that the increasing number of participating carbon atoms have no influence on the σ orbitals. However, the π orbitals move closer together resulting in a decreased gap between the highest occupied level and the lowest unoccupied level.

An extensive study on this topic was performed on linked Benzene molecules with an increasing number of rings that is shown in Fig. 2.3. A clear dependence between the decreasing width of the gap and the increasing size of the molecule was found [19].

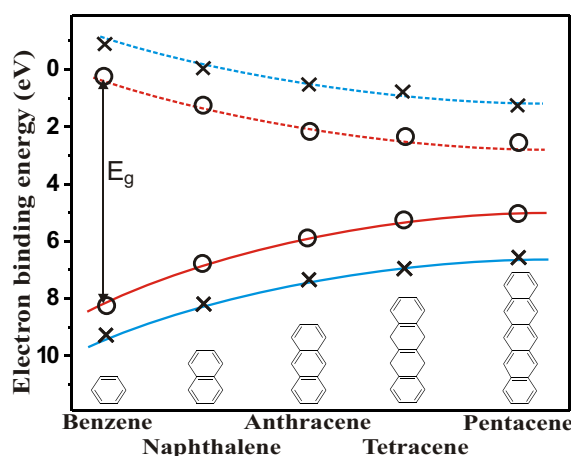


Figure 2.3: Dependence of the width of the bandgap E_g on the chain length for linked Benzene molecules in the gas phase (crosses) and in the solid state (circles). The dashed lines mark the lowest unoccupied orbital and the solid lines the highest occupied orbital. The binding energy is in reference to the vacuum level. With increasing number of delocalized electrons the gap size decreases, reproduced from [19].

The orbital energies resulting from the quantum-mechanical calculations can be associated with measurable quantities when applying the *Koopman theorem*. This theorem states that the ionization potential of a molecular system is equal to the orbital energy of the highest occupied molecular orbital (HOMO), even though the calculation by the LCAO is an approximative approach and does not yield quantitative results. The two main sources of error are the assumption of the one-electron process that neglects relaxation and polarization effects when changing the number of electrons in a system (see Chapter 2.1.2) and the approximative electron correlation. Despite the limited accuracy, the terms HOMO and LUMO (lowest unoccupied molecular orbital) will be used throughout this work synonymic with the ionization potential (IP) and electron affinity (EA) of the molecule, respectively.

2.1.2 Molecular Solids

Band Structure of a Molecular Crystal

The formation of an organic solid can be visualized starting with the Coulomb potential and atomic orbitals of a single atom (Fig. 2.4a). When several atoms are brought close together (b), the wells of the nuclei only merge in the upper part to form the previously mentioned MOs, including the HOMO and LUMO levels, while the deep AO stay localized; these are called the core level states. Finally, in the solid (c), the molecules interact only weakly so the MOs are typically localized in each molecule. This last point is only true for amorphous layers or single crystals at elevated temperatures. In the case of a pure and perfect single crystals, Bloch waves are observed at temperatures below 100 K [20]. Such an electronic structure determines the basic features of optical, electrical, and vibrational properties of molecular solids. As a result, a molecular solid behaves similar to the single molecules and intermolecular band widths of merely 0.1 eV to 0.4 eV [21, 22] have been reported. Therefore, the validity of band theory is limited which will be discussed later in this Section when describing the transport in organic solids.

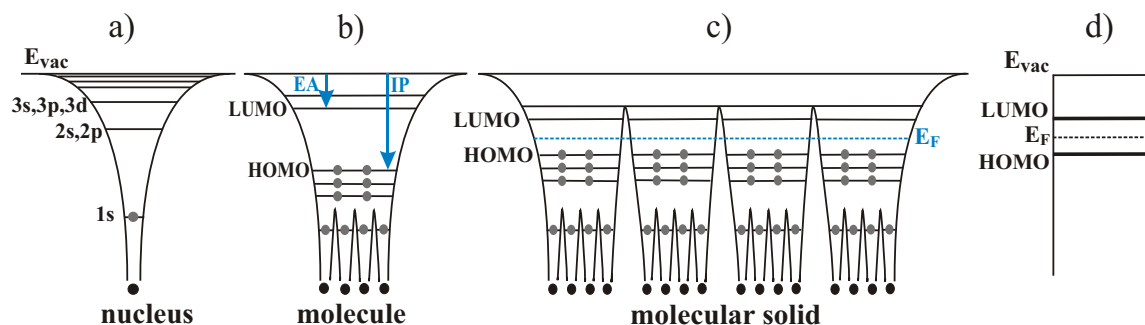


Figure 2.4: Electronic structures represented by potential wells: a) hydrogen atom, b) polyatomic molecule, and c) molecular solid. This last structure is usually simplified in a way shown in Figure d), reproduced from [23].

On the other hand, it has been observed that both the solid state ionization potential and electron affinity differ considerably from the values for the free molecule, as can be seen from the different values for solid state and gas phase measurements in Fig. 2.3. The formation of a solid seems to introduce changes in the electronic structure that are discussed in the following Paragraph.

Polarization Effects

In contrast to inorganic semiconductors, the π -conjugated molecules are a soft material with low charge carrier mobility and low dielectric constant. If an electron is added to, or removed from, the LUMO/HOMO state, the molecular shape and the lattice are deformed to compensate the significant changes in energy of the now populated LUMO or unpopulated HOMO. Hence, the HOMO and LUMO energies of the neutral system are not relevant when determining energy level alignments for

the transport properties and injection barriers. As a result of this many electron interaction, the charge carrier acts as a quasi particle called *polaron* that is composed of a charge and its interactions with the surrounding molecules. The formation of this quasi-particle includes effects of electronic, vibrational, and lattice polarization. To decide which of these effects influence the polaron in the organic layers under investigation, we have to compare the typical time a charge carrier is localized on a single molecule, that is in the range of $10^{-14} - 10^{-13}$ s [24], with the timescales of the different relaxation processes.

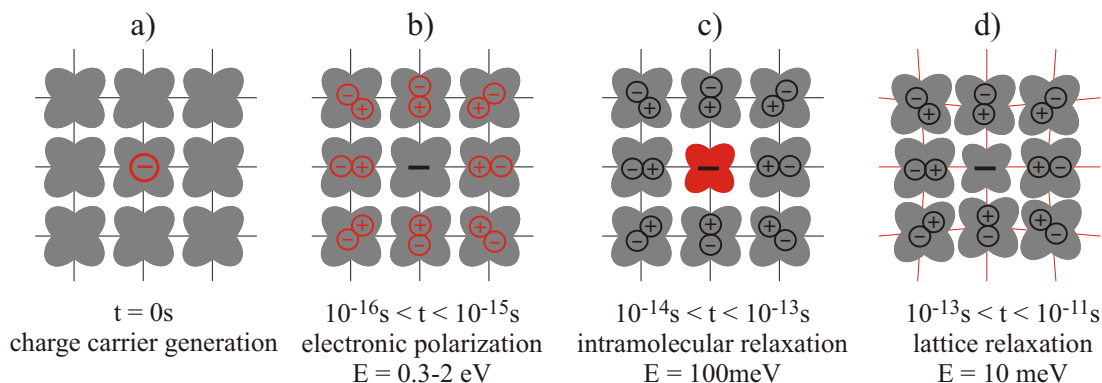


Figure 2.5: Relaxation processes after an electron is brought onto a molecule in an organic solid, with typical relaxation times and interaction energies. Given in red is always the particular relaxation effect: a) Introduction of the charge carrier to the molecule, b) electronic polarization of the surrounding molecules, c) intramolecular relaxation induced by the charged state of the molecule, d) lattice relaxation when the surrounding molecules react on the charged molecule.

After the charge is located on the molecule, the fastest process is the electrical polarization (Fig. 2.5b) with a timescale of $10^{-16} - 10^{-15}$ s, when the introduced charge induces dipoles in the neighboring molecules. This stabilizes the charge on the molecule and the IP becomes smaller relative to the isolated molecule by the positive polarization energy P^+ ; the EA is larger by the negative polarization energy P^- as is shown in Fig. 2.7. P^+ and P^- are equal as long as neither the anionic nor the cationic state have a permanent dipole moment. This effect can easily be quantified by measuring the IP and EA for molecules in a solid phase and compare this to the gas phase where the polarization stabilization is missing due to the large intermolecular distances. Typical values for P^+ are between 0.3 eV and 2 eV; some examples can be found in Table 2.1 where the values are taken from Ref. [25].

After this process, the intramolecular reorganization of the electron system takes place (c) with a delay time of $10^{-14} - 10^{-13}$ s, which is in the same time scale as the carrier hopping process. The charge located on the molecule changes the equilibrium configuration of the nuclei by influencing the bonding and antibonding states. The amount of change in HOMO / LUMO position is in the range of 100 meV. Whether this actually plays a role for a specific organic solid depends on the particular mobility of the layer.

The slowest process is the lattice polarization (d), when the surrounding molecules

change their relative positions in the lattice to react on the changed configuration of the charged molecule. This takes $10^{-13} - 10^{-11}$ s and has therefore no influence on the charge carrier. Furthermore, the effect is with 10 meV rather small.

material	IP _{gas} [eV]	IP _{solid} [eV]	P ⁺ [eV]
Pentacene	6.6	4.9	1.7
Naphtacene	6.9	5.1	1.8
TTF	6.4	5	1.4
Benzene	9.2	7.6	1.6
TCNQ	9.5	7.6	2.1

Table 2.1: Organic molecules with their ionization potentials in gas phase and solid phase. From the difference between the values, the polarization screening P⁺ can be estimated; values taken from Ref. [25]

Charge Carrier Transport in Ordered and Disordered Organic Solids

In the most general way, the current \vec{j} flowing in a medium can be described by Ohm's law and depends on the tensor of the conductance $\hat{\sigma}$ and the electric field vector \vec{E} :

$$\vec{j} = \hat{\sigma} \vec{E}. \quad (2.5)$$

In an isotropic medium, the conductance can be expressed as a function of net charge e , the charge carrier concentration n , and the mobility μ :

$$\sigma = en\mu. \quad (2.6)$$

For highly ordered inorganic semiconductors, the carrier transport can be described in the framework of Bloch wave functions [26]. Thereby, a delocalized electron is interacting with a periodic potential that is created by strongly overlapping wave functions of the neighboring atoms. However, most organic semiconductor solids are disordered systems where the Bloch theory cannot be applied. Furthermore, organic semiconductors usually have large HOMO - LUMO gaps in the range of 2 - 3 eV. Therefore, the concentration of thermally activated carriers is very small, rather comparable to an insulator. The intrinsic carrier density ρ in a semiconductor with gap E_g and effective density of states N_0 is given by:

$$\rho = N_0 e^{E_g/2k_B T} \quad (2.7)$$

Taking typical values of $E_g = 2.5$ eV and $N_0 = 10^{21}$ cm⁻³ yields a carrier density of 1 cm⁻³. This is of course unrealistically low and in real organic semiconductors, impurities will lead to much higher densities. However, the difference to inorganic semiconductors like silicon is obvious where the smaller bandgap of 1.12 eV and the

higher density of states leads to a carrier density of 10^{10} cm^{-3} . These properties lead to the fact, that the conductivity in organic semiconductors is with $\sigma \approx 10^{-10} \text{ S/cm}$ [7] very low compared to crystalline inorganic semiconductors with $\sigma \approx 10^{-5} \text{ S/cm}$.

An appropriate way to describe the charge transport in organic semiconductors is the model of Bässler [27]. The charge carrier transport occurs via hopping between localized states. Thus the transport depends on the probability of a hole / electron to tunnel from the HOMO / LUMO of one molecule to a neighboring one. To facilitate the hopping, lattice excitations are needed to provide identical initial and final state energies for the charge carrier. This results in an increase of the mobility with increasing temperature, following the phenomenologically found expression [28]:

$$\mu(T) \approx \mu_0 e^{-\frac{\Delta E}{k_B T}} \quad (2.8)$$

where ΔE is the activation energy of the transport process that not only consists of the difference between transport level and Fermi energy but contains effects like the energy to delocalize the carrier as well.

The organic layers under investigation in this work are normally formed in an amorphous or, at best, poly-crystalline form. This means that the molecules in the different locations have different environments and therefore experience different polarization screening. The individual HOMO and LUMO values of the molecules will be slightly different, resulting in a Gaussian broadening of the density of states (DOS) as shown in Fig. 2.6. The width of this broadening depends on strength of the polarization screening and the amount of disorder and is in the range of 0.25-0.5 eV [29].

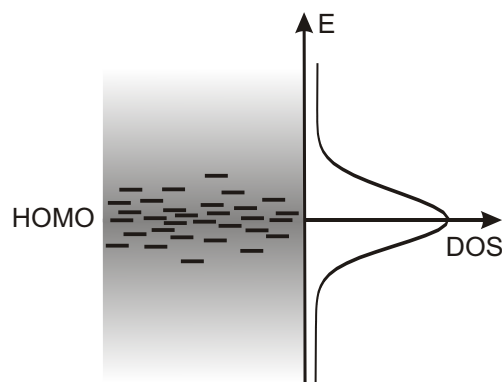


Figure 2.6: Disorder in a polycrystalline or amorphous layer. The different environments of the molecules induce different polarization energies, resulting in a distribution of the transport level that leads to a Gaussian broadening of the density of states.

2.1.3 Optical Properties

Due to the very weak van-der-Waals interaction between individual molecules, the optical properties are largely defined by the properties of the single molecules and not by the solid. When light is absorbed by a material, an electron - hole pair is created.

This so called exciton is bound together by the Coulomb force that is a function of the distance r , the dielectric constant ϵ_0 and the static relative permittivity of the layer ϵ :

$$E_{coul} = \frac{1}{4\pi\epsilon\epsilon_0} \frac{e^2}{r}. \quad (2.9)$$

Depending on the material properties of the semiconductor, there are two concepts that describe this process:

The first one is the so called *Mott-Wannier* exciton when the electron-hole pair is formed at a large distance r where it experiences only a small Coulomb interaction and therefore has a small exciton binding energy. This is however only applicable to materials that show delocalized Bloch states and a high dielectric constant ϵ , as it is the case for most inorganic semiconductors. In this case, the optical gap is comparable to the transport gap.

In organic semiconductors, however, the dielectric constant is very low and the electron-hole pair is located on a single molecule. These excitons are called *Frenkel excitons* and the radius of such an exciton can be estimated from the average separation of the electron from its corresponding hole on the same molecule which is typically $< 5 \text{ \AA}$. This leads to a large Coulomb interaction and strong exciton binding energies. Consequently, the optical gap is smaller than the transport gap by an amount of 0.3 eV to 1.5 eV [30, 31] as illustrated in Fig. 2.7.

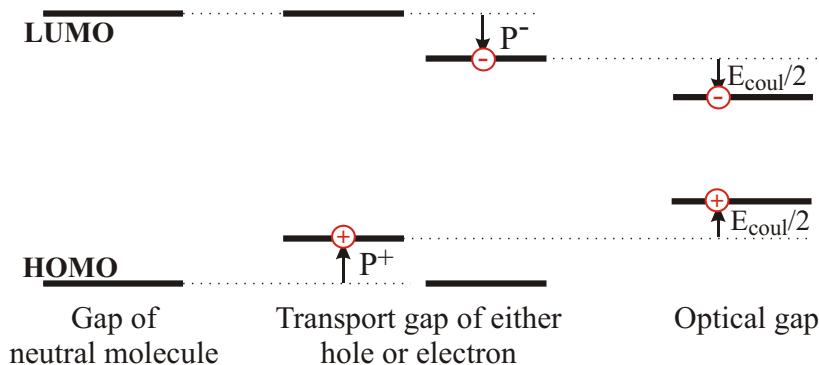


Figure 2.7: The different HOMO and LUMO positions of a neutral molecule (or molecule in gasphase) are illustrated and compared to the transport levels of an either positively or negatively charged molecule showing polarization relaxation. Finally, a molecule containing both charges is sketched forming an exciton. Here, the exciton binding energy E_{coul} decreases the gap size additionally.

The excitation follows the *Frank-Condon* principle: during an electronic transition from a ground state S_0 to an excited state S_1 , the vibrational levels that correspond to a minimal change in the nuclear coordinates and therefore have a large wave function overlap are favored. This is shown in Fig. 2.8. After the absorption of a photon, the S_1 state will therefore be in a higher vibrational and rotational state ν'_n and the total

energy is the sum of

$$E = E_{el} + E_{vib} + E_{rot} \quad (2.10)$$

where the rotational energy can usually be neglected, as the contribution to the total energy is rather small.

From this vibrationally excited state, the electron will rapidly decay into the lowest excited state ν'_0 via a non-radiative internal conversion process from which it then can decay back to a vibronic level ν_n of the ground state; this process is called fluorescence. This excitation and relaxation into higher vibrational states is the reason why molecules generally emit radiation at higher wavelengths than they absorb. This so-called *Stokes shift* is advantageous for organic light emitting diodes as a layer cannot reabsorb its emitted light.

An alternative process to fluorescence is phosphorescence: this is the emission from an excited triplet state T_1 with a total spin quantum number 1. This process has a much longer decay time, as the optical transition is forbidden and a spin flip process is necessary. The probability of such a phosphorescent decay can be enhanced by using molecules that have a heavy atom incorporated like iridium or platinum. The resulting strong coupling of the spin with the angular momentum weakens the selection rule.

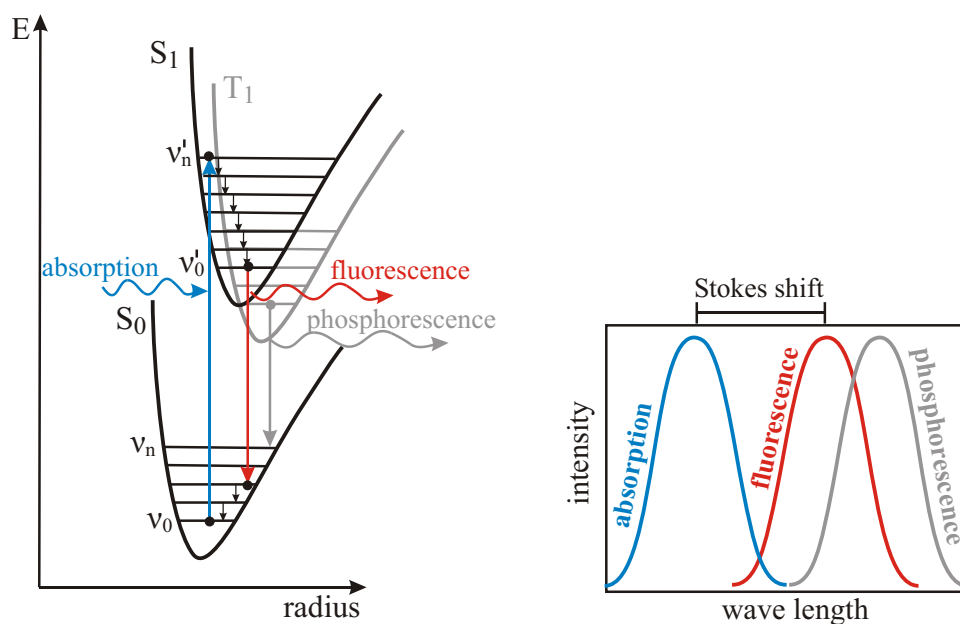


Figure 2.8: Illustration of the Frank-Condon principle: absorption of a photon leads to the excitation of an electron from the ground state S_0 in a higher electronic S_1 and vibrational ν'_n state. The relaxation can either take place via fluorescence (red) or for the case of an excited triplet state T_1 via phosphorescent (gray) after a spin-flip takes place. On the right side the schematic absorption spectra and the corresponding fluorescent and phosphorescent emission spectra as shown.

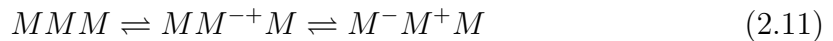
2.2 Principles of Doping

For inorganic semiconductors, the concept of doping was a breakthrough that allowed for a control of the transport properties, resulting in significant device improvements as well as new device concepts.

Organic materials have a very low conductivity as long as they are intrinsic, therefore having the possibility of a controllable doping technology is even more desirable. Upon doping, the charge carrier density can be significantly increased resulting in a good conductivity, ohmic injection at the contacts, and a negligible drop of voltage across these layers. Obviously, this concept allows for new device structures, like *pn*-junctions, that are known from inorganic semiconductors and can be applied to the field of organic devices as well.

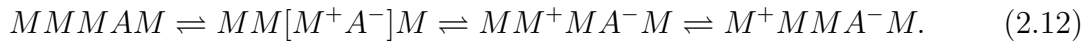
2.2.1 Fundamentals of Doping

A semiconductor is called intrinsic if the matrix molecules M themselves create the free charge carriers. Thereby, an electron is transferred from the HOMO to the LUMO leaving behind a hole:



In case of extrinsic semiconductors, another species is introduced that either accepts an electron or donates one which results in the formation of free charge carriers. In this Section, the process of p-doping will be discussed where an acceptor molecule A interacts with the matrix molecule M . The description of n-doping by a donor D is equivalent.

To create free charge carriers, first a charge transfer complex (CTC) between the molecule M and an acceptor A has to form, indicated by $[M^{+}A^{-}]$ in Eq. 2.12. To generate free charge carrier from this, the CTC has to dissociate, so that the charged molecule does not feel the Coulomb force by the ionized acceptor any more. Now the positive charge can move through the organic layer by hopping from one matrix molecule to the next. Schematically this process can be written as



To create this free charge carrier in an organic layer by molecular doping, the EA of the p-dopant has to be larger than the IP of the matrix as shown in Fig. 2.9. In this case, an electron will move from the HOMO of M to the LUMO of A .

In classical semiconductor theory, the number of charge carriers can be calculated from the Fermi-Dirac distribution depending on the energies of the valence E_V and conduction band E_C and their effective density of states N_V and N_C :

$$p = N_V \cdot e^{-\frac{E_F - E_V}{k_B T}} \quad \text{and} \quad n = N_C \cdot e^{-\frac{E_C - E_F}{k_B T}} \quad (2.13)$$

The total number of charge carriers ρ in an undoped semiconductor is given by

$$\rho = \sqrt{pn} = \sqrt{N_V N_C} e^{-\frac{E_C - E_V}{2k_B T}}. \quad (2.14)$$

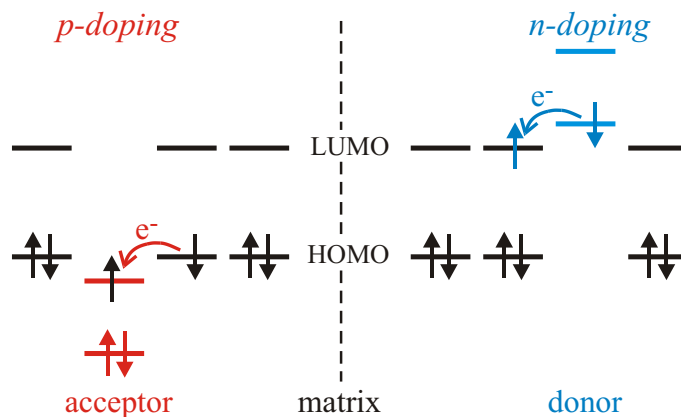


Figure 2.9: Doping mechanism of a molecular p-type dopant (left) where the dopant molecule acts as an acceptor for an electron, and n-type dopant (right) where the electron is transferred from the dopant to the matrix.

The position of the Fermi level is very close to the middle of the gap for an intrinsic semiconductor and is given by

$$E_F = \frac{E_C + E_V}{2} + \frac{k_B T}{2} \ln \frac{N_V}{N_C}. \quad (2.15)$$

Upon p-doping, an acceptor level E_A arises in the forbidden gap with a dopant density N_A and the Fermi level has to shift downward in the gap to preserve charge neutrality. The limiting cases of *deep acceptors* and *shallow acceptors* are distinguished and the relation between doping density N_A and the number of free charge carriers p differs between the two.

For deep acceptor states, the dopant level is far from the band edge compared to $k_B T$ and is located above the Fermi energy, so thermal activation is needed. The position of the Fermi energy is given by

$$E_F = \frac{E_C + E_V}{2} + k_B T \ln \frac{N_V}{N_A} \quad (2.16)$$

and the number of charge carriers is

$$p = \sqrt{N_V N_A} e^{-\frac{E_A - E_V}{2k_B T}}. \quad (2.17)$$

Therefore, the hole density in the deep acceptor limit increases with the square root of the doping density and is thermally activated.

On the other hand, shallow acceptor states are positioned close to the top of the valence band, with

$$E_A - E_V \leq k_B T \ln \frac{N_V}{N_A} \quad (2.18)$$

and require typically only energies corresponding to the thermal energy to be ionized. Therefore, all dopants are ionized even at low temperature and the number of free charge carriers equals the number of dopants and is not temperature dependent

$$p = N_A \quad (2.19)$$

with the Fermi energy at:

$$E_F = E_V + k_B T \ln \frac{N_V}{N_A} \quad (2.20)$$

Applying this to organic semiconductors, we simply associate E_V with the HOMO and E_C with the LOMO position. To fulfill the requirement of Eq. 2.18 at room temperature for shallow acceptor states, the difference between HOMO and acceptor level has to be in the range of 0.1 eV at a typical doping density of $N_V/N_A = 100$. The charge transfer state between the matrix molecule and the acceptor molecule can be described by the Coulomb force of Eq. 2.9. Taking a typical intermolecular distance of 1 nm, we get a bonding energy of the CTC of ≈ 0.5 eV, and therefore much larger than the required 0.1 eV for the shallow states. At first sight, one would thus expect that in organic semiconductors, the dopants form deep acceptor and deep donor states upon doping.

However, we cannot be sure that the same physics applicable to inorganic semiconductors can actually be applied here. Effects like the lower dielectric constant, the higher exciton binding energy, the strong polarizability, the amorphous growth mode, and the hopping transport greatly influence the physical properties.

2.2.2 Existing Doping Methods

Early doping experiments were mainly done on Phthalocyanines as this material class is easily p-dopable, e.g. by halogen gases [32–34] or small molecules like ortho-chloranil [35]. However, these early experiments were not done using doping by co-evaporation, but by surface doping. Even though the resistivity decreased during these experiments, often the effect reversed partly after the treatment by the gas was terminated.

Nowadays, it is more common for p-type doping to use metal halides co-evaporated with organic molecules (e.g. FeCl_3 [36] or CuI [37, 38]) as well as metal oxides (e.g. WO_3 [39], MoO_x [38, 40, 41], or ReO_3 [38, 42]). However, these systems suffer from the problem of diffusion since the dopants are small and mobile. This prevents an accurate tuning of the doping concentration and the production of stable devices. A more controllable way of doping can be achieved by using organic molecules with a high EA co-evaporated into a matrix. Some examples are the weak acceptors DDQ¹ [43, 44] and TCNQ² [43, 45] or the fluorinated versions F2-HCNQ³ [46] and the currently most common F4-TCNQ⁴ [47–49].

Until today, the concept of n-doping is more challenging. This is due to the fact that the IP of such a dopant has to be very small to realize an electron transfer to the matrix. This property makes the dopant very reactive with, e.g., oxygen. Until recently, practical n-doping of organic semiconductors employed alkali metals, which exhibit very low work functions and easy handling. Most commonly, Li or Cs are used

¹Dicyano-dichloro-quinone

²Tetracyano-quinodimethane

³3,6-difluoro-2,5,7,7,8,8-hexacyanoquinodimethane

⁴2,3,5,6-tetrafluoro-7,7,8,8-tetracyanoquinodimethane

in a ratio of one dopant per molecule, but other alkali metals work as well [50–54]. However, alkali atoms and ions, especially Li, are prone to diffusion due to their small radii and the positive counter-ion remaining after the charge donation can be strongly ion-paired with the doped molecule, trapping the donated electron.

As in the case of p-doping, it is advantageous to have small molecules that are more temperature stable and easier to control during co-sublimation. The first molecule to show a n-doping behavior was BEDT-TTF⁵ [55]; however, only a small increase in conductivity was achieved, as is the case for most of these stable molecular n-dopants investigated hereafter like TTN⁶[56], BTQBT⁷ [57], and AOB⁸ [58] that all have relatively high ionization potentials. This limits the range of possible matrix materials to those with high electron affinities. Recently, a proprietary small molecule material with the acronym NDN1 was released by the *Novaled AG* showing an excellent n-doping effect up to a matrix EA of ≈ 3.0 eV and a good temperature stability. As this material is not stable against air, it has to be handled under a nitrogen atmosphere.

Another approach for achieving lower IP molecules uses the thermal decomposition or irreversible reaction of precursor molecular salts to create in situ a volatile donor dopant. By this method, doping is achieved for the cationic dyes Pyronin B [59, 60] and Leuco Crystal Violet [61]. Even though this often leads to a considerable conductivity increase and an irreversible electron transfer, this method introduces additional uncontrolled impurities into the organic film. Finally, organometallic complexes like Ru(terpy)₂⁹ [17], CoCp₂¹⁰ [62, 63] and DMC¹¹ [64, 65] can have a n-type doping effect. However, these compounds have a high vapor pressure that makes them difficult to co-evaporate with a matrix layer. Usually, they are deposited from the gas phase by creating a partial background pressure of the dopant molecule during evaporation of the matrix molecules.

Typical doping concentrations in organic semiconductor layers are in the range of 1 to 10 dopant molecules per 100 matrix molecules, depending on the doping efficiency of the individual system. There are different ways to quantify the amount of doping. The most relevant one for quantitative evaluation is the indication of the molar ratio (MR), meaning the ratio of the number of dopant molecules n_D to the number of matrix molecules n_M :

$$\text{MR} = \frac{n_D}{n_M}. \quad (2.21)$$

However, more common is the usage of mole percent (mol%) that is the relative number of dopant molecules to the total number of molecules:

$$\text{mol}\% = \frac{n_D}{n_D + n_M} \cdot 100. \quad (2.22)$$

⁵Bis(ethylenedithio)-tetrathiafulvalene

⁶Tetrathianaphthacene

⁷Bis(1,2,5-thiadiazolo)- p-quinobis(1,3-dithiole)

⁸Acridine orange base

⁹Bis(terpyridine)ruthenium(II)

¹⁰Cobaltocene

¹¹Decamethylcobaltocene

Converting one value to the other can be done by

$$\text{mol}\% = \frac{100 \cdot \text{MR}}{1 + \text{MR}} \quad \text{and} \quad \text{MR} = \frac{\text{mol}\%}{100 - \text{mol}\%}. \quad (2.23)$$

Another way to quantify the amount of doping is the relative masses of the dopant (m_D) and matrix molecule (m_M) in a layer. This is especially necessary if the molar mass of one of the molecules is not known. Again, this can be expressed by weight percent (wt%) or weight ratio (WR) as

$$\text{wt}\% = \frac{m_D}{m_D + m_M} \cdot 100 \quad \text{and} \quad \text{WR} = \frac{m_D}{m_M}. \quad (2.24)$$

Recalculating the molar ratio from a given weight ratio can easily be done by weighing it with the relative molar masses of the dopant M_D and matrix molecule M_M

$$\text{MR} = \frac{M_M}{M_D} \cdot \text{WR}. \quad (2.25)$$

2.2.3 Investigation of the Doping Process in Organic Semiconductors

The effectiveness of molecular doping has been shown in numerous cases for single layers [9, 10, 43, 49, 66–70] as well as for devices [47, 48, 71, 72]. However, it is still a challenge to quantitatively describe the doping process in organic layers. One material combination that is very well investigated is ZnPc¹² doped by F4-TCNQ. Therefore, this system is chosen to discuss experimental results on a doped organic system.

The most important effect of doping is the increase in conductivity. Upon doping of a few molecular percent of F4-TCNQ into ZnPc, the conductivity can be increased by up to 6 orders of magnitude [7], and even more is possible for higher doping ratios. Comparing different doping ratios, Pfeiffer et al. [73] found that the increase is superlinear with doping ratio. The corresponding measurement is shown in Fig. 2.10. The explanation for this is given by a percolation model [7] that relies on the Gaussian distribution of transport states. The charge carriers that are located deep in the tails of this distribution are less mobile since there is a lower density of states and therefore less nearby states to hop onto in the energy range available within thermal energy. Upon doping the tail states fill up and the transport takes place at higher energy levels. The larger amount of available states leads to a higher mobility in the layer and to the superlinear increase.

These conductivity measurements also investigated the temperature dependence and show a thermally activated behavior with an activation energy of $E_{act} = 180$ meV at 1 mol% doping, i.e. the activation energy at room temperature still plays an important role.

¹²Zinc phthalocyanine

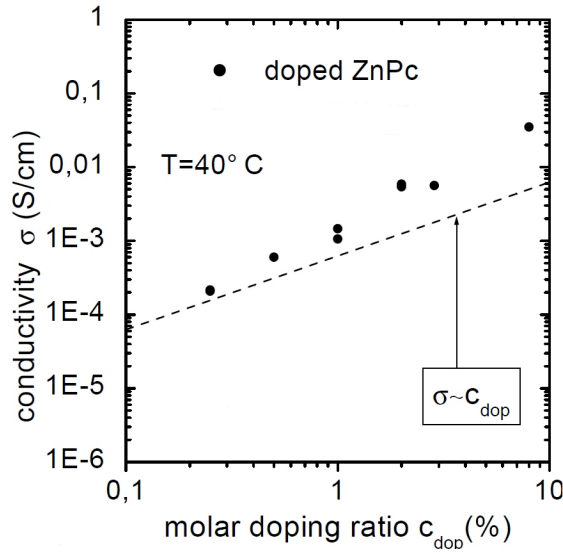


Figure 2.10: Double logarithmic plot of the dependency of the conductivity in a layer of ZnPc doped by F4-TCNQ on the dopant concentration. The dashed line resembles the linear dependency. From [73].

Deeper insight into the activation energy of a transport level E_μ of a doped layer can be achieved by *Seebeck measurements* [74]. There, the thermo-voltage between two contacts that have slightly different temperatures can be measured and is expressed by the Seebeck coefficient:

$$S(T) = \frac{E_F(T) - E_\mu}{eT} + \frac{k_B}{e} A \quad (2.26)$$

where A is a constant that can normally be neglected as long as $E_F(T) - E_\mu \gg k_B T$.

This shows that by Seebeck measurements, the transport type (p or n) can be distinguished by the sign of $S(T)$ as well as the distance of the transport level to the Fermi energy. For the ZnPc:F4-TCNQ system, it was shown that with increasing doping ratio, the Fermi level moves toward the HOMO [7, 9, 55], just as it is known from doping in inorganic semiconductors. With this method, it was furthermore proven that the increase in conductivity is indeed a doping effect and not a hopping transport on the dopant, as this would have led to transition from a positive Seebeck coefficient for the hole transporting intrinsic ZnPc to a negative Seebeck coefficient for the electron transporting F4-TCNQ.

The amount of charge transfer can be measured by infrared spectroscopy. One can observe the stretching mode of the C-N triple bond in the cyano group of the F4-TCNQ molecule within the matrix layer that is very sensitive to its charged state. The absorption mode $b_{1u}\nu_{18}$ changes from a frequency of 2228 cm^{-1} for the neutral molecule to 2194 cm^{-1} when the dopant becomes negatively charged. With this method, it was found that the fraction of charge transfer of F4-TCNQ in ZnPc is $Z = 1$ [75].

Finally, photoelectron spectroscopy (PES) is a well suited tool to study doping effects as it can probe relevant values like Fermi level position, and depletion layer widths. A detailed description on the method can be found in Chapter 3.3. The first

detailed investigation by UV photoelectron spectroscopy on a Schottky contact (see Chapter 2.3.2) was done by Blochwitz et al. [10] using ZnPc:F4-TCNQ on ITO and gold. They found a narrow depletion layer region of less than 5 nm and the Fermi energy positioned very close to the HOMO of the doped layer, just as expected for p-type doping.

2.3 Interface Formation in Organic Semiconductors

Whenever organic layers are used in devices like organic light emitting diodes (see Chapter 2.4.1) or organic solar cells (see Chapter 2.4.2), two aspects govern the device performance. Primarily, the transport and emission/absorption properties of the individual organic layers are important. Great effort has been put into designing better materials to increase the performance. Furthermore, the interfaces between the organic semiconductor and the metal contacts as well as the organic/organic interfaces play a significant role, especially as the number of layers is rising in the course of device optimization. The interfaces have a crucial influence on the charge balance in the device and the charge injection or extraction.

To estimate the barriers present in a stack of organic layers, the simple picture of vacuum level alignment was assumed for a long time and is still common today. This assumption was readily accepted, as one does not expect the closed-shell molecules to undergo significant interactions. Hence, e.g. the hole injection barrier ϕ is assumed to be the difference between the metal work function Wf_m and the ionization potential of the molecule. However, we know today from many studies that the assumption of vacuum level alignment, especially for metal-organic contacts, is not valid and can underestimate the injection barriers by as much as 2 eV [53, 64, 76–78].

In the following, it will be discussed which properties influence the alignment at the interfaces, how the alignment can be characterized, and in a few cases even predicted by theory. As the number of free charge carriers has a significant influence, there is a distinction between the alignment of intrinsic and doped organic layers.

2.3.1 Intrinsic Semiconductors

Intrinsic Semiconductor Layers on Metal Surfaces

Most obvious is the breakdown of the vacuum level alignment assumption when small molecules are evaporated on high work function clean metal substrates. In Fig. 2.11, an example is shown that gives the alignment of MeO-TPD¹³ on gold as one would assume from vacuum level alignment a) and as the result of a measurement by UV-photoelectron spectroscopy b). Instead of a vanishing hole injection barrier expected from the comparable metal work function and organic ionization potential, a barrier of $\phi = 1.1$ eV is present due to an interface dipole Δ that forms between the metal surface and the organic layer. Such a dipole is abrupt and arises within the first 1

¹³ N,N,N',N'-Tetrakis(4-methoxyphenyl)-benzidine

or 2 monolayers of the organic semiconductor deposition. It can have several origins which are shown in Fig. 2.12 and will be discussed in the course of this Chapter.

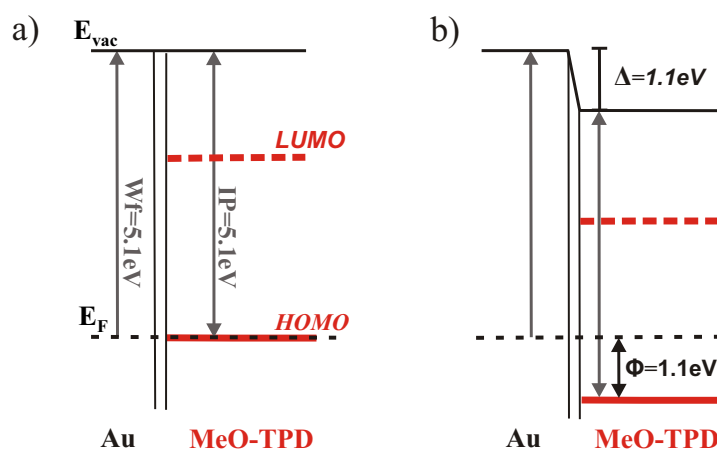


Figure 2.11: Energy diagram of a metal-organic semiconductor interface between gold and MeO-TPD a) as assumed from vacuum level alignment and b) result of a measurement by UV-photoelectron spectroscopy that shows that an interface dipole of 1.1 eV is present.

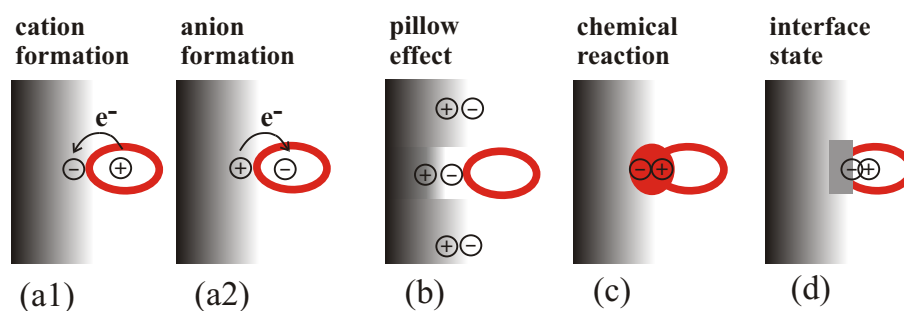


Figure 2.12: Possible origins of an interface dipole. a1) and a2): Charge transfer across the interface, b) pillow effect by rearrangement of electron cloud at the metal surface by a molecule due to a reduction of tailing of the electron charge density into the vacuum, c) strong chemical interaction between the metal and the adsorbate leading to a rearrangement of the electronic cloud, and d) existence of metal induced interface states serving as a buffer on charge carriers; reproduced from [23].

To describe the alignment between an organic semiconductor and a metal, the slope parameter S can be used. This parameter is well known in inorganic semiconductor physics and is defined as the change in electron injection barrier ϕ_e with the change of metal work function Wf_m which is equivalent to the change in organic work function Wf_{org} with Wf_m :

$$S = \frac{d\phi_e}{dWf_m} = \frac{dWf_{org}}{dWf_m}. \quad (2.27)$$

Two extreme cases can be considered for the slope parameter: If ϕ_e always shows the same amount of change as Wf_m , we have the *Schottky-Mott limit* with $S = 1$

(shown in Fig. 2.13a). On the other hand, if ϕ_e is constant, independent of the metal used, then $S = 0$ and the *Bardeen limit* is reached as show in Fig. 2.13b.

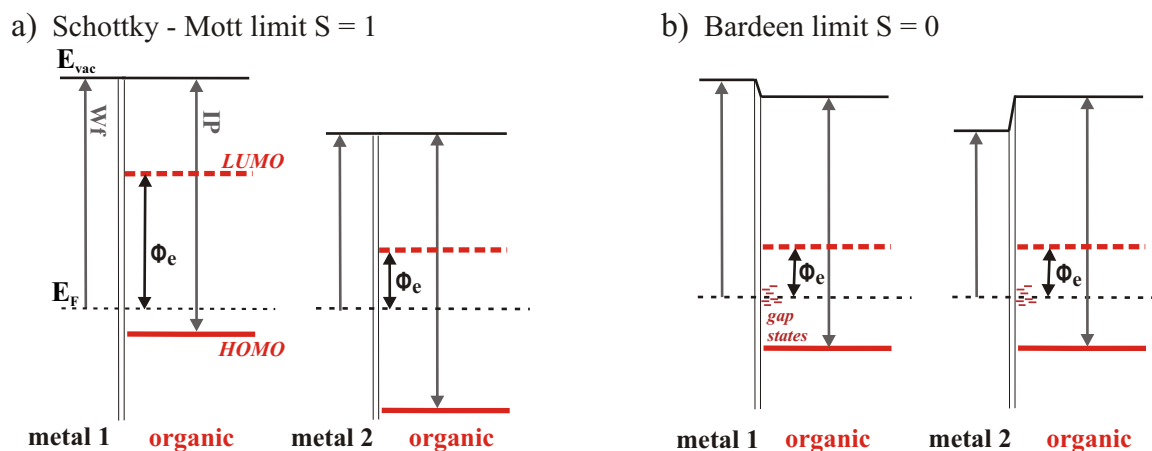


Figure 2.13: These schematic interface alignments between organic layers with either a high work function or a low work function metal show the limiting cases for the slope parameter S : a) Schottky-Mott limit: when modifying the metal work function, the electron injection barrier (and organic work function) changes by the same relative amount $\rightarrow S = 1$. b) Bardeen limit: independent of the metal work function, the injection barrier (and organic work function) stays the same $\rightarrow S = 0$; the effect illustrated here is due to the presence of gap states.

Both limits can only be observed in special cases. For the Schottky-Mott limit, interface reactions have to be avoided and the so called pushback effect of the metal that will be described later in this Chapter should not be present. A schematic example for the dependence of the organic work function on the substrate work function with a slope parameter of unity is shown in Fig. 2.14. It is obvious that the slope of unity cannot be achieved over the whole range of Wf_m since, at some point, the Fermi energy either approaches the HOMO or the LUMO of the organic layer. The Schottky-Mott limit will thus only hold as long as $EA < Wf_m < IP$; beyond that a charge transfer either from the metal to the LUMO or from the HOMO to the metal will take place (see Fig. 2.12a) that pins the levels and prevents further changes in Wf_{org} .

Usually, the Bardeen-limit is only found for molecules that have a large EA and therefore it is difficult to find a metal not pinning at the LUMO as it is the case for F16CuPc¹⁴ or PTCBI¹⁵ [76]. Another possibility is that a reactive molecule can chemically bind to the metal and thereby produce additional states in the gap (see Fig. 2.12c). This was observed for Alq₃¹⁶ at metal surfaces [79–81], where the molecule undergoes a reaction and forms an organometallic complex resulting in the formation of new trap states within the gap, that influence the energetic alignment. This is schematically depicted in Fig. 2.13b.

¹⁴copper hexadecafluorophthalocyanine

¹⁵3,4,9,10-perylenetetracarboxylic bisimidazole

¹⁶Tris(8-hydroxy-quinolinato)-aluminium

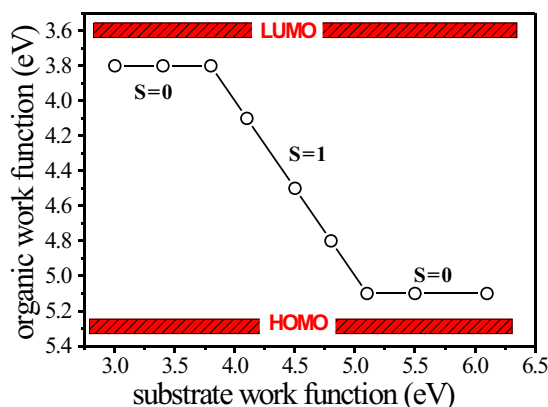


Figure 2.14: Schematic view of the dependence of the work function of an ideally behaving organic layer with $IP = 5.3$ eV and $EA = 3.6$ eV on the work function of the substrate. Three regimes can be found: as long as $Wf_m < EA$, pinning takes place at the LUMO and leads to $S = 0$, for $Wf_m > IP$ the same happens at the HOMO. For the values in between, there is a linear dependence with a slope of unity.

Comparing these pinning positions to the IP or EA values of the molecules, it was observed that the pinning usually sets in a few 100 meV before the HOMO or LUMO are actually reached (as indicated in Fig. 2.14). The reason for this distance is still under discussion and two theories will be mentioned here. On one hand, it is assumed to be a polaron state, a so called *integer charge transfer state* (ICT) [82–84], when the substrate work function is believed to align with an interface polaron state. These interface polaron states are relaxed further into the gap compared to a bulk polaron state due to the additional screening by the metal surface. If the metal Fermi energy reaches this state, charge transfer takes place and an interface dipole is formed.

The other possibility is that the pinning takes place at the HOMO or LUMO itself. The DOS reaches further into the gap than the cutoff position usually determined by UPS measurements (see Chapter 3.3). This tail of the density of states decays exponentially into the gap and shows a considerable density of states even 0.2–0.4 eV beyond the HOMO onset and offers enough charge carrier density to pin the Fermi energy [78, 85]. Both theories are supported by experimental evidence and further studies have to clarify the underlying physics of the pinning effect.

So far, we looked at cases where the slope parameter is equal to 0 or 1. More commonly, the interface dipole depends on the metal and therefore the slope parameter deviates from unity. If clean metal substrates are used, the most important interface effect is the so called *pillow* or *pushback effect* shown in Fig. 2.12b. The surface work function of a metal is the sum of the bulk chemical potential and the surface contribution. The latter appears, because the positive charge density from the nuclei drops abruptly to zero at the surface of the metal, while the negative charge density from the electrons leaks out into the vacuum where it decays exponentially in probability. When a molecule adsorbs on a metal surface it suppresses these tailing states by the Coulomb repulsion, lowering the surface contribution and thereby decreasing the work

function. This effect is large especially for noble metals and is the main reason for the interface dipole appearing in the measurement of Fig. 2.11b. It is important to note that this is not a dipole resulting from a charge transfer, but simply a modification of the electronic surface component.

This effect can be avoided by using passivated surfaces. For this purpose, it is often sufficient to expose the sample to air or cover it with hydrocarbons by a cleaning procedure e.g. with Ethanol. The ionization potential measured hereafter is reduced compared to the clean surface (for gold from 5.2 to 4.3 eV [77]) and no further pushback effect appears upon the deposition of the organic layer. However, if a high work function substrate is required, passivation is not an option. Rather substrates are used that exhibit fewer free electrons, e.g. the doped polymer PEDOT:PSS¹⁷. In this case, the work function is solely a bulk contribution due to the closed shell conformation of the polymer. PEDOT:PSS has an ionization potential of 5.1 eV which is comparable to clean gold. However, due to the missing pillow effect it always shows a smaller hole injection barrier compared to gold [76].

Even if the pushback effect is avoided and no pinning takes place, the slope parameter is not necessarily equal to unity. This deviation suggests the existence of states at the interface that act as a buffer on the charge exchange. These interface states limit the range of interface Fermi level excursion and even lead to a pinning if the number of states is large enough. Already a density of $5 \cdot 10^{13} \text{ cm}^{-2} \text{ eV}^{-1}$ is reported to have a significant impact on the alignment [78]. This appearance of *metal induced gap states* (MIGS) is well established in inorganic semiconductors [86, 87] and is described there by

$$\text{Wf}_{org} = S(\text{Wf}_m - EA) + (1 - S)E_{CNL} \quad (2.28)$$

in which S is given by

$$S = \frac{1}{1 + 4\pi^2 D_{is} \delta} \quad (2.29)$$

and δ is the effective metal semiconductor instance, D_{is} density of interface states, and E_{CNL} is called the *charge neutrality level*. It is obvious that S approaches 0 for large D_{is} .

A very successful method applying the MIGS to organic semiconductors is the *induced density of interface states* model (IDIS) [88, 89]: The metal electron wave function tails into the semiconductor with a penetration depth that mainly depends on the width of the band gap [90]. This broadens the semiconductor density of states and induces interface states in the gap (Fig. 2.12d). After the density of interface states due to the broadening is calculated (typical densities are $10^{14} \text{ cm}^{-2} \text{ eV}^{-1}$ [89, 91]), these states are filled with electrons equaling the number of electrons in the neutral molecules. The level up to which the IDIS are filled is the charge neutrality level E_{CNL} . When the interface is formed, charge transfer takes place between the Fermi energy of the metal and the E_{CNL} that results in the formation of a dipole. This theoretical approach achieves good agreement with experiments [91]. Some experimental

¹⁷Poly(3,4-ethylenedioxythiophene) poly(styrenesulfonate)

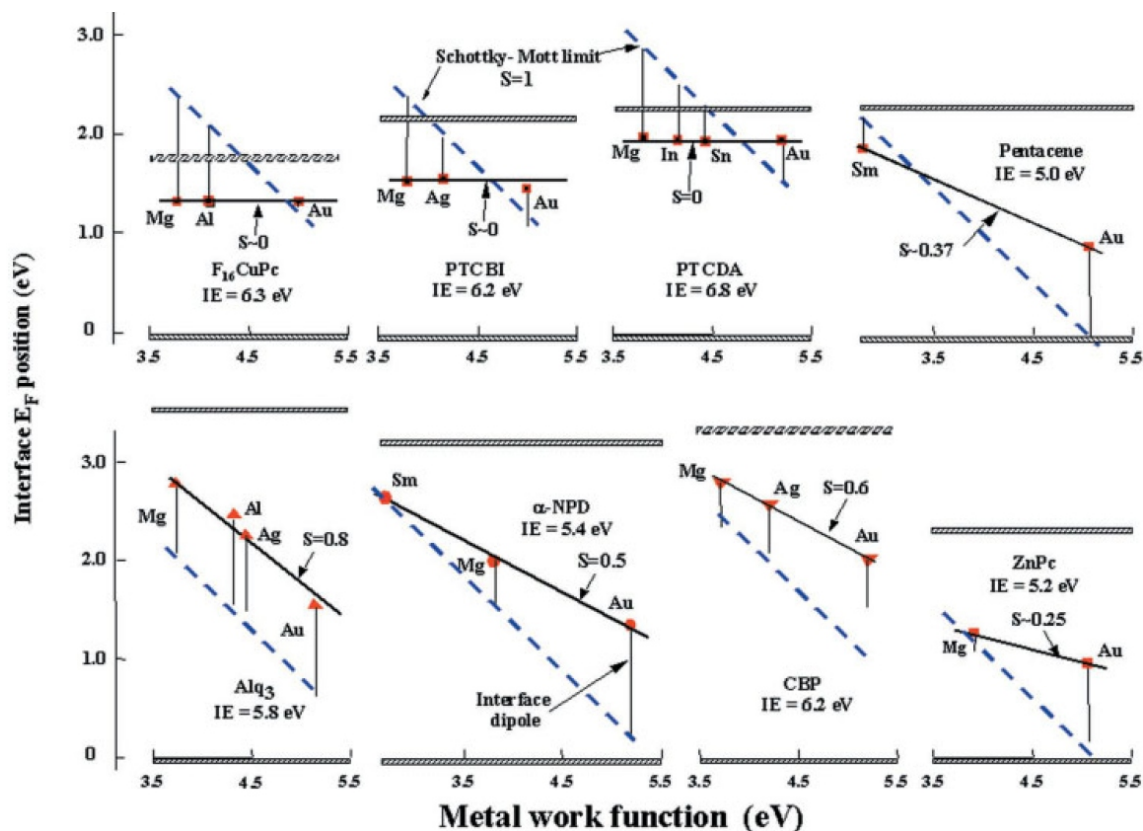


Figure 2.15: Measured interface position of E_F with respect to HOMO and LUMO as a function of the substrate work function for eight different organic materials. In each panel, the thick horizontal bottom and top bars represent the HOMO and LUMO, respectively. The data points were obtained via UPS measurements. The dashed oblique lines correspond to the Schottky-Mott limit of the Fermi level position, and the vertical lines give the magnitude of the measured interface dipole barriers; taken from [76].

examples where S varies between 0 and 0.8 are shown in Fig. 2.15 measured by UPS and taken from Ref. [76].

The discussion in this Chapter so far showed that the injection barrier in an intrinsic organic semiconductor crucially depends on the substrate and on interface reactions that can take place. Therefore, there is in general no Fermi level alignment between the metal and the intrinsic organic. As the HOMO-LUMO gap is usually much larger compared to the thermal activation energy, either an organic semiconductor with a considerable amount of free charge carriers (by intentional or unintentional doping) or a sufficiently thick layer is needed to achieve Fermi level alignment. We can roughly estimate the thickness needed for an intrinsic organic layer to achieve Fermi level alignment by taking typical values of charge carrier concentration 10^{15} cm^{-3} , relative dielectric constant $\epsilon = 3$, and a difference in work functions of $\Delta W_f = 0.5 \text{ eV}$. The depletion layer width can be calculated using the Poisson equation which results in a width of 400 nm. Such thick layers can be analyzed by Kelvin probe measurements. Hayashi et al. investigated the alignment of C60 on the substrates Au, Cu, and Ag [92]. They found that after approximately $0.5 \mu\text{m}$, the work function of C60

settled on the same value for all three substrates indicating a Fermi level alignment, compatible with a charge carrier concentration in C60 of $4.2 \cdot 10^{14} \text{ cm}^{-3}$. Normally the layer thicknesses used in organic semiconductor devices are far below this value and rather in the range of a few tenths of nanometers, so we do not expect Fermi level alignment to take place and flat band condition in intrinsic organic semiconductors.

Organic / Organic Interfaces

Much less interaction takes place when an interface between two organic layers is formed. The van-der-Waals intermolecular forces within and between those layers are weak, and one would therefore not expect any significant interaction between neighboring molecules, even of dissimilar species; partial charge transfer and therefore an interface dipole is not expected.

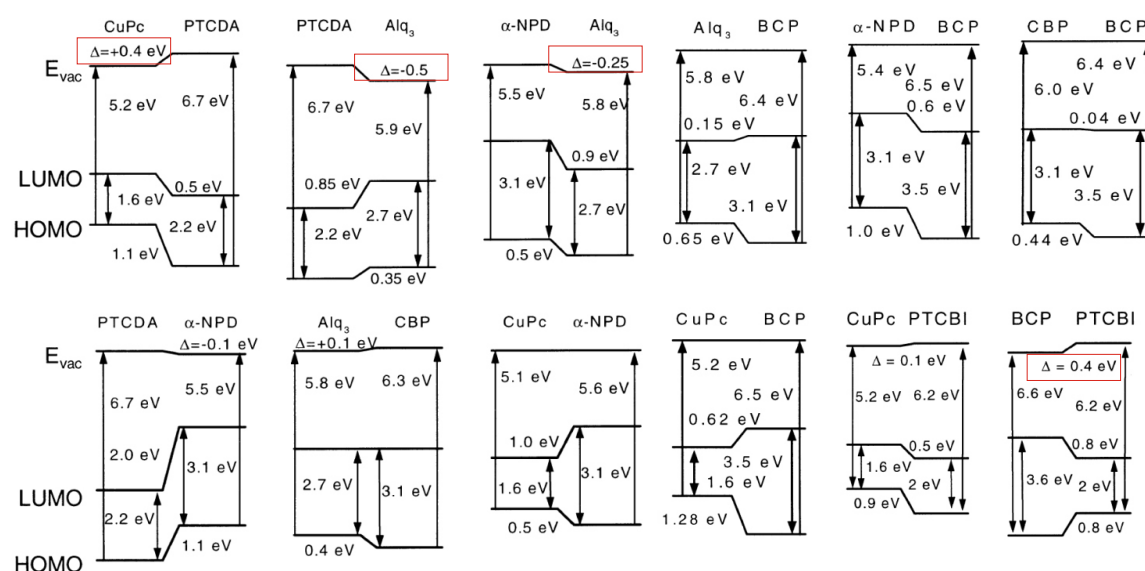


Figure 2.16: Various interface alignments at organic / organic heterojunctions measured by UPS. Mostly vacuum level alignment is observed, significant deviations are marked by the red boxes, taken from [93].

Indeed, there is mostly vacuum level alignment observed between two organic layers [93–97]. Hill et al. [93] looked at a large number of such interfaces and found within the experimental error ($\leq 0.1 \text{ eV}$) vacuum level alignment in most cases (see Fig. 2.16). Therefore, the energy level offsets between the HOMOs / LUMOs can be estimated from the differences of the IPs / EAs. However, there are exceptions to that rule and in these cases, vacuum level alignment does not take place.

Dipoles occur at interfaces between two materials of strongly differing ionization energies and electron affinities. Here, an electron can be partially transferred from the low ionization potential constituent to the high electron affinity molecule. An example is the combination of TTF¹⁸ and TCNQ where a dipole of 0.6 eV occurs

¹⁸Tetrathiafulvalene

due to the electron transfer from the electron donating TTF to the electron accepting TCNQ [98]. This is even more pronounced for material combinations whose bandgaps do not overlap. A dipole has to emerge in order for the Fermi energy to be positioned within the gaps. Tang et al. [99] investigated such an interface, where the EA of one molecule ($F_{16}CuPc$: EA = 5.2 eV) exceeds the IP of the other molecule ($CuPc^{19}$: IP = 4.8 eV), shown in Fig. 2.17a. At the interface, the dipole is built up due to a full charge transfer from the $CuPc$ to the $F_{16}CuPc$. This furthermore leads to level bending on both sides of the interface.

Interfaces between materials with different gap sizes or with an offset between the gaps can show a substrate dependent dipole formation too, as shown in Fig. 2.17b. Tang et al. [100] showed that the dipole depends on the work function of the first semiconductor and thereby on the substrate that is used. A $CuPc/Alq_3$ junction formed on an indium tin oxide substrate shows the classical vacuum level alignment; since the Fermi level is located close to midgap in the Alq_3 , the $CuPc$ evaporated on top can align without charge redistribution. The same junction formed on a Mg substrate exhibits Fermi level pinning at the LUMO of $CuPc$ accompanied by a charge transfer and level bending as the Wf of Alq_3 in this case is smaller than the EA of $CuPc$.

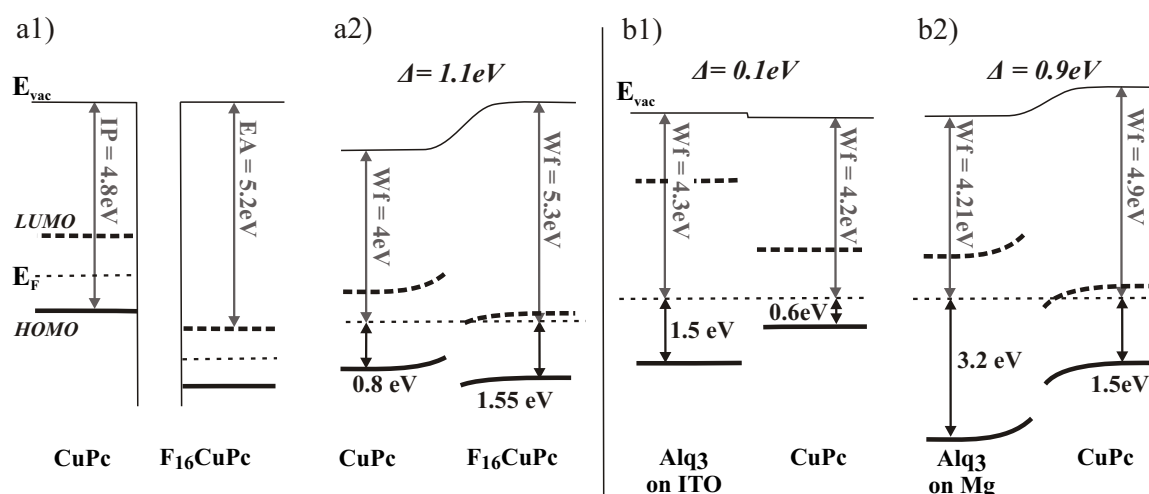


Figure 2.17: Examples for the appearance of interface dipoles for intrinsic organic semiconductor junctions. a1) Energy levels before the alignment and a2) after the alignment of $CuPc$ and $F_{16}CuPc$. Due to the non-overlapping gaps of the organic layers, a charge transfer takes place which results in an interface dipole and level bending; reproduced from [99]. b) Substrate dependent alignment between Alq_3 and $CuPc$: b1) for the deposition on ITO the Fermi levels can align without charge transfer. b2) due to a substrate induced change in work function for Alq_3 on Mg a charge transfer takes place and an interface dipole emerges; reproduced from [100].

There are theoretical approaches by Vazquez et al. [101] to predict the alignment at organic/organic interfaces by applying the same IDIS model known from

¹⁹Copper phthalocyanine

metal / organic interfaces to organic / organic interfaces. They propose that the offset between the charge neutrality levels (CNLs) of the organic layers give rise to a charge transfer across the interface, which induces an interface dipole that tends to align them. They state that the CNL (even though calculated by using the interaction between a metal and organic layer) is an intrinsic property of the organic semiconductor, nearly independent of the substrate the organic is evaporated on. Now the CNLs of the organic layers are considered as the effective Fermi levels of the system and the initial relative positions of the CNLs of the two organic materials determine how charge is transferred between them.

This initial difference in the energies of the CNL is again reduced by a screening factor S , following the Equation:

$$\Delta = (1 - S)(E_{CNL}^{org1} - E_{CNL}^{org2}) \quad (2.30)$$

where S in this case is related to the dielectric functions ϵ of the organic materials and is given by:

$$S = \frac{1}{2} \left(\frac{1}{\epsilon_1} - \frac{1}{\epsilon_2} \right). \quad (2.31)$$

This method gives good results that are similar to experiments, e.g. the interface dipole between PTCDA²⁰ and CuPc is calculated to be 0.43 eV and is measured as 0.4 eV. In agreement with the measurements mentioned before, most values calculated by this method are in the range of 0.1 eV and therefore close to vacuum level alignment [101].

2.3.2 Doped Semiconductors

Interfaces Between Doped Organic Semiconductor Layers and Metals

When doped layers are used, the alignment is more predictable, as now the organic semiconductor has enough charge carriers to reach bulk Fermi level alignment within a depletion layer thickness w of a few nanometers. In the case of a p-doped semiconductor, the mobile holes flow from the organic layer to the metal, building up a negatively charged layer while the metal becomes more positive. An electrostatic potential builds up that suppresses further flow of charge carriers until an equilibrium is reached. The alignment of such a so-called *Schottky contact* is shown in Fig. 2.18. The bending at the metal side can be neglected as the high density of mobile charge carriers levels out the potential drop at once. The magnitude of the built-in voltage V_B created in the semiconductor can be estimated from the difference in work functions:

$$V_B = W_{f_{org}} - W_{f_m} \quad (2.32)$$

²⁰3,4,9,10 perylenetetracarboxylic dianhydride

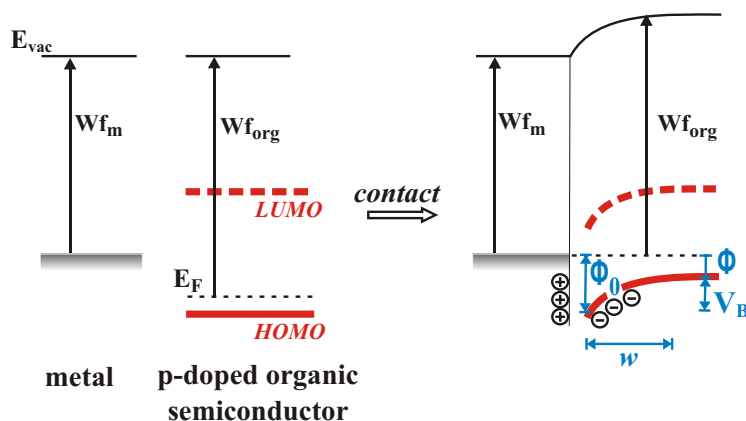


Figure 2.18: Alignment between a metal substrate and a *p*-doped semiconductor before and after contact. Fermi level alignment leads to the diffusion of mobile holes from the organic layer to the metal resulting in the formation of a depletion region.

Using the Poisson Equation, we can find the correlation between the change in potential V_B and the charge carrier density ρ . The latter one can be expressed by the number of free holes p and electrons n and number of ionized donors N_D^+ and acceptors N_A^- :

$$\frac{d^2V}{dx^2} = -\frac{\rho}{\epsilon_0\epsilon} = -\frac{e}{\epsilon_0\epsilon}(p - n + N_D^+ - N_A^-) \quad (2.33)$$

Assuming a complete depletion of charge carriers within the region of width w , the free charge carrier density can be approximated as:

$$\begin{aligned} \rho &= -eN_A^- & \text{if } x < w \\ \rho &= 0, \frac{dV}{dx} = 0 & \text{if } x > w \end{aligned} \quad (2.34)$$

As there is no change in potential outside the depletion layer, it is sufficient to limit the further examination to $x < w$. Consequently, the electric field E can be obtained by integrating Eq. 2.33, which yields:

$$E(x) = -\frac{dV}{dx} = -\frac{eN_A^-}{\epsilon\epsilon_0}(w - x) \quad (2.35)$$

and the potential can be written as:

$$V(x) = -\frac{eN_A^-}{2\epsilon\epsilon_0}w^2 \left(1 - \frac{x}{w}\right)^2 \quad (2.36)$$

Therefore, the potential parabolically depends on the distance in the depletion region. The maximum value is reached at the surface to the metal and is given by:

$$V(x=0) = V_B = -\frac{eN_A^-}{2\epsilon\epsilon_0}w^2 \quad (2.37)$$

and the depletion layer width can be calculated to

$$w = \sqrt{\frac{2\epsilon\epsilon_0 V_B}{N_A^- e^2}}. \quad (2.38)$$

This is of course the ideal case when there is no dipole at the interface arising from one of the various factors mentioned in Chapter 2.3.1. An additional interface dipole Δ will change the value of V_B according to

$$V_B = Wf_{org} - Wf_m - \Delta \quad (2.39)$$

where Δ is negative for a downward dipole and positive for an upward dipole from the metal to the organic layer.

Several studies on the interface alignment between metals and doped semiconductors can be found in literature. As photoelectron spectroscopy can probe all the values shown in Fig. 2.18, it is an ideal tool to study the effect of doping in organic semiconductors. The earliest data published for such a Schottky contact were measured by Blochwitz et al. [10] as already mentioned in Chapter 2.2.2 and shown in Fig. 2.19. Here, ZnPc was doped by F4-TCNQ at a molar ratio of 0.03. They were able to observe the expected low hole injection barrier due to the p-doping and the typical level bending behavior at the interface, resulting in a good ohmic injection. This shows that upon doping, organic and inorganic semiconductors in principle behave similar.

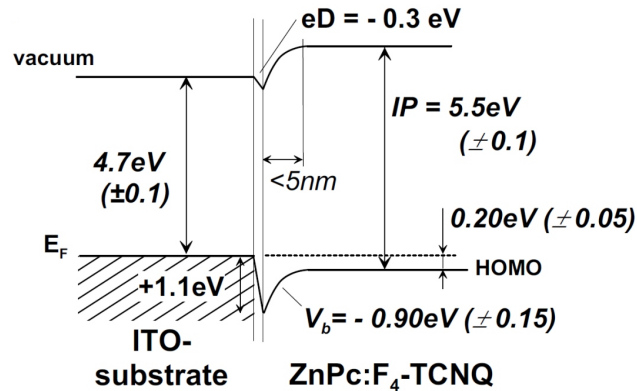


Figure 2.19: Energy level alignment of a Schottky contact between ITO and ZnPc doped by F4-TCNQ at a molar ratio of 0.03 measured by photoelectron spectroscopy; taken from [10].

Interfaces Between Doped Organic Semiconductors - pn and pin Junctions:

A rather new field in organic semiconductor devices is the investigation of interfaces between n- and p-doped layers or the alignment between doped and undoped layers. Such interfaces are relevant for the so-called *pn* junctions or *pin* junctions which are schematically shown in Fig. 2.20. These are of great importance both in modern electronic applications and in understanding basic physics of the doping in organic semiconductor layers. The interfaces are differentiated between *homojunctions*, with

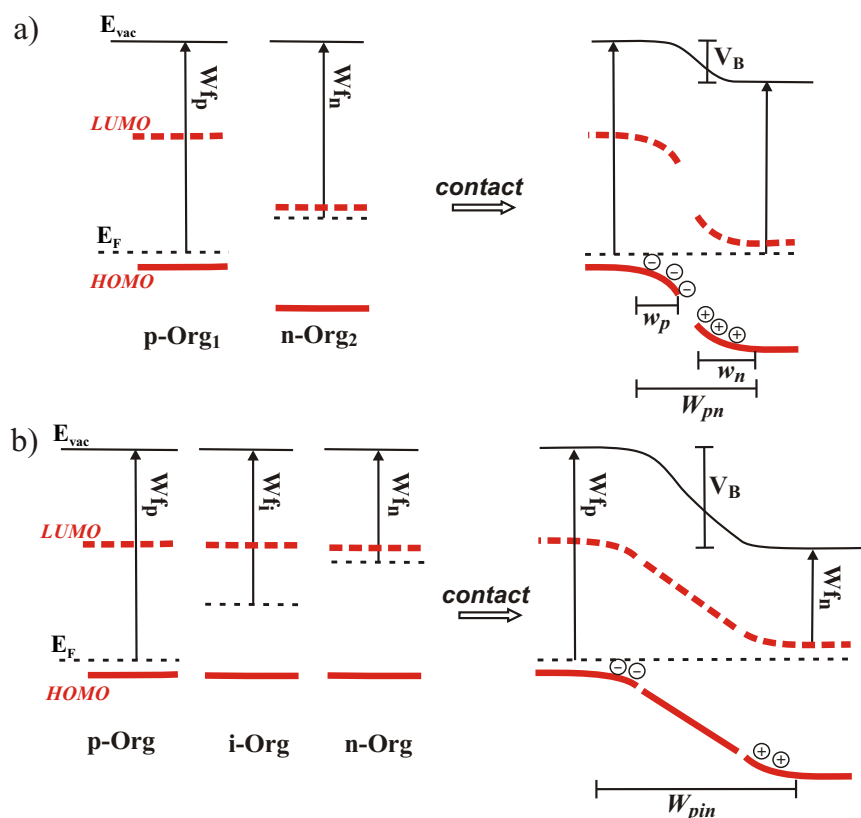


Figure 2.20: a) Schematic energy diagram before and after contact of a heterointerface between a *p*-doped organic1 and a *n*-doped organic2, forming a *pn* junction. b) Schematic energy diagram of a homojunction between a *p*-doped, intrinsic, and a *n*-doped layer of the same organic material forming a *pin* junction

the same matrix material forming the *p*- and *n*-doped layer (Fig. 2.20b), and *heterojunctions* where two different matrix materials are used (Fig. 2.20a).

Similar to the formation of a contact between a metal and a doped semiconductor, the Fermi level of the *pn* junction is aligned in equilibrium. Therefore, the electrons near the interface have to diffuse into the *p* region, leaving positively charged ions in the *n* region behind. Similarly, holes near the *pn* interface begin to diffuse into the *n*-type region, leaving behind fixed ions with negative charge. The regions close to the *pn* interfaces lose their neutrality and become charged, forming the depletion layers on the *p*-side w_p and *n*-side w_n . The electric field created by the depletion region again opposes the diffusion process for both electrons and holes and is in analogy to Eq. 2.35 given by:

$$E(x) = \frac{eN_A^-(x + w_p)}{\epsilon} \quad \text{if } -w_p \leq x < 0$$

$$E(x) = \frac{eN_D^+(x - w_n)}{\epsilon} \quad \text{if } 0 < x \leq w_n.$$
(2.40)

This results in a depletion layer width $W_{pn} = w_p + w_n$ of

$$W_{pn} = \sqrt{\frac{2\epsilon}{e} \left(\frac{N_A^- + N_D^+}{N_A^- N_D^+} \right) V_B}.$$
(2.41)

First experiments aiming to build such a *pn* junction device as known from inorganic semiconductors showed that this concept is not applicable to organic semiconductor devices. Due to the very narrow depletion width in the adjacent layers, blocking behavior for reverse bias is not achieved as the charge carriers can easily tunnel from the LUMO of the n-doped layer to the HOMO of the p-doped layer [17]. This results in almost symmetric ohmic behavior in forward and backward direction. For this reason *pin* junctions have to be used to prevent the tunneling process. In such a device, the built-in voltage drops across the intrinsic interlayer, having a thickness D_i and the depletion layer width is modified to

$$W_{pin} = w_p + D_i + w_n = \sqrt{D_i^2 + \frac{2\varepsilon}{e} \left(\frac{N_A^- + N_D^+}{N_A^- N_D^+} \right) V_B}. \quad (2.42)$$

2.3.3 Level Bending vs. Alternative Explanations

Since the first reports of level bending effects in intrinsic or doped organic semiconductors, there has been an ongoing discussion of whether this effect is really due to the same principles as in inorganic semiconductor physics. The appearance of level bending and the resulting depletion region implies the presence of ionized species, and therefore mobile charge carriers, which have been removed from the region which exhibits level bending [86]. There are several publications mentioning level bending in intrinsic layers [102–105]. This is rather unlikely, as typical charge carrier concentrations in purified intrinsic layers are in the order of 10^{-1} cm^{-3} to 10^{-15} cm^{-3} [92, 106, 107] and therefore should have depletion layer widths that are in the range of several hundred nm to a few μm .

Indeed, it was found that for intrinsic layers, other mechanisms lead to effects mimicking a level bending behavior at the interface which are shown in Fig. 2.21. First of all, the screening of a charge on a molecule depends on the polarizability of the surrounding [29, 108] and is therefore different at the surface of a metal compared to the bulk (see Chapter 2.1.2 and Fig. 2.21b). Therefore, the molecules in the first layer show a lower ionization potential (and higher EA) compared to the second and following layers. It can take several nm until the bulk value is reached. Characteristic for such a process is an abrupt change in vacuum level, indicating the interface dipole, and a slower change in HOMO position. Some studies on this effect can be found in Refs. [108–110] and an extensive review is published in Ref. [111].

This effect will take place for most interfaces to some extent, but other factors are present as well. For example, a change in growth mode can lead to a change in IP as well (Fig. 2.21c) since it will effect the intermolecular interaction which affects the π -electron system. This was shown in several studies for CuPc where the first monolayer tends to be rather flat on the surface, while in the following layers the molecules are standing upright [112, 113]. Furthermore, if the molecule has a strong tendency to cluster (e.g. NTCDA²¹) it might take some nm for the interface dipole

²¹1,4,5,8-naphthalene tetracarboxylic dianhydride

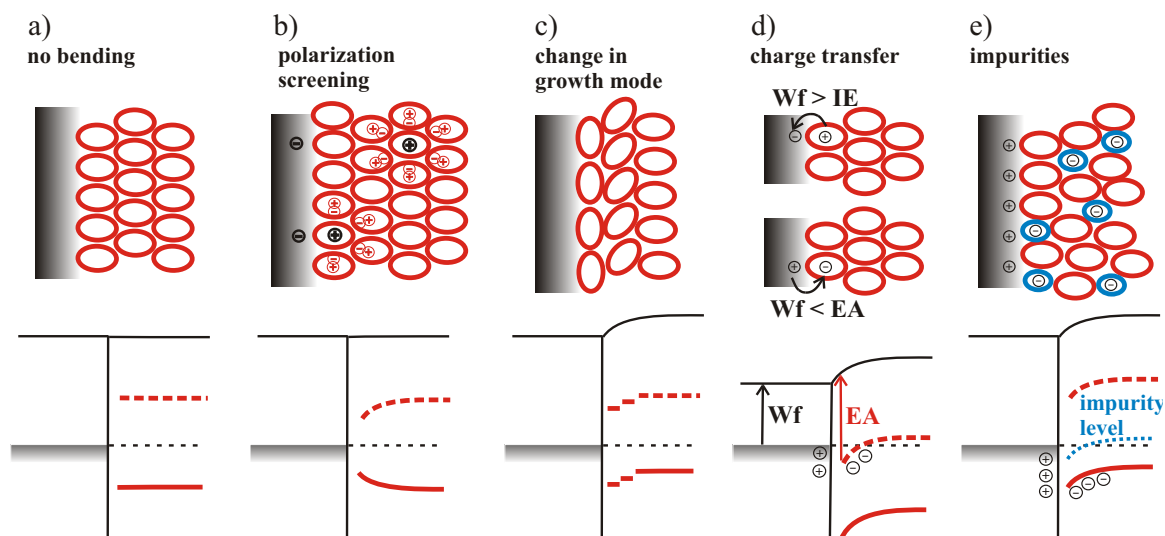


Figure 2.21: Different effects that can induce or mimic a level bending in intrinsic semiconductors. a) Ideal case where no level bending takes place, b) due to an increased polarization screening at the interface the HOMO and LUMO levels are relaxed further into the gap, c) a change in growth mode can lead to a change in HOMO/LUMO positions at the interface, d) in case of $W_f > IE$ or $W_f < EA$ a real charge transfer takes place leading to an depletion region, e) unintentional impurities by insufficient purification of the material or incorporation of residual gas during evaporation can induce a doping that increases the charge carrier concentration, making level bending possible.

to form, as the surface remains partially uncovered. This will result in a slow change in vacuum level that can be misinterpreted as a level bending; however, the HOMO level should not be affected except by the previously mentioned screening effect.

Only in one case, real level bending can take place for intrinsic semiconductors: if the work function of the metal exceeds the IP or is smaller than the EA, a charge transfer appears at the interface leading to an interface dipole that moves the HOMO below or lifts the LUMO above the Fermi energy, respectively (Fig. 2.21d). This results in a depletion region and thereby a level bending [114].

Finally, in some cases it has to be noted that either the purification process is insufficient leaving behind impurities, or the vacuum during processing is not sufficient and residual gas (mainly oxygen) is incorporated into the layer. This is called unintentional doping (Fig. 2.21e) and can lead to an increase in free charge carriers, promote conductivity, and produce a level bending [115]. However, more often this results in the appearance of trap states that decrease the conductivity and lead to lower device performance [111].

It has even been doubted that for doped layers a depletion layer is created. A decrease in hole injection barrier that is attributed to p-doping could, according to this theory, be due to a diffusion of the dopants to the metal interface where a CTC between the dopant and the metal is created. This CTC lowers the injection barrier and mimics a doping effect. Duhm et al. [116] were able to show this effect for a thin

CBP²² layer that was subsequently covered by F4-TCNQ. Even though the HOMO of CBP is too low to be dopable by F4-TCNQ, they were able to observe an energy level shift towards E_F .

Two characteristics have to be shown in an organic layer to prove that a level bending is really due to the presence of sufficient charge carriers forming a depletion region and not an effect of some other kind as mentioned before. The level bending must lead to an alignment of the substrate and semiconductor Fermi levels. Therefore, independent of the metal work function, the semiconductor work function always has to show the same value [117]. Furthermore, these charge carriers have to result in a significant increase in conductivity.

2.3.4 Metal Layers on Organic Semiconductors

The discussion so far was done on abrupt interfaces when soft and thermally slow molecules are deposited on a metal surface or on another organic layer. However, when forming a metal top contact, the metal atoms hitting the organic surface carry a significant thermal energy due to the high evaporation temperature. This can lead to a diffusion of the metal into the organic layer forming a deep mixed organic-metal layer at the interface. The physics happening here are more complex compared to bottom contacts and strongly depend on the combination of metal and organic material [23]. However, it is of crucial importance to understand this interface as it is present in any device.

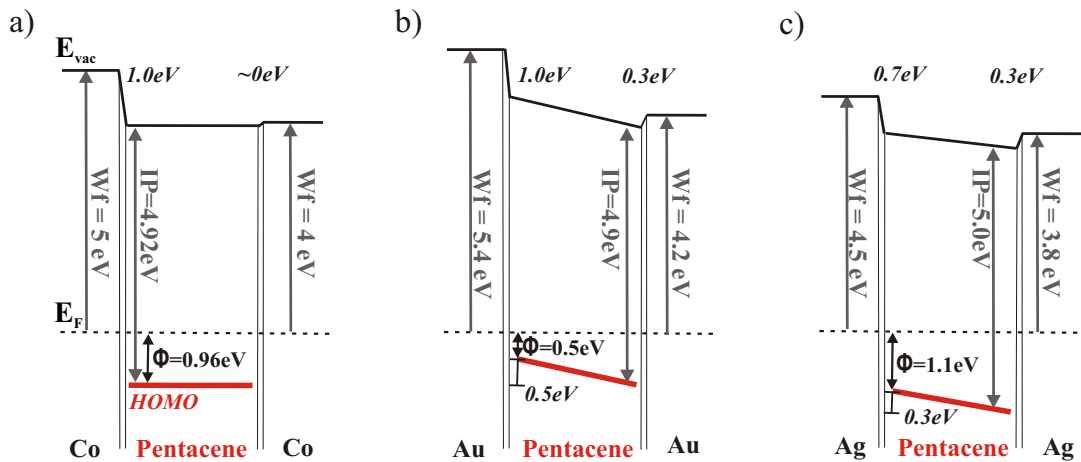


Figure 2.22: Energy diagrams for various interfaces between Pentacene and different metal bottom and top contacts: a) forming a symmetric alignment with Co, data taken from [118], and forming asymmetric contacts with b) gold, as well as c) silver, both taken from [119]. None of the top contacts show the expected work function seen in the bottom contact.

Measurements by UPS and XPS yield information on coverage and chemical reactions at such interfaces. Seki et al. [117] deposited 125 nm gold on top of 6P²³ and

²²4,4'-Bis(N-carbazolyl)-1,1'-biphenyl

²³P-sexiphenyl

found still the signal originating from the organic layer instead of a pure gold film. They concluded that gold diffuses into the 6P layer, leaving a surface dominated by 6P molecules. On the other hand, when they deposited 100 nm of Mg on top, this covered the organic layer of 6P, i.e. less diffusion seems to take place here. A similar observation was made by Watkins et al. [119] for gold and silver deposited on Pentacene. The signal from the organic layer did not vanish and so a pure metal spectrum was not achieved. This was different if they use Ca contacts with Pentacene; for this combination the metal top layer is closed, and the correct Wf for Ca was achieved. Furthermore, they found large differences in the hole injection barriers for the bottom and top contacts in the case of Au/Pentacene/Au and Ag/Pentacene/Ag as is shown in Fig. 2.22b,c. It can be concluded that effects like doping by the metal atoms or at least the formation of trap states pinning the Fermi energy have a large effect on the interface dipole formation. A different behavior was found by Popinciuc et al. [118] for Co/Pentacene/Co interfaces which exhibit identical injection barriers for bottom and top contacts. However, the Wf of the top metal contact was smaller by 1 eV compared to a pure Co layer (Fig. 2.22a).

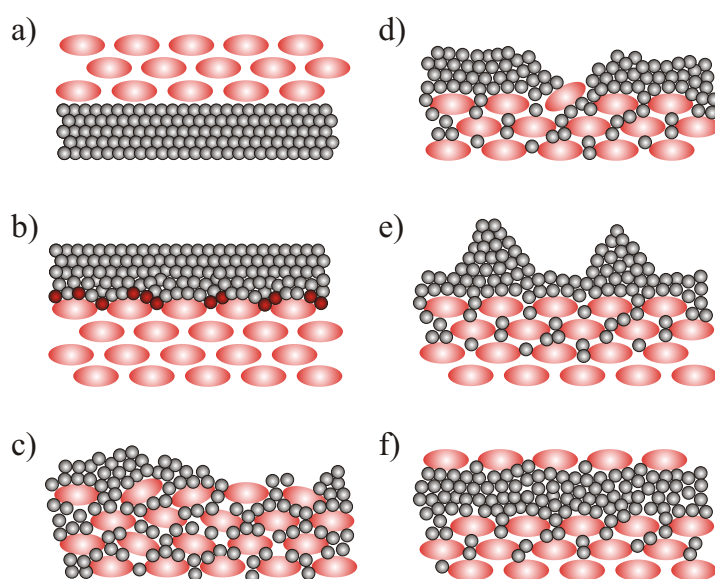


Figure 2.23: Different possible interface formations for metal contacts (black marbles) on a layer of molecules (red ellipses): a) Abrupt formation of a metal bottom contact, b) abrupt metal top contact due to reaction between metal and semiconductor, c) strong diffusion of metal atoms, leaving the bare surface, d) cracks in the metal surface due to different heat capacitance, e) island growth of metal atoms, f) monolayer of molecules on top of metal due to reduced surface energy or reabsorption of desorbed molecules after the metal evaporation process.

From these examples and many more studies that have been published [23, 76, 78, 120–124], it can be concluded that in most cases the interface formed at a metal top contact differs from a bottom contact. Furthermore, in almost all cases a residual signal from the organic layer is observed, and the metal top contact does not show

the correct work function even after the deposition of more than 100 nm. Several attempts to explain the interface formation between organic layers and metal top contacts have been published so far that are summarized in the following listing and are shown in Fig. 2.23:

- Abrupt interface formation (Fig. 2.23 b): This mainly takes place for reactive metals that can undergo a chemical bond with the molecule which stops the diffusion process as in the case of Pentacene-Ca [119] or CuPc-Sn [121]. It leads to a fast suppression of the organic features and the correct work function of the metal top layer is measured. Such an abrupt boundary was found for some interfaces with gold as well, e.g. for PTCDA - Au [120] or CBP - Au [125].
- Strong diffusion (Fig. 2.23c): This can explain a less efficient coverage on an organic layer as a large fraction of the atoms is diffusing into the organic layer leaving the surface partly uncovered [119]. However, such a model cannot explain why a metal contact much thicker than the organic film does not produce a closed layer.
- Cracks in the metal surface (Fig. 2.23d): Ihm et al. [122] investigated a 380 nm gold contact on Pentacene that still showed signal from the organic layer in their UPS measurements. With transmission electron spectroscopy they saw cracks in the top contact, exposing the underlying Pentacene layer, due to thermal contraction during the process of cooling down the sample after metal deposition.
- Island formation (Fig. 2.23e): If the metal atoms cluster during the evaporation and form islands on the surface two effects can appear: on the one hand a thinner effective thickness of the metal overlayer will form and secondly, the measured work function of such metal clusters differs from the value of the metal bulk [118].
- Reabsorption after metal evaporation (Fig. 2.23f): During metal evaporation, the temperature of the sample increases due to the hot metal atoms hitting the surface. This might desorb some of the organic molecules from the top which reabsorb as soon as the temperature of the sample is decreased again. This leads to a thin layer of organic material on top of the metal layer [122].
- Diffusion of molecules (Fig. 2.23f): As the organic layer typically has a lower free surface energy compared to a metal layer, it is energetically advantageous if a monolayer of organic molecules remains on top during the growth process of the metal layer [123, 126].
- Crystalline structure formation: Different single crystal faces of the metal surface are created upon deposition on the organic layers. These have Wfs that differ from the value of the polycrystalline metal [124].

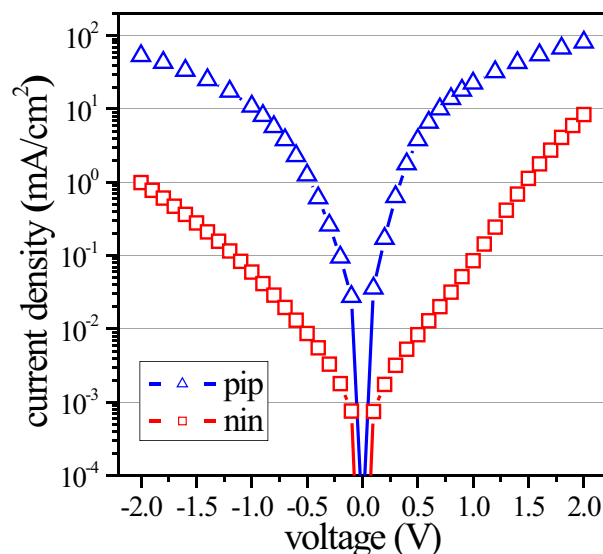


Figure 2.24: Current density-voltage characteristics of a symmetric *nin* electron only device (squares) consisting of Ag - BPhen:Cs - BPhen - BPhen:Cs - Ag and a *pip* hole only device (triangles) consisting of Ag - MeO-TPD:F4-TCNQ - MeO-TPD - MeO-TPD:F4-TCNQ - Ag, taken from [127], showing that for *p*-doped layers a symmetric hole injection from the bottom and top contact is achieved while for *n*-doped layer, the electron injection from the top contact is favored.

A further significant way of investigating the formation of bottom and top contacts is the measurement of current-voltage characteristics for devices, where an organic layer is sandwiched between two identical metal contacts. The behavior of such devices in forward and backward direction seems to strongly depend on the material combination. In some cases, symmetric injection from both contacts has been observed [128–130] while in other cases one of the two directions is more favorable [131–136]. Symmetric injection has even been observed in cases where UPS measurements show different injection barriers as it is the case for the Mg-Alq₃ vs. Alq₃-Mg interface [129]. In a few cases, the asymmetry was found to originate from a contamination of the bottom electrode before the organic layer was evaporated on top [133]. However, even if the vacuum was not broken and contamination cannot be the reason the injection behavior differs. In these cases, a doping effect by penetrating metal atoms [131] or a reaction with the metal atoms [135] are responsible for the effect.

For the injection into doped layers an asymmetric behavior was found as well. The effect is especially pronounced for *n*-doped layers as can be seen in Fig. 2.24 (from Ref. [127]). Here, the electron only device, consisting of BPhen doped by Cs, has a much higher injection from the top contact compared to the bottom one. This is attributed to an additional doping effect by the Al atoms diffusing into the BPhen layer, introducing new states in the gap that facilitate the electron injection [127]. In the *p*-doped layer in Fig. 2.24, consisting of MeO-TPD doped by F4-TCNQ, no difference between the injection from bottom or top contacts is observed.

2.4 Optoelectronic Applications of Organic Semiconductors

The quickly growing field of optoelectronic devices based on organic semiconductors offers the potential to surpass the current technology based on silicon in some applications. The advantages of organic electronics mainly lie in the potential of low cost production and the much easier handling of the materials. Furthermore, the thin organic layers can be produced on a large variety of substrates, including flexible transparent foils. The two most important device concepts will be introduced in the following, being organic light emitting diodes (OLEDs) and organic solar cells.

2.4.1 Organic Light Emitting Diodes

In organic light emitting diodes, holes and electrons are injected into a device consisting of semiconducting layers where they move towards the opposite electrode under the electric field and recombine to produce light. Current high performance OLEDs consist of a so called *pin* stack, where the intrinsic light producing layer is incorporated between p- and n-doped transport layers. Such a device is shown in Fig. 2.25. The doped hole transport layer (HTL) and electron transport layer (ETL) allow for ohmic injection, good transport properties, and high mobility. These layers make up most of the thickness of the device (≈ 200 nm). Electron and hole blocking layers (EBL/ HBL) are needed next to the transport layers. On the one hand, these act as a spacer to the dopants that would otherwise quench the electroluminescence, and on the other hand, these layers avoid losses due to either electrons or holes traveling through the complete device which then cannot contribute to the emission. In the middle of the OLED stack is the emission layer (EML), where the light is generated, either by a fluorescent molecule or a phosphorescent emitter. In most phosphorescent OLEDs, the emission layer is a host-guest system. There, the phosphorescent emitter material is doped into a matrix material which itself does not contribute to the light emission.

These intrinsic layers in the OLED stack are typically only 40 nm thick and are chosen in a way that allows for a good charge balance, which means that the number of holes and electrons in the EML is comparable. In such a device, with a red phosphorescent emitter, typical brightnesses of 100 cd/m^2 are achieved at 2.4 V [137] which is a sufficient brightness for displays.

As anode material, mostly indium tin oxide (ITO) is used as it has a low sheet resistance of $20\text{-}30 \text{ }\Omega/\text{cm}^2$, is transparent with a transmission of 90%, has a high work function, and can be produced very smooth with a roughness of around 1 nm. Through this layer the light is coupled out, while for the cathode a thick metal layer is used that reflects the light. An alternative to this so called *bottom-emission OLED* is the *top-emission OLED* where a thin transparent metal top contact is used to couple out the light.

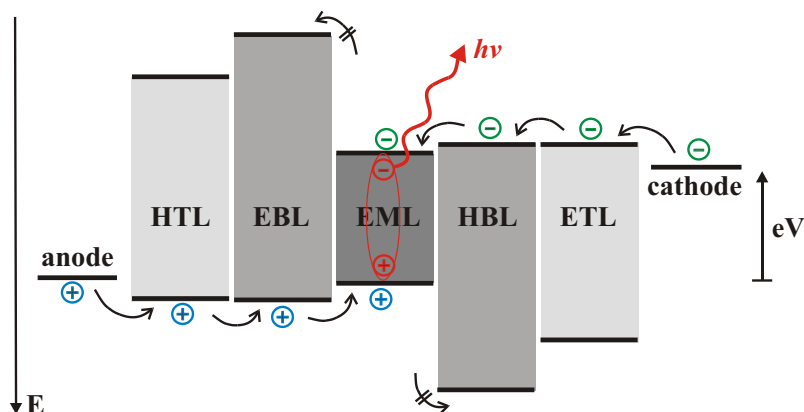


Figure 2.25: Schematic band diagram of a multilayer OLED device where a voltage eV is applied to inject the charge carriers that form excitons in the emission layer (EML) and emit light. The doped hole and electron transport layers (HTL/ETL) lead to good carrier injection and the hole and electron blocking layers (HBL/EBL) confine the charge carriers in the emission layer.

2.4.2 Organic Solar Cells

In organic solar cells, light is absorbed by an active layer and converted into a current. This cannot be achieved efficiently by a single layer, as the exciton binding energy in organic semiconductors is too high to separate the exciton produced by a photon and therefore conversion efficiencies are below 0.1%. To circumvent this problem, an exciton separating interface is introduced which is schematically shown in Fig. 2.26. Here, a preferably hole conducting material (donor) and a electron conducting material (acceptor) are used. The absorption of light in either one of these layers leads to the formation of an exciton that diffuses to the donor-acceptor interface, where an offsets between the LUMOs and HOMOs in the range of 0.5 to 0.6 eV separates the charge carriers. Then, the charge carriers diffuse through the transport layers to the anode and cathode where they can be extracted. It is crucial that these transport layers show a good conductivity (achievable by doping), have large band gaps so that no light absorption takes place, and furthermore excitons cannot diffuse to the metal contacts where they would be quenched. At the donor-acceptor interface, a Fermi level splitting appears under illumination due to the separation of the charge carriers that can be measured as the *open circuit voltage* V_{OC} of the device. The value depends on the $\text{HOMO}_{\text{donor}} - \text{LUMO}_{\text{acceptor}}$ offset at the interface as well as the exciton binding energy.

The disadvantage of this device architecture is the limitation to thin absorption layers. As the exciton diffusion length is in the range of 10 nm, the thicknesses of the absorption layers are limited to this value, otherwise the excitons will not reach the donor-acceptor interface. However, thicker layers would lead to more absorption and therefore higher efficiencies. Two concepts can be used to overcome this problem. First of all, mixed active layers can be used where donor and acceptor material are co-evaporated. This way, there are exciton separating interfaces throughout the whole

layer, but it has to be assured that the materials form paths, so the produced charge carriers reach the transport layers from which they can be extracted. Again, the layers cannot be chosen too thick.

Furthermore, *tandem cell* structures can be used. In such a device, two or more solar cells are stacked and connected via recombination layers. The effective thickness of the absorption layer is increased and furthermore different absorption bands can be used. Currently organic solar cells with such a *pin* tandem structure reach certified efficiencies of 6.1 % on an area of 2 cm² [11].

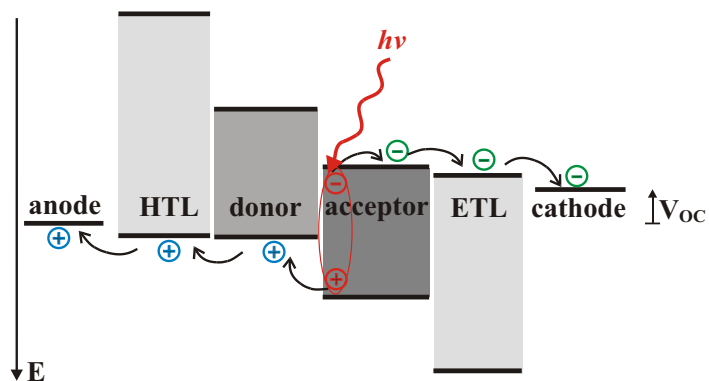


Figure 2.26: Schematic band diagram of an organic solar cell device. Absorption of light produces excitons on either side of the donor-acceptor interface. At the interface they are separated into free charge carriers, which leads to a Fermi level splitting of V_{OC} , and are transported to the contacts through the doped transport layers.

3 Materials and Experimental Setups

In this Chapter, we describe the molecules under investigation and their main physical properties as well as the process of sample preparation. Then, the experimental setup of photoelectron spectroscopy is introduced. The different methods of UV photoelectron spectroscopy and x-ray photoelectron spectroscopy are discussed in detail, combined with an instruction for the data evaluation. Finally, further measurement techniques of current voltage measurements and impedance spectroscopy are described.

3.1 Materials

The molecules used in organic electronic applications are composed mainly of carbon atoms which introduce the semiconducting properties due to their delocalized π -electron system. Other low atomic-number atoms like O, N, and S are also common building elements that have an influence on the electronic and optical properties. The experiments are limited to the so called small molecules, with molar masses between approximately 300 and 1500 g/mol. Heavier molecules tend to disintegrate before they reach the temperature necessary for evaporation.

Throughout this work, a large number of materials are used that are shown in Fig. 3.1 to 3.4. They can be divided into five classes that are shortly introduced in the following paragraphs. An overview of the materials and their properties can be found in Table 3.1 on page 58. All molecules have been purified by a two step vacuum gradient sublimation, unless stated otherwise.

Hole transport materials: These materials show a good hole mobility; those presented here have an ionization potential that is low enough to be dopable by F4-TCNQ, so below 5.4 eV. The chemical structures of these hole transport materials are given in Fig. 3.1. Most extensively used throughout this work is *N,N,N',N'*-tetrakis(4-methoxyphenyl)benzidine (MeO-TPD) that is a good injection layer for organic solar cells as well as OLEDs [138–141]. This molecule forms smooth amorphous layers and the low IP of 5.1 eV leads to an efficient p-doping and therefore high conductivities. The large optical gap of 2.96 eV makes the material transparent which is important

for optoelectronic devices. The disadvantage is the rather low glass transition temperature T_g of 55°C.

N,N'-Di(4-(2,2-diphenyl-ethen-1-yl)-phenyl)-*N,N'*-di(4-methylphenyl) benzidine (PV-TPD) is another wide gap molecule (optical gap 2.77 eV) that is easily dopable due to an IP of 5.2 eV. The higher T_g value of 118°C makes it more stable compared to MeO-TPD. So far it has mainly been employed in solar cells [142] where the large IP leads to an efficient exciton blocking.

N,N'-Di(naphthalene-1-yl)-*N,N'*-diphenyl-benzidine (α -NPD) exhibits in general the same properties as the previously mentioned molecules regarding the good hole mobility, the amorphous growth mode, and the transparency (optical gap 3.12 eV). However, the larger IP of 5.4 V reduces the efficiency of the doping process, therefore much higher doping concentrations are needed. The material is rather used as blocking layer in OLEDs [143] to stop the electrons from moving through the whole device.

The remaining two molecules *Pentacene* and *Zinc-phthalocyanine* (ZnPc), which was three times sublimated, have smaller optical gaps of 1.82 eV and 1.5 eV so they show absorption in the visible range. Accordingly, they are not suited as hole transport layers in optoelectronic devices even though they are easily dopable with an IP of 5.1 eV in both cases. The small transport gap leads to a high electron affinity ($EA_{ZnPc} = 3.3$ eV, $EA_{Pentacene} = 2.8$ eV) and therefore these molecules are n-dopable as well. This makes them suitable for the use in *pin* homojunctions. Furthermore, ZnPc is commonly used as an absorber in solar cells as well [144]. Pentacene is less suitable for such an application as it produces very rough layers.

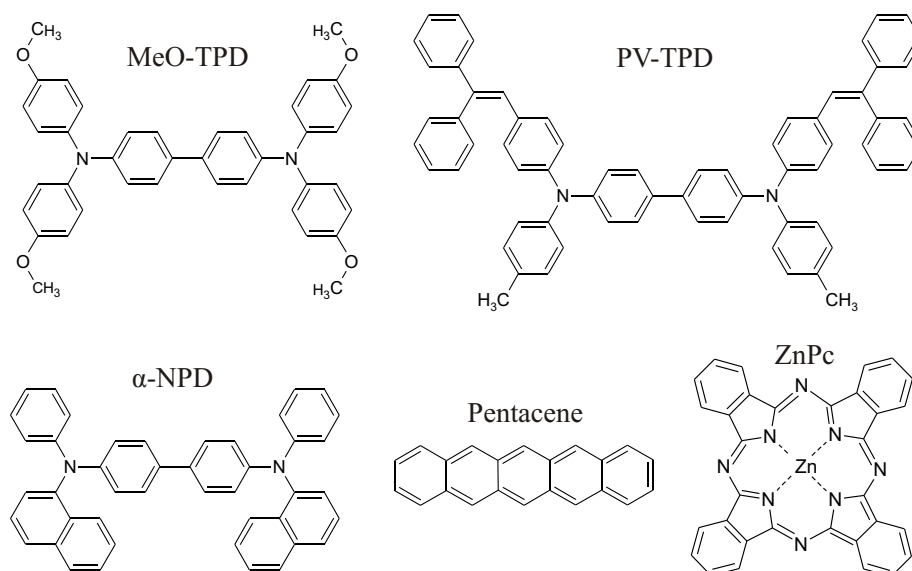


Figure 3.1: Shown are the structures of the molecules used as hole transport materials throughout this work.

Electron transport materials: This class of material shows a dominant electron conduction and the chemical structures of those investigated in this work are shown

in Fig. 3.2. The best known material is C60, which has been three times sublimated, that has a high electron affinity of 4 eV and is therefore dopable by any of the n-dopants mentioned later in this Section. The ionization potential is measured to be 6.4 eV. The optical gap of 1.95 eV makes it less suitable for transport layers in OLEDs where it would lead to absorption; the main application is rather as an absorber in organic solar cells [144, 145]. For this purpose, the good stability and high triplet diffusion length is advantageous as well.

4,7-diphenyl-1,10-phenanthroline (BPhen) is a wide gap electron transport material ($E_g^{opt} = 3.52$ eV) well suitable for the application as electron injection layer for OLEDs when n-doped by Cs atoms. Due to an electron affinity of approximately 2 eV it is not dopable by most molecular n-dopants. It is furthermore used as a hole blocking material in OLEDs, but as it shows an increased reactivity with emitter molecules the lifetime of such devices is decreased. The much better suited material for this blocker layer is *Aluminum(III)bis(2-methyl-8-quinolino)-4-phenylphenolate* (BALq) that has an IP of 6.08 eV and an optical gap of 3.44 eV. This material is furthermore used for the Zener diodes presented in this work as electron transport material.

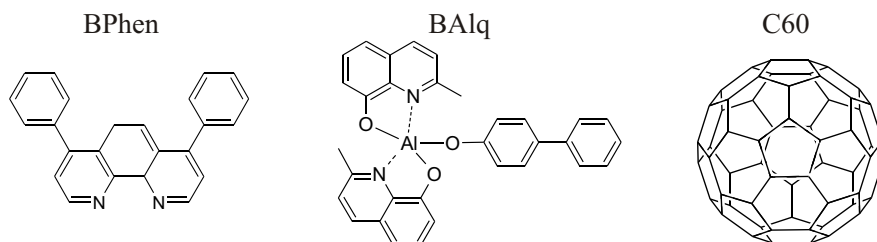


Figure 3.2: Shown are the structures of the molecules used as electron transport materials throughout this work.

Dopant molecules: All the hole transport material mentioned so far can be p-doped by co-evaporation with the small molecule *2,3,5,6-tetrafluoro-7,7,8,8-tetracyanoquinodimethane* (F4-TNCQ) which has been one time sublimated; typical doping ratios are between 4 mol% and 30 mol%. The EA was measured to be 5.24 eV [8] so it provides an efficient charge transfer for molecules with $IP \leq 5.2$ eV. It was found that it can dope materials down to $IP = 5.4$ eV, however a larger amount of the dopant is necessary. Due to the small molecular weight of this compound, it has a low evaporation temperature around 70°C and behaves very volatile inside a preparation chamber. Adjacent materials commonly show an unwanted background doping after some time.

This is the reason why in some experiments the more stable p-dopants NDP2 and NDP9 are used, provided by the Novald AG, that do not show the volatile behavior and have higher evaporation temperatures. The structures of these molecules can not be shown as they are proprietary commercial materials. Both molecules have a lower lying LUMO compared to F4-TNCQ and can therefore dope materials with

even higher values of IP. It is possible to use NDP2 down to an IP_{matrix} of 5.5 eV and NDP9 for $IP_{\text{matrix}}=5.6$ eV.

A new dopant that was investigated during the work on the thesis is the fluorinated Fullerene C60F36 that was published to have a doping effect in P3HT¹ [146]. Due to its large molecular weight it has an evaporation temperature of 120°C and shows a doping strength comparable to NDP2. The ionization potential is measured to be 8.38 eV and the optical gap is 2.48 eV.

The most common small molecule n-dopant is *3,6-bis(dimethylamino)acridine* (AOB). It has an IP of 4.98 eV and was found to be able to dope materials with an EA of 4 eV or more. Hereby, the doping is achieved by an irreversible redox reaction with matrix molecules that only takes place if the sample is illuminated during the deposition of the layer. This molecule has again a very low evaporation temperature and shows volatile behavior. As an alternative, there is a n-dopant provided by Novald under the acronym of NDN1. It shows a higher evaporation temperature and higher doping strength. Due to its very low ionization potential it is however very reactive and can only be kept and transferred under nitrogen atmosphere which makes the handling challenging.

A much easier way to achieve a n-type doping is by the co-evaporation of Cs atoms. This leads to a good conductivity of e.g. $2 \cdot 10^{-5}$ S/cm in BPhen at a ratio of 1 Cs atom per molecule. However, the small atoms have the disadvantage that they tend to diffuse.

The chemical structures of these dopants are given on the left side of Fig. 3.3.

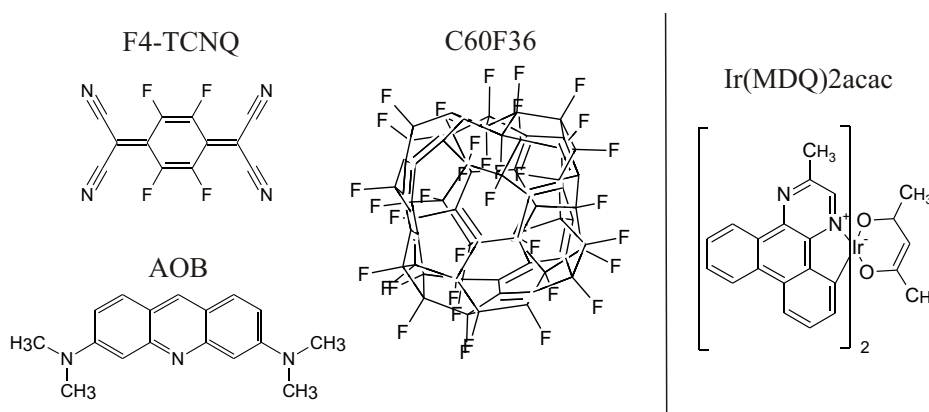


Figure 3.3: The left side shows some of the dopants used throughout this work. The proprietary dopant materials NDP2, NDP9 and NDN1 can not be shown. The right side shows the emitter material $Ir(MDQ)_2(acac)$.

Emitter molecule: Emitter molecules are used in OLEDs to generate the characteristic light emission by exciton recombination. Most commonly, phosphorescent molecules are used where the light is produced by a triplet exciton. For this spin-forbidden transition to be possible, these phosphorescent molecules have a heavy atom

¹Poly-3-hexylthiophene

incorporated that leads to a mixing of singlet and triplet states via spin-orbit coupling. The molecule under investigation in this work is *Iridium(III)bis(2-methyldibenzo[f,h]-quinoxaline)(acetylacetonate)* ($\text{Ir}(\text{MDQ})_2(\text{acac})$) where the heavy atom is Iridium. The IP is 5.36 eV and the EA measured by cyclic voltammetry 2.76 eV. The phosphorescent molecule emits an orange red light with a maximum at 614 nm.

Contact materials: Throughout this work, mostly an amorphous silver foil (99.995 % purity, 0.25 mm thickness) is used as substrate for the evaporated layers; furthermore the usage of gold foil is possible (99.99 % purity, 0.125 mm thickness). The substrates are cleaned by argon sputtering before performing the first measurement to achieve a clean metal surface. These substrates can be reused several times by again performing argon sputtering to remove the organic layer investigated during the previous measurement. The argon gas is used at a partial pressure of $3 \cdot 10^{-5}$ mbar at 1.6 kV; the sputter time depends on the thickness of the contamination layer and ranges from 4 to 20 min.

Furthermore, the conductive polymer *Poly-(3,4)ethylenedioxythiophene* (PEDOT) doped by *Polystryrene sulfonate* (PSS) is used that is shown in Fig. 3.4a. This PEDOT:PSS layer is prepared by a spin cast process on a glass substrate and shows a conductivity of 10^{-5} S/cm. The Wf of this doped polymer is 5.1 eV and therefore comparable to gold. It can be used as an alternative transparent anode material to ITO [147]

Finally, the transparent metal oxide *indium tin oxide* (ITO) is used in a few cases, as this is a typical anode material for organic semiconductor devices. The sample consists of 90 nm thick ITO on top of a glass substrate and shows a very low roughness of 1 nm at a sheet resistance is 20-30 Ω/cm^2 . For the UPS measurements, samples fully covered by ITO are used (provided by IPMS²) while for the conductivity, current voltage, and impedance spectroscopy measurements the ITO is pre-structured as is shown in Fig. 3.4b.

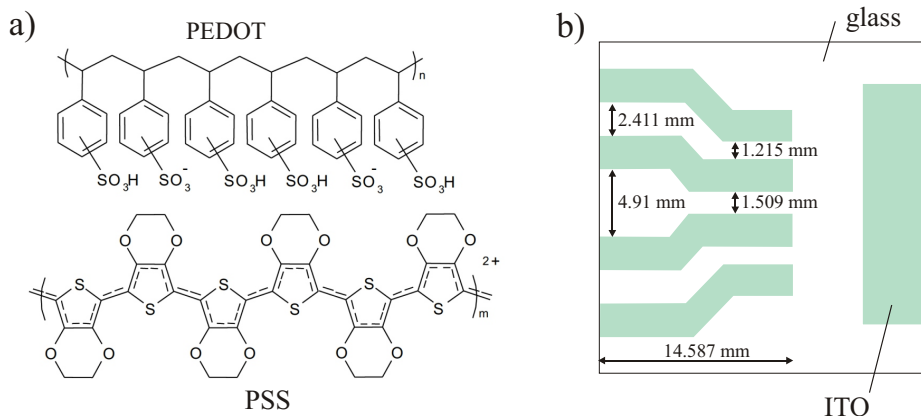


Figure 3.4: a) Chemical structure of the doped conductive polymer PEDOT:PSS. b) Sketch of the sample design of a pre-structured ITO substrate.

²Fraunhofer Institut für Photonische Mikrosysteme

<i>organic material</i>	<i>supplier</i>	<i>sum formula</i>	<i>molar mass (g/mol)</i>	<i>density (g/cm³)</i>	<i>IP (eV)</i>	<i>EA (eV)</i>	<i>optical gap (eV)</i>
MeO-TPD	Sensient	C40H36N2O4	608.73	1.463	5.1	1.9 ^[b]	2.96
α -NPD	Sensient	C44H32N2	558.74	1.14	5.4	2.52 [8]	3.12 [30]
PV-TPD	Sensient	C66H52N2	873.13	1.15	5.2	2.1 ^[b]	2.77
ZnPc	ABCR	C32H16N8Zn	577.92	1.55	5.1	3.3 [30]	1.5 [148]
Pentacene	Sensient	C22H14	278.35	1.35	5.1	2.8 [30]	1.82 [149]
C60	Bucky USA	C60	720.64	1.54	6.4	4.0 [150]	1.95 [30]
BPhen	Aldrich	C24H16N2	332.13	1.244	6.46	2 ^[c]	3.52
BAlq	Sensient	C32H25AlN2O3	512.53	1.33	6.08	3 [151]	3.44 [151]
F4-TCNQ	TCI	C12F4N4	276.15	-	8.34 [8]	5.24 [8]	-
C60F36	[g]	C60F36	1404.58	1.5 ^[a]	8.38	≈ 5.4 ^[b]	2.48
NDP2	Novaled	-	-	-	-	≈ 5.4	-
NDP9	Novaled	-	-	-	-	≈ 5.5	-
AOB	Aldrich	C17H19N3	265.4	-	4.98	-	-
NDN1	Novaled	-	-	-	-	-	-
Ir(MDQ) ₂ acac	TCI	C39H30N4Ir	780.92	1.5 ^[a]	5.36	2.76 ^[d]	2.02 ^[e]
PEDOT:PSS	H.C. Starck	polymer	-	-	5.1 (Wf)	-	-
<i>inorganic material</i>	<i>supplier</i>	<i>Wf (eV)</i>	<i>density (g/cm³)</i>	<i>conductivity (S/cm)</i>	<i>purity</i>		
Au foil / rod ^[h]	Goodfellow / Chempure	5.1	19.32	$4.5 \cdot 10^5$	99.99% / 99.9%		
Ag foil / rod ^[h]	MaTeck / Chempur	4.26	10.5	$6.3 \cdot 10^5$	99.995% / 99.9%		
Al	Chempur	4.28	2.7	$3.77 \cdot 10^5$	99.999%		
Cesium	Saes	2.14	1.87	$4.89 \cdot 10^4$	bound in alloy		
ITO	Thin Film Devices Inc.	3.7-4.1 ^[f]	-	$1 \cdot 10^4$ [152]	-		

Table 3.1: Properties and further relevant information on the organic materials and substrates used in this work. The values are measured at the institute if not stated otherwise. The shortcuts mean: [a] average value used as no measurement is available, [b] estimated from optical gap and an exciton binding energy of 0.3 to 0.5 eV, [c] estimated from UPS measurement on the n-doped system (see Ch. 7.1). [d] measured by cyclic voltammetry by Novaled, [e] phosphorescent peak, [f] values are for sputtered ITO and depends on the sputtering process, [g] material provided by Prof. Nir Tessler (Israel Institute of Technology in Haifa, Israel), [h] pieces of the rod are used for the metal evaporation.

3.2 Sample Preparation

The preparation of the samples under investigation takes place in an ultra high vacuum (UHV) system under a base pressure of $\leq 10^{-8}$ mbar. The multichamber evaporation tool consist of five individually pumped chambers, shown on the left side of Fig. 3.5. Four of these are used to evaporate organic molecules whereby different chambers are used for p- and n-doping as well as intrinsic layers to avoid cross contamination. The fifth chamber is equipped for the evaporation of metal layers.

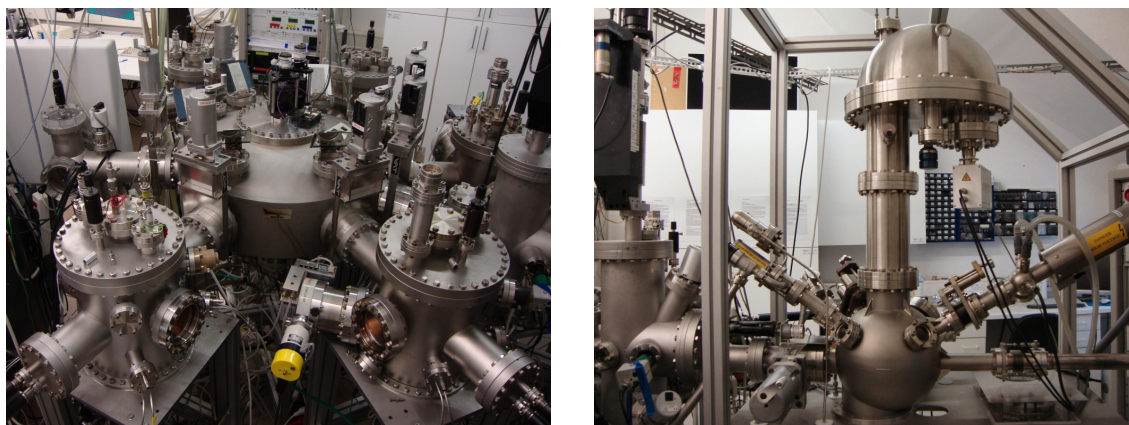


Figure 3.5: Photos of the multichamber evaporation tool UFO1 (left side) for the preparation of the samples as well as the measurement chamber Phoibos 100 (right side) for the UPS and XPS investigations that is directly connected to the multichamber tool.

The organic substances, in form of a powder, are filled into crucibles that are located at the bottom of the UHV chambers. These can be heated by a copper coil that surrounds the crucible. The molecules are evaporated and condense on a sample that is located above the sources as sketched in Fig. 3.6b. Mostly amorphous layers form at typical thicknesses of 1 to 100 nm. The evaporation rate is usually kept in the range of 0.1 \AA/s for matrix materials and 0.01 \AA/s for the dopants. This rate is monitored by quartz crystals (Leybold Inficon). The vibration frequency of these crystals changes when the mass increases due to the additional material evaporated on top. With the knowledge of the density of the material, the thickness can be calculated. Each chamber is equipped with at least two of these thickness monitors to allow for co-evaporation and the doping of layers. Thereby, one monitor measures the thickness of the matrix and the other one the dopant (see Fig. 3.6). Molar doping ratios down to $\text{MR} = 0.005$ can be achieved this way.

The evaporation of the metals gold and silver takes place out of resistively heated molybdenum boats, while for aluminum a specially constructed ceramic evaporator is used, build by the company *Creaphys*. The measurement of the layer thickness is again done by quartz crystals

Two different sample designs are used. The one for photoelectron spectroscopy measurements is shown on the left side of Fig. 3.6 and consists of an Omicon-type

a) PES sample design:

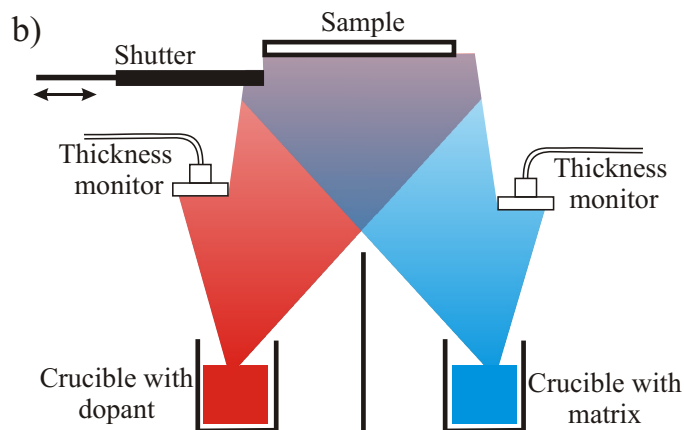
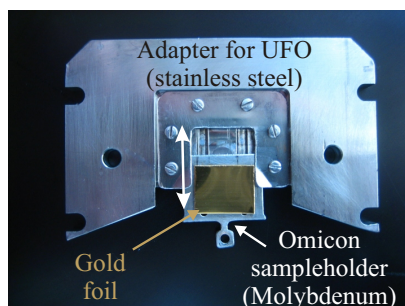


Figure 3.6: a) Sample design for the PES measurements; for the transfer into the measurement chamber the Omicron type holder is removed from the adapter. b) Illustration of the setup used for the co-evaporation of organic molecules. From heated crucibles the molecules are evaporated at rates that can be independently controlled by the quartz crystals and the sample can be separated from the molecular beam by a shutter.

sample holder, made from molybdenum, onto which a $1 \times 1 \text{ cm}^2$ gold / silver foil or an ITO covered glass plate is mounted by a UHV-compatible tape. In the UPS chamber, only this holder is used, the adapter is needed to be compatible with the UFO 1 sample design.

The second sample design is used for the measurement of conductivity, the IV characteristic and impedance spectroscopy. A teflon adapter is used carrying a 2.5 cm^2 glass plate pre-structured with four transparent ITO fingers and an ITO counter electrode (sketched in Fig. 3.4).

3.3 Theory of Photoelectron Spectroscopy

Basics of Photoelectron Spectroscopy

Photoelectron spectroscopy (PES) is one of the most important methods to study matter in gas phase or solid state. The method provides a maximum amount of chemical and electronic information within a single technique, is essentially nondestructive for most material systems, and is extremely surface sensitive. First experiments on organic semiconductors started in the 1950s but widespread recognition was only gained after 1980 when numerous works of William Salaneck and Kazuhiko Seki were reported.

In the photoelectron spectroscopy experiment, photons from an ideally monochromatic light source are directed onto a sample and photoelectrons are emitted that are measured by an electrostatic analyzer. The underlying principle is the external photoeffect, described by Einstein in 1905, which relates the maximum kinetic energy E_{kin}^{max} of an electron escaping from a sample to the frequency ν of the exciting photon:

$$E_{kin}^{max} = h\nu - Wf. \quad (3.1)$$

Depending on the energy of the photons, either the DOS of the delocalized valence band of the molecule is observed or the localized core level peaks of the individual atoms. This leads to the distinction between UV photoelectron spectroscopy (UPS) for energies below 50 eV and x-ray photoelectron spectroscopy (XPS) above this energy. Commonly gas discharge lamps are used for the generation of UPS photons and soft x-ray sources for XPS. Another possibility is the utilization of synchrotron radiation.

Electrons as means of investigation are advantageous because of their small mean free path in solids. Even though the photons penetrate several μm into the sample, the probing depth is limited to a few Ångströms depending the electron kinetic energy. In Fig. 3.7 the mean free path λ (given in monolayers) is shown as function of the electron kinetic energy. Especially in the region of 10 eV to 1 keV the emitted electrons can only originate from the topmost layers of molecules.

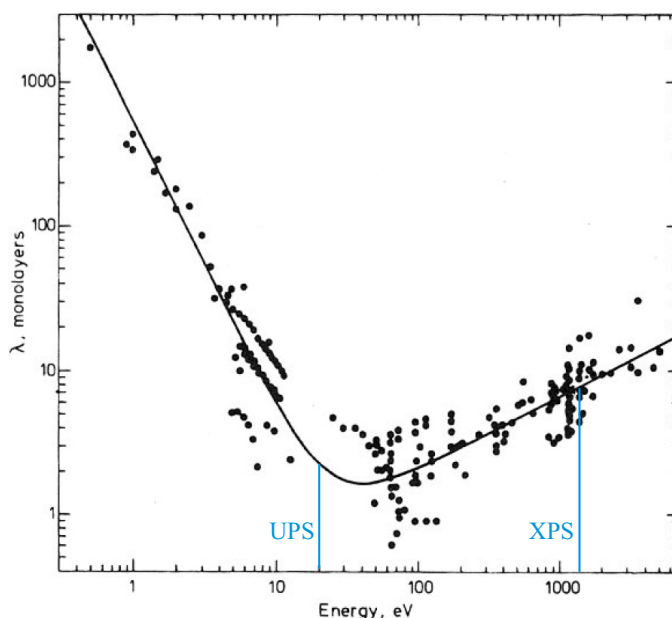


Figure 3.7: Mean free path of electrons in solids as a function of their kinetic energy. The data points reflect electrons originating from different elements (from Ref. [153]). The energy used for UPS and XPS measurements throughout this work are indicated in the graph.

This surface sensitivity is needed when investigating the detailed alignment between two organic materials or between a metal and an organic layer. Thereby, the interface is built incrementally by evaporating the second layer in Å steps onto the first one and checking the DOS for every layer thickness. With this method it is possible to observe level bending effects or see chemical reactions taking place at the surface that modify the DOS.

If, on the other hand, the electronic bulk energy states are supposed to be investigated by PES, the results have to be viewed with care. The topmost layer in organic semiconductors experiences a lower polarization screening compared to the bulk molecules as it is exposed to the vacuum. This usually leads to an increase

in ionization potential. Several papers have been published on this topic where the authors compare surface sensitive and bulk sensitive measurements by varying either the photon energy or the detection angle. While earlier experiments [29] and calculations [154] found a decrease of the polarization screening at the surface by 0.3-0.4 eV, newer experiment using synchrotron high resolution UPS limit the effect to less than 100 meV [155].

Measurement Setup

The PES setup is directly connected to a multichamber evaporation tool. In total approximately 25 sources for the evaporation of varying materials are accessible without breaking the vacuum. The PES setup used for this work is a *Phoibos 100* built by the company Specs, a picture is shown on the right side of Fig. 3.5. The instrument is incorporated in a UHV chamber at a base pressure of $<1 \cdot 10^{-10}$ mbar. It is crucial for the experiment to keep a low pressure, as even the smallest traces of surface contamination would affect the measurement. Assuming a sticking coefficient of unity for the residual gas in a chamber, Langmuir's law states that one monolayer is formed at a pressure of 1 Torr ($= 1.332$ mbar) in 10^{-6} s. At a chamber pressure of 10^{-8} mbar, this time is increased to somewhat more than two minutes, which is still insufficient for PES measurements. At a pressure of 10^{-10} mbar, the time for a monolayer to form is 4 h. The sticking coefficient at the closed shelled molecular surface will not be unity, but it is obvious that a low pressure is essential.

A schematic view of the Phoibos 100 setup is given in Fig. 3.8. The photogenerated electrons originating from the sample, indicated by red lines, enter into the first stage of the detection system that contains a set of ten lenses (T1 to T10). The voltages applied to the individual lenses determine the kinetic energy of the electrons, the sampling area, and the detected emission angle; for this several lens modes are applicable by the software. With an adjustable iris the aperture can be influenced.

The instrument is operated in the so called *Fixed Analyzer Transmission Mode*. Here, the kinetic energy of the electrons entering the detector is set fixed, called the *pass energy* E_{pass} . Successively, all electrons originating from the sample have to be decelerated to this energy. By the lens system the electrons are focused on a first slit S1 at which point they are slowed down by the retardation voltage V_0 , which is the difference between the nominal kinetic energy and the pass energy. Then, they pass into the hemispherical analyzer that consists of two halve spheres with radii $R_{in} = 75$ mm and $R_{out} = 125$ mm. The radial electrical field between the half spheres ($V_{in}-V_{out}=\Delta V = -e \cdot 0.9375 \cdot E_{pass}$) deflects the electrons into elliptical trajectories and only electrons which have a centrifugal force equal to the electrostatic force can travel through and enter the second slit S2. To image the complete DOS the retardation voltage V_0 is swept. The choice of E_{pass} determines the energy resolution of the measurement that is furthermore influenced by geometric values of $R_0 = (R_{in} + R_{out})/2$ and the slit sizes s_1 and s_2 and follows the relation [156]

$$\Delta E_{detector} = E_{pass} \cdot \left(\frac{s_1 + s_2}{4R_0} - \frac{\alpha^2}{4} \right) \quad (3.2)$$

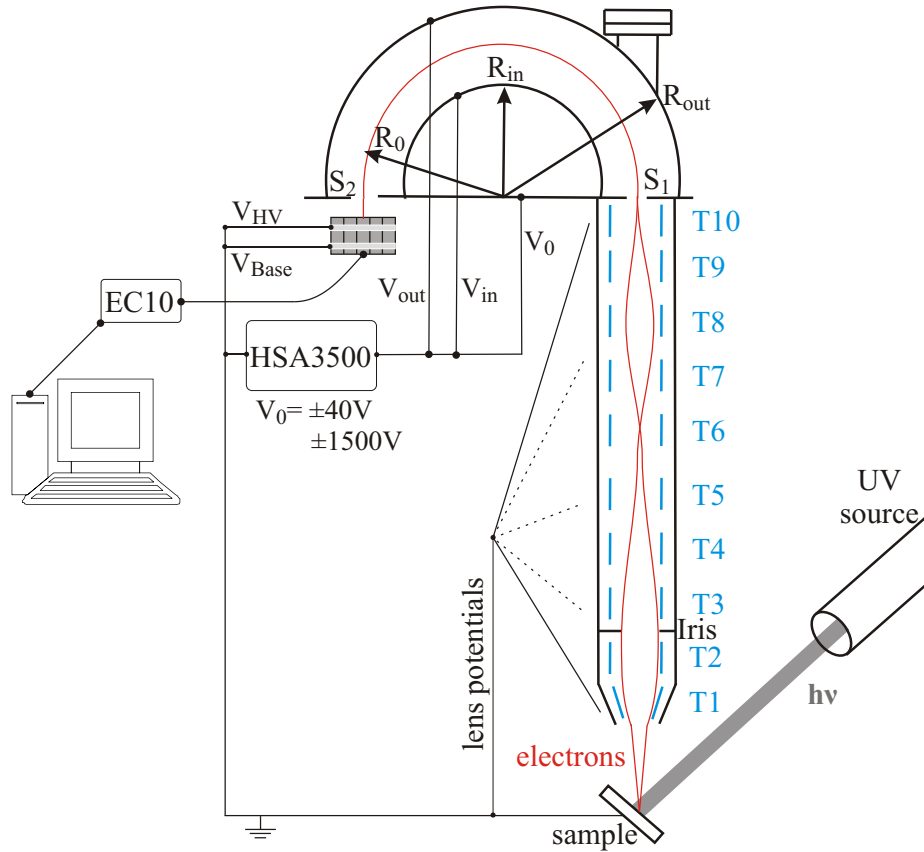


Figure 3.8: Schematic view of the Phoibos100 setup and the photoionization process. Photons from a x-ray or UV source hit out electrons (red lines) from a sample positioned in the focus of the detector (for this setup 40 mm). The lens system T1 to T10 determines the imaged spot size and measurement angle. The retardation voltage V_0 applied by the power supply HSA3500 decelerates the particles and they are deflected according to their kinetic energy by the voltages applied to the two half spheres ($V_{in} - V_{out}$). $V_{Channel/Base}$ is the anode/cathode potential of the channeltrons and the detector voltage is $V_{HV} - V_{Base}$. Electrons that are imaged have to pass through the slits S1 and S2. The interface to the computer is realized by a Can-Ethernet adapter EC10.

where α is the angle under which the electrons enter into the detector. There are additional contributions to the linewidth like the inherent width of the atomic level and the natural linewidth of the excitation source. The full width at half maximum (FWHM) is therefore given by

$$FWHM = \sqrt{\Delta E_{detector} + \Delta E_{level} + \Delta E_{excitation}}. \quad (3.3)$$

The electrons are detected by an array of five channel electron multipliers (CEMs). Each consists of a glass tube in which the wall is coated with a high resistance material. This coating becomes a continuous dynode when a potential is applied between the ends of the tube. The impact of an electron results in secondary electrons that are released from the CEM walls. These electrons are accelerated by the high voltage connected to the CEM ($V_{det} = V_{HV} - V_{Base}$) and release additional secondary electrons

by the impact with the wall further along in the CEM. This effect is successively repeated, until finally an electron cloud is present at the exit of the CEM. Usually the minimum gain for saturated operation is about 10^7 , i.e. an electron cloud of more than 10^7 electrons leaves the CEM [156]. The spectrometer and the sample are connected to ensure that the Fermi energies are at the same reference level.

Principle of UPS Measurements and Data Evaluation

The UV photoelectron spectroscopy measurements are performed using a helium discharge lamp (*UVS10/35*, Specs). As it is not possible to couple UV light into the chamber via a window, the He plasma has to be ignited inside the chamber. A two stage pumping line is used to keep the UHV inside the measurement chamber, while the discharge works at a He pressure of $1 \cdot 10^{-1}$ mbar. The main HeI excitation line is at 21.22 eV and photo currents of 20 nA are achieved. From Fig. 3.7 the mean free path of the electrons at this energy can be estimated to be 2-3 monolayers.

In order to show the material properties accessible by UPS, Fig. 3.9 illustrates how photons with an energy $h\nu$ excite electrons from the valence band above the vacuum level for a gold sample and a layer of C60. The kinetic energy distribution directly resembles the DOS of the bound electrons. The calculation of the binding energy from a measured kinetic energy is done by

$$E_B = h\nu - E_{kin} - Wf_{det} - eV_{sample}. \quad (3.4)$$

The term Wf_{det} appears since the detected electrons have to overcome the work function of the detector. This value has to be determined experimentally and is inserted into the measurement software so it is included automatically. Furthermore a bias $V_{sample} = -8V$ is applied to the sample to ensure that the kinetic energy of the emitted electrons is larger than the Wf of the detector (measured as 4.56 eV). This additional bias has no effect on the shape of the measured curve, but simply leads to a constant shift in the measured binding energy that is later subtracted again.

In the spectra a polynomial background of secondary electrons appears, that is created by electrons that experience an inelastic scattering before leaving the surface. The point at low kinetic energies where this background ends abruptly is called *high binding energy cutoff* (HBEC). These electrons have just enough energy to get over the vacuum level and can give information on the work function of the sample:

$$Wf = h\nu - E_{HBEC}. \quad (3.5)$$

For a metal surface the fastest electrons originate from the Fermi energy at $E_B = 0$ eV; in the case of an organic semiconductor, they originate from the HOMO cutoff position E_{HOMO} . The hole injection barrier ϕ can be calculated from the difference in Fermi energy and HOMO cutoff position:

$$\phi = E_F - E_{HOMO}. \quad (3.6)$$

The ionization potential is given by the difference of the excitation energy and the width of the measured spectrum

$$IP = h\nu - (E_{HBEC} - E_{HOMO}). \quad (3.7)$$

Commonly the vacuum level at an interface is not constant, but shows an interface dipole Δ that can be caused by several effects that are described in Chapter 2.3.1. This results in different HBEC positions as it is indicated in Fig. 3.9:

$$\Delta = E_{HBEC}^{gold} - E_{HBEC}^{C60}. \quad (3.8)$$

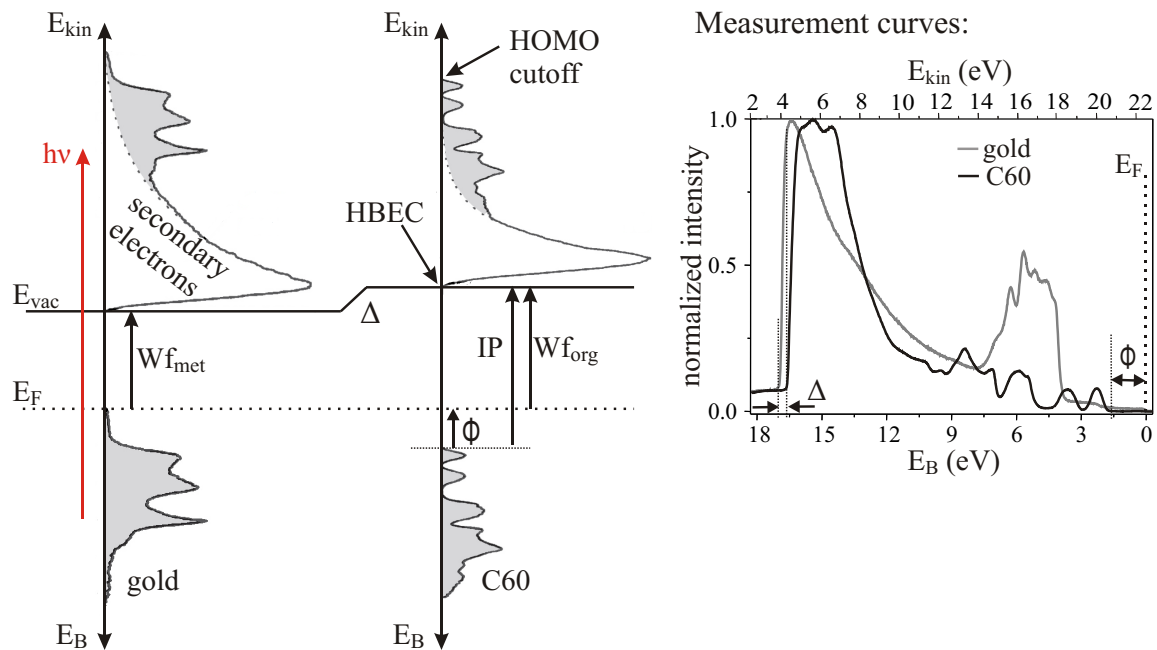


Figure 3.9: The left side shows the schematic process of UV excitation in a sample of gold and the organic semiconductor C60 by a photon with the energy $h\nu$. The measurement accesses the values of work function (Wf), ionization potential (IP), hole injection barrier (ϕ) and interface dipole (Δ). The right side shows typical UPS measurements of the two materials as a function of kinetic energy and binding energy.

On the right side of Fig. 3.9, typical measurement curves of the organic semiconductor C60 and a gold surface are shown. Plotted is the normalized count rate per second of the CEMs versus the binding energy (or kinetic energy). Throughout this work, usually only parts of the spectrum are shown. Relevant for the data evaluation are only the HBEC and the valence band region, so these are always shown as close-up as it is displayed in Fig. 3.10a for C60. This graph shows in detail how the value of the HBEC and HOMO position are evaluated. In both cases the leading edge is approximated by a line and the intersection with the background is taken as the corresponding value. The scale is always given as binding energy, so the Fermi energy is positioned at zero energy.

In Fig. 3.10b the Fermi edge of gold is shown. It is used to calibrate the energy scale of the detector; furthermore the width gives the energy resolution of the UPS measurement. At room temperature the inherent width is $4.4 \cdot k_B T$ according to Fermi-Dirac statistics. At room temperature this corresponds to 110 meV. The measurement on gold shows a width of 120 meV between 10 % and 90 % intensity. If one assumes the same broadening of HOMO peaks of the organic layers, the measured hole injection barriers are too small by 10 meV. However, due to uncertainties in the estimation of the actual cutoff position, the error is estimated to be ± 50 meV throughout this work for UPS measurements. This value reflects the reproducibility in different samples prepared under the same conditions as well.

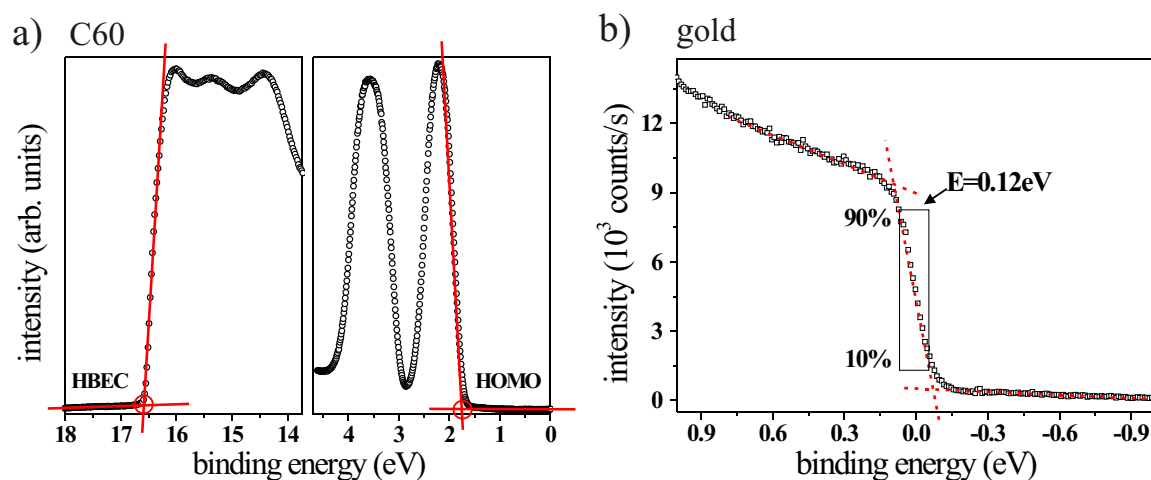


Figure 3.10: a) Typical diagram of the C60 UPS measurement already presented in Fig. 3.9 to show how the HBEC and HOMO cutoff position are determined. b) Fermi edge of a gold sample. The width of this structure gives information on the resolution of the measurement setup.

It is important to consider in what state the molecule is in when the HOMO position is measured by UPS. Estimating an average kinetic energy of the electrons of 15 eV and a distance across a molecule of 10 \AA , a possible interaction time of the charge carrier with the molecule of $1 \cdot 10^{-15}$ s can be calculated. In Chapter 2.1.2, the different contributions to the relaxation of the molecule after the introduction of a charge carrier were discussed. The effects of intramolecular relaxation and lattice relaxation are slower than this time span and most likely do not influence the emitted electron. However, the largest effect of electronic polarization takes only 10^{-16} s and is therefore certainly included in the photoemission process. This means that UPS does not measure the energy of a neutral molecule, but the energy of the polaronic state. This is important, since this is the relevant value for describing the transport in organic solids.

Finally it has to be mentioned, that a helium discharge lamp is of course not a monochromatic light source. There is another prominent line, called He II, in the UV part of the spectrum at 40.82 eV that has however not been used for the studies presented in this work. Furthermore, there are some satellite lines in the region of

the He I excitation which result in additional features superimposed on the originally 21.22 eV excitation. The most prominent secondary lines in our case are at the excitation energies at 23.09 eV ($\approx 2\%$ intensity), 23.75 eV ($\approx 0.5\%$ intensity), and 24.05 eV ($\approx 0.2\%$ intensity). Due to the much lower intensity these can normally be neglected. However, in a few cases the signal from the satellite lines has to be subtracted to see weak features, e.g. in the gap of a semiconductor. A method how this can be done is given in the Appendix.

Principle of XPS Measurements and Data Evaluation

The XPS measurements are performed with the soft x-ray source *XR 50* by Specs, that is equipped with a twin anode made from aluminum and magnesium which can be used separately for the excitation. The corresponding energies are $\text{Al K}_{\alpha 1/2} = 1486.61$ eV and $\text{Mg K}_{\alpha 1/2} = 1253.64$ eV. No monochromator is integrated in this system, therefore the linewidths of these excitations are rather large with 850 meV for the Al excitation and 680 meV for Mg [156]. The probing depth can be estimated from Fig. 3.7 to be 8-10 monolayers. This larger depth compared to UPS measurements is helpful when a layer deeper down in a sample has to be investigated, e.g. to see if it shows a change in energetic position as reaction to the layer evaporated on top.

The technique of x-ray photoelectron spectroscopy is also known as *electron spectroscopy for chemical analysis* (ESCA) due to its ability to see the chemical composition of a sample. The working principle is shown in the left side of Fig. 3.11. The much higher photon energy compared to UPS leads to the release of core level electrons from the individual atoms making up the molecules. As these core levels have characteristic energies, it is possible to associate them to the corresponding elements.

A typical spectrum of an organic material containing several different atoms is shown in the top of Fig. 3.11 for the case of the molecule DCV3T³ (sum formula: $\text{C}_{20}\text{H}_8\text{N}_4\text{S}_3$). In the region from 50 eV to 460 eV binding energy, several peaks are visible with the element and level notation indicated for each of them. The solid red line is a *Shirley background* that corresponds to the signal originating from scattered electrons. For a quantitative analysis, the characteristic peaks are measured individually as it is shown in Fig. 3.11 for nitrogen, carbon, sulfur, and gold (the last signal originates from the substrate). For these examples, the detailed shape of XPS peaks can be discussed. In the first example of the nitrogen 1s signal, the data can be fitted by a single peak⁴. The line shape is given by a mix of Lorentzian and Gaussian contributions (given as value L:G in the graph, L:G=0 means pure Gaussian and L:G=100 is pure Lorentzian). The first contribution originates from the natural linewidth of a core level as well as the width of the excitation energy and the Gaussian contribution originates from the response function of the analyzer. Further fit parameters are the energetic position, the area, and the FWHM.

For some transitions, more than one peak appears in the spectrum as it is the case

³Dicyanovinyl-terthiophen

⁴All fits are performed with a freeware program called XPSPEAK4.1, written by Raymund Kwok

for the other three elements in Fig. 3.11, which can have two fundamentally different reasons: In the case of sulfur and gold the two peaks are created by the spin-orbit splitting. The final state of the electron system after the removal of an electron can be in two states depending on the alignment of the spin (s) of the remaining unpaired electron with its angular momentum (l). The total momentum is given by $j = |l \pm s|$. Therefore, every level except for the s level, is split into two. The relative intensities depend on the degeneracy of the level and are $1 : 2j + 1$ (e.g. $p_{1/2} : p_{3/2} = 1 : 2$, $d_{3/2} : d_{5/2} = 2 : 3$, etc.). The magnitude of the splitting depends on the atomic number Z which is the reason, why the splitting for Au is much larger than for S.

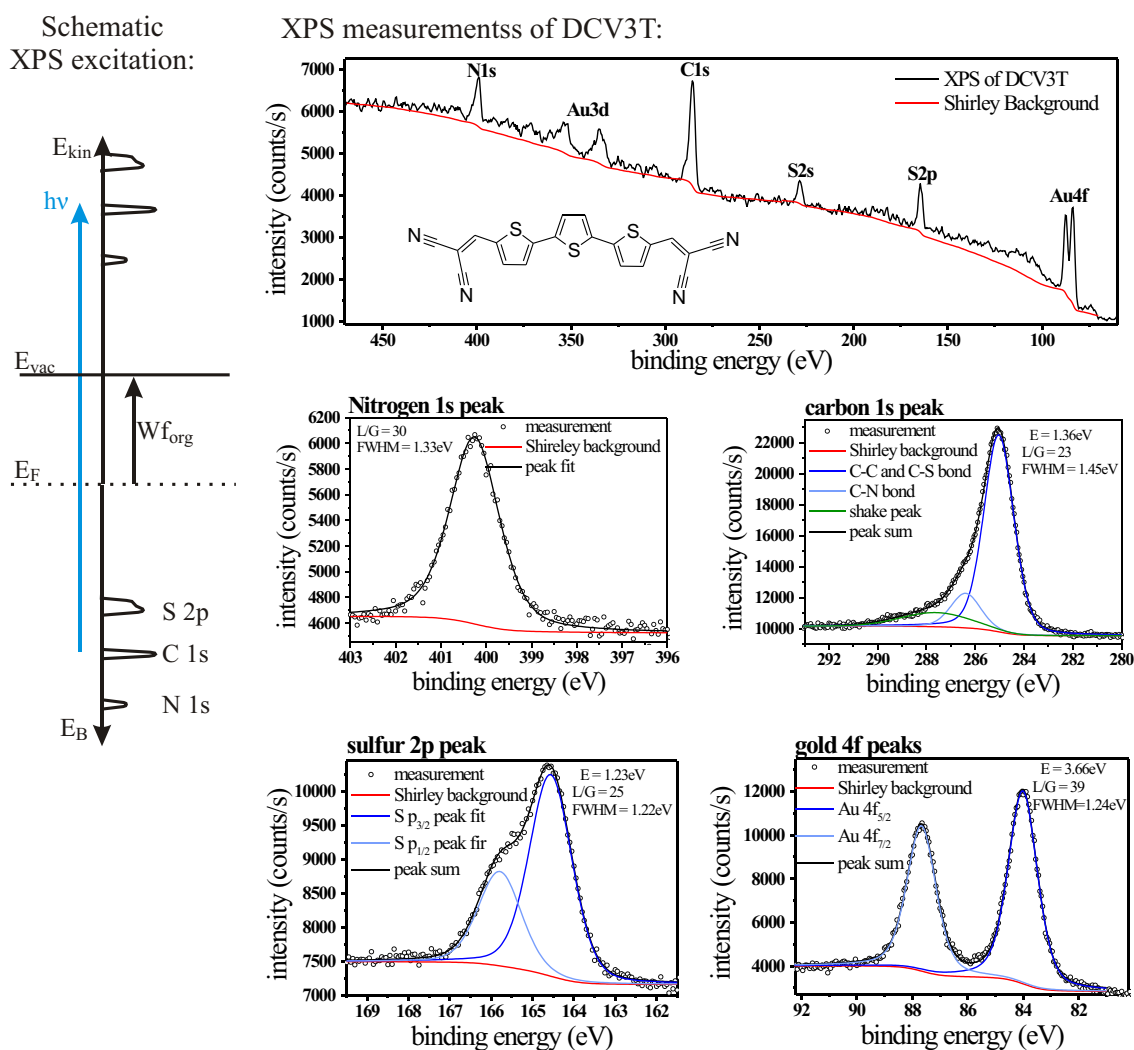


Figure 3.11: The left side shows the schematic process of x-ray excitation in a DCV3T sample by a photon with an energy $h\nu$ large enough to remove core level electrons. The top graph on the right side shows an overview scan of this sample where the peaks are correlated to an element and the level it originated from. The red line corresponds to a Shirley background. The remaining graphs show close-ups of the nitrogen, carbon, sulfur, and gold signals fitted by mixed Lorentzian-Gaussian peaks when a Shirley background is assumed. The parameters (Lorentz to Gauss ratio L:G, FWHM, and energy splitting ΔE) from the peak fits are indicated in the graphs.

In case of the carbon peak in Fig. 3.11, the multiple peaks can not be due to spin-orbit splitting since this is a 1s peak. Here we see a very important aspect of XPS. The binding energy of a core level electron is influenced by the bonds created by the outer electrons due to the reorganization of the electron density distribution within the atom. If carbon binds to an atom with a larger electron affinity, an electron of the valence band is partly removed (polar bond). The remaining electrons of the carbon atom feel less repulsion by the valence electrons and the binding energy increases. In analogy to *nuclear magnetic resonance* spectroscopy (NMR) this is called the *chemical shift*. In the XPS spectrum shown above, the difference between the C-C bond and C-N bond can be seen. The C-S bond can not be distinguished from the C-C bond as the electronegativities of the two atoms are comparable in magnitude. Furthermore, a broad shake peak is observed in this spectrum. This appears when a photogenerated electron, while leaving the atom, transfers some of its energy to an electron in a higher level that gets either excited to a higher bound state (*shake-up peak*) or is removed from the atom as well (*shake-off peak*). This is only observable for peaks with high count rates as it is otherwise within the noise level of the experiment.

The fitting of these multiple peaks is done by assuming identical L:G ratios and FWHM values for the signal originating from the same element. For the spin-orbit split peaks, the relative peak intensities known from the degeneracy are fixed as well. In general the parameters used for the different elements should be comparable, as they mainly depend on the analyzer transmission function and the pass energy. Typical values at a pass energy of $E_{pass} = 20$ eV are 1.2-1.4 eV for the FWHM and between 20 and 40 for L:G.

By comparing the relative heights of the peaks shown in Fig. 3.11, the elemental composition of the sample can be calculated. However, this is not straight forward. The intensity of the signal depends on (i) the concentration of the element in the sample, (ii) the cross section of the interaction between the photon and the observed transition, (iii) the mean free path of the emitted electron in the sample, (iv) geometrical factors like the distance from the x-ray source to the sample and the angle between x-ray source and detector, (v) spectrometer properties like transfer characteristic and lens modes, and (vi) the power applied to the x-ray gun. Since we only compare the relative intensities, e.g. carbon to fluorine signal, the points (iii)-(vi) can be neglected, as they will influence all electrons the same way. The most important influence is by the cross section (ii). This is considered by multiplying the measured intensities by the *relative sensitivity factors* (RSF), which are calibrated to the carbon intensity which has $RSF = 1$. An extensive list of RSFs for different elements has been published in Ref. [157] for an angle of 54° between x-ray source and analyzer for the excitation lines of Al and Mg (in the Phoibos setup this angle is 60°). In the work presented here, some of the values are taken as published in Ref. [157], but in a few cases the RSF factors were measured by using known compositions of stable molecules. The positions and RSF factors of the most important XPS peaks are given in Table 3.2. The positions of the non-metal elements stated in this Table above are not absolute as the work function of the containing molecules will change depending

element	level	E_B (eV)	RSF
Ag	3d _{3/2}	368.25	18.04
Au	4f _{5/2}	83.96	17.12
C	1s	284.7	1
N	1s	400.3	1.8
O	1s	533.2	2.93
F	1s	686.2	4.96
Cs	3d _{3/2}	725.9	23.76

Table 3.2: The Table shows frequently used XPS core level peaks. The list contains the notation of the levels, the binding energies, and the relative sensitivity factors.

on the alignment with the substrate or the doping concentration.

The calculation from measured kinetic energy to binding energy is done the same way as for UPS (Eq. 3.4), except that no bias V_{sample} has to be applied here, as the electron kinetic energies are much larger than the detector work function. In principle, the valence band can be observed as well with the method of XPS. However, the worse resolution and the lower intensity makes UPS much more suitable for that energy range. During interface resolved measurement a level bending is observable for the XPS peaks just as in UPS, as the core levels follow the same shift as the valence band. There can be minor differences in the absolute value of the shift as XPS probes deeper into the sample and averages over several monolayers.

Performing Experiments

Typical measurements are either performed on a single thick layer, in case only the properties of a new material are investigated, or a series of measurements on a layer with increasing thickness is done to learn on the interface alignment to a neighboring layer. Regarding the first case, a layer of 10-30 nm thickness is evaporated either on a gold or silver foil that has been previously sputtered to remove any contamination. The chosen thickness depends on two factors: (i) If the conductivity of the samples is low the layers should not be above 10 nm, otherwise the sample charges since the holes generated by the photoemission process do not reach the substrate fast enough. This shows in a shifting of the complete spectrum during the measurement time. To exclude this, the HBEC is always measured twice with some minutes of exposure time in between. (ii) Thicker layers have to be chosen, if the smoothness of layer is insufficient (e.g. NTCDA needs 30 nm). This can be estimated from remaining substrate peaks or the observation of the substrate Fermi edge.

For the second case of thickness resolved measurements, the interface is built incrementally, typically using the step widths of 2 Å, 5 Å, 10 Å, 20 Å, 50 Å, 100 Å, The measurement is complete, when the UPS and XPS signals saturate and show no further change with thickness. The relevant signals are the HBEC, the HOMO cutoff position, and the characteristic core level peaks. All of these values should show the same change in energetic position for interface resolved measurements.

In general, UPS and XPS measurement are always performed together to access the maximum amount of information. The UPS experiments are performed at a low pass energy of $E_{pass} = 3$ eV to reach a high energy resolution and energy step widths of 0.007 eV to 0.02 eV at an integration time of 0.1 s are used. Typical exposure times to the UV light are less than 5 min. For the vast majority of organic materials, this is not harmful, however in a few cases a change in DOS during the exposure time has been observed (e.g. BA1q). An angle between detector and normal on the sample surface of 30° is chosen. This yields a maximum count rate as the sample surface directly faces the UV beam that way (see Fig. 3.8). The full spectrum is recorded at the lens mode *Small Area 2*, that exhibits a strong acceleration of the electrons in the first stage to minimize stray magnetic fields and is therefore appropriate to observe the slow electrons at the HBEC. Since in this mode, the signal to noise ratio in the region of the Fermi energy is not very good due to the small sampling area of 0.1 mm^2 , the region at higher kinetic energies is measured again in the *Low Angular Dispersion Mode*. Here the sampling size is 1.2 mm^2 leading to much higher count rates.

For the XPS investigations the Al K_α source is used, operated at a power of 300 W. The normal of the sample surface is this time parallel to the analyzer setup due to geometrical constraints. For the measurements, a higher pass energy of $E_{pass} = 20$ eV is chosen for the detection. Due to the much broader excitation by the x-ray source a lower pass energy brings no advantage in resolution and this higher E_{pass} results in higher count rates. The lens mode called *Large Area* is chosen that maps as much sample area as possible (5 mm^2) at a step width of 0.05 eV and an integration time of 0.1 s. XPS has the problem of low count rates due to a much lower photon flux compared to UPS. Therefore the characteristic peaks have to be scanned several times, depending on the signal intensity between 10 and 60 times. This leads to much longer measurement times in XPS of up to 20 min per peak. However, due to the low photon flux, no degradation has ever been observed during an experiment. Even though the XPS peaks are broadened by approximately 500 meV due to non-monochromized excitation, the same reproducibility as in UPS measurements of ± 50 meV is found between repeated experiments.

The measurement software is provided by the company Specs and is called *Specs-Lab* (version 2.35). The computer is connected via an EC10 Can-Ethernet-Adapter to the HSA3500 power supply. This last one is either used in the ± 40 V range for UPS measurement or ± 1500 V range for XPS (see Fig. 3.8).

3.4 Further Measurement Techniques

3.4.1 Electrical Measurements

Conductivity measurement: The measurement of the conductivity is performed by applying a voltage of 10 V between the center two ITO stripes shown in Fig. 3.4. These stripes have an effective distance of $d = 1.6$ mm and a length of $l = 14.5$ mm. Onto this sample the doped organic material is evaporated and the current flowing between the ITO finger through the doped organic layer is measured by a source measure unit (SMU 2400 Keithley Instruments Inc.). The conductivity σ is then given by

$$\sigma = \frac{I}{V} \frac{l}{dh} \quad (3.9)$$

where h is the thickness of the organic layer. The value of I/d is given by plotting the current over the thickness and fitting of the slope linearly. The measurements are typically performed up to a layer thickness of 20 nm.

Current-voltage characteristics: The measurements of the current-voltage characteristics are performed on encapsulated⁵ completed device stacks of an OLED, solar cell, or *pn/pin* junction. The device is connected to the SMU 2400 and the voltage between anode and cathode is ramped while measuring the resulting current. In the case of the measurements on solar cells the device is illuminated by a sun simulator (Steuernagel SoCo 1200 MHG, 90 lm/W) in a nitrogen atmosphere during the measurement.

3.4.2 Impedance Spectroscopy

With this method again a complete device stack is investigated. Between anode and cathode a DC voltage is applied with a superimposed AC voltage. By varying either the AC frequency or the DC voltage, this technique provides the time and voltage dependent electrical small signal response. Accordingly, one can extract information on the dominant transport mechanism as well as the formation of charged and depleted regions in the stack.

The relevant quantity is the impedance of the sample measured at a constant frequency when the voltage is swept. This is measured by the combination of a SMU 2400 with a Precision LCR-meter (4248 A, Hewlett Packard). The second instrument is capable to measure the phase φ of the current, the ohmic resistance R , and the capacitive resistance X .

The measurements presented are performed on *pin* structures. In order to evaluate the measured data and extract a capacity C , an equivalent circuit representing the device has to be assumed. In general, every layer has an ohmic and a capacitive contribution and the contact to the metals introduces further ohmic resistors as it

⁵Devices are encapsulated with cavity glass lids by an epoxy glue under the nitrogen atmosphere of a glovebox that is directly attached to the vacuum system

is shown in the top circuit of Fig. 3.12. However, the main advantage of such a *pin* structure is the fact that the doped layers show a low resistance R and can be kept rather thick due to the good conductivity, so the capacitance C of these layers is small.

In contrast, the thin intrinsic layer has a large ohmic resistance and a large capacitance. Since the electrical response is dominated by the RC-unit with the highest time constant

$$\tau = R \cdot C \quad (3.10)$$

one can reduce the complexity of the equivalent circuit of Fig. 3.12 to the one shown at the bottom. Hence, the RC-unit of the intrinsic layer is the dominant part of the circuit. The validity of the particular equivalent circuit can be checked by comparing the impedance frequency spectrum to the modeled response of the assumed circuit.

This simple picture is however only valid, as long as no considerable current is flowing through the device. If a voltage larger than the built in voltage in forward direction is applied or a high backward bias so tunneling takes place, the model breaks down due to the changing parallel resistance R_i .

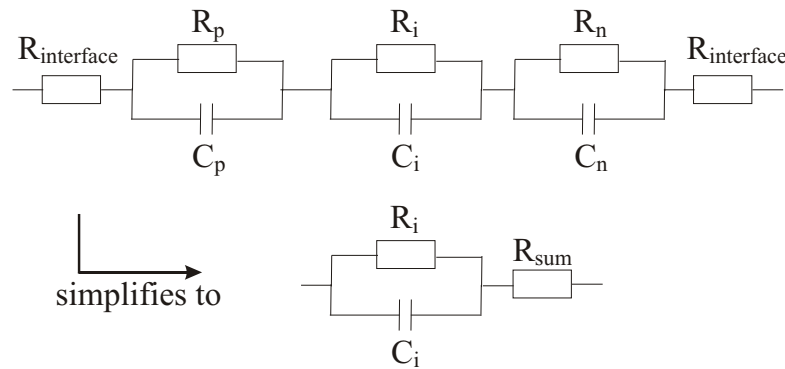


Figure 3.12: The top sketch shows the equivalent circuit for a *pin* device. Every layer is represented by an ohmic resistance R and a capacity C and furthermore the metal contacts introduce a contact resistance as well. This circuit can be simplified to the one shown at the bottom due to the high capacitive resistance of the doped layers relative to their ohmic resistance. The resistances $R_{\text{interface}}$, R_p and R_n can then be combined to a single resistance R_{sum} .

4 Interface Formation at Metal Contacts

As mentioned in Chapter 2.3.4, there are major differences in the formation of metal bottom and top contacts. Depending on the choice of organic material and metal, symmetric or asymmetric injection behaviors can occur and transitions from an abrupt interface formation to intermixed layers have been reported. In the first part of this Chapter, experimental investigations by photoelectron spectroscopy on the alignment between metal bottom and top contacts with doped layers are presented. The goal is to understand why contacts to p-doped layers lead to a symmetric injection from bottom and top contact whereas this is not the case for n-doped layers. Furthermore, the formation of ultra-thin metal top contacts for transparent electrodes is investigated. Here, the choice of metal used in contact to the organic layer determines the morphology of the interface formation and therefore the performance of the device.

4.1 Injection Barriers between Metal Contacts and Doped Layers

The hindered injection of electrons into a n-doped organic layer via the bottom contact compared to the top contact mentioned in Chapter 2.3.4 is disadvantageous for *inverted OLEDs* where the electron injection is taking place via the bottom. Thus, inverted devices have a loss in performance compared to non-inverted OLEDs and need a 1-2 V higher driving voltage before a comparable luminance is reached [127]. The reason for this was suggested to be a self-doping effect by the diffusion of the metal atoms of the top contact into the doped layer [127]. This would introduce additional states that improve the carrier injection.

To gain a detailed understanding of the physical origin of this effect, the difference in the energy level alignment has to be investigated. Therefore, interface resolved PES measurements are performed on different bottom and top contacts. First, the results of a p-doped system are shown, using MeO-TPD doped by F4-TCNQ, that does not exhibit an asymmetry in the IV-characteristic (see Fig. 2.24 on page 48). This is followed by experiments performed on the asymmetrically behaving system of BPhen n-doped by Cs.

4.1.1 Energy Level Alignment between Silver Bottom and Top Contacts with Doped MeO-TPD

The thickness resolved measurements of the bottom contact are performed on a silver substrate at layer thicknesses of MeO-TPD doped by F4-TCNQ ranging from 2 Å to 15 nm. A doping ratio of $MR=0.04$ is chosen, as this is a typical value used in optoelectronic devices. The actual doping concentration in the organic layer is checked by comparing the XPS peak intensities of oxygen (only present in the matrix material) and fluorine (only present in the dopant) which results in $MR=0.045$.

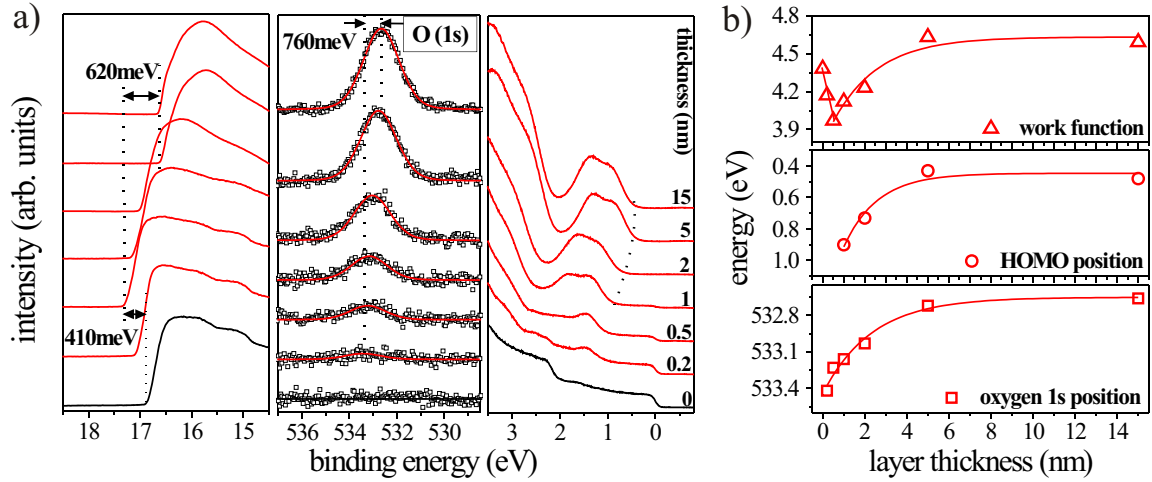


Figure 4.1: a) Interface resolved PES measurement of the alignment between a silver bottom contact and a MeO-TPD layer doped with F4-TCNQ at a molar ratio of 0.045. Shown is the development of HBEC, oxygen 1s peak, and valence band region. b) Change in Wf and HOMO cutoff as well as the O 1s position depending on the organic layer thickness.

In Fig. 4.1a the UPS and XPS measurements are shown. In addition to the HBEC and valence band region, the oxygen 1s peak is displayed as well. The latter one is fitted by a mixed Gaussian and Lorentzian line shape. The shift of this peak is a better indication of the level bending compared to the signal from the HOMO. The oxygen peak can be fitted even at the lowest coverage of 0.2 Å whereas the HOMO cutoff position can only be clearly observed after 1 nm of MeO-TPD deposition. The corresponding shifts are plotted in Fig. 4.1b together with the change in work function depending on the organic layer thickness.

The pristine silver foil substrate shows a work function of 4.38 eV. Upon deposition of the first 0.5 nm of the organic layer, an interface dipole of 0.41 eV is observed in the HBEC. After the first monolayer is completed at approximately 1 nm, the level bending due to the doping takes over that shifts the vacuum level upward by 0.62 eV. It shows a saturation after approximately 5 nm, when the end of the depletion region is reached. At this layer thickness, a hole injection barrier of $\phi = 0.48$ eV is found. The injection barrier at the interface can be calculated by adding the 0.76 eV shift measured for the O 1s peak to the value of ϕ and consequently results to $\phi_0 = 1.24$ eV.

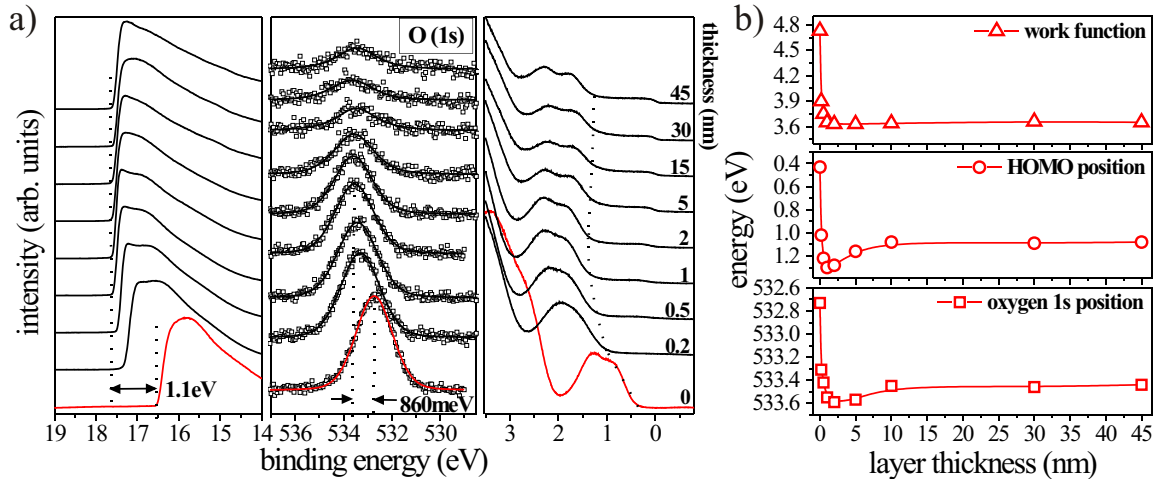


Figure 4.2: a) Interface resolved PES measurement of the alignment between a MeO-TPD layer doped with F4-TCNQ at a molar ratio of 0.049 and a subsequently deposited silver top contact. Shown is the development of HBEC, oxygen 1s peak, and valence band region. b) Change in Wf and HOMO cutoff as well as the O 1s position depending on the metal layer thickness.

To compare this alignment to the one created by a metal top contact, a sample with 15 nm doped MeO-TPD (MR = 0.049) is prepared and successively covered by an Ag layer, ranging in thickness from 2 Å to 45 nm. The PES measurements are shown in Fig. 4.2a. The p-MeO-TPD layer shows a similar alignment as the one in Fig. 4.1a with $W_f = 4.73$ eV and $\phi = 0.43$ eV. The shift of work function, HOMO position, and O 1s position are given in Fig. 4.2b. Already the deposition of the first 2 Å of silver has a strong effect on the alignment by increasing the hole injection barrier and decreasing the work function by several 100 meV. After the deposition of 1 nm, a value of $\phi = 1.3$ eV and $W_f = 3.65$ eV is reached. This strong decrease of the Wf is unexpected, since the work function of amorphous silver is in the range of 4.3 eV; however, even the following coverage by 45 nm of the metal does not change that value. This clearly indicates that a pristine silver top contact is not formed, as it is described in Chapter 2.3.4. The reason could be an insufficient coverage or a diffusion of molecules to the surface.

The change in HOMO and oxygen 1s position are alike, however, they behave anomalously as well. After 1-2 nm coverage, the maximum of the shift of 0.87 eV for the HOMO and 0.86 eV for O 1s peak is reached after which the shifting reverses. After 45 nm of silver, the HOMO is moved by 0.22 eV towards the Fermi energy again and for the O 1s peak this shift is 0.15 eV. The fact that the oxygen 1s peak and especially the HOMO of MeO-TPD are still observable even after the deposition of 45 nm again indicates an incomplete or contaminated silver layer.

The rate at which the Ag top layer covers the MeO-TPD layer can be checked by the corresponding XPS and UPS peak intensities. There, the measured intensity I from a signal originating from the substrate I_0 is attenuated exponentially when

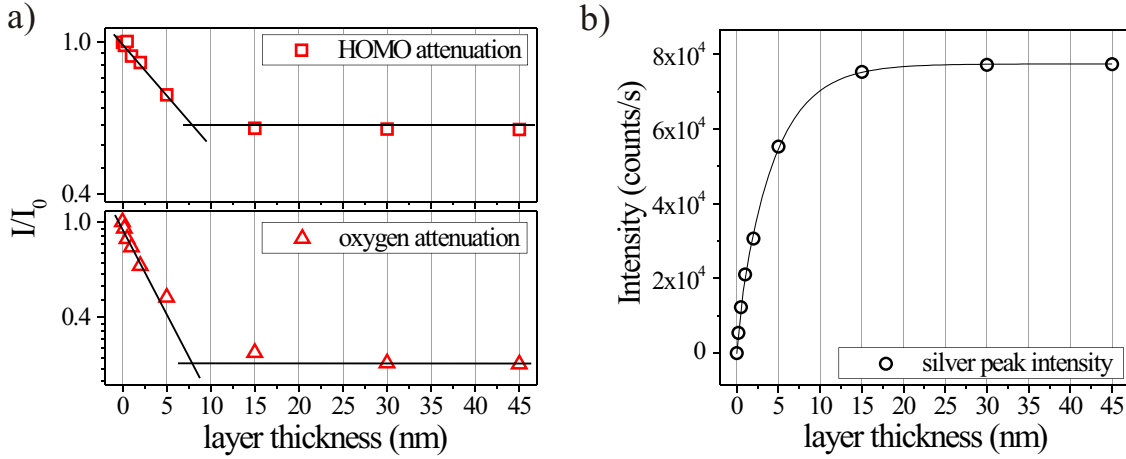


Figure 4.3: a) Relative attenuation of the pristine HOMO and oxygen $1s$ signals I_0 of the p -MeO-TPD layer depending on the coverage by the silver top contact. b) Intensity of the silver $3d_{3/2}$ peak depending on the silver coverage.

putting a layer of d nm on top, and therefore is given by:

$$\ln\left(\frac{I}{I_0}\right) \propto -d \quad (4.1)$$

Semilogarithmic plots of I/I_0 of the HOMO and oxygen peak intensities vs. the silver top contact thickness is shown in Fig. 4.3a. Clearly, two regimes can be separated. Up to ≈ 7 nm the expected linear correlation shows and then a saturation sets in. In the same thickness range, the intensity of the silver $3d_{3/2}$ signal saturates (Fig. 4.3b), so clearly the interface formation is completed. Since UPS is more surface sensitive compared to the XPS measurement, the fact that the oxygen signal is reduced to $0.22 \cdot I_0$ and the HOMO signal only to $0.56 \cdot I_0$ suggests that the origin of the residual organic signal is due to a surface contamination that floats on top of the metal layer, independent on how thick this layer is grown. Therefore, it can be assumed that the change in the direction of shifting of the HOMO and O $1s$ peak at 2 nm coverage happens when we change from observing the shifting of the underlying MeO-TPD layer in contact to silver to observing the molecules that are merely positioned on top of the closed metal layer. We best use the value at 2 nm coverage to estimate the layer alignment between MeO-TPD and silver.

The resulting interface alignment of the bottom and top contact is illustrated in Fig. 4.4. Within the experimental error of the measurement technique, the alignment is symmetric at both contacts concerning ϕ and ϕ_0 . Only the work function of silver differs considerably, which is caused by the contamination of the top contact. The depletion layer width can only be measured for the bottom contact. Since the level bending is comparable on both sides, the depletion width is most likely comparable as well.

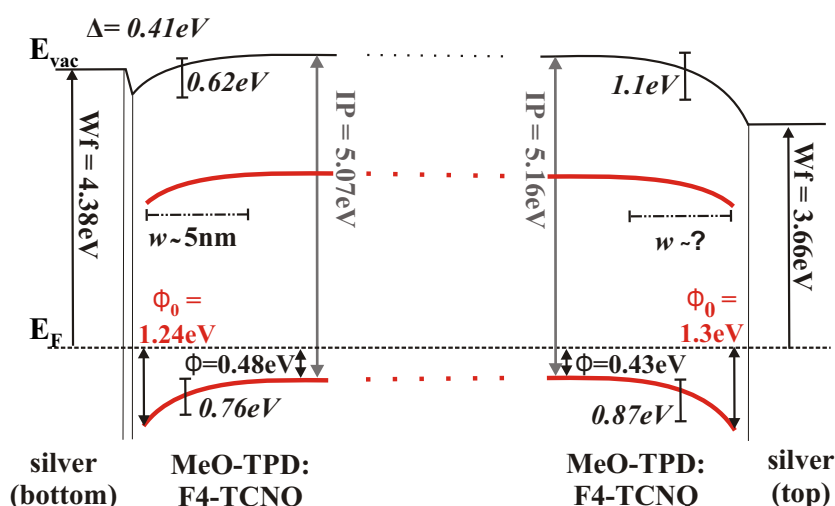


Figure 4.4: Resulting from the PES measurement presented in this Section, this illustration shows the schematic energy level alignment between a silver bottom contact (left side) and a silver top contact (right side) with MeO-TPD doped by F4-TCNQ at a molar ratio of 0.045 and 0.49, respectively.

4.1.2 Energy Level Alignment between Silver Bottom and Top Contacts with Doped BPhen

The same experiments are performed on the interfaces of silver and BPhen doped by Cs. The doping concentration is chosen to give a typical conductivity of the organic layer of $2 \cdot 10^{-5}$ S/cm. This results in a doping concentration of 0.5 to 1 Cs atom per BPhen molecule, measured by comparing XPS signals of Cs and nitrogen.

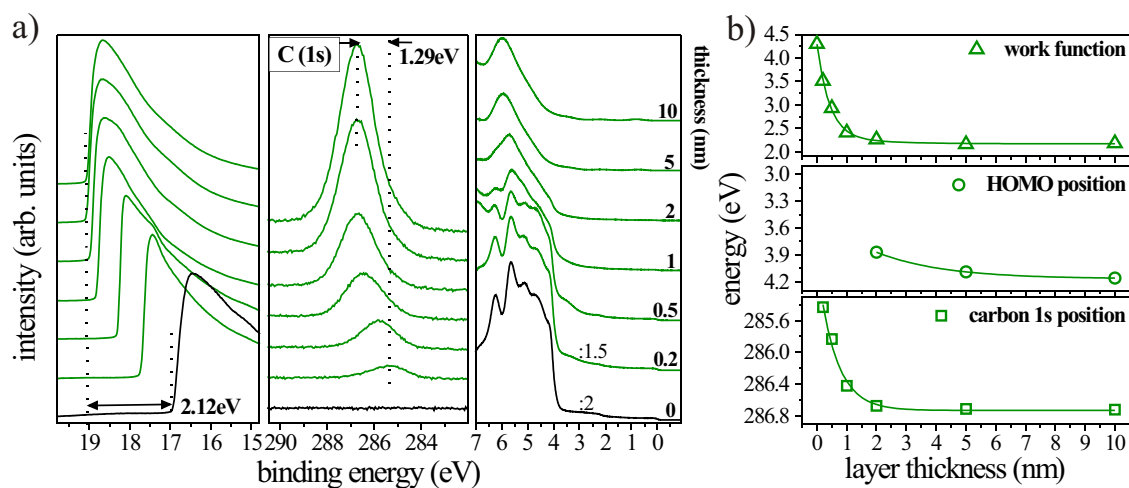


Figure 4.5: a) Interface resolved PES measurement of the alignment between a silver bottom contact and a BPhen layer doped with Cs at MR=0.71. Shown is the development of HBEC, carbon 1s peak, and valence band region. The UPS spectrum of pure silver and 0.2 nm n-BPhen coverage are reduced in height for a better comparability. b) Change in the Wf and HOMO cutoff as well as the C 1s position depending on the organic layer thickness.

The PES measurements between the silver bottom contact and n-BPhen doped at $MR = 0.71$ are shown in Fig. 4.5a. Again, the evolution of the HBEC and valence band region are displayed; furthermore the carbon 1s peak is shown. The corresponding shifts are plotted in Fig. 4.5b. For this interface, it is not possible to identify the HOMO position of BPhen for coverages below 5 nm, as the HOMO is located around 4 eV which is the same energy range the silver 4d states are located at. Therefore, again the XPS signal is used to measure the energy level shift. The C 1s peaks shifts within the first 2 nm deposition of the BPhen layer by 1.29 eV away from the Fermi energy. The Cs doping seems to be very efficient, resulting in such a small depletion layer width. The change in vacuum level position is rather large with a total shift of 2.12 eV. At this interface, the level bending and the interface dipole go in the same direction and are not distinguishable. The hole injection barrier of the 10 nm thick n-BPhen layer accounts for $\phi = 4.16$ eV. In combination with the shift of the C 1s peak, the interface injection barrier can therefore be estimated to be $\phi_0 = 2.87$ eV.

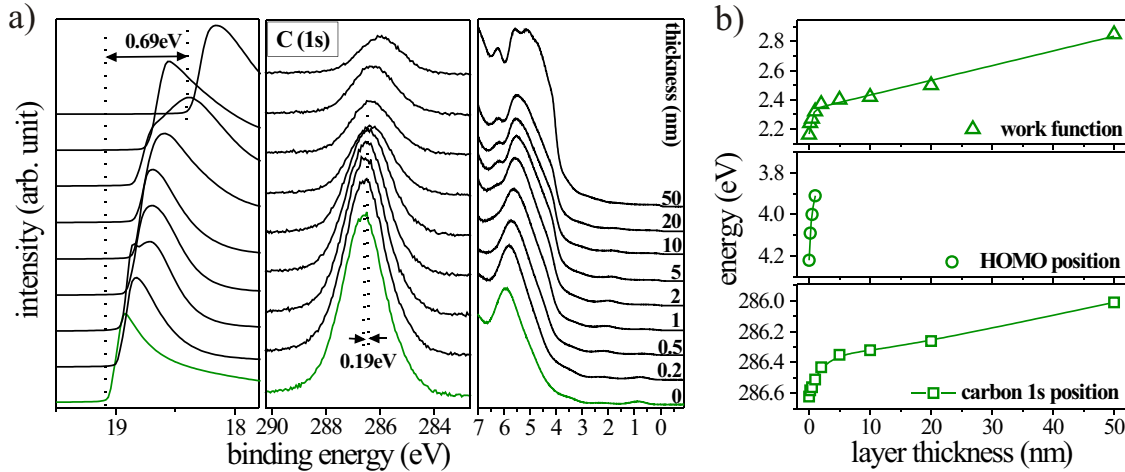


Figure 4.6: a) Interface resolved PES measurement of the alignment between a BPhen layer doped with Cs at $MR = 1.16$ and a silver top contact. Shown is the development of HBEC, carbon 1s peak, and valence band region. b) Change in the Wf and HOMO cutoff as well as the C 1s position depending on the metal layer thickness.

The measurement of the metal top contact is given in Fig. 4.6. In analogy to the top contact on p-MeO-TPD, the correct silver work function is not achieved either. After a fast change in the HBEC for the first 2 nm, the shift continues much slower and after 50 nm, a value of $Wf = 2.85$ eV is reached. However, this time no saturation of the shift takes place. The C 1s peak shows the same behavior of a rapid shift in the beginning that levels off after 2 nm deposition. In total, the peak moves towards the Fermi energy by 610 meV. The HOMO peak is observable up to 2 nm coverage before it becomes shielded by the silver states.

The attenuation of the substrate carbon peak and the intensity of the silver $3d_{3/2}$ peak are plotted in Fig. 4.7 and two regimes appear again; here as well, a surface contamination is found. This time the HOMO intensity cannot be fitted, as the silver 4d states interfere. For this interface no saturation of the signal intensity sets

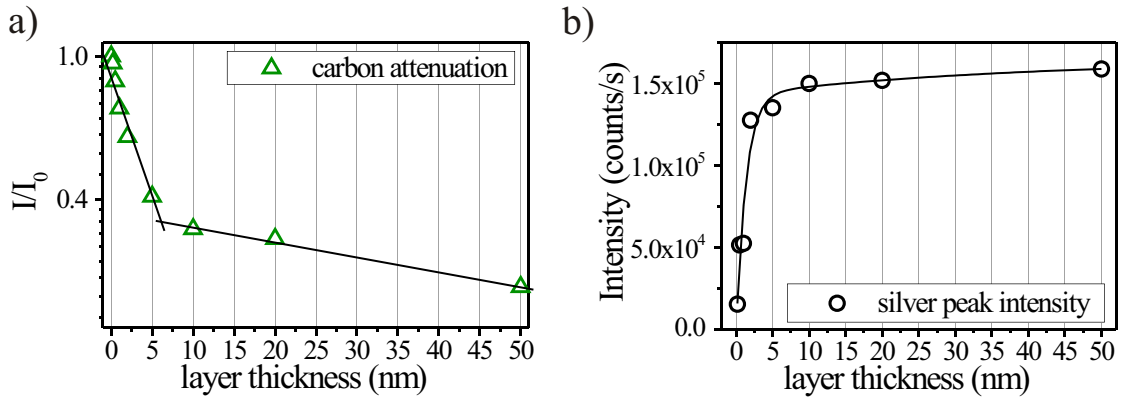


Figure 4.7: Relative attenuation of the pristine carbon 1s signal I_0 of the n-BPhen layer depending on the coverage by the silver top layer. b) Intensity of the silver 3d_{3/2} peak depending on the silver coverage.

in, just a change in slope after 6 nm. This means the contamination of the surface decreases with increasing silver thickness.

Just as in the case of p-MeO-TPD, the values reached at 2 nm coverage are used to find the alignment of the top contact. Using the shift of the carbon peak of 190 meV and subtracting this from the hole injection barrier of the pristine n-BPhen layer of $\phi = 4.22$ eV results in $\phi_0 = 4.03$ eV. The measurements lead to the alignment shown in Fig. 4.8 for doped BPhen with a silver bottom and top contact.

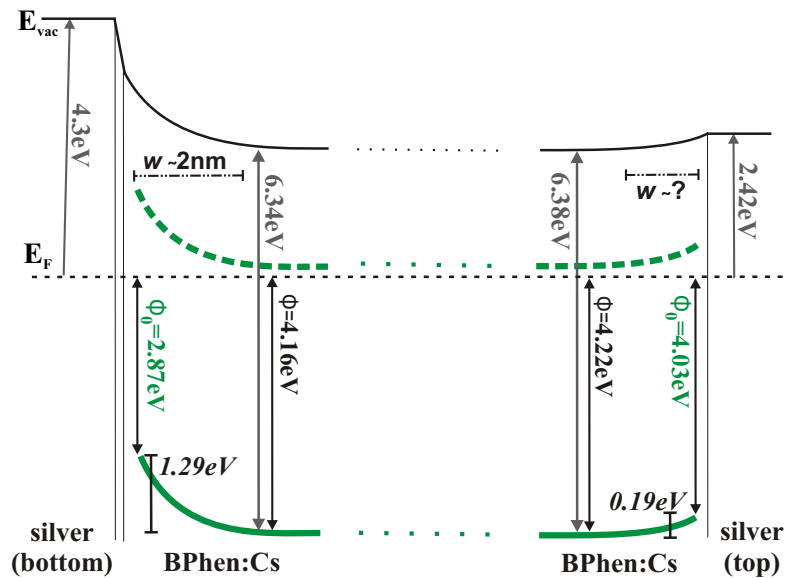


Figure 4.8: Schematic energy level alignment between a silver bottom contact (left side) and a silver top contact (right side) with BPhen doped by Cs at a molar ratio of 0.71 and 1.16 for the bottom and top contact, respectively.

Clearly, the alignment is asymmetric as the top contact shows almost no level bending and the LUMO is very close to the Fermi energy even at the interface. The depletion layer width cannot be measured for the top contact. Since the built-in

voltage of the depletion layer is just $V_B^{top} = 0.19$ eV, the width is most likely even smaller than the 2 nm observed at the bottom contact where $V_B^{bottom} = 1.29$ eV. This alignment leads to a more efficient tunneling into the LUMO at the top contact and therefore to the higher injection current.

Gap state formation: Commonly, gap states are observed in UPS measurements in the case of n-doping [51, 64, 158]. There, the dopant introduces new states between the HOMO and the Fermi edge, e.g. by the formation of a charge transfer complex. For the two interface resolved measurements shown in this Section, the evolution of these gap states are shown in Fig. 4.9 to explore the reason for the asymmetric alignment. Shown is a magnification of the region between the HOMO of BPhen and the Fermi energy. To identify the weak features, the signal produced by the satellite excitation lines of the He discharge lamp have been subtracted by the method described in the Appendix. Furthermore, the curves are smoothed by adjacent averaging over 5 data points to obtain a better signal to noise ratio.

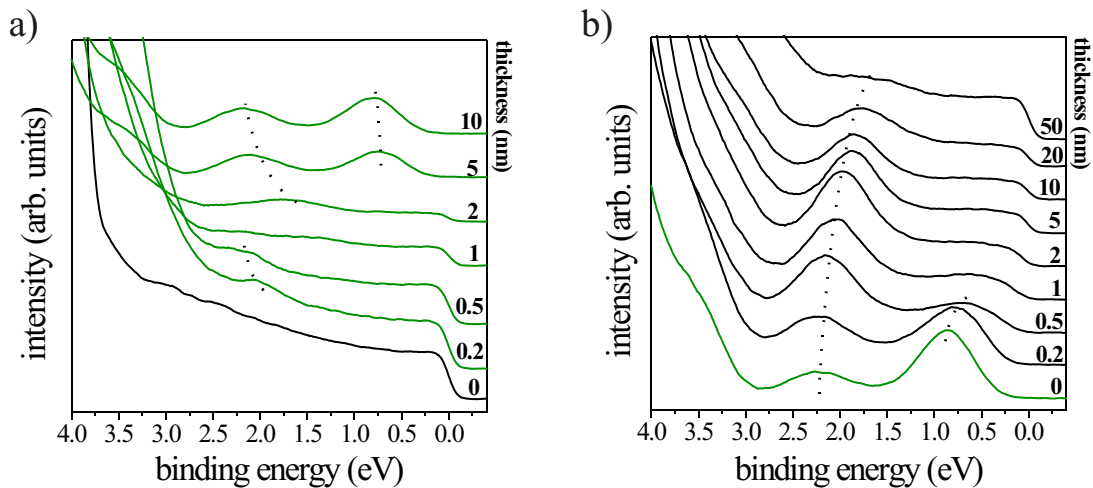


Figure 4.9: UPS measurement of the interface state and gap states forming between the HOMO onset and the Fermi energy during the formation of a) the silver - BPhen:Cs and b) the BPhen:Cs - silver interface

On the left side, the UPS measurements on the metal bottom contact are shown. For 2 Å and 5 Å n-BPhen thickness, a weak interface state appears around 2 eV that is not visible any more after the first monolayer is completed. The typical gap states for BPhen doped by Cs appear only after 5 nm coverage at 0.8 eV and 2.1 eV (peak positions). For the reverse deposition, the UPS spectra are shown on the right side of Fig. 4.9, where we see a clear influence of the deposited silver atoms. The first 0.5 nm of metal deposition suppresses the gap state at 0.8 eV, while the second gap state between 2 and 2.5 eV is either increased in intensity or this is a new gap state arising at the same energy range. This indicates a reaction between BPhen and silver atoms accompanied by a charge transfer. This is further supported by the energetic position of the silver $3d_{3/2}$ state during the interface formation that is plotted in

Fig. 4.10. A shift by 330 meV towards lower binding energy takes place for the first 5 nm deposition before the typical bulk value of $E_B = 368.25$ eV is reached. For the first few nm, the silver atoms are positively charged, therefore the BPhen experiences an additional n-doping by the penetrating metal atoms.

Further indications for this process come from laser desorption/ionization time-of-flight mass spectrometry (LDI-TOF-MS) measurements where a complexation between the topmost organic layer of BPhen and Al or Ag has been observed [127].

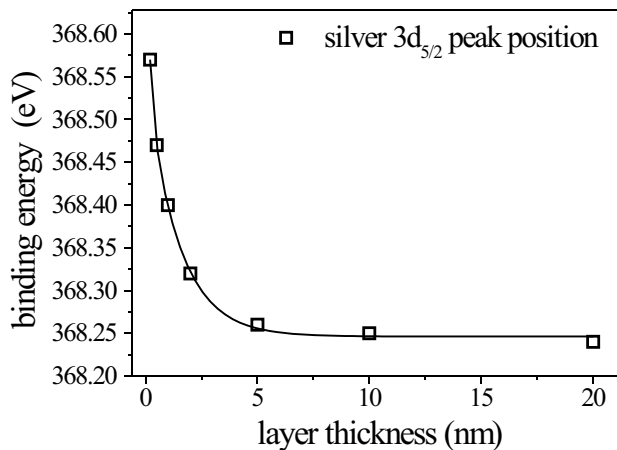


Figure 4.10: Shift in binding energy of silver $3d_{3/2}$ peak during the interface formation of the metal top contact on n-BPhen depending on the top layer thickness. The measurement indicates a charge transfer between Ag and BPhen.

4.2 Formation of Ultra-Thin Metal Top Contacts

It was reported in the previous Section that the formation of silver metal top contacts goes along with a contamination by the molecules in the case of MeO-TPD and BPhen. This is not an important issue when thick, intransparent metal top contacts are used as it is the case for bottom emitting OLEDs or conventional organic solar cells. Here, the light is coupled out or in via the transparent bottom ITO substrate. Typical top contact thickness are in the range of 40 to 100 nm. However, if top emitting OLEDs [159, 160], transparent OLEDs [161], or transparent solar cells [162–164] are realized, the top contact has to be as thin as possible to prevent losses due to absorption. This makes it necessary to find a top contact that shows a good coverage at low thickness and little or none intermixing with the organic layer. Silver is in general a well suited top contact material due to its excellent electrical [165] and optical [166] properties. However, optoelectronic devices made with a 15 nm transparent silver top contact have an inferior performance compared to conventional devices. In an effort to improve this, it has been figured out that upon insertion of a 1 nm aluminum surfactant layer between the organic material and the thin Ag (or Au) layer, the performance of such a noble metal top contact can be improved [163].

This behavior can be partly understood from Fig. 4.11, showing scanning electron microscopy (SEM) micrographs of two samples made from 7 nm BPhen (the topmost organic layer employed in typical device stacks) that is either covered by 15 nm of silver (left image) or 1 nm aluminum and 14 nm silver (right image). As substrate, Borofloat 33 glass plates (Schott AG, Germany) are used. Clearly the morphology is significantly different, with the sample containing no surfactant layer being rougher, while the 1 nm Al leads to more closed and smooth layers. Since the total metal layer thickness is the same (15 nm) for both cases and should be above the coalescence threshold [167], the different growth modes must have their origin in processes on the atomic scale, e.g. the surfactant changing the layer growth mode.

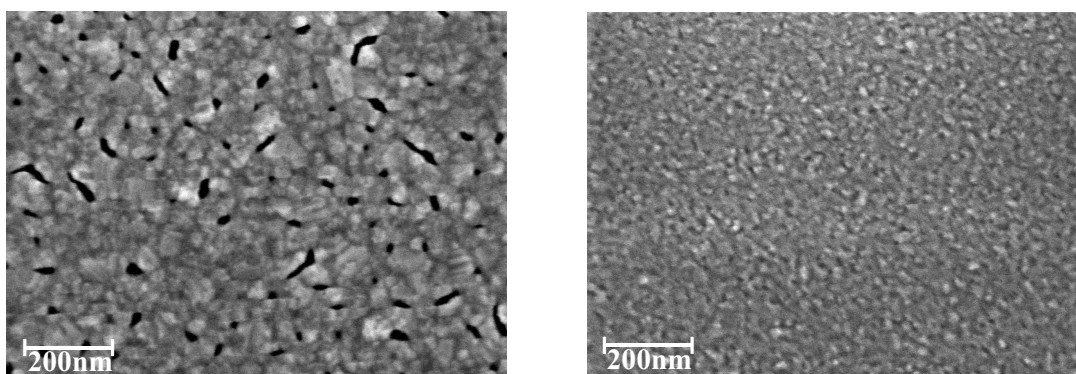


Figure 4.11: SEM micrographs of the two different metal over layers on glass substrates covered by 7 nm thick BPhen layers. Left: covered by 15 nm Ag. Right: with 1 nm Al and 14 nm Ag; taken from [168].

From the SEM image, the details of this surfactant effect caused by the 1 nm Al cannot be resolved. Therefore, comparative PES studies are performed of the top contact formation between BPhen and silver (sample 1) and BPhen with a 1 nm Al interlayer and 14 nm silver (sample 2) to gain detailed information on the interaction of the two metals with the organic layer. As substrate, ITO is used to ensure a smooth surface. Before the BPhen is evaporated onto this substrate, it is cleaned by organic solvents, followed by 4 minutes of sputter treatment with argon ions at 1.3 kV under UHV conditions to remove residual surface contamination. This is found to be necessary to ensure a good sticking of the BPhen molecules to the surface.

The results of the UPS measurements of sample 1 are shown in Fig. 4.12. In principle, the measurement resembles that presented in Fig. 4.6, with the difference that this time an undoped BPhen layer is used. The left side shows the HBEC, the middle graph shows the DOS of the valence band area, and the right image is a magnification of the gap region of BPhen. To see the weak features in the gap the satellite lines are subtracted (see Appendix). The BPhen layer shown in curve (a) has a work function of 2.89 eV and a hole injection barrier of $\phi = 3.76$ eV, marked by the solid vertical line. After deposition of 1 nm of Ag (curve b), the DOS shows no significant change and the HOMO of BPhen is still clearly visible, being slightly shifted away from the Fermi energy by 200 meV. Two gap states show up at 0.36 eV

and 1.65 eV that indicate the formation of charge transfer complexes between BPhen and silver, as it was already observed between silver deposited on n-doped BPhen in Fig. 4.6. The Fermi edge of the silver layer is not visible. This means that the Ag atoms corresponding to 1 nm layer thickness do not form a closed layer, but almost fully penetrate into the BPhen bulk where they lead to a n-doping effect. After an additional coverage by 14 nm Ag (curve c), the DOS starts showing additional substructures, but still bears similarity to the BPhen features. The typical 4d valence states of Ag located between 4-6 eV binding energy are not present and the Fermi energy shows only weakly. Just as observed in the previous Section, the work function of 2.59 eV is too low for an amorphous Ag bulk layer.

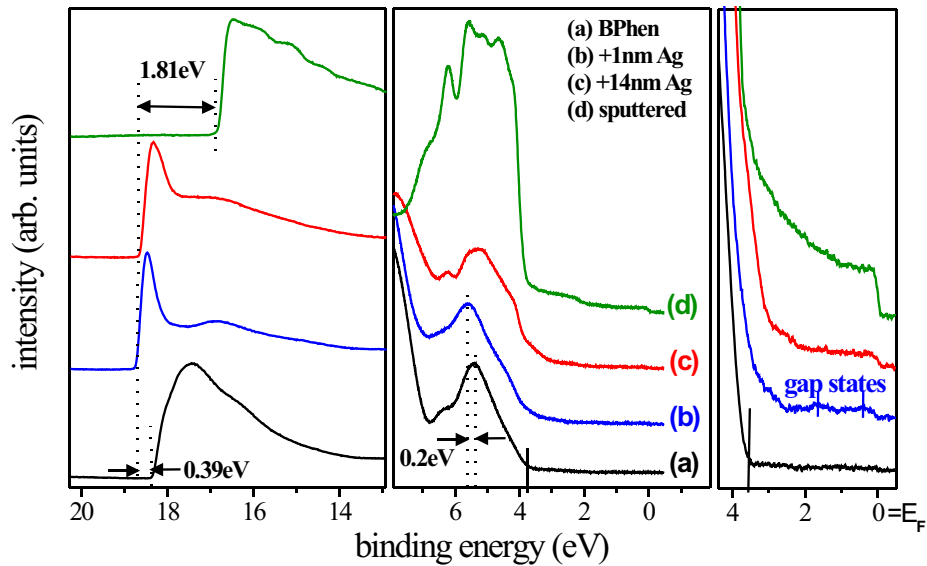


Figure 4.12: UPS measurements of sample 1. The left side shows the HBE, the middle graph displays the valence band features and the right side shows a magnification of the region within the BPhen gap. Shown are the measurements of 10 nm BPhen where the HOMO onset is marked by a solid vertical line (a), a coverage by 1 nm Ag (b), an additional coverage by 14 nm Ag (c), and the same sample after a 30 s sputtering process (d).

This time the assumption of a thin surface contamination is tested by exposing the sample for 30 s to an argon ion sputter beam to remove the top few Å of material. This should only lead to the disappearance of the carbon signal if indeed a layer of BPhen is located on top. If cracks in the surface or an insufficient coverage due to e.g. island formation are the reason, the sputtering should not be able to remove the carbon signal. The UPS spectrum taken after the sputtering treatment is shown in curve (d). A drastic modification can be seen, the work function changes by 1.81 eV and reaches a value typical for amorphous silver of 4.4 eV. The valence band features change as well, now showing the valence band of silver and the Fermi edge appears.

We thus conclude that some amount of BPhen covers the metal surface. To find out how much of the organic semiconductor is present there, the measurement of the contaminated surface of Fig. 4.12c is compared to a separate sample where BPhen

is evaporated in sub-nm steps onto an ITO sample covered by 15 nm of clean silver. This measurement shows at which thickness the UPS measurement of the BPhen covered silver resembles that of the contaminated silver top contact. Furthermore, it is investigated at which point the same ratio of Ag to C peak intensities is reached in XPS measurements. Figure 4.13a shows the valence band region of UPS measurements of the different coverages by BPhen from 0 Å to 14 Å in different shades of gray as well as the measurement of the contaminated silver from Fig. 4.12c as red dashed line for comparison. The valence band shape is not exactly reproduced when BPhen is evaporated on silver, most likely due to less intermixing during this evaporation sequence. The closest resemblance is achieved for the thicknesses of 6 Å and 8 Å. The measurement of the XPS peak intensities supports this finding. In Fig. 4.13b, the dependence of the relative silver and carbon peak intensities I_{Ag}/I_C is plotted vs. the BPhen layer thickness. For the measurement of the contaminated silver top contact, this ratio is found to be $I_{Ag}/I_C = 19.7$. This value is indicated in the graph by the horizontal red dashed line. A similar ratio is therefore reached after 8 Å.

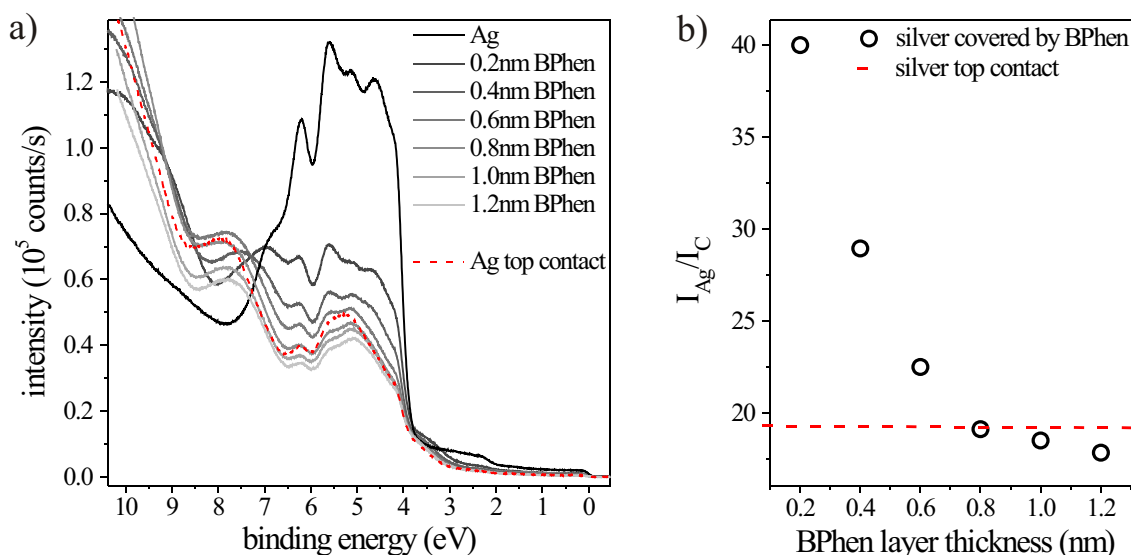


Figure 4.13: a) UPS measurement of the valence band region of amorphous silver onto which subsequently a (sub-)monolayer of BPhen is evaporated. The red dashed line is the measurement of the contaminated silver top contact of Fig. 4.12c. b) Dependence of the relative intensities of the silver to carbon XPS peak intensity on the BPhen layer thickness. The dashed horizontal line shows the value for the contaminated silver top contact.

Furthermore, sample 2 is investigated, where 1 nm of aluminum is inserted between the organic layer and the silver top contact which is shown in Fig. 4.14. The UPS spectrum of BPhen presented in curve (a) shows a similar alignment compared to the measurement in Fig. 4.12a. However, the modified metal top contact exhibits a completely different behavior. The evaporated thin Al interlayer shown as curve (b) covers the BPhen well enough to suppress the HOMO features and makes it difficult to quantify its shifting. We can conclude that 1 nm Al is able to form a closed layer on BPhen. From the carbon 1s core level shift of 0.39 eV towards lower binding energy,

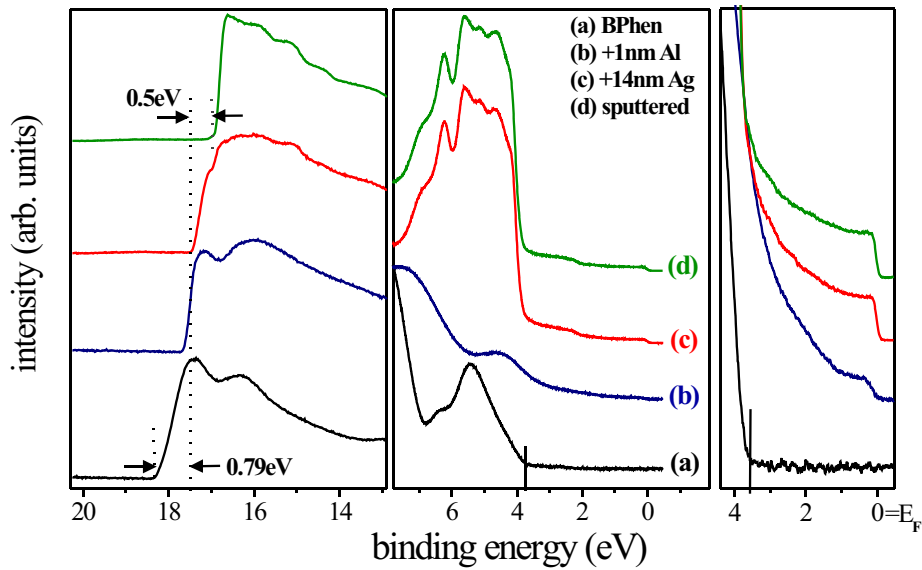


Figure 4.14: UPS spectra of sample 2. The left side shows the HBE, the middle graph displays the valence band features and the right side shows a magnification of the region within the BPhen gap. Shown are the measurements of 10 nm BPhen where the HOMO onset is marked by a solid vertical line (a), a coverage by 1 nm Al (b), an additional coverage by 14 nm Ag (c), and the same sample after a 30 s sputtering process (d).

measured by XPS, a p-type doping can be concluded. It is not likely that aluminum has a p-doping effect in BPhen, the reason must therefore be the oxygen that is always incorporated when evaporating the very reactive Al, even at pressures of 10^{-8} mbar. Judging from the various bonding states of Al and the appearance of an O 1s peak in the XPS measurement (data not shown), one can conclude that the aluminum is indeed oxidized. However, this layer exhibits a metallic character as the Fermi edge is clearly visible. The 14 nm silver evaporated onto this interlayer in curve (c) exhibit a work function of 3.8 eV, which is already much closer to the expected value of 4.3 eV compared to sample 1 and show the typical Ag states and the Fermi edge. This sample is sputtered for 30 s as well, however this time no change in the valence band features can be observed in the resulting curve (d) and the height of the Fermi energy stays the same. This is not surprising, as it already looked like a clean surface after the silver deposition. There is a change in the vacuum level by 0.5 eV that results in a proper silver work function of 4.31 eV, indicating that a very small amount of surface contamination is present.

To obtain more information on the composition of both samples, the sputtering of the surface is continued. In this so called *x-ray depth profiling*, the topmost layers are successively removed by Argon sputtering and the relative peak intensities are measured by XPS depending on the distance from the former surface. It is, however, not straightforward to correlate the sputter time to an actual depth due to inhomogeneities in the sputter profile and the probing depth of a few nm when using XPS that can only give an average of the signal of the topmost layers. Furthermore, atoms

are not always removed by the sputtering, but can partly be pushed into the underlying layers as well. However, even without exact knowledge of the actual depth, this method is well suited for a qualitative comparison of the composition between samples of similar structure.

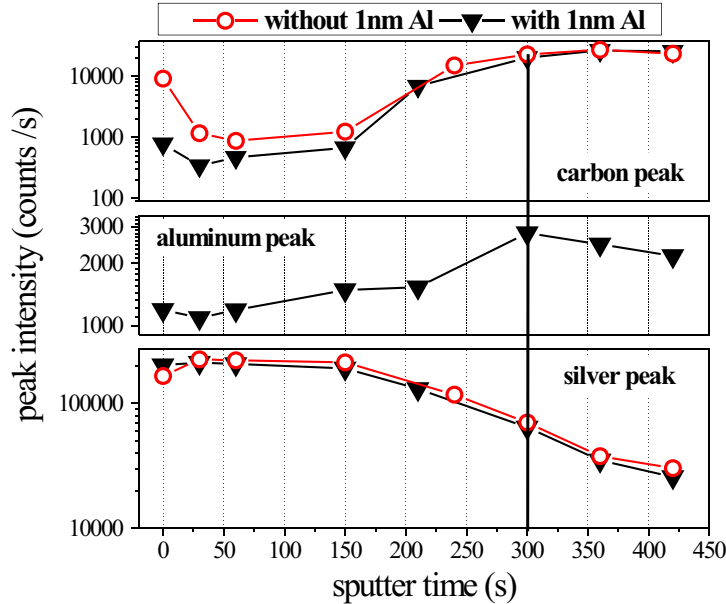


Figure 4.15: x-ray depth profile measurement of sample 1 (without Al, empty circles) and sample 2 (with Al, filled triangles). The changes in carbon, aluminum, and silver peak intensities are plotted depending on the sputter time and therefore the distance from the former surface.

The results of the depth profiling of both samples are shown in Fig. 4.15. The first two measurement points show the contaminated surface and the previously mentioned 30 s cleaning procedure. After further sputter steps of 30 to 90 s duration, the intensity of the carbon and metal peaks are recorded. An estimation of the sputter time at which the silver top layer is completely removed can be achieved from the measurement of the aluminum signal; after 300 s this peak reaches its maximum, marked by the vertical line in Fig. 4.15.

The intensity scale is chosen logarithmic in order to show the relevant behavior of the carbon peak intensity at low sputter depths. Before sputtering, sample 1 shows a higher carbon signal and lower silver signal compared to sample 2 due to the previously discussed contamination layer on top. After 30 s of sputtering, this layer is removed and both samples show nearly identical peak intensities of the silver signal. However, the carbon intensity remains larger for the sample without the aluminum throughout the whole metal top contact. This suggests a contamination throughout the silver layer by BPhen in sample 1 which is not present in sample 2.

From these measurements, we can conclude that at low silver coverages the metal atoms diffuse into the BPhen leaving almost a bare BPhen surface behind. For larger thicknesses, a small concentration of BPhen molecules remains in the metal layer and a BPhen monolayer ($\approx 8 \text{ \AA}$) forms on top of the metal contact. Therefore, there is

no abrupt interface from BPhen to Ag. In the case of a thin aluminum interlayer, the interface is abrupt as the aluminum binds at the surface to the BPhen, preventing a diffusion of the subsequently deposited silver atoms. This way, a pure metal layer can form on top, which is advantageous for the metallic behavior and smoothness as could be shown by the SEM images. This is the reason why organic solar cells employing Al surfactant layers between organic materials and noble metal top electrodes exhibit superior performance compared to top electrodes consisting of only noble metals like Ag or Au.

5 Investigation of the p-Doping Process in Organic Semiconductors

During the last years, the performance of organic devices like organic light emitting diodes and organic solar cells could be significantly improved by the concept of doping due to a decrease in series resistance, a significant increase in carrier density, and the realization of ohmic injection. Currently, the most efficient white OLEDs [169] and certified organic solar cells with an area $>1\text{ cm}^2$ [170] are using molecularly doped layers. In this Chapter, we investigate the basic characteristics of a doped organic semiconductor system regarding the shift of the Fermi level position, the change in conductivity, and the change in depletion layer thickness depending on the doping concentration. This is compared to the basic theory of doping conventional semiconductors as it was discussed in Chapter 2.3.2. We focus on the concept of p-doping for which we use the material combination of MeO-TPD doped by F4-TCNQ. In a few cases, the results are compared to different dopant and matrix molecules to check the validity of the results.

5.1 Current Status of the Field

As already mentioned in Chapter 2.3.2, Blochwitz et al. [10] were first to investigate the interface between a metal and a doped organic semiconductor by UPS. They used ZnPc doped by F4-TCNQ and compared the alignment on ITO and gold where they found small hole injection barriers and a thin depletion region. Several studies by other groups were able to support the findings by Blochwitz et al. for p-doped systems [41, 49, 68, 69] as well as for n-doped systems [52, 60, 63, 64, 171]. However, few extensive and systematic studies of the work function change and modification of depletion layer width with doping concentration have been done so far. Gao et al. [171] attempted a systematic variation of the doping concentration of the inorganic donor Cs in CuPc, but as this was done by simple interface doping with some diffusion taking place, the results are of limited significance. Lately, Kröger et al. [41] looked at α -NPD¹ and CBP doped by co-evaporation of the acceptor type metal

¹N,N'-bis(1-naphthyl)-N,N'-diphenyl-1,1'-biphenyl-4,4'-diamine

oxide Mo_3O_9 . Both studies found for low doping concentrations (< 0.15 MR Cs and < 2 mol% Mo_3O_9) an unusually rapid shift of the Fermi level towards the respective transport states. A further increase of the doping concentration leads to a pinning of the Fermi level several 100 meV beyond the conduction band edge.

In particular, an extensive study on small molecule dopants has not been published up to now. Gao et al. compared two different doping ratios of F4-TCNQ in α -NPD [69] and saw no change in hole injection barrier ϕ between the two. Therefore, they concluded a pinning mechanism here as well. Chan et al. [64] compared 3 different doping ratios of the organo-metallic complex DMC doped into CuPc and saw E_F approach the LUMO for increasing DCM concentration. However, they drew no conclusions from the magnitude of this shift.

5.2 Testing the Stability of the Matrix - Dopant System

Before presenting the extensive studies performed on the matrix material MeO-TPD doped by the small molecule F4-TCNQ, we have to test that this combination is a stable system that can be used for the subsequent measurements. There are some reports in literature stating that F4-TCNQ tends to diffuse within a matrix. However, this seems to hold true only for crystalline materials and not for amorphous ones like MeO-TPD [8]. To test if diffusion takes place, an experiment similar to the one of Ref. [8] is performed. A silver foil is covered by 1 nm F4-TCNQ and the intensity of the fluorine signal is measured. On top of this, 10 nm of intrinsic MeO-TPD are deposited and this sample is left in UHV at room temperature for 22 hours. At various times the sample is measured by XPS to see if the intensity of the fluorine signal increases, which would mean that the dopant diffuses towards the surface. The change in intensity of the fluorine signal is shown in Fig. 5.1.

In this plot, the first measurement point is the one of the pristine F4-TCNQ layer; upon coverage by MeO-TPD, this signal almost vanishes. Therefore, the inset shows the same data set without this first measurement point. As XPS has a probing depth of several nanometers, the fluorine signal is still measurable, even though we have to assume large error bars due to the poor signal to noise ratio. Within the first 3 h, no increase in dopant signal is detected. Over longer time scales, an increase by a factor of 1.4 seems to take place, indicating a slow diffusion process into the MeO-TPD. We can still assume a constant doping profile in our mixed layers under investigation as the collection of the data takes much less than this time and furthermore, the diffusion is here driven by a gradient in the dopant concentration that is not present in the samples under investigation, since we study samples with homogeneous doping profiles.

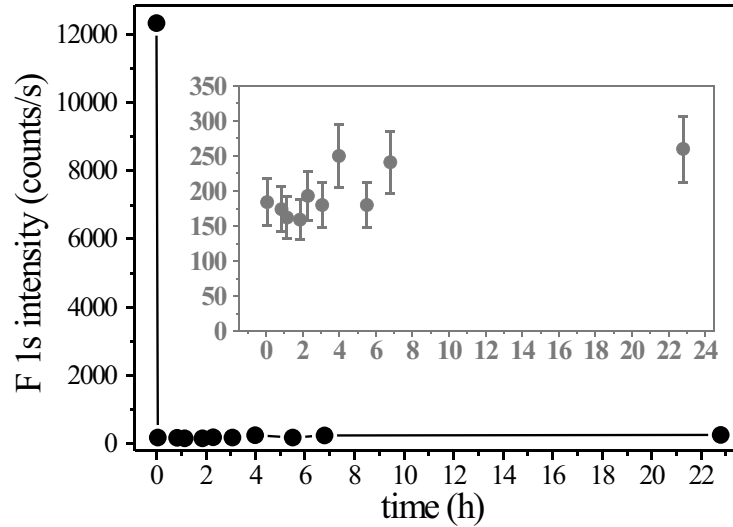


Figure 5.1: Plot of the F 1s peak area from the F4-TCNQ molecules over a time of 22 h in a sample where 10 nm MeO-TPD are deposited on 1 nm F4-TCNQ to check the diffusion of the dopant; the first measurement point is the signal from the pure F4-TCNQ layer, the following ones are taken with the MeO-TPD on top. The inset shows the same graph without the first measurement point.

5.3 Dependence of the Hole Injection Barrier on the Substrate Work Function

For undoped organic semiconductors, interface induced states play a major role on the alignment which was already discussed in Chapter 2.3. It has been shown in various studies that the work function of the organic semiconductor, and thereby the hole injection barrier ϕ , strongly depends on the material used as substrate. In contrast to that, in doped organic semiconductors the high concentration of free charge carriers on the order of 10^{18}cm^{-3} should align the Fermi level with the substrate, instead of being defined by the vacuum level or the interface induced states. In that case, $W_{f_{org}}$ should not depend on the contact material, but only on the organic material used as a matrix and the amount of doping.

To verify this assumption, MeO-TPD is doped by approximately $MR \approx 0.04$ of F4-TCNQ (a typical value for devices) and the alignment on three different substrates is investigated, depending on the layer thickness of the organic material. The substrates chosen for the study are commonly used in device fabrication and span a wide range of physical and chemical properties. These are sputter cleaned silver foil, sputter cleaned ITO, and the spin coated polymer PEDOT:PSS that is heated for 30 min in air at 130°C prior to transferring it into vacuum.

The UPS measurements in Fig. 5.2a and b show the thickness dependent development of the high binding energy cutoff, oxygen 1s peak, and valence band region of the measurements performed on ITO and PEDOT:PSS. The measurement performed on the silver foil has already been shown in Fig. 4.1 on page 76 in a different context.

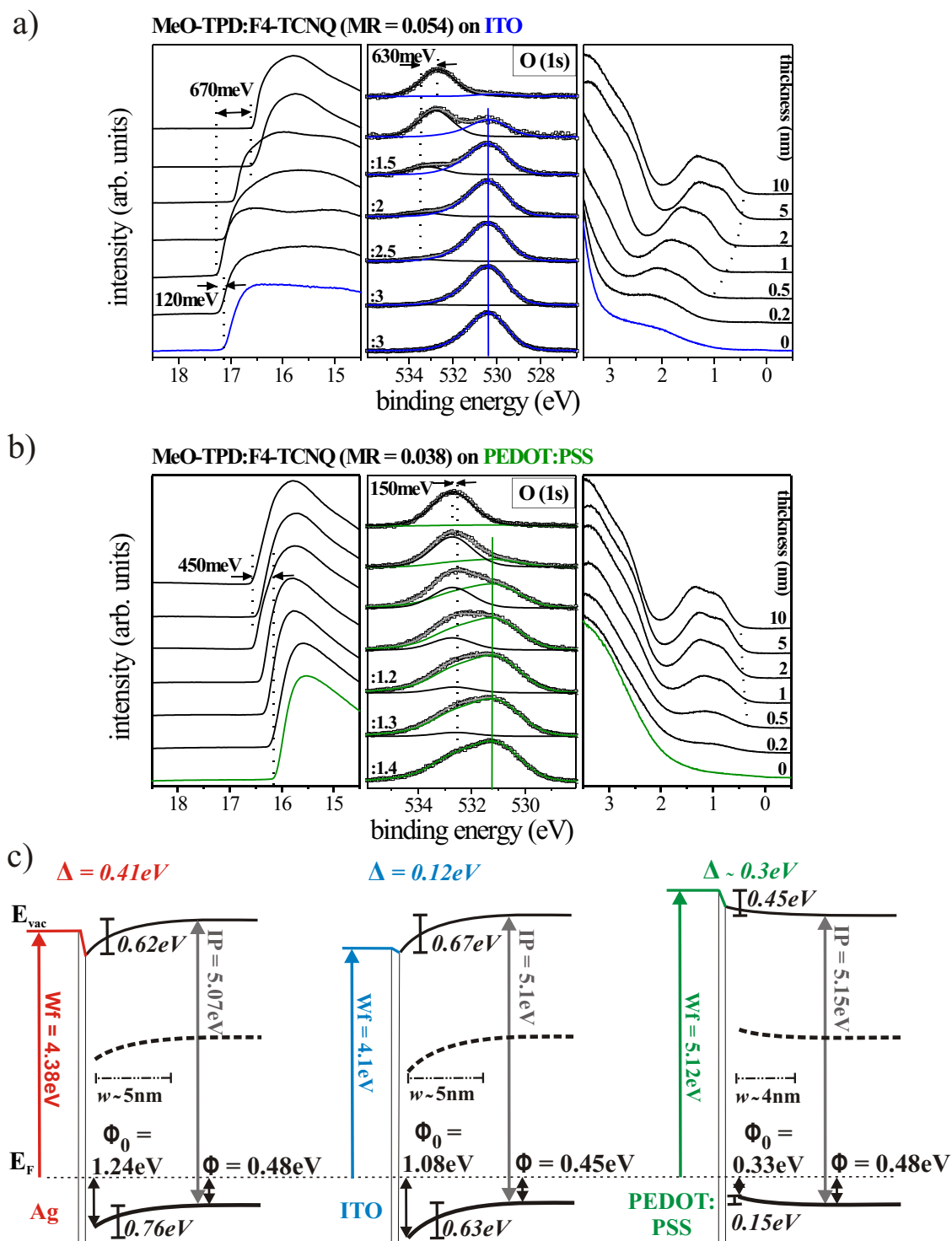


Figure 5.2: UPS measurement of the HOMO and HBEC region as well as XPS oxygen 1s peak of MeO-TPD doped with a molar ratio of ≈ 0.04 of F4-TCNQ stepwise evaporated onto a) ITO and b) PEDOT:PSS. Some of the XPS curves have been reduced in intensity for better comparability, the corresponding numbers divided by are given at the spectra. c) Resulting schematic energy diagrams for the interfaces on the different substrates including the measurement on silver already shown in Fig. 4.4.

The oxygen peak is chosen as it is only present in the matrix material and not in the dopant, so it can be specifically observed how the shift takes place for the energy levels of the MeO-TPD molecules. A minor drawback is that oxygen is also present in the substrates ITO and PEDOT:PSS. However, as the binding energy of the substrate peak is different, the peaks can easily be separated. The O 1s signal originating from the substrate is marked by solid vertical lines in Fig. 5.2 and as expected they are not influenced by the organic evaporated on top. The information of the MeO-TPD oxygen peak shift is needed, since at low coverages it provides a more accurate determination of the level bending compared to the HOMO cutoff.

The relevant values taken from these two measurements and the one with silver as substrate are shown as schematic energy diagrams in Fig. 5.2c. There is no vacuum level alignment at the interface, but an interface dipole is present, especially in the case of the silver substrate. The value of ϕ_0 directly at the interface is influenced by the work function of the substrate and the amount and direction of the interface dipole. After about 1 monolayer deposition, the level bending becomes obvious and continues for approximately 4-5 nm. In the case of PEDOT:PSS, the interface dipole and level bending cannot be held apart because both go into the same direction. By subtracting the shift of the oxygen peak from the total vacuum level shift, it can be estimated that $\Delta \approx 0.3$ eV. For all substrates, the final alignment after the level bending is completed yields a ϕ that is between 0.45 eV and 0.48 eV. The remaining difference is most likely due to variations in the exact doping concentration between the samples (the values are given above the plots of the UPS measurements). This independence of the work function of the organic semiconductor on the substrate is a clear sign of Fermi level alignment between substrate and organic semiconductor that, as said before, is not the case for undoped organic layers at least in the thickness range relevant for devices [111]. Thus, it is shown that level bending compensates any effect of the substrate properties within a width of 5 nm when a doping ratio of $MR = 0.04$ is used. Even though the choice of substrate influences ϕ_0 , this value will only play a minor role in a device since the depletion layer can easily be tunneled through.

5.4 Systematic Variation of the Doping Concentration

5.4.1 Change in Fermi Level Position

In further experiments the dependence of the hole injection barrier ϕ on the doping concentration is investigated. For this purpose, silver is used as a substrate and 15 different doping ratios are prepared, ranging in the molar ratio from 0 to 0.62 (corresponding to a doping concentration between 0 mol% and 38.2 mol%). The actual doping ratio for each of the samples is determined by the relative peak intensities of the MeO-TPD oxygen peak and the F4-TCNQ fluorine peak. This is necessary since

F4-TCNQ shows a very volatile behavior and a substrate dependent sticking coefficient, so the intended doping ratio chosen during the co-evaporation is not necessarily achieved.

For the organic layer thickness, a value of 15 nm is aimed for, assuming a comparable contribution of dopant and matrix molecules to the total layer thickness, therefore adding up the thicknesses shown by the two quartz crystals. As this might not be the case (as will be shown later) the exact thickness is unknown. However, the actual value does not play a role as long as we are above the depletion layer width. In Fig. 5.3, the UPS and XPS measurements of the different doping concentrations are plotted with the change in HBEC, oxygen 1s position, and valence band region, ranging from the lowest doping concentration at the bottom to the highest ratio at the top.

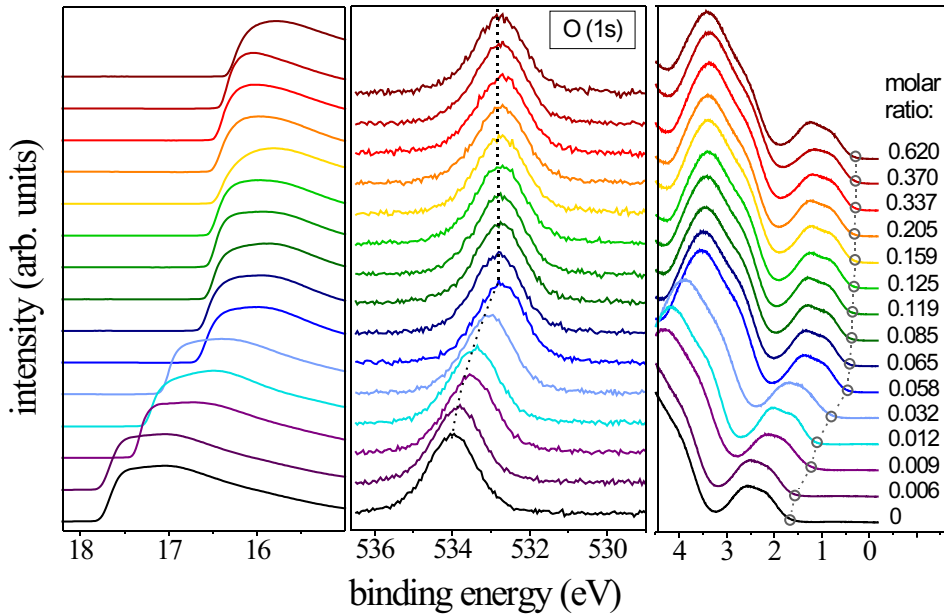


Figure 5.3: UPS spectra and XPS O 1s core level peak taken from 15 differently doped MeO-TPD samples deposited on silver substrates. The amount of doping by F4-TCNQ is varied and ranges from MR=0 to 0.62. The HOMO cutoff positions are marked by open circles and the change in O 1s position by the dotted line.

The intrinsic MeO-TPD layer shows $\phi = 1.68$ eV. As the band gap of this material is 3.2 eV [140] this means that the Fermi energy is positioned close to mid gap. For increasing doping ratios the HOMO position, marked by circles, gets closer to the Fermi energy, as it is expected due to the increasing number of free charge carriers. The total shift amounts to 1.33 eV. The shifts in vacuum level and O 1s peak position behave similarly and show a total change 1.43 eV and 1.29 eV, respectively.

For non-degenerate inorganic semiconductors, a linear dependence of the Fermi level position with doping ratio in a semilogarithmic plot is observed with a slope of $k_B T \approx 0.0259$ eV (see Eq. 2.16). The change of the hole injection barrier ϕ and O 1s position vs. the doping ratio are shown in the semilogarithmic plot of Fig. 5.4.

Two regimes can clearly be identified. For doping ratios below $MR = 0.1$, the Fermi energy rapidly shifts towards the HOMO until a minimum hole injection barrier ϕ_{min} is reached; afterwards no further change can be achieved, even by an increase of the doping ratio by a factor of 6. For the O 1s peak, the same saturation happens already at $MR = 0.07$. This difference could be due to inhomogeneities within the sample as UPS only probes the top few nm, but XPS averages over a larger thickness. In both cases, the change in energetic position with the natural logarithm of the doping ratio has a slope of $0.43 (\pm 0.03)$ eV and therefore $\approx 15 \cdot k_B T$ in the region $< MR = 0.1$. Both effects, the disproportionate slope and the saturation of the doping induced shift, need further consideration.

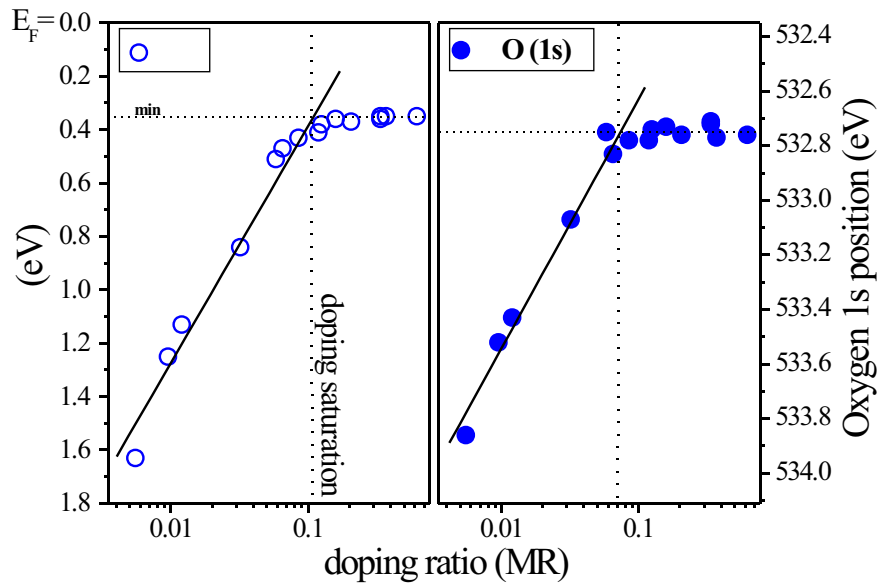


Figure 5.4: Change in hole injection barrier ϕ (empty circles) and O 1s peak position (filled circles) as a function of the logarithmic doping ratio of MeO-TPD:F4-TCNQ; the values are taken from the measurements in Fig. 5.3.

As a reason for the disproportionate slope, one can assume substrate effects and therefore an influence of interface states for the undoped and weakly doped samples, where Fermi level alignment cannot be assumed yet. However, no transition between surface pinning and Fermi level alignment can be observed in the range between the molar ratio of 0 and 0.1, even though we know from the previous Section that at $MR = 0.04$, Fermi level alignment is already achieved. A further aspect could be a clustering of F4-TCNQ molecules; however, this would rather lead to a lowering of the slope since not all of the dopants are in contact with the matrix material and this should get more prominent for higher doping ratios.

A similar kind of excessive slope was published by other groups for two other doped systems mentioned in the beginning of this Chapter. In the case of CuPc doped by Cs [171], the slope was four times $k_B T$ and explained by a broadening of the energy distribution due to a coupling to the dopant atoms and / or molecular vibration. Under this assumption, the slope is not $k_B T$ any more, but corresponds to the width of

the broadening. However, in our case, the broadening would have to be extremely high to explain a slope of $15 \cdot k_B T$. The second publication on α -NPD p-doped by the metal-oxide Mo_3O_9 makes no assumptions on the reason for the disproportionate slope and the exact value is not stated [41]. From the published graph it can be estimated to be around four times $k_B T$ as well. More investigations into this topic are needed to clarify this effect.

Referring to the second observation, the saturation of the doping induced shift, it is at first surprising that it is not possible to move the HOMO any closer to the Fermi energy than $\phi_{min} = 0.35 \text{ eV}$. A guess would be that there is a critical density of dopant molecules up to which the effect of doping increases the amount of charge carriers and afterwards, no increase is possible any more. If this would be true, the same saturation should be seen in the doping dependent conductivity increase of a p-MeO-TPD layer.

To test this, conductivity measurements are performed over a range of doping ratios, spanning from a molar ratio of 0.18 to 0.73 (1.8 mol% to 42.3 mol%). The measurements are carried out on a glass substrate pre-structured with 90 nm thick ITO stripes at a distance of 1.6 mm. The current through a 20 nm thick layer of doped organic deposited between the stripes is recorded at a voltage of 10 V with a source measure unit (Keithley SMU236). The results of these measurements are shown in Fig. 5.5 and can be linearly fitted in the double logarithmic plot up to a molar ratio of 0.24 (19.4 mol%). Here, we again have a disproportionate dependence of the conductivity on the doping ratio with a slope of 1.85 instead of the expected slope of unity. This is however a common effect for doped organic semiconductors and was observed for other systems before (see Fig. 2.10 on page 30) and is discussed in Chapter 2.2.3.

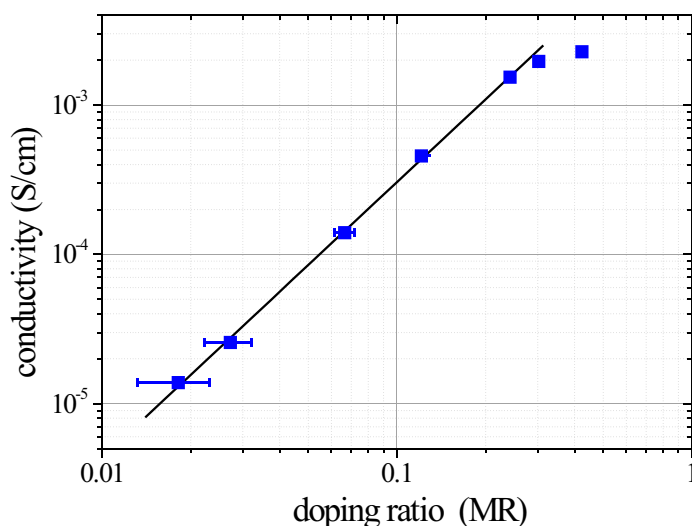


Figure 5.5: Measurement of the increase in conductivity through a layer of MeO-TPD upon increasing doping ratio with F4-TCNQ. The molar ratios range from 0.018 to 0.423.

There is no hint for a deviation from the linear behavior in the range of $\text{MR} = 0.07 - 0.1$ where the saturation is visible in UPS/XPS. However, at a molar ratio of 0.24

even the conductivity starts to saturate. This is not surprising, since here we have a mixed layer rather than a doped one and the disorder created by the F4-TCNQ molecules suppresses the carrier hopping rate and overcomes the advantage of the increased doping ratio [172].

As a saturation of the doping effect cannot be the reason for $\phi_{min} = 0.35$ eV, it is likely to be some kind of pinning effect at a state above the HOMO in the gap of the semiconductor. This could, for example, be a gap state created by the interaction between dopant and matrix molecules that pins the Fermi energy in the gap but is too faint in intensity to be seen by UPS. To exclude this effect, we compared the pinning position obtained with the F4-TCNQ molecule with three different dopants.

Comparison to Other Dopants and Matrix Materials

If a filled LUMO state of the dopant is the reason for the pinning at $\phi_{min} = 0.35$ eV, a change of dopant should result in a change of this value. The dopants C60F36 and the proprietary dopants NDP2 and NDP9, made available by Novald AG, are used in comparison. In all samples a rather high doping ratio is used to reach the range where pinning takes place. The doping concentrations are again checked by XPS and are measured to be MR = 0.128 (C60F36), MR = 0.189 (NDP2), and MR = 0.1 (NDP9). In Fig. 5.6a, the valence band regions of these highly doped MeO-TPD samples with the three dopants are compared to a measurement with F4-TCNQ doped at MR = 0.159. Even though the dopants differ in their EA and therefore their doping strength, they all show the same ϕ_{min} of (0.35 ± 0.02) eV. It is unlikely that the four dopants would all produce a pinning state at the same energetic distance from the HOMO, therefore ϕ_{min} must be a property of the matrix material MeO-TPD.

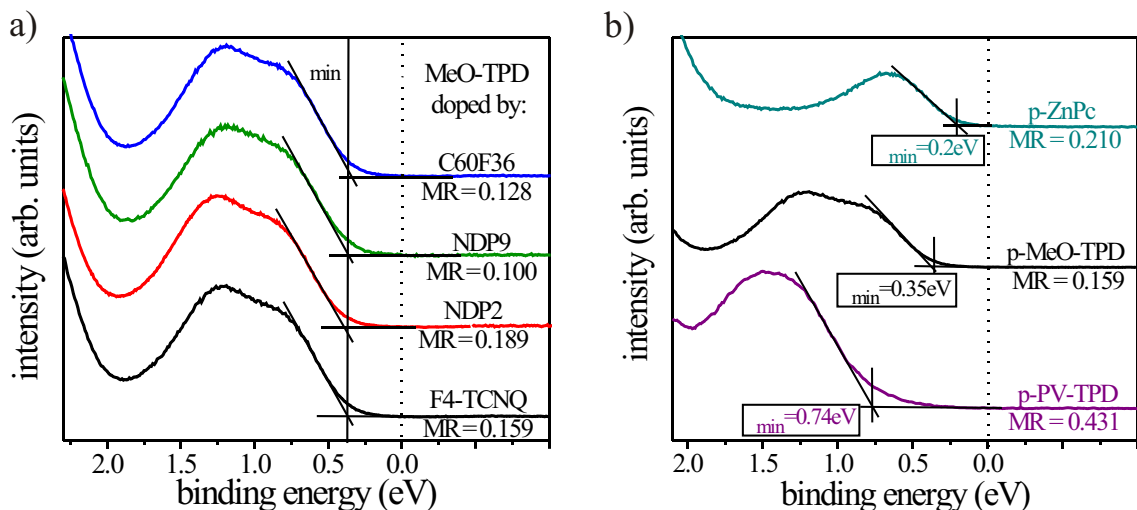


Figure 5.6: a) Valence band region of the UPS measurements of MeO-TPD highly doped by four different dopants that are indicated in the graph. b) Valence band region of the UPS measurements of three different matrix materials all highly doped by F4-TCNQ. In both graphs the solid vertical lines mark the commonly assumed HOMO cutoff position and the dotted lines show the Fermi level position.

To test this assumption, we change the matrix material. Here, it is important to find materials with a comparable ionization potential, so the doping process has the same efficiency. Otherwise a less favorable charge transfer can introduce additional effects. We choose as alternative materials ZnPc that has an IP = 5.1 eV and PV-TPD with IP = 5.2 eV.

Indeed, we observe large differences in ϕ_{min} by changing the matrix material as shown in Fig. 5.6b. With ZnPc doped by F4-TCNQ at a MR = 0.19, it is possible to move up to 0.2 eV towards the Fermi energy, while doped PV-TPD shows $\phi_{min} = 0.74$ eV even at extremely high doping concentrations up to MR = 0.43. Therefore, the reason for pinning has to originate from the matrix material itself. How this takes place is discussed in the next Paragraph.

Direct Observation of Tail States

This pinning of the Fermi energy in an organic layer a few 100 meV away from the HOMO has been observed before when undoped organic semiconductors are put in contact to substrates with a work function larger than the ionization energy of the semiconductor. This is explained either by a pinning on a polaron/bipolaron state or by a tailing of the HOMO into the gap (see Chapter 2.3.1). However, these tail states have only been postulated [41] and not directly been observed so far.

In general, the position of the HOMO indicated in the measurements shown so far has been extrapolated by the intersection between the leading edge of the HOMO peak and the background, the so called HOMO cutoff position. This is the conventional way this value is determined (a discussion on this method can be found e.g. in Ref. [31]). However, since the HOMO decays exponentially into the gap, the DOS reaches further than the such fitted value; this is especially obvious for the measurement of PV-TPD in Fig. 5.6b. By having a close look at the region beyond the HOMO, it should be possible to measure how far the DOS actually reaches into the gap.

This cannot be done in a straightforward manner with an UPS measurement taken with a He discharge lamp, as this is not a monochromatic light source and shows some further satellite lines in the region of the prominent excitation line at 21.22 eV. One has to carefully subtract the signal originating from these additional excitation lines from the 21.22 eV spectra as it is described in the Appendix. This is done for the curves in Fig. 5.7 which shows the same data as in Fig. 5.6b. After the pure spectra of the 21.22 eV excitation are obtained, one can see from the blown up curves on the right side of this Figure that the highly doped ZnPc, PV-TPD, and MeO-TPD all show a DOS that actually reaches up to the Fermi energy. Considering this, it is not surprising that the Fermi energy cannot be moved closer to the HOMO but is stopped by the increasing number of states. These tail states are not introduced by the doping, but are already present in the intrinsic layer; we do not observe any change in width or intensity of these states upon doping in contrast to what has been suggested in literature [172].

Therefore, the difference in pinning positions for the different materials is an indication on how far the DOS extends beyond the commonly assumed HOMO cutoff

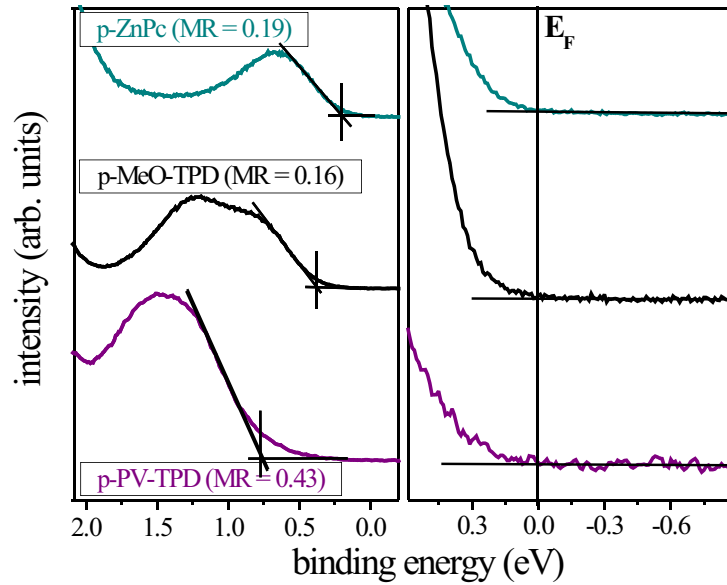


Figure 5.7: The left side shows once more the valence band region of the highly doped ZnPc, MeO-TPD and PV-TPD from Fig. 5.6b. The right side shows the same curves, but this time magnified around the region of the Fermi energy. It can be seen that the DOS extends up to the Fermi energy that is located at 0 eV.

position. This seems to depend strongly on the organic molecule. ZnPc that shows the smallest ϕ_{min} is known to form ordered polycrystalline layers while the other two materials have an amorphous layer structure. As the PV-TPD molecule has a more twisted structure compared to MeO-TPD, this could lead to a higher disorder in the layer. From such a higher disorder, a broader DOS can be expected due to local changes in the polarization screening (see Fig. 2.6 on page 22). Therefore, a higher disorder corresponds to a wider HOMO tail.

It is important to clarify whether these states participate in the transport in the organic material. This would mean that the IP of an organic semiconductor is commonly overestimated as lower lying states show occupation as well. From UPS it is not possible to estimate the amount of charge carriers in these tail states. However, the DOS at the pinning position has to be in the order of the amount of free charge carriers created by the doping to prevent the Fermi level from further moving into the band. There should then be enough carriers to promote the conduction as well. This can furthermore explain why doping works so well, even if the IP of the matrix slightly exceeds the EA of the dopant as it is the case for α -NPD (IP = 5.4 eV) doped by F4-TCNQ (EA = 5.24 eV) [8]. Here, the dopant can use these lower lying exponentially decaying states for the charge transfer.

Further support for the assumption that transport takes place in the tail states comes from Seebeck measurements. Pfeiffer et al. [71] measured a distance between transport level and Fermi energy in ZnPc doped by 8 mol% F4-TCNQ to be 50 meV. This is already much less than the 200 meV observed in Fig. 5.6b by UPS for a sample with considerably higher doping ratio.

5.4.2 Change in Depletion Layer Thickness

By probing the depletion layer thickness, we can gain information on the amount of free charge carriers and thus on the efficiency of the charge transfer from the dopant to the matrix. In a first experiment, thickness resolved measurements are done on a silver substrate with several doping ratios, similar to those shown in Fig. 5.2a. However, the interface to silver bears two major problems: i) the dipole created at the interface overlaps with the V_B of the built-in voltage and makes the determination of the value V_B difficult, and ii) the different sticking coefficient of F4-TCNQ in the MeO-TPD matrix and on the silver prevents a constant doping profile. This is especially pronounced for high doping concentrations. In Fig. 5.8, the black crosses show the measured molar ratio of a p-MeO-TPD layer with an intended MR=0.4 depending on the layer thickness on a silver substrate. As the F4-TCNQ sticks more efficiently to the silver, the doping ratio at the interface shows an increase by a factor of 8, suggesting that at least one monolayer of pure F4-TCNQ forms at the interface. Approximately 4 nm of p-MeO-TPD are needed until the doping ratio saturates at the intended value. The same problem shows more or less on any surface tested thereafter, namely PEDOT:PSS, gold, and ITO. Therefore, we have to decouple the doped layer from the substrate by 5 nm of intrinsic MeO-TPD before starting to evaporate the doped layer. To make sure that this layer really is intrinsic, it is evaporated in a separate chamber, as F4-TCNQ is known to be very volatile and contaminates materials in the chamber it is used in. With this structure, one can safely assume that the sticking coefficient is the same throughout the investigated interface which is shown in Fig. 5.8 (blue circles).

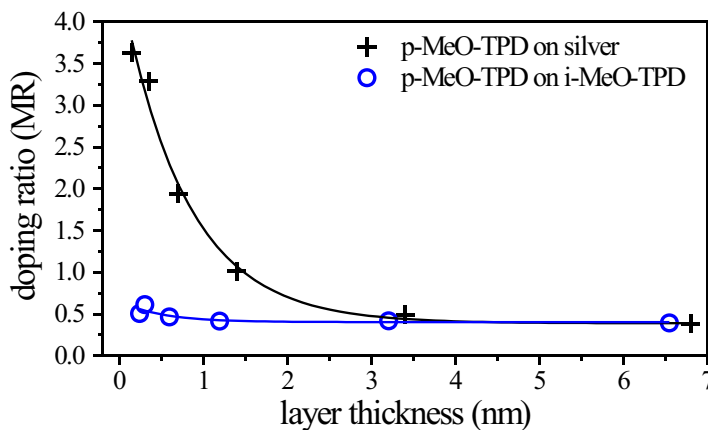


Figure 5.8: Profile of the doping concentration depending on the layer thickness in a sample where doped MeO-TPD is directly evaporated on a silver substrate (crosses) and when a buffer layer of 5 nm intrinsic MeO-TPD is first evaporated on the silver (circles). The intended molar ratio is 0.4 in both cases, however, in the case of the silver substrate a strong excess in doping concentration is found at the interface.

The valence band regions of the interface resolved UPS measurements are shown in Fig. 5.9a-d where four different doping ratios are compared with molar ratios of 0.032, 0.065, 0.205 and 0.37 (corresponding mol%: 3.1, 6.1, 17, and 27).

The bottom curves give the measurement of the underlying intrinsic MeO-TPD layer on a silver substrate. The value of ϕ of this layer decreases during the time span these measurements are taken (from 1.75 eV to 1.36 eV), indicating a contamination even of the intrinsic chamber with traces of F4-TCNQ. The amount of F4-TCNQ incorporation is however too low to be detectable by XPS. For the interpretation of the data, this is of minor importance as the resulting decrease of V_B simply results in a smaller depletion layer width w and the carrier concentration can nonetheless be calculated correctly.

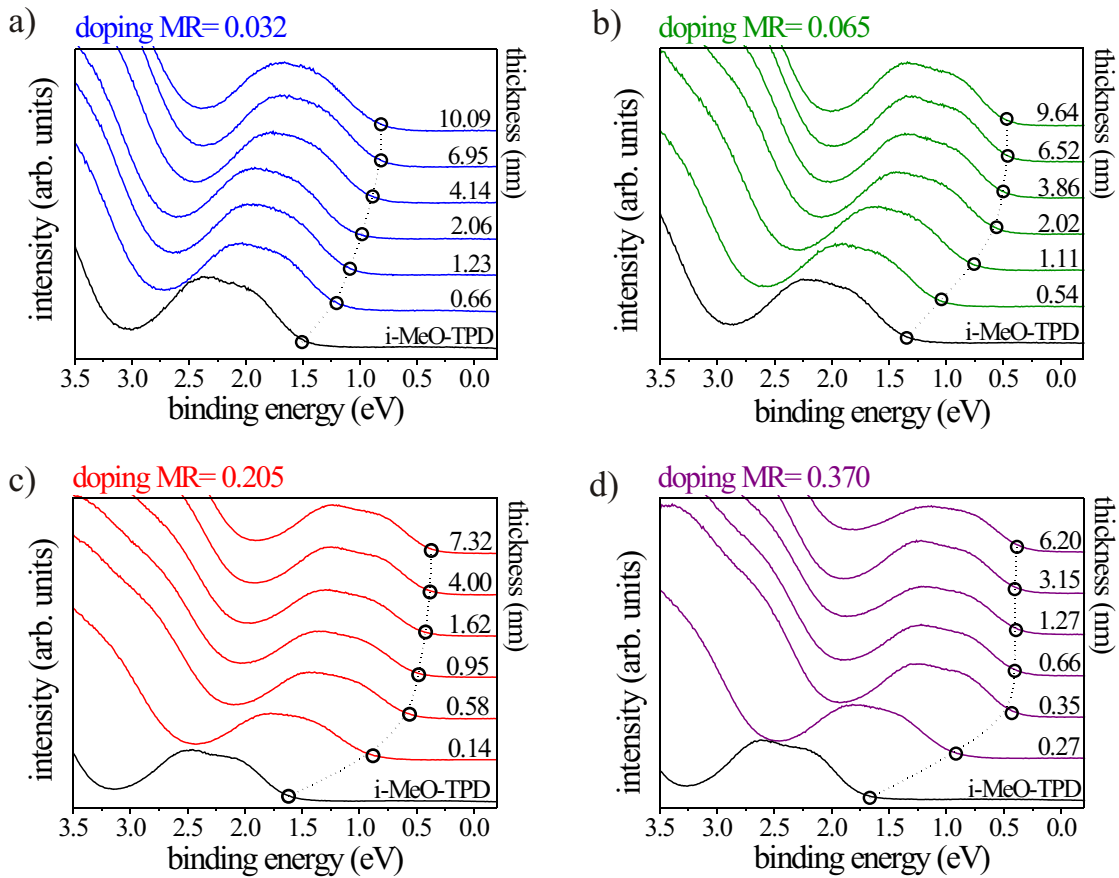


Figure 5.9: UPS measurements of the valence band regions for the investigation of the depletion layer width for different doping ratios. Shown are the valence band regions of interface resolved measurements for MeO-TPD doped with F4-TCNQ at molar ratios of 0.032 in a), 0.065 in b), 0.205 in c), and 0.37 in d) on top of a silver substrate pre-covered by 5 nm intrinsic MeO-TPD. The HOMO cutoff positions are marked by circles.

The true thickness of these layers is a crucial value for this experiment and cannot be simply taken as the sum of the MeO-TPD and F4-TCNQ layer thicknesses (intended to be 10 nm for all of the samples), as the size of the molecules is quite different and it is not clear how they arrange. Therefore, the thickness x is calculated by the attenuation of the Ag 3d substrate peaks, similar to the method described in

Ref. [173]. The layer thickness is given by

$$x = -\lambda \left(\ln \frac{I^{Ag}}{I_0^{Ag}} \right) \quad (5.1)$$

where λ depends on the density of the organic material as well as the kinetic energy of the electrons originating from the silver 3d states. For the fitting of the value of λ , the measurement with the lowest doping ratio is used where the amount of dopant is negligible to the layer thickness. It is, however, not possible to use the simple equation above to reproduce the layer thickness. This is not surprising as further effects, e.g. the morphology of the layer, play a role as well. An appropriate form to describe the thickness of the MeO-TPD layer is found to be

$$x = -2.44 \left(\ln \frac{I^{Ag}}{I_0^{Ag}} \right) + 0.16 \left(\ln \frac{I^{Ag}}{I_0^{Ag}} \right)^2. \quad (5.2)$$

This equation is then used to fit the data of the other three samples and the resulting thicknesses are given next to each measurement curve. Interestingly, the calculated layer thicknesses coincide quite well with the thickness of the pure MeO-TPD layer. For example, the intended 10 nm total layer thickness in measurement (d) was tried to be achieved by co-evaporation of 6.65 nm MeO-TPD and 3.35 nm F4-TCNQ. As the calculated total layer thickness is just 6.2 nm, the small F4-TCNQ molecules do not seem to contribute to the layer thickness at all.

The change of ϕ depending on the calculated layer thickness for the four samples is shown in Fig. 5.10a. As expected, the built-in voltage increases with doping while the depletion layer width w significantly decreases.

The curves in Fig. 5.10a are similar to those expected when evaporating a doped layer onto a metal substrate. However, the actual physics happening in the layer is different due to the underlying intrinsic organic layer. It is not the topmost doped layer where the bending takes place, but the energy levels of the intrinsic layer underneath get pulled upward when more of the doped layer is put on top. This is illustrated schematically in Fig. 5.11 where the alignment directly on a metal and with an intrinsic interlayer are compared.

For the estimation of the density of ionized dopants, the change of the potential depending on the distance x from the metal interface is calculated by using the measured values of the built-in potential V_B and width of the depletion layer w . We assume no doping in the $d = 5$ nm thick intrinsic layer and a constant doping concentration in the adjacent layer. For a rough estimate we analytically integrate the Poisson equation using Equation 2.42 under the condition of an abrupt end of the depletion region and zero field from there on. A more realistic approach can be achieved by a numerical drift-diffusion model calculating the charge carrier distribution under the given conditions self-consistently, which leads to a smooth transition of the depletion density and hence in a higher carrier concentration N_A^- . These calculations are done by Wolfgang Tress and the output of this model for the level alignment of the different doping ratios is shown in Fig. 5.10b. It can be seen that the voltage drop

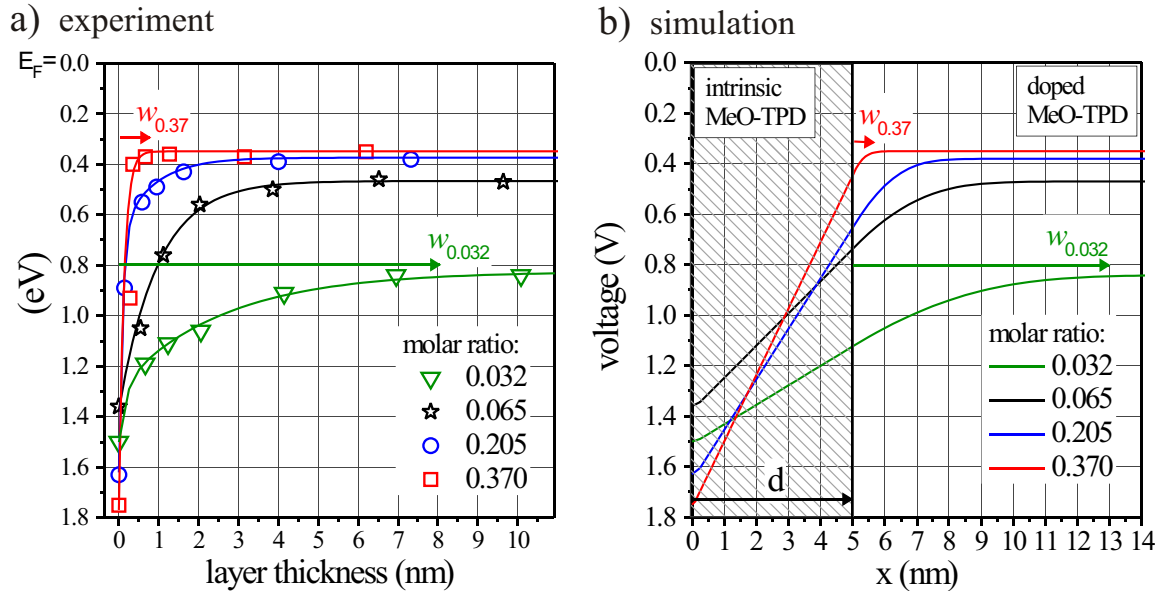


Figure 5.10: a) Measured change of the hole injection barrier as a function of layer thickness of p-MeO-TPD for different concentrations of F4-TCNQ which are indicated in the graph. As substrate silver is used with an interlayer of 5 nm intrinsic MeO-TPD. The line through the data points is a guide for the eye and the horizontal arrows show the width of the depletion layer w for the lowest and highest doping ratio. b) Simulation based level alignment of the measurements shown in (a) with the intrinsic MeO-TPD layer included. This shows that the voltage mainly drops across this i-MeO-TPD layer.

mainly takes place in the intrinsic layer that ends at $x = 5$ nm. For the low doping concentrations, there is level bending taking place in the doped layer as well, but for the high ratios this is rather negligible.

The values gained from the measurement that are used for the calculations mentioned above are listed in Table 5.1 together with the results for the amount of free charge carriers N_A^- given by the analytical Poisson integration and the numerical simulation. Both methods yield values of the charge carrier density within the same order of magnitude. Since many experimental errors enter into this calculation, like the resolution of the UPS measurements, the estimation of the depletion layer width, and errors in the actual layer thickness, these values should just give an idea of the order of magnitude and not be taken as exact values.

The fraction of ionized dopants is estimated by using the density of MeO-TPD of $\rho = 1.463 \text{ g/cm}^{-3}$ and therefore a molecular density of $1.45 \cdot 10^{21} \text{ cm}^{-3}$. The calculated values for the fully ionized dopants are surprisingly low and for most doping ratios in the range of 5%. This means that only a small fraction of dopants actually provide free charge carriers, even though in earlier experiments by infrared spectroscopy it was found that 73% undergo charge transfer with MeO-TPD [71]. The results suggest that most of the dopants undergo a strongly bound charge transfer to the MeO-TPD molecule. However, only in a few cases this charge transfer is complete, resulting in a free charge carrier. At the highest doping ratio, this fraction seems to be much higher,

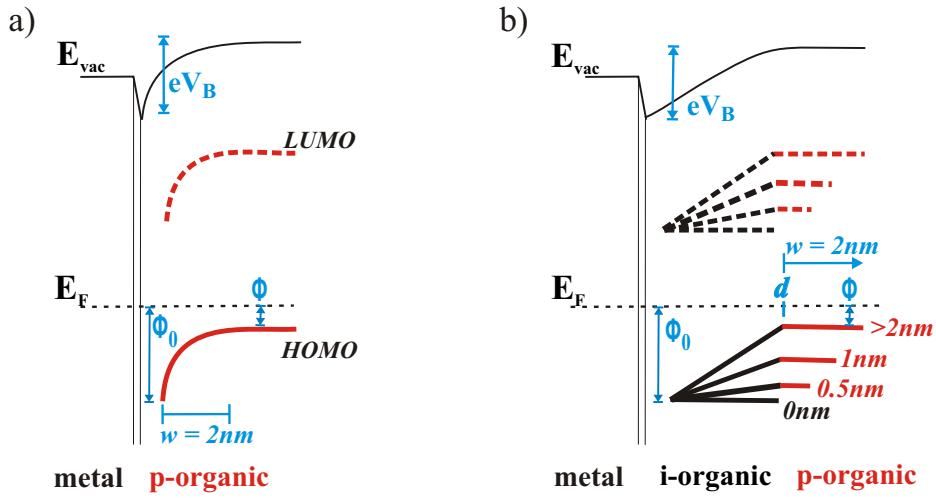


Figure 5.11: Schematic sketch to show the difference between the alignment of a) a highly doped layer (*p*-organic) directly on a metal compared to the case when b) an intrinsic organic (*i*-organic) interlayer is put in between. The different lines of HOMO and LUMO give the alignment for different thicknesses. The second case is the correct model for the calculation of the carrier concentration of the Ag/*i*MeO-TPD/*p*-MeO-TPD samples of Fig. 5.10.

doping (MR)	w (nm)	ϕ_0 (eV)	ϕ (eV)	eV_B (eV)	N_A^- (cm ⁻³) analyt. / num.	ionized dopants (%) analyt. / num.
0.032	8 ± 1	1.5	0.84	0.66	$1.5 \cdot 10^{18} / 2.0 \cdot 10^{18}$	4.3 / 3.3
0.065	5 ± 0.5	1.36	0.47	0.89	$4.0 \cdot 10^{18} / 6.0 \cdot 10^{18}$	6.4 / 4.2
0.205	2.8 ± 0.3	1.63	0.38	1.25	$1.2 \cdot 10^{19} / 1.5 \cdot 10^{19}$	5.0 / 3.9
0.370	0.6 ± 0.2	1.75	0.35	1.4	$7.3 \cdot 10^{19} / 1.0 \cdot 10^{20}$	18.6 / 13.6

Table 5.1: Experimental results from the measurement of the depletion layer thickness depending on the doping concentration and the resulting number of charge carriers as well as fraction of ionized dopants calculated by the analytical integration of the Poisson equation (analyt.) and the numerical simulation (num.) assuming $\epsilon = 3$.

around 20%. Probably, the very high concentration of dopants leads to additional effects during the interface formation as can be seen from the very thin depletion layer of 0.6 nm that is below one monolayer. We have to assume that the model is not applicable to this case.

Furthermore, we can try to calculate the position of the acceptor level E_A relative to the Fermi energy. For that we assume a thermal activation of the dopant states and a discrete trap level. With the equation

$$E_F - E_A = k_B T \ln \frac{N_A^-}{n_h} \quad (5.3)$$

we obtain an acceptor level depth of 70 and 80 meV for the two lower doping ratios, where the pinning of the HOMO does not take place, yet. However, it is doubtful that

this value has physical meaning as we already saw the theory of classical semiconductors fails in describing the slope of Fermi level position vs. doping concentration in Fig. 5.4.

5.5 Interface Doping vs. Bulk Doping

Finally, the concept of interface doping is investigated. Here, a (sub-) monolayer of a strong acceptor is evaporated onto a substrate to increase the work function. The following organic layer sees this higher work function and usually aligns differently compared to the pristine metal surface, resulting in a reduction of ϕ [174–176]. Alternatively, a donor can be used to decrease the electron injection barrier at the cathode. In such an arrangement an actual charge transfer due to doping happens at the interface only and the conductivity of the layer is not enhanced. However, the injection barrier is decreased, ideally allowing for an ohmic injection. Thus the device performance can be increased, for example by the insertion of F4-TCNQ [177], Ca [178], or LiF [179]. This method can be an adequate alternative to improve the device performance if doping by co-evaporation is not possible due to technical restraints.

It has even been suggested in literature that the concept of doping by co-evaporation is merely an effect of interface doping due to the diffusion of dopants through the matrix to the metal interface where it modifies the hole injection barrier and leads to an improvement of the injection behavior [116]. Of course, this can be easily disproved by testing the increase of conductivity in such a co-evaporated layer, that can only be due to the creation of free charge carriers and therefore is a true doping effect.

For the experiments comparing interface and bulk doping, varying layer thicknesses of F4-TCNQ on a silver substrate are prepared and afterwards covered by 10 nm MeO-TPD. The hole injection barriers, achieved with the different amounts of interface doping, are then compared to equal concentrations of bulk doping. We define an equal doping concentrations, such that the doped sample contains roughly as much F4-TCNQ molecules as the sub-monolayer interface doping evaporated on the silver. For example, in a 10 nm thick MeO-TPD:F4-TCNQ sample with a MR = 0.01, it can be estimated that the contribution of the F4-TCNQ molecules is 0.1 nm and can therefore be compared to a sample with an interface doping of 0.1 nm F4-TCNQ.

In Fig. 5.12, the UPS spectrum of an intrinsic MeO-TPD layer (top graph) is compared to three samples with interface doping (middle graph) that have F4-TCNQ layer thicknesses of 0.1 nm, 1 nm, and 2 nm. The bottom graph shows the corresponding samples having bulk doping with MR = 0.012, 0.095, and 0.205.

Comparing the measurements of the lowest interface and bulk doping values in Fig. 5.12, one sees that for the interface doping the hole injection barrier decreases from $\phi = 1.68$ eV to 1.1 eV, while for bulk doping a value of $\phi = 1.13$ eV is reached. Therefore, the same improvement is achieved for both samples. For the next combination of MR = 0.095 and a F4-TCNQ interface thickness of 1 nm, the results are already quite different. For the interface doping, the hole injection barrier is now $\phi = 0.93$ eV while for the bulk doping, we are already in the pinning regime with

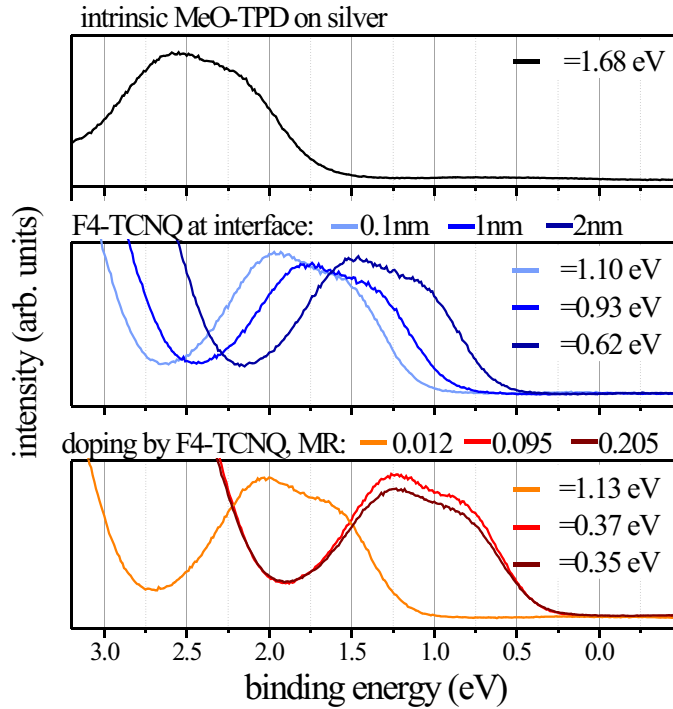


Figure 5.12: Comparison between interface doping and bulk doping. The top graph shows intrinsic MeO-TPD on silver. The middle graph shows three different thicknesses of interface doping by F4-TCNQ between silver and MeO-TPD while the bottom graph shows MeO-TPD that is co-evaporated with F4-TCNQ. The amount of dopant present in the layer is comparable for each of the three curves (e.g. 0.1 nm F4-TCNQ at the interface equals a MR = 0.01 in the bulk). The numbers given in the graphs give the corresponding hole injection barriers.

$\phi = 0.37$ eV. Clearly the bulk doping has a stronger effect on the alignment. Finally, the insertion of 2 nm of F4-TCNQ between silver and MeO-TPD leads to a further decrease to $\phi = 0.62$ eV. However, this is still considerably larger than the value for the sample with MR = 0.205 that shows $\phi = 0.35$ eV.

5.6 Conclusion

Doping by co-sublimation can be used to control the conductivity and the Fermi level position in a qualitatively similar way to standard inorganic semiconductors. However, there are significant quantitative differences in the effects of doping, especially in the amount of doping induced Fermi level shift that exceeds $k_B T$ by a factor of 15 in the MeO-TPD:F4-TCNQ system investigated here. A moderate doping ratio of 0.04 already yields a carrier concentration large enough to result in a final energetic alignment independent of the substrate. This means that Fermi level alignment between substrate and organic semiconductor is achieved and interface effects as well as the substrate Wf only play a minor role for the energy alignment. The Fermi energy position within the gap can be controlled over 1.33 eV by the doping ratio and the conductivity of the sample can be tuned over several orders of magnitude. For

doping ratios larger than $MR = 0.1$, the Fermi level is pinned 350 meV beyond the conventionally assumed HOMO onset at the exponentially decaying tail of the DOS. Consequently, we observe a DOS that reaches up to the Fermi energy upon strong doping. Thereby, the width of this HOMO tail depends on the disorder in the organic layer. By determining the depletion layer thicknesses at various doping concentrations, typical charge carrier concentrations in doped organic semiconductors ranging from $2 \cdot 10^{18}$ to $2 \cdot 10^{20} \text{ cm}^{-3}$ for weakly and strongly doped samples are deduced. By comparing this value with the amount of dopants present in the layer, it was found that only about 5% of the dopants are fully ionized. Finally, it was shown that the application of interface doping does not yield the same effect of Fermi level change as the doping by co-sublimation.

6 Investigation of pn Junctions and Related Devices

Despite the successful commercial application of devices like OLEDs or organic solar cells, the general field of organic semiconductors is still rather immature. Many basic devices known from inorganic semiconductors have only recently been shown to work for organic devices or have not been realized so far. In this Chapter, we will investigate devices employing either pn junctions or pin junctions. We start with measurements on a basic organic pn junction. Such an interface can be used to realize recombination contacts in tandem solar cells. This is possible as these pn junctions have no blocking behavior in backward direction due to an efficient tunneling process through narrow depletion regions. If a blocking behavior is wanted, pin junctions have to be employed, where an intrinsic interlayer prevents this tunneling process. Such a homojunction device is investigated in the second part of this Chapter. Finally, the concept and alignment of a Zener diode is introduced. Here, the intrinsic interlayer in a pin junction is tuned in such a way that the breakdown voltage in backward direction can be controlled.

6.1 Recombination Contacts in a MeO-TPD/C60 Tandem Solar Cell

Organic solar cells were introduced in Chapter 2.4.2, together with the concept of tandem solar cells that help to overcome the problem of the narrow absorption bandwidths of the organic active layers. Here, two solar cells are built on top of each other and are connected by a recombination layer that converts the electron current from the first solar cell into a hole current for the second solar cell (see Fig. 6.2a). Theoretical calculations of the efficiencies of such tandem solar cells result in values of 16% to 23%, in contrast to 10% to 15% for organic single solar cells [180–182]. In order for the two solar cells to work together optimally, such a contact needs to meet two requirements: i) the splitting of the quasi Fermi level at the junction has to be avoided so no reverse voltage is produced and ii) an efficient tunneling between electron and hole states at the interface has to be provided.

Commonly, such a recombination contact is achieved by insertion of metal clusters [183, 184] or thin metal layers [185, 186] at the connecting interface. In this case,

the metal islands quench the excitons and thus remove the Fermi level splitting. However, the metal layers introduce absorbance and reflectance that lead to losses and an unbalanced absorption in the subcells, reducing the power conversion efficiency. Furthermore, the performance of such contacts was found to very sensitively depend on the material combination which makes it challenging to find properly working systems [187]. Only three optimally working combinations have been found that actually double the open circuit voltage [183, 188, 189].

It was shown by Harada et al. [190] that organic *pn* junctions show no blocking behavior in backward direction and therefore typically have symmetric IV-characteristics in forward and backward direction. The reason is the very narrow depletion layer of just a few nm thickness that can easily be tunneled through. Such an interface could therefore be a suitable recombination contact for tandem solar cells. A current density-voltage curve of such a *pn* junction in comparison to an intrinsic junction is shown in Fig. 6.1. Both samples have the same injection layers consisting of an ITO anode and MeO-TPD doped by NDP2 for the hole injection and C60:NDN1 with an Al cathode for the electron injection. The filled black squares show the measurement of a sample where a *pn* junction consisting of MeO-TPD doped by F4-TCNQ (35 wt%) and C60 doped by AOB (13 wt%) is inserted. The current in backward direction is only rectified by a factor of 3 at ± 1.5 V. In contrast, the sample containing an intrinsic junction of MeO-TPD and C60 (empty circles) shows a rectification of 120, as the tunneling in backward direction is strongly suppressed. The whole curve is shifted by 0.53 eV because the measurement is done under illumination and the intrinsic interface produces an open circuit voltage.

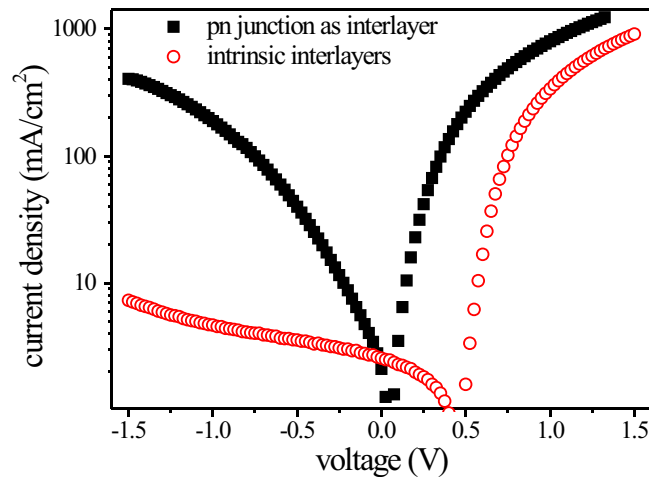


Figure 6.1: Black squares: IV characteristic of a sample containing a *pn* junction: ITO / MeO-TPD:NDP2 (5 wt%) / MeO-TPD:F4-TCNQ (35 wt%) - C60:AOB (8 wt%) / C60:NDN1 (13 wt%) / Al. Red circles: measurement of the same stack with intrinsic layers instead of the *pn*-junction: ITO / MeO-TPD:NDP2 (5 wt%) / MeO-TPD / C60 - C60:NDN1 (13 wt%) / Al. Measurement shown by courtesy of Ronny Timmreck.

Recently, this concept of highly doped layers that form a *pn* recombination contact between the two sub-cells has been shown to work for tandem solar cells [191]. By

comparing this stack to those without interface modification and with insertion of metal clusters, it was shown that the method employing pn junctions works very efficiently, compared to the metal clusters, and that such a recombination contact is independent of the materials used, as long as the doping process is efficient. The stack with the organic materials used for this investigation is shown in Fig. 6.2a, the active materials are MeO-TPD and C60. The measured current-voltage characteristics of the solar cells under illumination are shown in Fig. 6.2b (from Ref. [191]). A single solar cell of this type produces an open circuit voltage of $V_{oc} = 0.53$ eV and is plotted as curve SC with blue open squares.

In this Section, we present UPS measurements on equivalent pn tandem cell structures as published in [191]. In accordance to this paper, the results are furthermore compared to recombination contacts without any modification and to structures with metal clusters. At each of these interfaces, thickness resolved UPS measurements are performed that follow the level bending effects and investigate the built-in voltages between the layers.

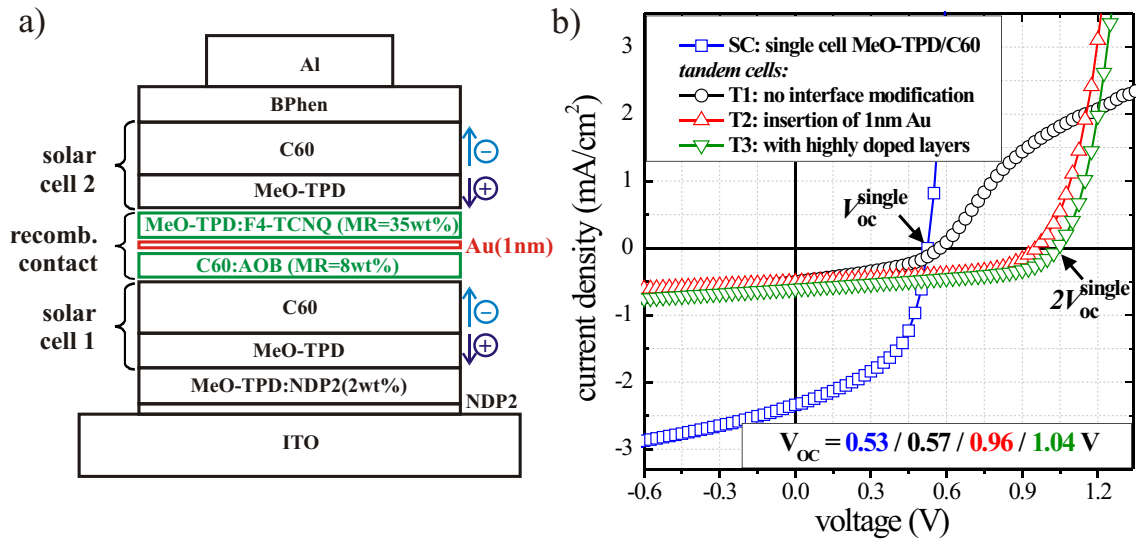


Figure 6.2: a) Structure of the different tandem solar cells containing MeO-TPD/C60. SC: single solar cell with a MeO-TPD/C60 interface (e.g. solar cell 1), T1: tandem cell stacked without interface modification (no metal or doped layers), T2: tandem cell with 1 nm Au but no doped layers, and T3: tandem cell connected by doped layers with molar ratios of 8 wt% for n -doping and 35 wt% for p -doping. b) Current density-voltage characteristics of the structures SC, T1, T2 and T3. In the lower part of the graph the corresponding open circuit voltages are indicated; taken from [191].

Intrinsic Contact Between MeO-TPD and C60

We start by studying the interface without any modification of the recombination contact. As can be seen from the stack in Fig. 6.2a, this means that the C60 layer from solar cell 1 is in direct contact with the MeO-TPD from solar cell 2. This contact between the two sub-cells works as an additional solar cell connected in backward

direction and cancels the performance of one of the other solar cells. Therefore, the open circuit voltage of this device T1 is not increased, but resembles that of the single cell SC in the measurement of Fig. 6.2b.

For the UPS measurement of this interface, a sub-structure similar to the stack for the IV-measurement is used to ensure the same energetic position relative to the Fermi energy. It consists of sputter cleaned silver foil with 30 nm gold and 10 nm MeO-TPD doped by NDP2 at a concentration of 2 wt%. On top of this, 8 nm C60 are deposited and measured by UPS, shown as the bottom curve in Fig. 6.3a. The MeO-TPD interface is built onto this layer with the thicknesses of 0.2 nm, 0.5 nm, and 1 nm. For every layer, an UPS spectrum is recorded as shown in Fig. 6.3a. For layer thicknesses greater than 1 nm the sample shows charging. This is expected, as the deeper lying HOMO of C60 forms a barrier for the holes generated by the removal of the photoelectrons during the measurement. The fact that this happens very fast gives first insight on the blocking behavior of this contact and that it does not work as a recombination contact.

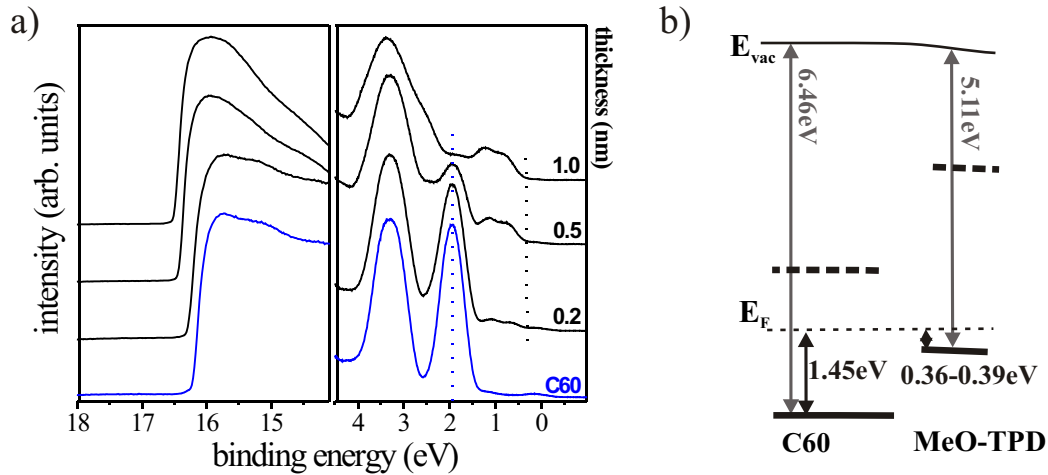


Figure 6.3: UPS measurements of the interface between C60 and MeO-TPD. The position of the C60 HOMO peak and MeO-TPD HOMO cutoff position are indicated by the dotted lines. For layers thicker than 1 nm, the sample shows charging during the UPS measurement, so the investigation can not be carried on. The right side shows the schematic energy level alignment between the two organic layers.

Figure 6.3b shows the schematic energy alignment. Due to the vacuum level alignment at the interface between the two intrinsic layers, the MeO-TPD HOMO is positioned very close to the Fermi energy with $\phi = 0.36$ eV. The position of the C60 HOMO shows no change upon MeO-TPD coverage, so no charge transfer is taking place. The HOMO of MeO-TPD shows a small downward bending. However, this is rather due to the formation of the first monolayer and not a real level bending. Assuming an EA of C60 of 4 eV [150], the offset between the LUMO of C60 and the HOMO of MeO-TPD is 1.37 eV. The reasons why the open circuit voltage $V_{oc} = 0.53$ eV measured for such an single cell is smaller are (i) the tail states that result in a density of states reaching further into the gap than the HOMO cutoff position (≈ 0.5 eV) and

(ii) the exciton binding energy that further reduces the offset between the HOMO and LUMO (≈ 0.3 - 0.5 eV).

Insertion of an Au Conversion Layer Between C60 and MeO-TPD

By repeating the measurement with the same stack and inserting a thin metal layer at the interface between C60 and MeO-TPD, the alignment is significantly modified. In Ref. [191], 1 nm of Au was used. However, this is not reasonable here, as 1 nm fully covers the C60 layer and the valence band features of C60 are not visible any more. Therefore, 0.5 nm Au are used that are known to produce a working recombination contact as well.

The UPS measurement of the C60 layer in Fig. 6.4 shows within the experimental error the same alignment as in Fig. 6.3. When 0.5 nm gold are evaporated on top, the HOMO of C60 exhibits a significant shift away from the Fermi energy by 230 meV and therefore a n-type doping is introduced by the gold atoms, leading to an accumulation of electrons at the interface. This is accompanied by a sudden downward shift of the vacuum level of 310 meV. The Fermi edge of the gold layer is visible in the UPS spectrum; therefore, we have a DOS at the interface reaching up to the Fermi energy. As before, MeO-TPD is incrementally built on top. This layer is affected by the gold interlayer as well and shows a ϕ_0 smaller by 320 meV at the interface compared to the bulk value. This indicates an accumulation of holes at the interface. During the interface formation, the C60 shows no further change in HOMO position, so the charge transfer is solely between the MeO-TPD and Au. The measurement can only be continued until 5 nm coverage, thereafter, again a charging of the sample is observed. We can conclude that the conversion at the interface is much better than in case of the intrinsic interface, but still the process is not perfect, leading to an accumulation of photogenerated holes.

The resulting energetic alignment is shown in Fig. 6.4b. The total built-in potential of this interface, taken from the change in vacuum level position, is $V_B^{metal} = 0.75$ eV. This is most likely not achieved by a level bending, as the layers are intrinsic and do not have sufficient charge carriers. Therefore, the changes in HOMO and vacuum level position are shown as a constant drop in voltage across the whole layer. It is obvious that due to the gold DOS reaching up to the Fermi energy, no Fermi level splitting can occur. Furthermore, the gold atoms lead to an advantageous doping effect on both layers that promote electron-hole conversion due to an accumulation at the interface.

The IV measurement of a solar cell device containing 1 nm of gold is shown in Fig. 6.2 as red triangles. A value of $V_{oc} = 0.96$ V is achieved which is a 9% loss compared to twice the voltage of the single cell.

Recombination Contacts by Highly Doped MeO-TPD and C60 Layers

For the very efficient recombination contact employing a *pn* junction, we use F4-TCNQ as the p-dopant for the MeO-TPD layer at a doping concentration of 35 wt% and AOB

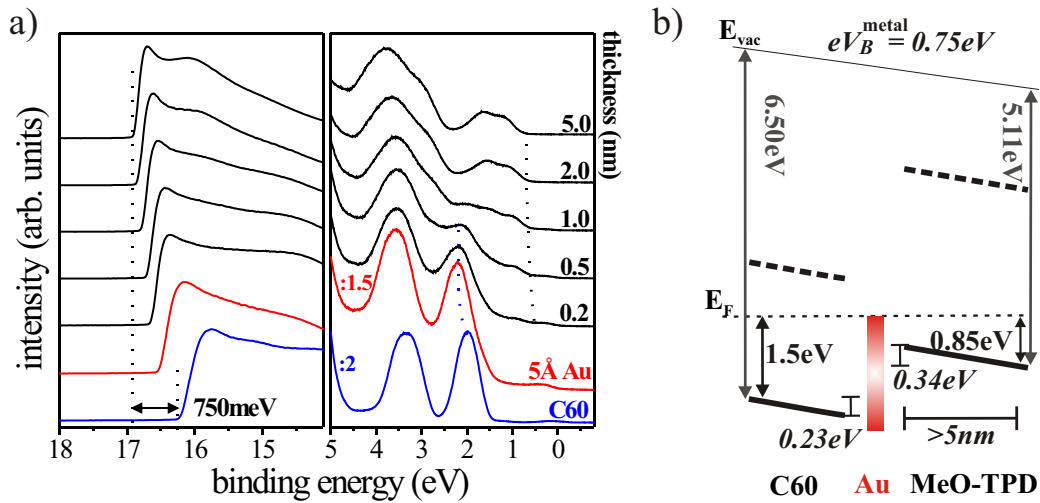


Figure 6.4: UPS measurements of the interface between C60 and MeO-TPD when 0.5 nm of gold are deposited in between. The position of the C60 HOMO peak and MeO-TPD HOMO cutoff position are indicated by the dotted lines. For layers thicker than 5 nm the sample showed charging during the UPS measurement and the data therefore can not be shown. The right side shows the schematic energy level alignment between the two organic layers.

as the n-dopant in C60 at 8 wt%.

For this sample, the n-doped C60 layer is directly put on a gold covered silver foil, in contrast to the solar cell stack used for the IV measurement. The p-doped MeO-TPD can be omitted as the high doping concentration in C60 leads to Fermi level alignment of the layer, independent of the adjacent layers (see Chapter 5.3). The UPS measurements are shown in Fig. 6.5. As expected, the energetic position of C60 differs from the ones in Fig. 6.3 and Fig. 6.4 as this time the n-doping leads to an alignment where the Fermi energy is close to the LUMO of C60. Upon the deposition of doped MeO-TPD, the C60 level shows a strong upward bending, typical for the formation of a depletion region due to charge transfer across the *pn*-junction. The HOMO of C60 can only be observed up to 0.5 nm MeO-TPD deposition. By then it shows a level shifting of 920 meV. The HOMO of MeO-TPD shows no shift at all, and is located at $\phi = 0.35$ eV. It was found in Chapter 5.4.1 that this is the pinning position for the HOMO at the tail states. Clearly, the 35 wt% doping by F4-TCNQ in MeO-TPD produces considerably more free charge carriers than the 8 wt% doping of C60 by AOB; therefore, the entire voltage drop takes place in n-C60. The change in vacuum level position is $V_B^{pn} = 0.91$ eV. The spectra do not show charging during the measurement done up to 10 nm thickness.

From these measurements we only know the amount of shifting and not the width of the depletion region in n-C60; therefore we repeat the measurement and change the deposition sequence. This time p-MeO-TPD is deposited on a gold layer, followed by the stepwise deposition of n-C60 using the same doping concentrations as before.

The p-MeO-TPD layer shows the same alignment as in the last measurement. Just as before, the deposition of n-C60 does not lead to a change in the MeO-TPD

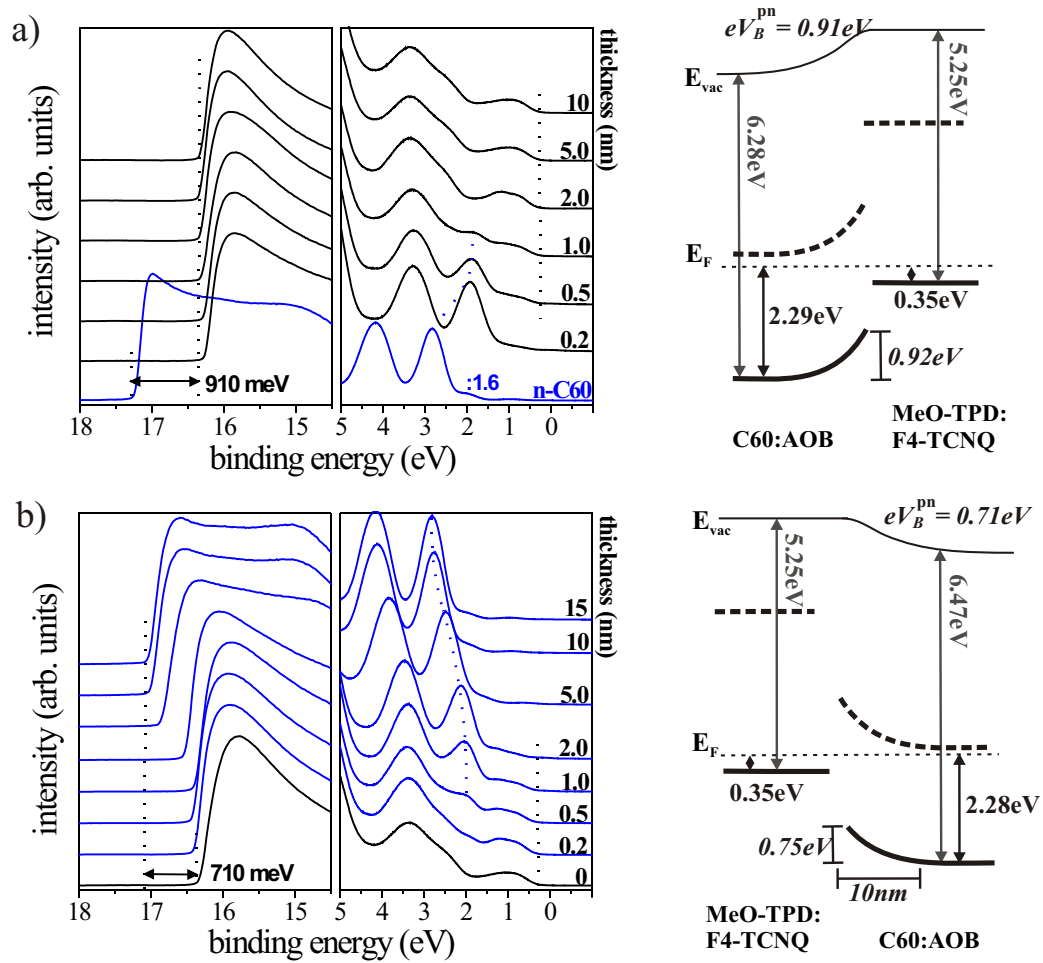


Figure 6.5: a) UPS measurements of the interface of C60 doped by AOB (8wt%) and MeO-TPD doped by F4-TCNQ (35wt%), the dotted lines mark the change in HBEC, C60 peak position and MeO-TPD HOMO cutoff. The right side shows the schematic energy level alignment between the two doped organic layers. b) Measurement of the same stack with an inverted deposition sequence, again the right side shows the schematic energy alignment.

HOMO position. All the level bending takes place in the C60 which is found to be 10 nm wide during which the HOMO shifts by 750 meV. The built-in voltage is in this case $V_B^{pn} = 0.71$ eV. This is less than in the forward measurement. The reason is the difference in ionization potential of C60 in the two measurements. Why the IP of the first measurement is lower is not clear; it could be the result of a different growth mode on gold compared to MeO-TPD or it could be due to a higher doping concentration that can lead to changes in IP as will be shown in Chapter 6.2.

The IV measurement of a solar cell device containing such a highly doped *pn* junction as recombination contact is shown in Fig 6.2 as green downward pointing triangles. A value of $V_{oc} = 1.04$ V is achieved which is merely a 1.9% loss compared to twice the value of the single cell.

Conclusion

Concluding, it can be said that *pn*-junctions are a suitable way to realize recombination contacts. The IV characteristics show a nearly symmetric behavior in forward and backward direction. The reason for this is obvious from the energetic alignment gained by the UPS measurements in Fig. 6.5. There is only small HOMO - LUMO offset, separated by the narrow depletion region with a high built-in voltage of ≈ 800 meV. A comparable contact realized by the insertion of metal clusters shows a built-in voltage of 750 meV. However the voltage drop shows the opposite sign. This means that there is an accumulation of holes and electrons at the interface that favors the recombination even though the offset between HOMO and LUMO is larger in comparison. In both cases, a splitting of the Fermi energy is prevented by a DOS that reaches up to the Fermi energy. In the case of the metal clusters, this is the DOS of the gold and for the doped layer the tail states of the LUMO and HOMO that pin at the Fermi energy.

6.2 PES Investigation of a Pentacene *pin* Homojunction

Recently, Harada et al. [17] reported the first stable and reproducible organic homojunction based on p- and n-doped layers of the organic semiconductor ZnPc. The challenge in realizing stable molecularly doped layers for a homojunction lies in the selection of a matrix material that is p- as well as n-dopable. As mentioned in the last Section, it was found that these devices have to be realized in the form of *pin*-junctions, where the intrinsic interlayer is needed to avoid tunneling due to the rather narrow depletion layers in doped organic semiconductors [17]. More recently, a *pin*-homojunction could also be realized in Pentacene [190], showing an exceptionally large built-in potential. In this device the p-dopant F4-TCNQ and the n-dopant Ru(t-but-terpy)₂¹ were employed.

In this Section, we investigate a similar Pentacene (PEN) *pin* homojunction by UPS to obtain information on the basic alignment within the device, including interface dipoles, band bending effects, and the built-in potential. The whole stack is built incrementally and each interface is investigated by thickness resolved measurements. Finally, these results are compared to current-voltage measurements and impedance spectroscopy. The dopants used for this investigation are NDN1 and NDP2. We chose different ones than used in the publication by Harada since these Novaled dopants are easier to handle and provide a more stable performance.

The samples are prepared on a sputter cleaned silver foil and the investigated thicknesses of the different layers range from 2 Å up to 30 nm. For the doped layers a doping ratio of MR = 0.02 is used. In order to avoid cross contamination, the intrinsic and doped layers are evaporated in three different chambers.

¹Bis(4,4',4''-tri-tert-butyl-2,2':6',2''-terpyridine)ruthenium

For obtaining the true energetic alignment in the actual device, it is not sufficient to prepare the device in only one deposition direction, as it is unknown how the underlying layers react upon deposition of the top layers. Therefore, two samples are investigated. On one sample (sample A) the interfaces silver to p-Pentacene, p-Pentacene to i-Pentacene, and finally i-Pentacene to n-Pentacene are measured interface resolved. The same device is then built once more in reversed order (sample B) to gain the full information on the alignment.

Measuring the pin Stack of Sample A

Sample A starts with the measurement between silver and Pentacene doped by NDP2 at MR = 0.02 up to a layer thickness of 30 nm. This is followed by a stepwise deposition of further 30 nm of intrinsic Pentacene and finally 20 nm of Pentacene n-doped by NDN1 at MR = 0.02. The resulting UPS spectra are shown in Fig. 6.6. The left side of the image shows the normalized HBECs and the right side the valence band region with the HOMO cutoffs marked by circles. The respective layer thicknesses are denoted next to it. Furthermore the XPS spectra originating from the carbon 1s peak are shown. The changes in work function (circles), C 1s position (triangles), and HOMO cutoff positions (squares) are shown in Fig. 6.7.

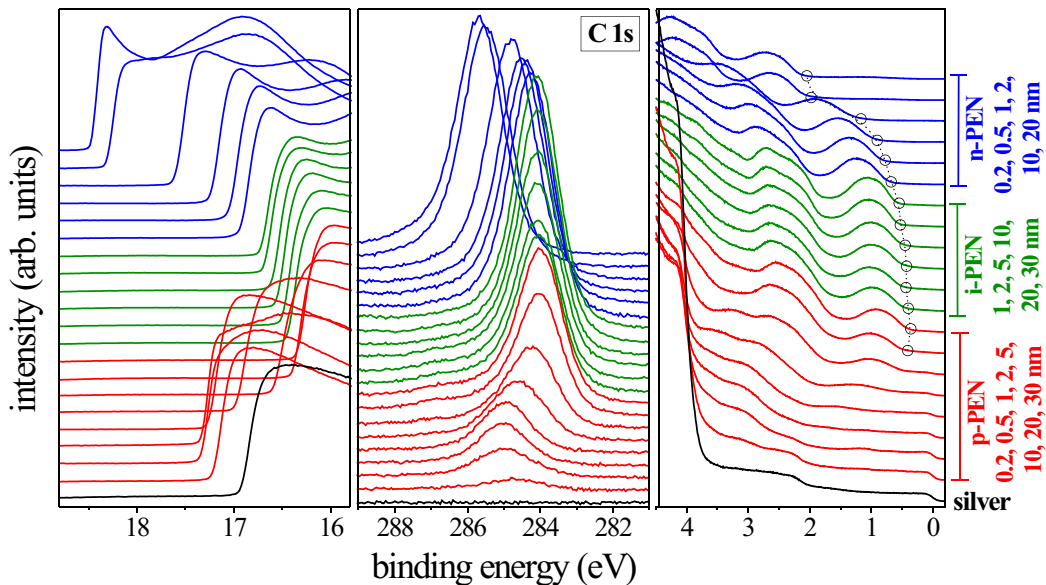


Figure 6.6: UPS and XPS measurements of sample A. On top of a silver sample (black curve) p-doped Pentacene is evaporated (red curves) followed by intrinsic Pentacene (green curves) and n-doped Pentacene (blue curves). The corresponding layer thicknesses are denoted next to the graph; the left side shows the HBEC, the middle graph the carbon 1s peak and the right side the valence band region with the HOMO cutoff marked by open circles.

The freshly sputtered silver foil (lowest curve in Fig. 6.6) shows a Wf of 4.3 eV. Upon the deposition of the first monolayer of p-Pentacene (~ 1 nm), an abrupt shift to higher binding energy by 0.4 eV is observed in the HBEC as an interface dipole

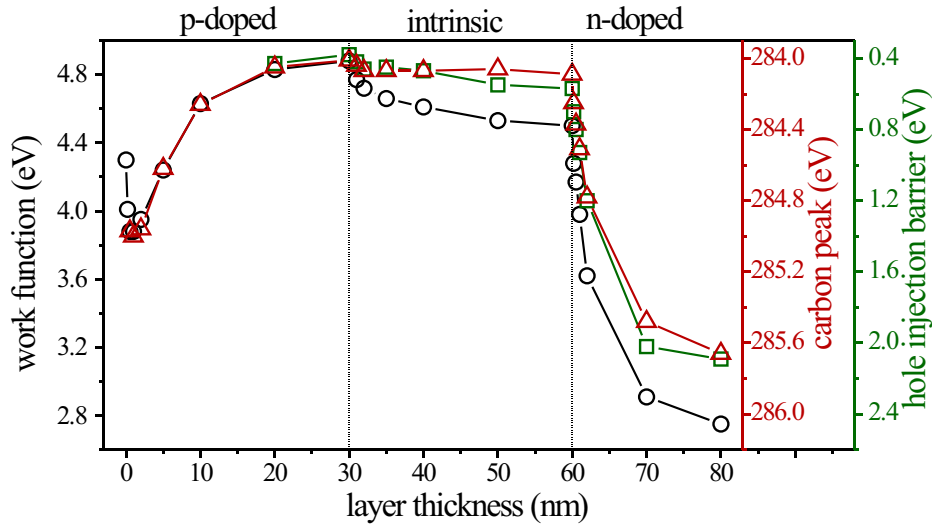


Figure 6.7: Shift of the work function (circles, left x-axis), carbon 1s position (triangles, first x-axis on the right) and HOMO cutoff position (squares, second x-axis to the right) of sample A; the values are taken from Fig. 6.6. Vertical lines mark the interfaces between the doped and intrinsic layers.

is created. This shift is reversed for increasing thickness by a gradual level bending, clearly indicating a depletion region due to the p-doping. The overall shift in vacuum level is 1 eV and takes about 20 nm. The carbon peak shows the same shift of 0.99 eV. The depletion layer width is surprisingly large compared to earlier results, e.g. MeO-TPD doped by F4-TCNQ, where typical values are well below 10 nm. The HOMO position of Pentacene can only be distinguished after 10 nm of coverage and the Fermi edge of the underlying silver can be seen up to this point. This suggests a rough, island-like growth of Pentacene on silver, which has been reported before [192, 193]. The ionization potential of the 30 nm thick p-doped Pentacene is found to be 5.26 eV and the hole injection barrier is $\phi = 0.38$ eV.

Upon deposition of the intrinsic Pentacene (green curves in Fig. 6.6), no interface dipole is observed. However, there is a gradual downward shift of the vacuum level across the 30 nm thick layer by 400 meV, accompanied by a somewhat smaller shift in the HOMO cutoff position of 200 meV and an even smaller shift by only 80 meV of the carbon peak as can be seen in Fig. 6.7. The dissimilar shift of these values is due to a change in the ionization potential, as the intrinsic layer shows a lower value of IP = 5.07 eV, which will be discussed later in this Chapter. After 30 nm of intrinsic Pentacene, a value of $\phi = 0.57$ eV is reached, but no saturation of the shift is yet achieved. The measurement is not carried on, as this is a typical thickness of the intrinsic layer used in a Pentacene homojunction device.

On top of this intrinsic layer, n-doped Pentacene is evaporated (blue curves in Fig. 6.6). Immediately after the first 0.2 nm coverage, a strong downward shift is observable in the vacuum level as well as in the HOMO position. Since the HOMO signal at that point still originates from the underlying intrinsic Pentacene, it is obvious that not only the n-Pentacene is shifting, but rather the intrinsic layer is

pulled downward at the interface to the doped layer. The shift saturates after about 10 nm coverage with a total change in vacuum level energy of 1.7 eV, in HOMO position of 1.52 eV, and a C 1s shift of 1.57 eV. At 20 nm thickness, the n-doped layer reaches $IP = 4.84$ eV and $\phi = 2.09$ eV.

The deposition of the n-doped layer does not only have an influence on the alignment of the intrinsic layer, but on the p-doped layer as well. This can be observed by a change in position of a characteristic core level peak of the p-dopant by XPS that is still visible during the deposition of the n-Pentacene. The p-layer layer is pulled downward at the interface to the intrinsic layer and a depletion layer forms. As NDP2 is a proprietary material, this data can not be shown. This change in position accounts for 780 meV.

Measuring the nip Stack of Sample B

For sample B, the deposition sequence is reversed, starting with the n-doped Pentacene layer on silver, followed by the intrinsic and p-doped layers. The resulting spectra are plotted in Fig. 6.8 and the changes in work function (circles), carbon 1s position (triangles), and HOMO cutoff position (squares) are shown in Fig. 6.9.

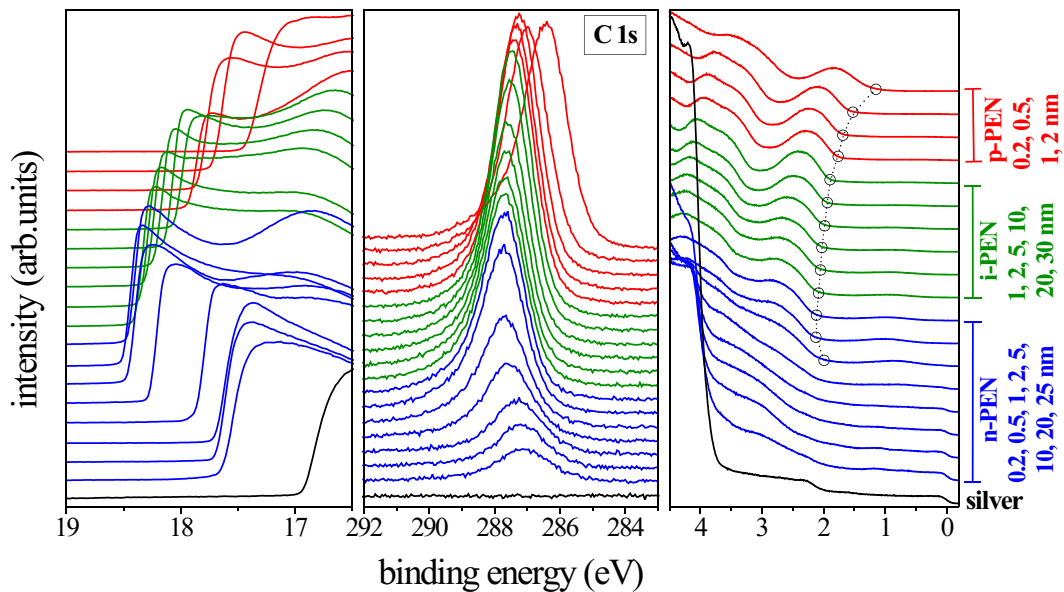


Figure 6.8: UPS and XPS measurements of sample B. On top of a silver sample (black curve) n-doped Pentacene is evaporated (blue curves) followed by intrinsic Pentacene (green curves) and p-doped Pentacene (green curves). The corresponding layer thicknesses are denoted next to the graph; the left side shows the HBE, the middle graph the carbon 1s peak and the right side the valence band region with the HOMO cutoffs marked by open circles.

The freshly sputtered silver foil shows again a Wf of 4.29 eV. With the deposition of the first sub-monolayer of n-Pentacene on Ag, a strong downward shift of the vacuum level is observed as again an interface dipole is created. This shift is now followed by a downward level bending, therefore this time both shifts go in the same direction

and are not distinguishable. Only the total change can be stated to be 1.53 eV. After about 10 nm, the level bending saturates which is faster than for the p-side layer, indicating a more efficient doping by NDN1. The HOMO cutoff can be seen after 10 nm coverage and again the Fermi edge is visible until then, as was the case for the p-doped layer. In general the growth modes of p- and n-doped layers seem to be the same. The ionization potential of the 25 nm thick n-Pentacene layer is 4.86 eV and $\phi = 2.1$ eV as it was found for the topmost layer of sample A. This reproducibility proves that in sample A, the equilibrium alignment has indeed been reached for the n-doped layer. When the intrinsic layer is evaporated on top, the vacuum level aligns with the n-doped layer and therefore starts at a different energetic position compared to sample A. Throughout the intrinsic layer, a gradual upward shift of the vacuum level by 410 meV is observed, accompanied by a smaller 200 meV shift in the HOMO as again the ionization potential is changing. After 30 nm coverage, an IP of 5.07 eV is reached, now at $\phi = 1.9$ eV. Upon deposition of the p-type layer, a strong upward shift is seen in the vacuum level and HOMO position. Again this shift happens mainly in the intrinsic layer, even though a characteristic core level peak of NDN1 indicates an upward shift by 270 meV of the n-doped layer as well.

The measurement can only be done up to 2 nm p-Pentacene coverage, since for thicker layers the sample starts to charge. This is expected since in this direction, the sample acts as a blocking device for the holes created in the photoemission process and the intrinsic interlayer inhibits the tunneling process that took place for the *pn* junction presented in the previous Section. At this point, the vacuum level has shifted by 0.6 eV but the bending is not completed yet. It can be assumed that as in the previous case, the final position of the p-doped layer will be the same as directly on the silver as it was measured in sample A.

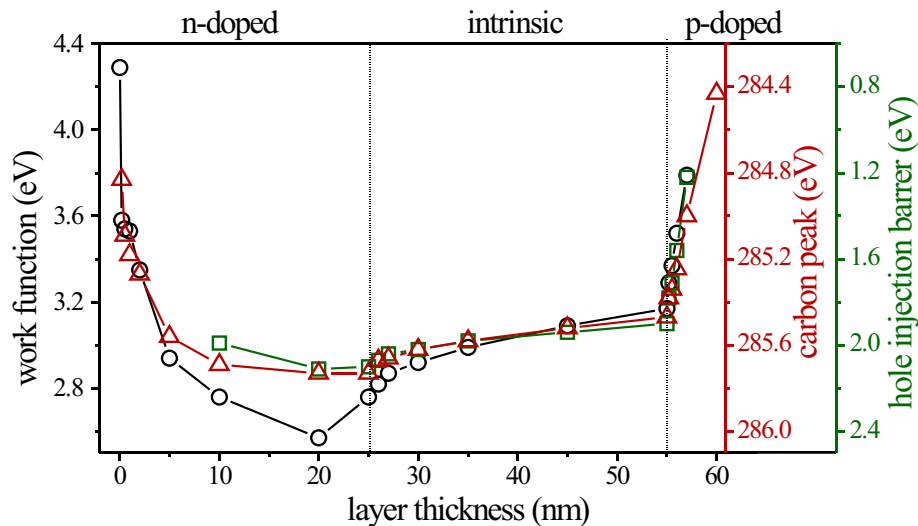


Figure 6.9: Shift of the work function (circles, left x-axis), carbon 1s position (triangles, first x-axis on the right) and HOMO cutoff position (squares, second x-axis to the right) of sample B; the values are taken from Fig. 6.8. Vertical lines mark the interfaces between the doped and intrinsic layers.

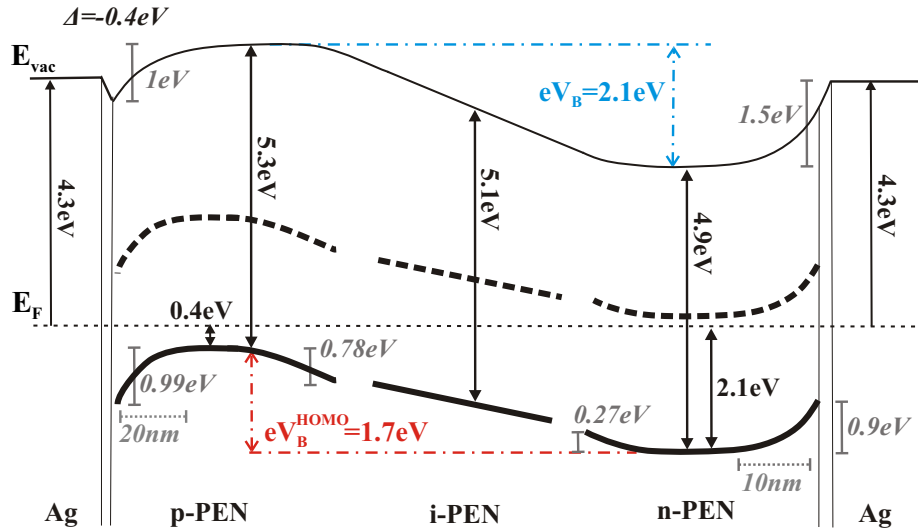


Figure 6.10: Schematic device alignment of the *pin* Pentacene homojunction concluded from the PES measurements of samples A and B. The values of the ionization potentials, the hole injection barriers, the amount of level bending, and the depletion layer widths are stated. Furthermore, two built-in voltages are stated, one is calculated by the difference in work function (V_B) and the other one by the difference in hole injection barrier (V_B^{HOMO}).

Figure 6.10 summarizes the results of the forward and backward measurement of the *pin* homojunction and displays the alignment of the full device. Here, we assume the ideal case that a silver top contact on n-Pentacene would create the same energetic alignment as the measured bottom contact. This is most likely not the case (see Chapters 2.3.4 and 4.1), but in this work we are mainly interested in the organic interfaces and their built-in potential and therefore omit this point. The built-in potential V_B of a device is usually given by the difference in work function of the n- and p-doped layers, which accounts for $eV_B = 2.1 eV$. However, of more interest for the device performance is the voltage needed to achieve a flatband condition. Because the ionization potentials of the p-doped, n-doped, and intrinsic layers differ, the built-in voltage of the transport levels is only $eV_B^{HOMO} = 1.7 eV$. Thereof, $0.65 eV$ drop across the intrinsic layer and $1.05 eV$ drop across the depletion layers of the doped Pentacene.

Change in Polarization Energy and Valence Band Features upon Doping

It was already indicated that the ionization potential of Pentacene is changing upon doping. For p-doping the value increases ($IP_p = 5.3 eV$) and for n-doping it decreases ($IP_n = 4.9 eV$) compared to the value of intrinsic Pentacene ($IP_i = 5.1 eV$). To figure out the reason for this, Fig. 6.11 compares the valence and HBEC regions of doped and undoped Pentacene layers. The graph shows the measurements for 30 nm p-Pentacene, 30 nm i-Pentacene, and 20 nm n-Pentacene.

Here, the spectra of i-Pentacene and p-Pentacene are shifted in energy to match the HOMO peak position of n-Pentacene (the values are given in the graph) and the peak height is adjusted as well to give good comparability.

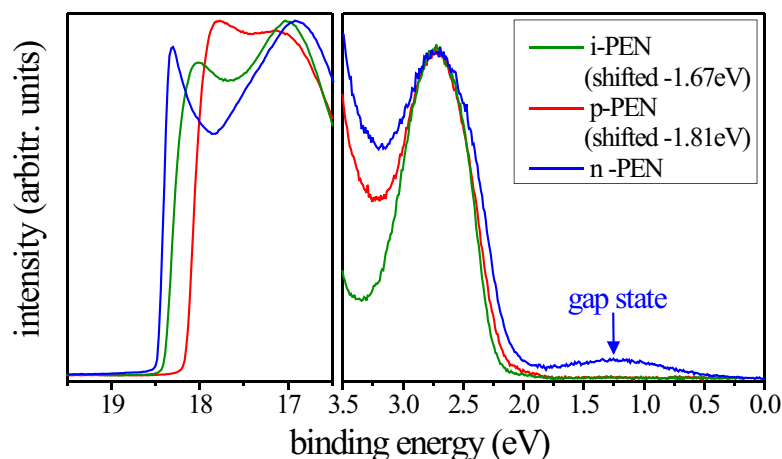


Figure 6.11: Comparison of HBEC and valence band region between layers of 30 nm *p*-doped, 30 nm intrinsic, and 20 nm *n*-doped Pentacene. For better comparability, the curves are shifted to the same HOMO peak position by the values given in the graph, as well as adjusted to similar peak heights.

The graph shows that intrinsic Pentacene has the narrowest HOMO peak. Upon *n*-doping, the peak broadens and an additional gap states appears, reaching from the HOMO up to 0.3 eV below the Fermi energy. As already mentioned before, this is typical for *n*-doping and results from a charge transfer between the Pentacene and the dopant. The HBECs of the intrinsic and *n*-doped layer are only 100 meV apart, the additional 100 meV difference results from the HOMO broadening, possibly due to an additional charge transfer state close to the cutoff position. In the case of *p*-doping, the HOMO only slightly broadens, but this time the HBEC is notably shifted compared to the intrinsic case.

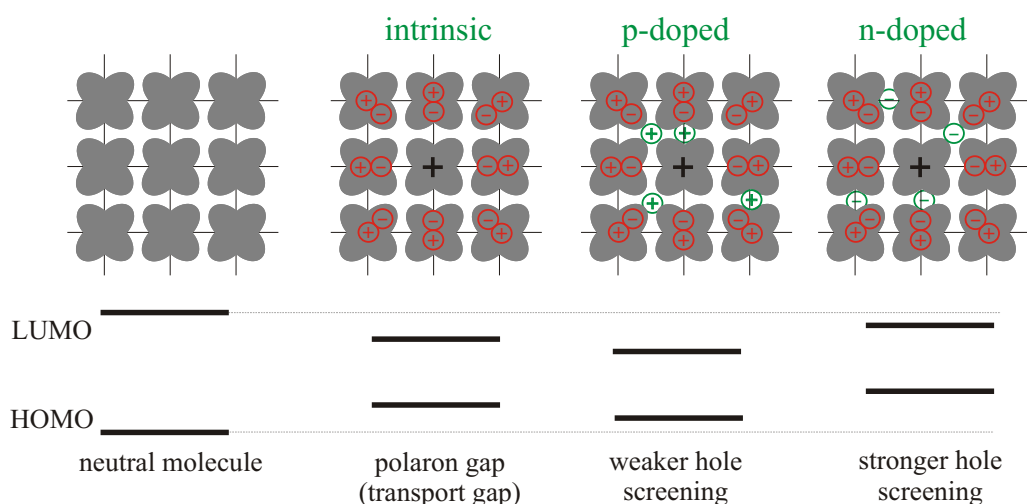


Figure 6.12: Schematic view of a molecular solid and its HOMO and LUMO values. The left image shows the neutral solid, followed by the case of a positive charge in an intrinsic system where the HOMO-LUMO gap is decreased by the polarization screening. The third image shows the same case for a *p*-doped solid where additional holes weaken the hole screening. Finally, for a *n*-doped solid the hole screening is increased by the free electrons that are present.

The effect of a changed IP upon doping has been observed before for NTCDA doped by PyB [60], where it was explained as a structural and energetic disorder effect caused by the dopant. However, we doubt that this really plays a major role and suggest a change in polarization energy (see Chapter 2.1.2) due to the doping. The introduction of additional positive charges should weaken the screening of a hole that is produced in the photoemission process, which leads to a decrease in polarization energy and therefore an increase in IP. At the same time, the screening of an electron should increase, so the LUMO relaxes further into the gap and the EA increases which can not be observed by UPS. Upon n-doping the opposite effect takes place, the EA decreases as well as the IP. In Fig. 6.12 the different scenarios for the screening of a hole are illustrated.

Further support for this assumption comes from the measurements of different amounts of p-doping of MeO-TPD by F4-TCNQ that are shown in a different context in Fig. 5.3 on page 96. The ionization potentials of these measurements are plotted vs. the molar ratio of F4-TCNQ in Fig. 6.13. Clearly, there is a linear dependence between the two values with the ionization potential increasing with increasing amount of doping.

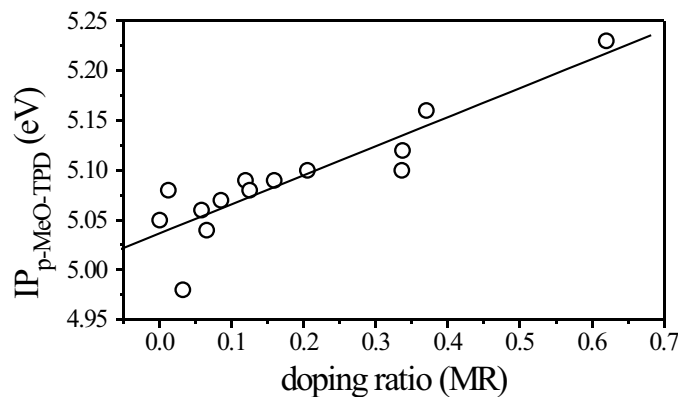


Figure 6.13: Measured change in ionization potential upon increasing doping ratio of MeO-TPD doped by F4-TCNQ. The data points are taken from measurement presented in Chapter 5, Fig. 5.3 on page 96.

Current - Voltage and Impedance Measurements

Current-voltage and especially impedance spectroscopy measurements are another way to characterize the energetic structure of a device. Therefore, these techniques are used on a device similar to the one investigated by UPS. The structure consisted of ITO /PEN:NDP2 (4wt%, 50 nm) / PEN(30 nm) / PEN:NDN1(4 wt%, 80 nm) / Al(50 nm). The resulting current density - voltage curve is plotted in Fig. 6.14. The blocking behavior achieved with this device is not very high with a rectification ratio of only 50 at ± 4 V. Earlier samples showed 10^5 [190], but there thicker intrinsic layers of 50 nm were used and a doped ZnPc layer was inserted between ITO and p-Pentacene to achieve smoother layers.

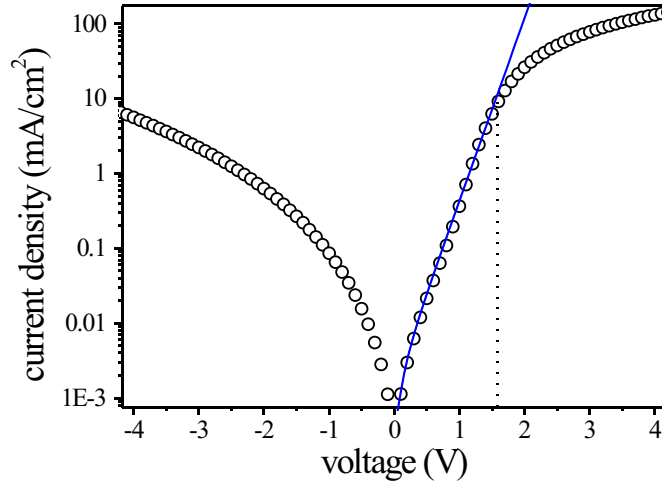


Figure 6.14: Current density-voltage characteristic of a Pentacene homojunction consisting of 50 nm *p*-Pentacene, 30 nm *i*-Pentacene and 80 nm *n*-Pentacene. The data points in forward direction are fitted by the Shockley equation. Shown by courtesy of Hans Kleemann.

In general, the IV characteristic can be described by a drift-diffusion model expressed in the Shockley equation (also known as diode equation)

$$j = j_0 \left[\exp \left(\frac{eV}{nk_B T} \right) - 1 \right] \quad (6.1)$$

where j_0 is the saturation current and n is the ideality factor that gives the deviation from an ideal diode with $n = 1$. These deviations are due to effects like recombination of charge carriers, charge carrier generation, and a change of barrier heights with the applied voltage. For significant series resistance, the equation has to be modified to

$$j = j_0 \left[\exp \left(\frac{e(V - jR_s)}{nk_B T} \right) - 1 \right] \quad (6.2)$$

where R_s is the additional series resistance. Thus, at high currents under forward bias, there is a deviation from the exponential behavior and the IV-curve becomes dominated by the properties of the transport layers, which is usually ohmic as long as the performance of the device is not injection limited.

The transition between the diode like behavior and the ohmic behavior gives an estimation of the built-in potential of the device. Before this voltage is reached, the current is generated by drift-diffusion processes and only above V_B the series resistance has a notable influence. In Fig. 6.14 this point is reached at 1.6 V forward bias, marked by the dotted line, which corresponds well to the value found by the UPS measurement of $V_B^{HOMO} = 1.7$ V. However, this is not an exact method, as it is not clear up to which point the IV-curve actually follows the physics described by the diode equation. Furthermore, the presence of traps in the layers can significantly influence the shape of the IV-curve at low bias.

Therefore, impedance spectroscopy is performed as well at a frequency of $f = 1$ kHz and an amplitude of $V_{pp} = 20$ mV. The resulting plot of the phase vs. the

voltage is shown in Fig. 6.15a. It can already be seen in this graph that in the region of 1.7 V, where the flat band condition is reached, the response of the device changes drastically from a capacitive to an ohmic behavior. To gain quantitative results from this measurement, an equivalent circuit has to be assumed which is shown as inset in Fig. 6.15b. Assuming such a circuit, the capacitance can be calculated which relates to the built-in voltage by the equation

$$C = \frac{\varepsilon\varepsilon_0 A}{\sqrt{\frac{2\varepsilon\varepsilon_0(V_B - V)}{N_A} + d_i^2}} \quad (6.3)$$

where A is the area of the device under investigation.

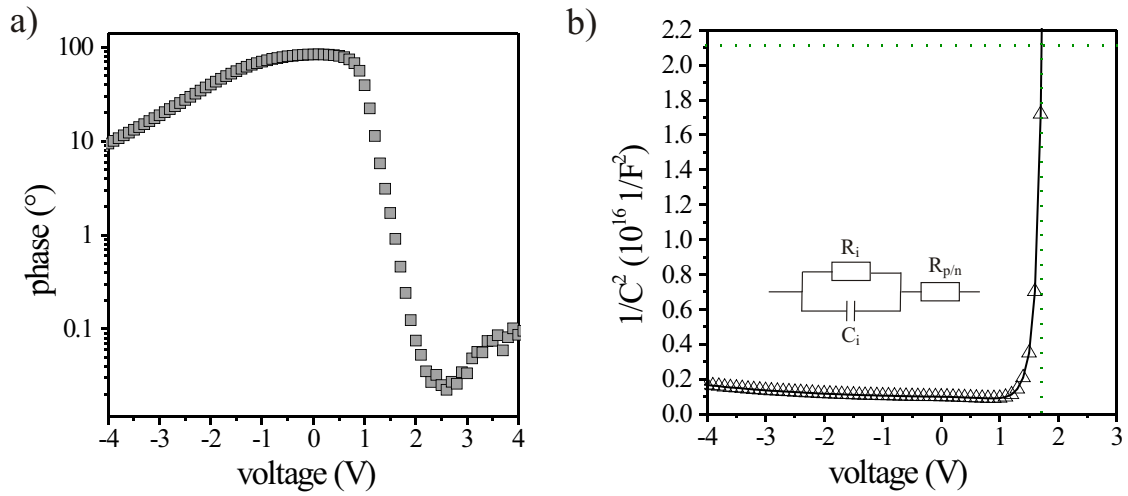


Figure 6.15: a) Impedance spectroscopy measurement of the phase vs. the voltage at a 1 kHz sinusoidal modulation of $V_{pp} = 20 \text{ mV}$. b) Calculated plot of the square of the inverse capacitance vs. the applied voltage. The equivalent circuit is shown as inset in the graph (R_i , C_i : resistance and capacity of intrinsic layer, $R_{p/n}$: resistance of the doped layers). The vertical dotted line gives the calculated contribution by the doped layers. Shown by courtesy of Hans Kleemann.

In Fig. 6.15b $1/C^2$ is plotted vs. the applied voltage. For increasing bias the capacitance increases and therefore $1/C^2$ decreases. This continues until the applied voltage approaches the built-in voltage. At this point the capacitance of the intrinsic layer breaks down and the device is limited only by the capacitance of the doped layers. The value of V_B can therefore be found by matching the point in which the device shows the same value of $1/C^2$ as the doped layers. When using $\varepsilon = 5$ for Pentacene, the capacity of the doped layers can be calculated to be

$$C = \varepsilon\varepsilon_0 \frac{A}{d} = 5 \varepsilon_0 \frac{6.38 \text{ mm}^2}{50 \text{ nm} + 80 \text{ nm}} = 2.1 \text{ nF} \quad \text{and} \quad \frac{1}{C^2} = 2.1 \cdot 10^{17} \frac{1}{\text{F}^2}. \quad (6.4)$$

This value is indicated by the horizontal dotted line in Fig. 6.15b and crosses the measurement at $V = 1.72 \text{ eV}$.

Conclusion

In this Section, the energetic alignment in a complete Pentacene *pin* homojunction device has been presented. The built-in voltage was found to be $eV_B = 2.1$ eV. The measurements showed that not all of the voltage drop happens across the intrinsic layer since considerable depletion regions form at the interfaces between the p- and n-doped layers with the intrinsic layer as well. Furthermore, the Pentacene layer showed a change in ionization potential upon doping due to a modified polarization screening resulting in a 0.4 eV lower IP for n-doped layer compared to p-doped Pentacene. This lead to a different built-in voltage of the transport levels compared to the vacuum level of $eV_B^{HOMO} = 1.7$ eV. To achieve flat band conditions, it is therefore sufficient to apply this lower voltage. The validity of this last value was furthermore supported by investigations of the current-voltage and impedance measurements. These two methods resulted in values of the built-in voltage of 1.6 eV and 1.72 eV, respectively.

6.3 PES Investigation of a Zener Diode

A Zener diode is a special kind of *pin* diode, known from inorganic semiconductors. It conducts current not only in the forward direction like a conventional diode, but also in the reverse direction if the voltage is larger than the breakdown voltage also known as *Zener voltage*. When the Zener voltage is applied under operation in backward direction, the device becomes conductive and the current increases. For devices made from inorganic semiconductors, this happens because charge carriers are transferred to higher bands by the large electric field.

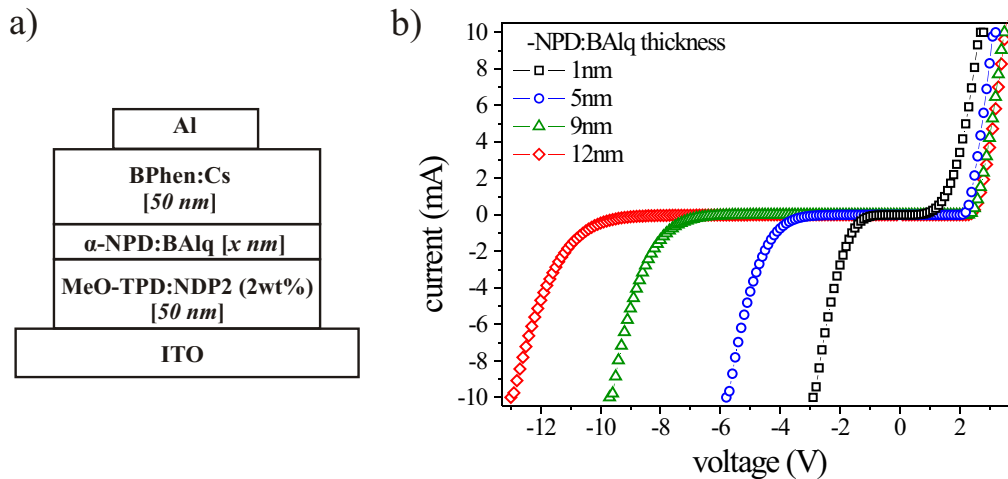


Figure 6.16: a) Schematic layer structure of a Zener diode. b) IV-curves of several Zener diodes having different thicknesses of the intrinsic BALq/ α -NPD interlayer and therefore different breakdown voltages under reverse bias. Shown by courtesy of Hans Kleemann.

From the two Sections presented in this Chapter so far, it can already be guessed that a similar device can be made from organic semiconducting layers. It was shown that *pn* junctions show no blocking behavior under reverse bias, while a good blocking

can be achieved with a *pin* junction as the tunneling is suppressed by the intrinsic layer. However, if the thickness of such an intrinsic layer is chosen in a way that it prevents tunneling at low electric fields and allows tunneling for high fields, Zener diode properties can be achieved. The breakdown voltage can be tuned by this thickness. The experiments on such devices presented in this Section have been done in cooperation with the PhD student Hans Kleemann.

Figure 6.16 shows current - voltage measurements of a series of such devices. For the p-side MeO-TPD doped by NDP2 was used and BPhen doped by Cs for the n-side. As intrinsic layer, a mixture of BA1q and α -NPD was chosen at different thicknesses indicated in the graph. This material combination is used, as BA1q is more electron conducting while α -NPD is hole conducting. This leads to equal barriers in the HOMO and LUMO levels and therefore to balanced tunneling rates. With this structure, the Zener voltage can be tuned from -2 V (black squares) to -10 V (red diamonds) by increasing the thickness of the intrinsic layer from 1 nm to 12 nm without much change in the forward bias behavior. Only the curve with 1 nm interlayer thickness shows a slight deviation, which suggests that an interlayer thickness in the range of only one ML is not suitable.

In this Section, such a Zener diode is investigated by photoelectron spectroscopy. The stack used for this investigation is similar to the one shown in Fig. 6.16, but it was not possible to use Cs as a dopant. Therefore, BPhen was doped by NDN1 for the measurement which produces working Zener diodes as well. In the following, the interface resolved measurements in both deposition sequences are presented. The resulting energy level alignment is then compared to results gained by current-voltage measurement and impedance spectroscopy.

Investigation of the Mixed Layer of α -NPD and BA1q

Before investigating the alignment in the complete stack, it has to be clarified how the energy levels within the mixed layer of α -NPD and BA1q align. First, 10 nm thick pure layers of each of the two materials are deposited on an amorphous silver foil. In Fig. 6.17 the resulting spectra for α -NPD (blue) and BA1q (green) are shown. Then a mixed layer is investigated where the two molecules are co-evaporated at a weight ratio of 1:1 which is shown as the red curve. The resulting ionization potentials are $IP_{\alpha\text{-NPD}} = 5.39$ eV, $IP_{\text{BA1q}} = 6.08$ eV, $IP_{\text{mix}} = 5.25$ eV.

The right side of Fig. 6.17 shows the valence band region of these three measurements. In this plot a polynomial background is subtracted to remove the signal originating from the scattered electrons from the measurement. The spectra of α -NPD and BA1q are fitted by Gaussian peaks and shifted in intensity and position to obtain the best fit for the curve of the mixed layer. This fit is plotted as black curve and reproduces the shape of the co-evaporated layer well. The energetic alignment of the two materials can be deduced from this fit. The difference in hole injection barrier of BA1q and α -NPD in the mixed film is $\Delta\phi = 0.68$ eV which equals the difference in ionization potential of the single layers ($\Delta IP = 0.69$ eV). The vacuum levels of the molecules are therefore aligned in the mixed film.

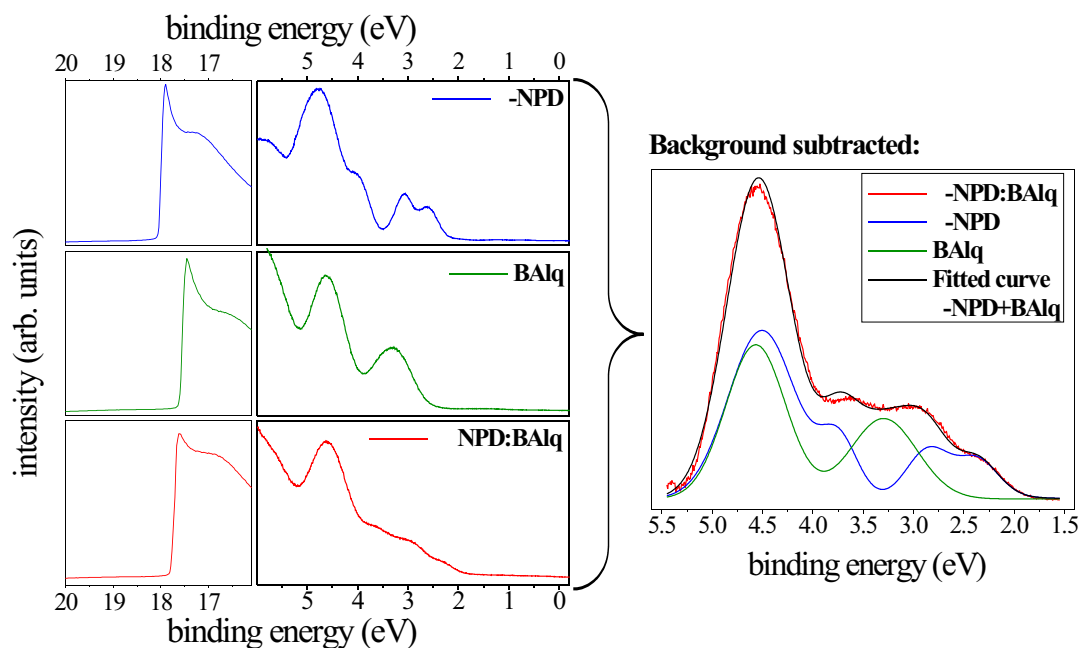


Figure 6.17: Left side: UPS measurements of a 10 nm layer α -NPD, 10 nm BALq, and 10 nm of a co-evaporated layer of α -NPD:BAIq at a weight ratio 1:1. Right side: the three valence band regions are plotted without the polynomial background signal. The curves of the pure layers are shifted in position and intensity to reproduce the shape of the mixed curve. This way the energetic alignment between the organic materials can be found.

Measurement in the pin Direction

The measurement of the alignment within a Zener diodes starts with a silver foil covered by 10 nm MeO-TPD doped with NDP2 at 4 wt%. The UPS spectra are shown as black curve in Fig. 6.18. On top of this layer, the co-evaporated α -NPD:BAIq at a weight ratio of 1:1 is stepwise evaporated up to a thickness of 5 nm (red curves). Finally, the alignment of 20 nm BPhen doped by 8 wt% NDN1 is investigated, shown by the green curves. The change in HOMO positions mentioned in the text and indicated in Fig. 6.18 can not always be found directly. For most measurements the HOMOs overlap. Therefore, these values are gained by using a peak fit program where the valence band regions of the different materials are fitted onto the curve of a given measurement.

The doped MeO-TPD layer shows a hole injection barrier of $\phi = 0.37$ eV. This value increases during the evaporation of the following layers by 0.68 eV, marked by the black crosses in Fig. 6.18. Therefore, a depletion region is created at the interface to the intrinsic layer due to a diffusion of holes. A characteristic core level peak of the p-dopant supports this finding and shows approximately the same shift. The mixed layer starts off at $\phi = 0.77$ eV, indicated by the red vertical lines, and slowly moves away from the Fermi energy for increasing thickness. After 5 nm a value of $\phi = 1.47$ eV is reached. Upon contact with n-BPhen this layer is pulled downward in energy even more due the alignment with the doped layer and reaches $\phi = 2.18$ eV. The BPhen layer takes 15 nm to reach the end of the depletion region and settles on the bulk

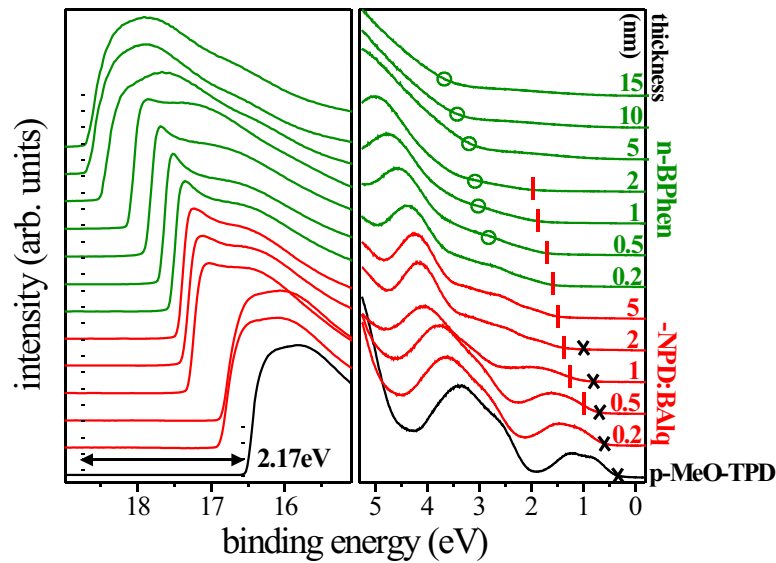


Figure 6.18: UPS measurement of the Zener diode starting from the 10 nm MeO-TPD:NDP2 (4 wt%) layer, followed by the mixed layer of α -NPD and BAIq (weight ratio 1:1), and BPhen:NDN1 (8 wt%). In the valence band region the crosses mark the HOMO onset of MeO-TPD, the vertical lines those of α -NPD:BAIq, and the circles indicate the value for BPhen. These values are gained by a peak fit program to separate the individual signals as well as possible.

value. This is much larger compared to BPhen doped by Cs (see e.g. Fig. 4.5 on page 79) which is due to the less efficient doping by NDN1. The hole injection barrier shows a change by 1.06 eV before it reaches the final value of $\phi = 3.85$ eV which is again an indication for the less efficient doping: using Cs a value of $\phi = 4.16$ eV is reached. The total change in vacuum level and therefore the built-in potential of the device is $eV_B = 2.17$ eV.

Measurement in the nip Direction

The second PES measurements are performed in reverse deposition direction. A silver layer is covered by 15 nm n-BPhen before the interface to the 5 nm mixed layer is investigated. Afterwards, the p-MeO-TPD is evaporated. However, this last layer can only be measured up to 0.5 nm thickness for UPS and 1 nm for XPS. At this point, the sample shows charging due to the photogenerated holes. The corresponding measurements are shown in Fig. 6.19 using the same color coding as in the previous graph.

Similar to the last measurement, the BPhen HOMO is positioned at $\phi = 3.83$ and shows only a small change by 0.09 eV upon the evaporation of the first 0.5 nm of the mixed layer. For thicker layers a characteristic core level peak of the dopant NDN1 can be used to look at the further change and shows a total bending by 0.46 eV. The mixed layer starts at $\phi = 2.5$ eV and moves towards the Fermi energy for increasing thickness up to a value of $\phi = 2.11$ eV. After the evaporation of 0.5 nm p-MeO-TPD

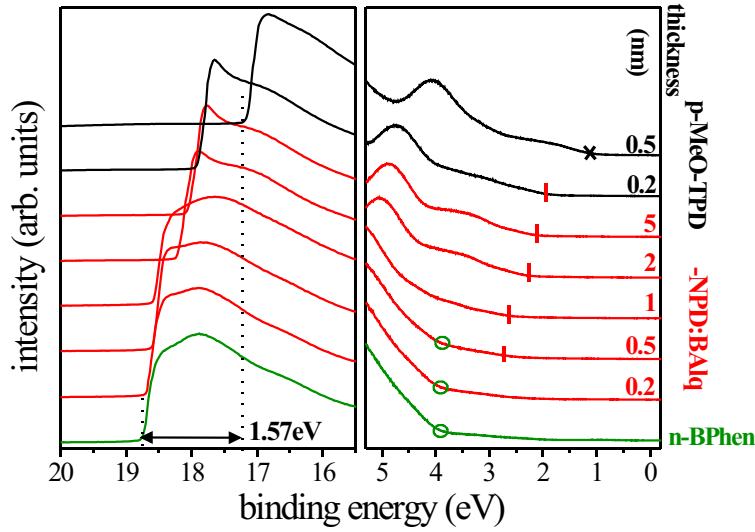


Figure 6.19: UPS measurement of the Zener diode starting from the 15 nm BPhen:NDN1 (8 wt%), layer followed stepwise by the mixed layer of α -NPD and BAIq (weight ratio 1:1), and MeO-TPD:NDP2 (4 wt%). In the valence band region the crosses mark the HOMO onset of MeO-TPD, the vertical lines those of α -NPD:BAIq, and the circles give the value for BPhen. The values are gained by a peak fit program to separate the individual signals as well as possible.

this value is further decreased to $\phi = 1.3$ eV. As the deposition of the p-doped layer could not be continued, it is not clear how much further the HOMO of the mixed layer would have moved. The HOMO of MeO-TPD appears at 1.04 eV, which is in agreement with the measurement in forward direction. The change in vacuum level for this measurement is only 1.57 eV due to the incomplete deposition of the p-side

The full alignment concluded from the two measurements is shown in Fig. 6.20. The built-in voltage of this device is $eV_B = 2.17$ eV. A considerable amount of this, i.e. 1.14 eV, drops across the depletion region of the doped layers while the rest drops across the intrinsic layer.

We have seen for the Pentacene homojunction that the built-in potential is not necessarily equal to the voltage where flat band condition is reached. To estimate V_B^{HOMO} the exact amount of the shift in the mixed layer would have to be known. This is difficult to estimate and in the schematic view only the lowest and highest HOMO values measured by UPS are stated. However, some of the change in the HOMO position of the intrinsic layer for small thicknesses could be due to the superimposed shift of the underlying doped layers that can not be told apart. The actual value of the voltage drop lies between $V_B^i = 2.5$ eV $-$ 0.77 eV $=$ 1.73 eV, if all the measured shifting actually takes place in the mixed layer, or $V_B^i = 1.73$ eV $-$ 0.68 eV $-$ 0.46 eV $=$ 0.59 eV if the shifting that is shown by the doped layers has to be subtracted as it is superimposed. The actual value will be somewhere in between. The voltage V_B^{HOMO} at which the flat band condition is achieved in the device can therefore not be calculated as easily as in the case of the Pentacene homojunction, where merely the total shift in Pentacene HOMO position had to be considered. Adding up the bending present in the layers leads to 1.73 eV $\leq V_B^{HOMO} \leq 2.78$ eV.

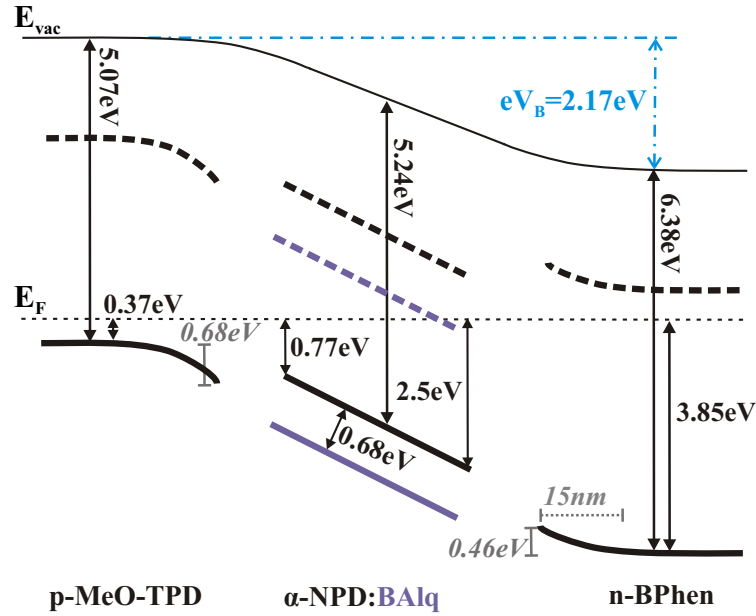


Figure 6.20: Schematic energy level alignment in a Zener diode composed of MeO-TPD:NDP2 (4 wt%)/ α -NPD:BAIq (1:1)/BPhen:NDN1 (8 wt%) resulting from the interface resolved PES measurements in forward and backward deposition sequence. The gap of α -NPD is assumed to be 3.1 [93] and for BAIq $E_g = 3.08$ eV is used [151]. The second one is probably underestimated, as the LUMO would lie below the Fermi energy.

Current - Voltage and Impedance Measurement

By performing current-voltage and impedance measurements, it is tried to determine the exact value of V_B^{HOMO} . The sample stack used for these measurements is ITO / Al (50 nm) / MeO-TPD:NDP2 (4 wt%, 50 nm) / BAIq: α -NPD (1:1, 5 nm) / BPhen:NDN1 (8 wt%, 50 nm) / Al (100 nm). The plot of the current density vs. the applied voltage is shown in Fig. 6.21. The black circles are plotted in a linear scale. The device shows the Zener diode behavior with a breakdown voltage at a backward bias of -5 V. The blue squares are plotted in a logarithmic scale and fitted for low forward bias by the Shockley equation (Eq. 6.1). This fit does not work as well for this measurement as for the Pentacene homojunction (Fig. 6.14). The data do not show a simple exponential behavior at low voltages which suggest a filling of trap states in this range. The point at which the measurement deviates from the Shockley-like behavior is at $V = 2.05$ V, but due to the influence of the trap states this value has been viewed sceptically.

On the same sample, impedance spectroscopy is performed and the plot of the phase vs. the applied voltage is shown in Fig. 6.22a. The capacity of BPhen:NDN1 layer shows a significant influence of trap states in this measurement which makes the equivalent circuit used for Pentacene less applicable here. This problem can be reduced by decreasing the modulation frequency of the measurement from 1 kHz to 500 Hz as these trap states have a different time constant compared to the intrinsic interlayer. However, the plot of $1/C^2$ in Fig. 6.22b is not as straightforward to evaluate as in the case of the Pentacene homojunction. The calculated value of the doped layers

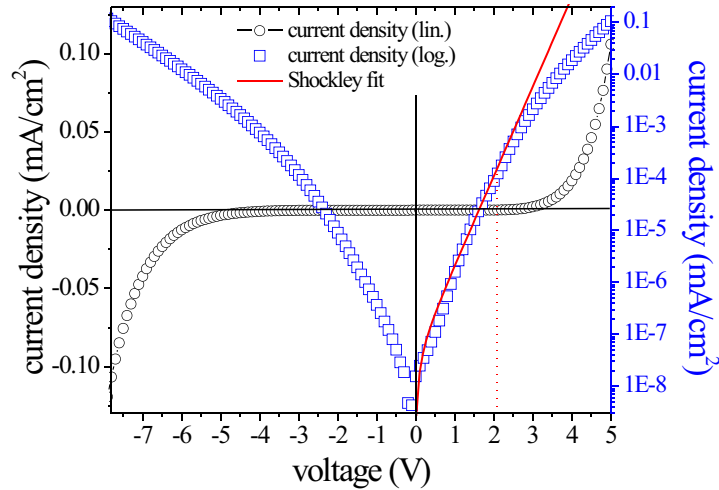


Figure 6.21: Current density-voltage measurement of a Zener diode consisting of 50 nm p-MeO-TPD, 5 nm BAQ: α -NPD and 50 nm n-BPhen. The black circles are a linear plot to show the Zener breakdown in backward direction. The blue squares show the same measurement on a logarithmic scale and the data points in forward direction are fitted by the Shockley equation giving the red solid line. Shown by courtesy of Hans Kleemann.

of $1/C^2 = 3.5 \cdot 10^{17} 1/F^2$ is not reached, as the capacity of the BPhen:NDN1 layer dominates over the p-MeO-TPD layer and furthermore the trap states introduce an additional capacity making the calculation of the correct value imprecise. Once more, only the limiting cases of the built-in voltage can be stated, as we know it has to be in the region of Fig. 6.22b where the capacity of the device shows a strong change in magnitude. This is marked by the vertical lines and gives $2.2 \text{ eV} \leq V_B^{HOMO} \leq 2.7 \text{ eV}$.

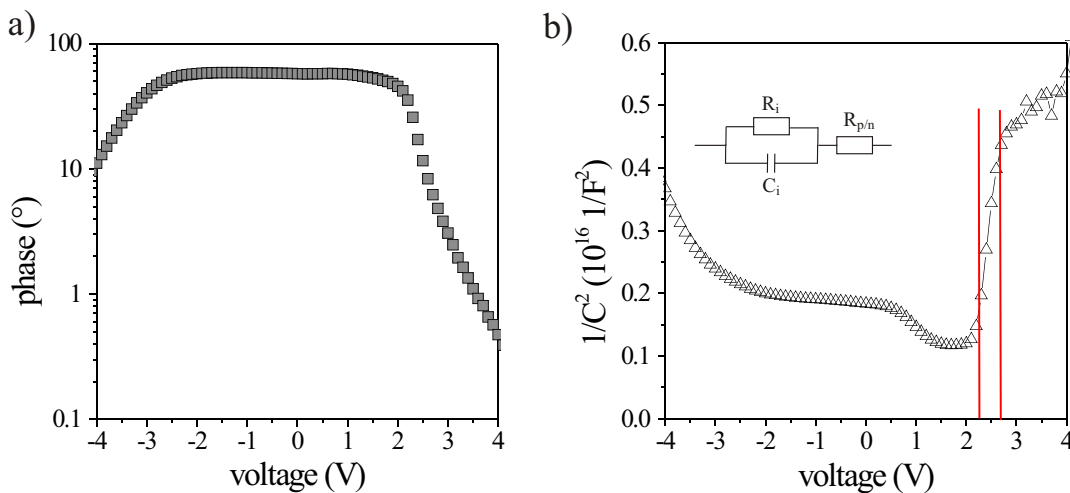


Figure 6.22: a) Impedance spectroscopy measurement of the phase vs. voltage at a 500 kHz sinusoidal modulation of $V_{pp} = 20 \text{ mV}$. b) Calculated dependence of the square of the inverse capacitance vs. the applied voltage. The equivalent circuit used for the calculation is shown as inset in the graph (R_i , C_i : resistance and capacity of intrinsic layer, $R_{p/n}$: resistance of the doped layers). The vertical dotted lines give the margin of the area of the built-in voltage in this device. Shown by courtesy of Hans Kleemann.

Conclusion

In this Section, the alignment within a Zener diode was investigated, where a thin intrinsic interlayer consisting of BA1q and α -NPD at a ratio of 1:1 separates a pn -junction. The investigation of this intrinsic interlayer showed that the vacuum levels of the co-evaporated molecules are aligned and therefore the HOMO offset is $\Delta\phi = 0.68$ eV. The measurement of the complete stack showed a built-in voltage of $eV_B = 2.17$ eV. The intrinsic interlayer in this device is only 5 nm thick, and therefore a considerable voltage drop of 1.14 V takes place across the doped layers. This makes estimating the voltage drop across the HOMO of the mixed layer difficult as the shifts of the doped layers are superimposed on it. The measurement of the change in capacity of the device on the voltage by impedance spectroscopy met difficulties as well. Due to a large number of traps in the BPhen layer, the capacity can not be calculated correctly. The transport level built-in voltage, at which the flat band condition is reached, can only be given to lie within the region of $2.2 \text{ eV} \leq V_B^{HOMO} \leq 2.7 \text{ eV}$.

7 Investigation of a Complete OLED Device

In this Chapter, we increase the complexity of the investigated sample and use photoelectron spectroscopy to study the electronic structure and energy level alignment of a complete organic light emitting diode. With rising complexity of the state-of-the-art device stacks, the interfaces between the organic layers become increasingly important for the OLED performance. Therefore, it is crucial to understand the alignment between the numerous organic layers for simulation and optimization of these devices. We present interface-resolved measurements of all metal/organic and organic/organic interfaces that occur in a typical OLED stack.

7.1 Photoelectron Spectroscopy Measurements

We choose the structure of a state-of-the-art long living and highly efficient orange/red phosphorescent device for these studies. The performance of this OLED is reported in Ref. [137]. In this stack, an ITO anode is contacted by a hole injection layer consisting of MeO-TPD doped at a molar ratio of 0.04 with F4-TCNQ and an electron blocking layer of α -NPD. This is followed by the light emitting layer, composed of α -NPD co-evaporated with 10 wt% of the phosphorescent red emitter Ir(MDQ)₂acac¹, and a hole blocking layer of BPhen. Finally, the device consist of an electron injection layer of BPhen doped by Cesium and a silver top contact.

For the UPS and XPS measurements, the whole device is incrementally built and each interface is investigated. Thereby, different chambers for n- and p-type doping as well as for intrinsic layers are used to avoid cross contamination.

Interface alignment between ITO and MeO-TPD:F4-TCNQ: The first interface is the one from the anode ITO to the hole injection layer MeO-TPD p-doped with F4-TCNQ at a molar ratio of MR = 0.04. This interface was already discussed in Chapter 5.3 for the investigation of the alignment of a p-doped layer with different substrates and is shown in Fig. 5.2 on page 94. At the interface, a dipole of -120 meV is observed, followed by an upward bending of 670 meV. After a depletion region of 5 nm, the energy levels saturate, showing a ϕ of 0.45 eV and the ionization potential

¹Iridium(III)bis(2-methyldibenzo[f,h]quinoxaline)(acetylacetonate)

is 5.1 eV. The resulting energy diagram for this interface can be found in Fig. 5.2 on page 94.

Interface alignment between MeO-TPD:F4-TCNQ and α -NPD: For the investigation of the interface between MeO-TPD:F4-TCNQ and the intrinsic α -NPD blocking layer, a 6 nm thick layer of doped MeO-TPD is prepared on a silver foil and subsequently α -NPD is evaporated. Silver is used here and for all the following investigations as substrate instead of ITO since it is more reproducible and easier to handle. It was shown in Chapter 5.3 that this has no influence on the energetic alignment.

A dipole is not observed at the interface as can be seen from the constant HBEC in Fig. 7.1a, so there is vacuum level alignment between the two layers. The IP of the 5 nm thick α -NPD layer is 5.45 eV and the hole injection barrier is $\phi = 0.85$ eV as is shown in Fig. 7.1b. Here a transport gap of 3.1 eV is assumed for α -NPD [93].

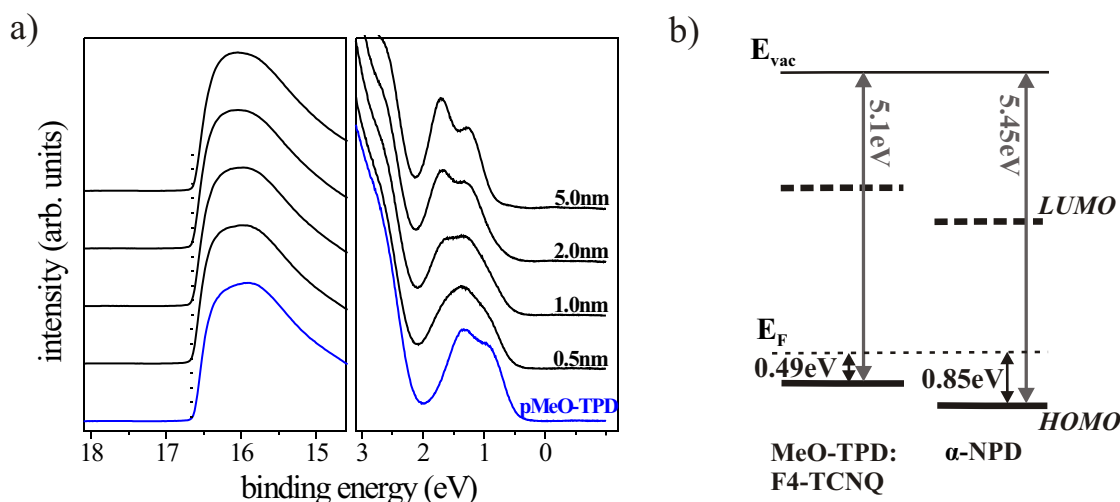


Figure 7.1: Interface between doped MeO-TPD and intrinsic α -NPD. a) Development of the HBEC and valence band region of the UPS spectra as a function of increasing thickness of the α -NPD layer. The dotted vertical line marks the HBEC position. b) Resulting schematic energy level diagram.

Interface alignment between α -NPD and α -NPD:Ir(MDQ)₂acac: On a further sample, the interface between intrinsic α -NPD and the active layer where α -NPD is co-evaporated with 10 wt% of the phosphorescent emitter Ir(MDQ)₂acac is investigated. On a silver sample, 6 nm of doped MeO-TPD are covered by 3 nm intrinsic α -NPD. The α -NPD has to be kept thin to prevent charging of the sample, as this layer shows a low conductivity for the photogenerated holes. On top, the mixed layer of α -NPD:Ir(MDQ)₂acac is deposited stepwise.

The measurements in Fig. 7.2 show a small downward shift of the vacuum level and the α -NPD HOMO position at first by -100 meV that saturates after 1 nm when approximately the first ML is completed. The mixed layer shows $\phi = 0.9$ eV and the IP remains the same as for intrinsic α -NPD.

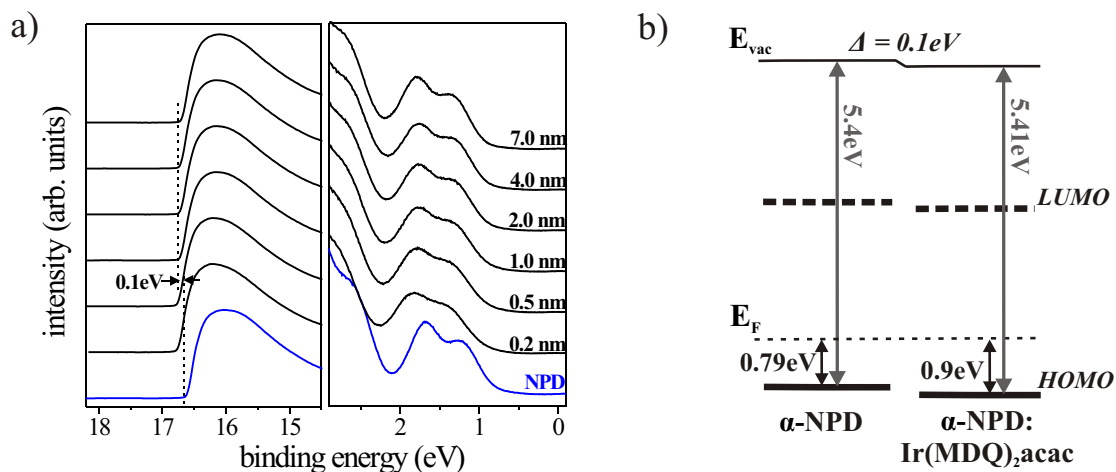


Figure 7.2: Interface between α -NPD and α -NPD co-evaporated with 10 wt% $\text{Ir}(\text{MDQ})_2\text{acac}$. a) Development of the HBE and valence band region of the UPS spectra as a function of increasing thickness of the co-evaporated layer. The dotted vertical line marks the change in the position of the HBE. b) Resulting schematic energy level diagram.

Since the electron transport in the device does not take place on the host material but on the LUMO of the $\text{Ir}(\text{MDQ})_2\text{acac}$ [137], it is important to know the position of the $\text{Ir}(\text{MDQ})_2\text{acac}$ HOMO and LUMO within the α -NPD matrix. The 10 wt% doping ratio used in the experiment does not produce distinct HOMO features from the iridium complex molecules. Therefore, two more samples are prepared, one with a doping ratio α -NPD: $\text{Ir}(\text{MDQ})_2\text{acac}$ of 1:1 and a pure $\text{Ir}(\text{MDQ})_2\text{acac}$ sample.

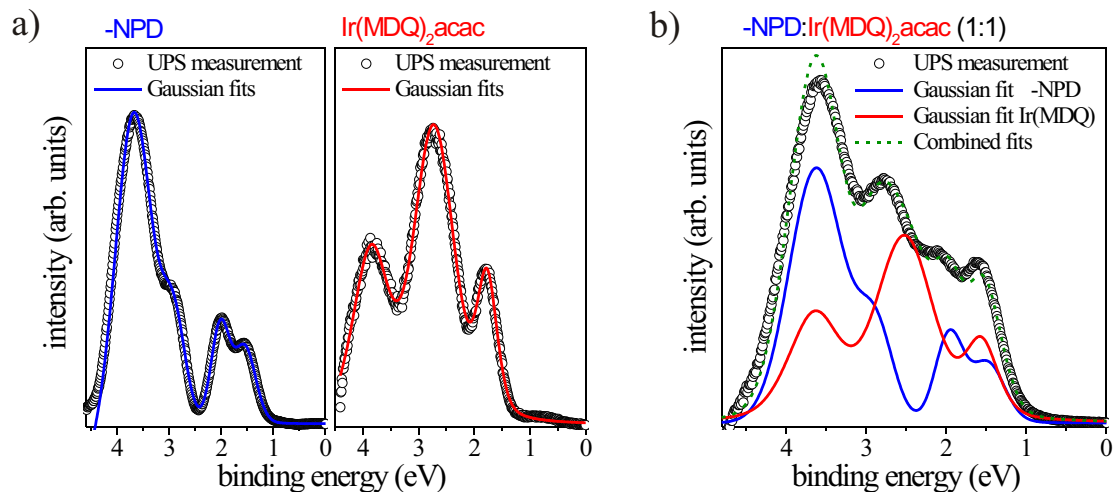


Figure 7.3: a) UPS valence band regions of pure α -NPD and pure $\text{Ir}(\text{MDQ})_2\text{acac}$; the two measured curves are fitted by multiple Gaussian peaks after a polynomial background is subtracted b) UPS valence band region of a 1:1 ratio of α -NPD mixed with $\text{Ir}(\text{MDQ})_2\text{acac}$ after a polynomial background is subtracted. The Gaussian fits of the pure α -NPD and $\text{Ir}(\text{MDQ})_2\text{acac}$ layers are used to fit the measured data and gain information on their relative alignment.

In Fig. 7.3a, the valence band region of the pure α -NPD layer and the pure Ir(MDQ)₂acac layer are shown, fitted by multiple Gaussian peaks after a polynomial background is subtracted. These two fits are used in the valence band region of the 1:1 mixed layer (Fig. 7.3b) and shifted in relative position and intensity to match the measured data. This fit shows that the HOMO cutoffs are at the same position, so the HOMO of the α -NPD and the iridium complex molecule are aligned in the mixed layer. This is due to the vacuum level alignment between the two molecules that have similar ionization potentials. The position of the Ir(MDQ)₂acac LUMO can be estimated from the 2.6 eV transport gap measured by cyclic voltammetry to be 0.5 eV below the LUMO of α -NPD.

Interface alignment from α -NPD:Ir(MDQ)₂acac to BPhen and to BPhen:Cs:

For the investigation of the interface between α -NPD:Ir(MDQ)₂acac and the hole blocking layer BPhen, a silver foil with 5 nm doped MeO-TPD and 5 nm α -NPD:Ir(MDQ)₂acac is prepared. Here, the intrinsic α -NPD had to be left out to prevent a charging of the sample during measurement. This has no effect on the alignment since it does not lead to a change in the energetic position of the mixed layer, as can be seen in the same ϕ of α -NPD:Ir(MDQ)₂acac in Fig. 7.2b and 7.4f.

The UPS measurements in Fig. 7.4a and the resulting values in Fig. 7.4c show that upon BPhen deposition, the HOMO of α -NPD:Ir(MDQ)₂acac exhibits a downward shift of -590 meV and ϕ increases to 1.49 eV. The HOMO of BPhen can be distinguished after 0.5 nm of coverage. For increasing thickness, it shows a downward bending of -200 meV (Fig. 7.4e). The energetic alignment of this interface is shown in Fig. 7.4f.

Such a strong vacuum level shift when depositing an intrinsic layer is rather unusual. However, it has been shown before by matrix assisted laser desorption/ionization time-of-flight mass spectrometry (MALDI-TOF-MS) that during the operation of such an OLED, the Ir(MDQ)₂acac molecules dissociate and the Ir(MDQ)₂⁺ fragments react with the BPhen molecules [137]. This leads to the creation of a dipole layer at the interface that is observed in the UPS measurements.

Since UPS has only a small probing depth, the change in position of the iridium 4f core level peaks is observed by XPS as well (Fig. 7.4a right side), which yields additional information on the behavior of the mixed layer. These core level peaks show a downward shift by -410 meV in Fig. 7.4d, following the UPS shift in shape, but not in intensity. This can have two different reasons: (i) XPS probes deeper into the sample, so the bending of a lower layer is observed or (ii) the reaction between the iridium complex molecules and BPhen at the interface could induce a different energy shift of the α -NPD compared to the Ir(MDQ)₂acac.

A total BPhen thickness of only 5 nm is chosen, since on the same sample, the measurement is continued with the electron injection layer of BPhen doped with Cesium atoms. A thicker intrinsic BPhen layer would increase the probability of charging during the following measurement.

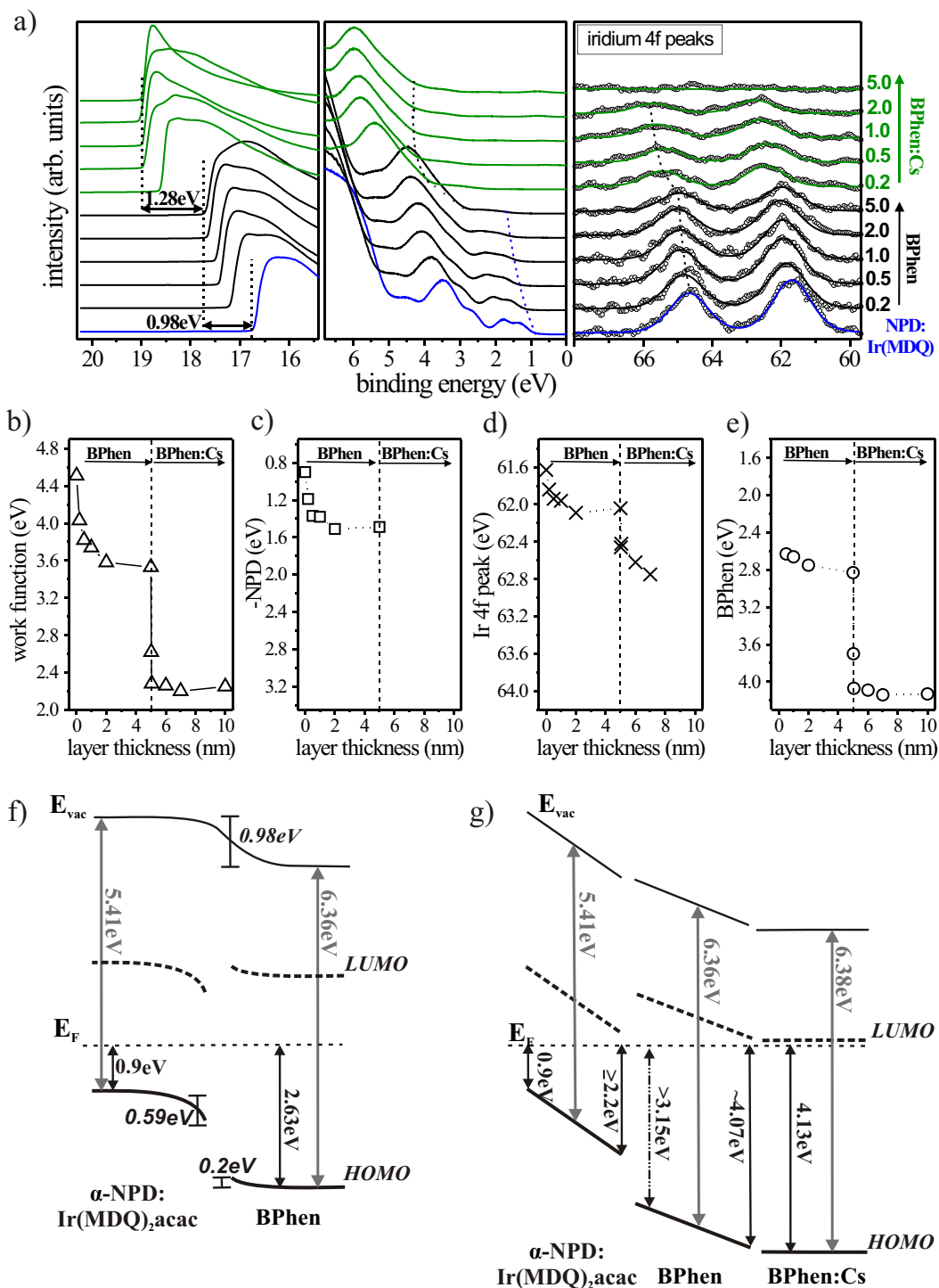


Figure 7.4: Measurement of the interface from α -NPD:Ir(MDQ)₂acac to BPhen and to BPhen:C₆. a) Development of the HBEV, valence band region, and Ir 4f peaks with increasing thickness of the organic layers; the dotted vertical lines mark the change in the position of the HBEV, HOMO and Ir 4f_{7/2} peak. Plots of the corresponding shifts are shown for b) the work function, c) the α -NPD hole injection barrier, d) the Ir 4f_{7/2} peak, and e) the BPhen hole injection barrier as a function of the increasing BPhen and BPhen:C₆ layer thickness; the dashed vertical line marks the start of the doped BPhen layer. f) Schematic energy level diagram for BPhen deposited on α -NPD:Ir(MDQ)₂acac. g) Schematic energy level diagram when BPhen:C₆ is deposited on α -NPD:Ir(MDQ)₂acac / BPhen.

Instantaneously after the deposition of 2 Å of doped BPhen, the work function changes by -900 meV and the BPhen HOMO moves downwards by -920 meV, as can be seen at the dotted vertical line in Fig. 7.4b and e. Since at such low coverage the HOMO signal originates mostly from the underlying intrinsic BPhen, this must mean that at the interface the energy levels of the intrinsic BPhen layer shift downward to achieve alignment with the doped BPhen. Upon further deposition, the vacuum level moves downward even more, resulting in a total shift of -1.28 eV while the HOMO shows a total shift of -1.3 eV. The doping ratio can be estimated from the relative Carbon and Cesium XPS peak intensities and accounts in this case for one Cesium atom per BPhen molecule.

Interfaces from BPhen:Cs to BPhen and to α -NPD:Ir(MDQ)₂acac: Further measurements are needed to determine the HOMO position of the intrinsic BPhen at the contact to α -NPD:Ir(MDQ)₂acac and to learn more about the alignment between BPhen and BPhen:Cs. Therefore, the reversed deposition sequence is investigated as well and is shown in Fig. 7.5a. 10 nm BPhen:Cs are prepared on a silver foil, followed by a stepwise deposition of 10 nm intrinsic BPhen. The measured values in Fig. 7.5c reveal a small interface dipole of approximately 200 meV that is created within the first ML when the ϕ changes from 4.24 eV for the doped layer to 4.04 eV for the intrinsic one. The schematic energy alignment is shown on the left part of Fig. 7.5e. On top of this layer, α -NPD:Ir(MDQ)₂acac is evaporated. The HOMO of BPhen gradually shifts upward by 180 meV upon the deposition of the mixed layer and the HOMO of α -NPD:Ir(MDQ)₂acac shows a shift of 480 meV as can be seen in Fig. 7.5d starting from the dashed line. Since the BPhen layer shows only a small change in energetic position here, the backward measurement demonstrates that most of the shifting seen in the forward measurement (Fig. 7.4g) occurs in the mixed layer.

It would be interesting to know how the layers react when p-MeO-TPD is evaporated on top. This should pull the HOMO of the mixed layer up to $\phi = 0.9$ eV again and might influence the energetic position of the intrinsic BPhen. However, it is not possible to do this measurement as the sample shows immediate charging.

Interface alignment between BPhen:Cs and silver: The last interface to be investigated is the one from BPhen:Cs to the silver top contact. This measurement has already been shown in Fig. 4.6 on page 80 during the investigation of the metal top contact formation of doped layers (Chapter 4.1.2). There, it is found that the organic shifts upward by 190 meV, while the position of the vacuum level changes by about 260 meV, resulting in a work function of 2.42 eV. As mentioned in Chapter 4.2, this incorrect silver work function is due to the monolayer of BPhen that remains on top of the metal layer. It is assumed in Fig. 7.6 that the silver top contact has a work function of 4.3 eV even though it is not observable by UPS because of the residual BPhen on top. The thickness of the depletion layer cannot be derived from this measurement. However, from Chapter 4.1 we know that the depletion region at a bottom contact is only 2 nm wide.

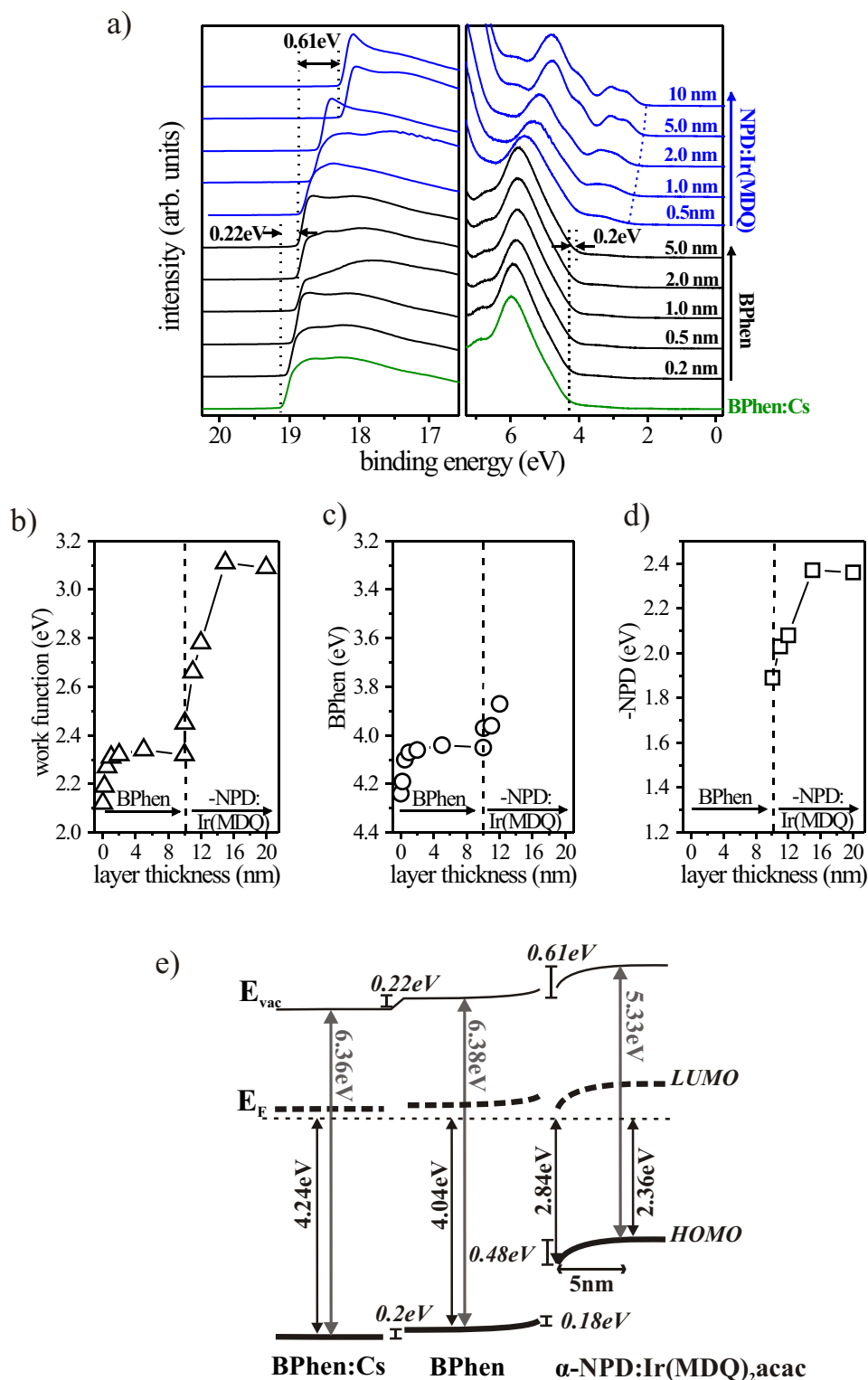


Figure 7.5: Interface from BPhen:Cs to BPhen and to α -NPD:Ir(MDQ)₂acac. a) Development of the HBE and valence band region of the UPS spectra with increasing thickness of the organic layers. Plots of the corresponding shifts are shown for b) the work function, c) the BPhen hole injection barrier, and d) the α -NPD hole injection barrier as a function of the BPhen and α -NPD:Ir(MDQ)₂acac layer thickness; the dashed vertical line marks the start of the α -NPD:Ir(MDQ)₂acac layer. e) Resulting schematic energy level diagram. Taken from Ref. [194].

Full device alignment: From the combined measurements in forward and backward direction, the alignment of the interfaces are derived and the schematic energy level diagram of the red phosphorescent OLED stack is shown in Fig. 7.6. The data shows that there is no common vacuum level throughout the device. This is due to the interface dipoles, level bending effects, and the built-in potential created by the doped layers. This built-in potential accounts for $eV_B = 2.53\text{ eV}$ and mainly drops across the α -NPD:Ir(MDQ)₂acac layer. The small voltage drop of 0.18 eV across the intrinsic BPhen layer could be underestimated, as it is measured without evaporating the p-doped layer on top. Furthermore, there could be some part of the voltage dropping across the intrinsic α -NPD layer as well. It could not be included in the stack for most of the measurements due to charging.

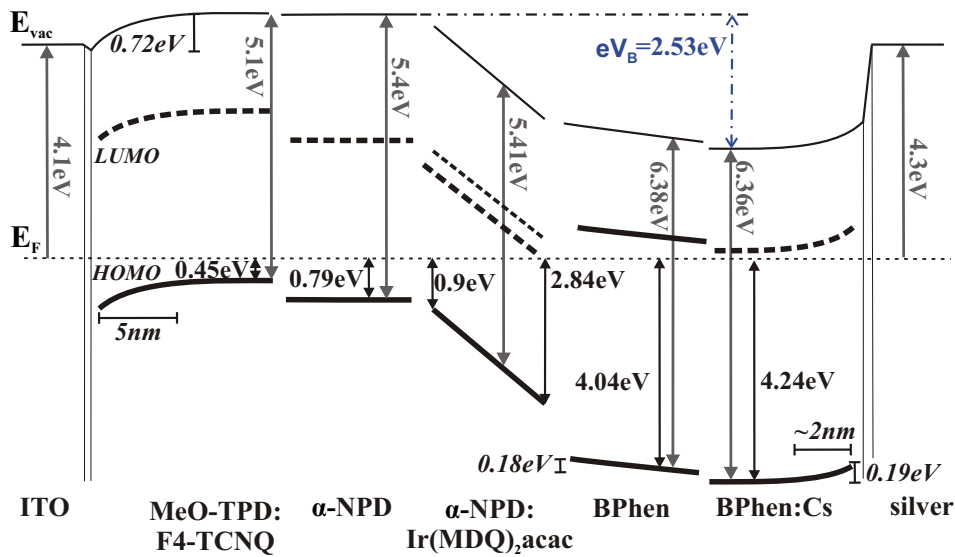


Figure 7.6: Schematic energy diagram of the full OLED device as it can be derived from the measurements presented in this Chapter. The LUMO of the α -NPD is shown only as a thin line since the electron transport happens on the LUMO of the Ir(MDQ)₂acac. The built-in potential V_B is calculated from the offset between the vacuum levels of the doped layers.

7.2 Comparison to IV Characteristics

In a next step, the results from the UPS measurements are compared to current-voltage measurements. For this purpose, identical OLED stacks with different layer thicknesses of the α -NPD:Ir(MDQ)₂acac layer ranging from 5 nm to 20 nm are prepared. Changing this thickness has no influence on the built-in potential and merely changes the resistance within the OLED. The samples are prepared in the Lesker UHV system at a base pressure of $1 \cdot 10^{-8}\text{ mbar}$. Here, it is possible to fabricate devices with different structures on the same substrate ensuring equal evaporation conditions for a high comparability. After preparation, the devices are encapsulated with cavity glass

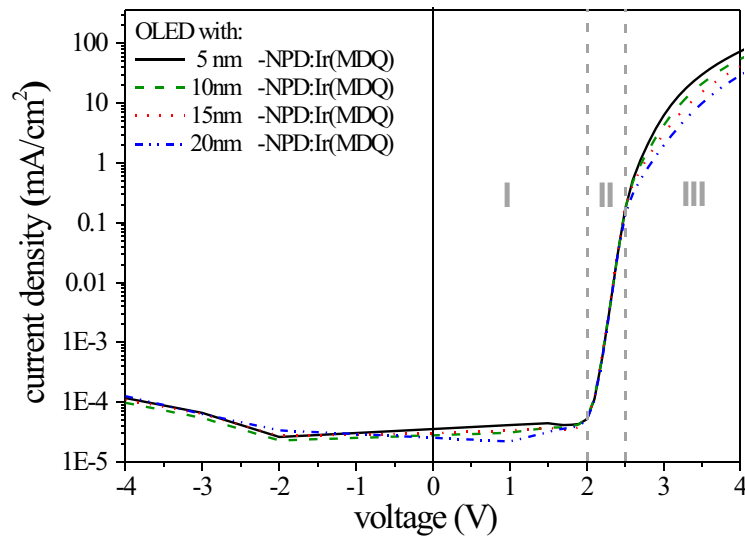


Figure 7.7: Current density-voltage characteristic of the red phosphorescent OLED stack at different thickness of the emitting layer α -NPD:Ir(MDQ)₂acac. The current can be divided into three regions (I) leakage current (II) drift-diffusion dominated and (III) recombination / ohmic conduction dominated region.

lids by an epoxy glue under the nitrogen atmosphere of a glovebox that is directly attached to the vacuum system.

The current density-voltage characteristics of four of these samples are shown in Fig. 7.7. The current characteristics can be divided into three regions. For voltages below 2 V, leakage currents dominate. In the range from 2 V to approximately 2.5 V, all curves coincide and in this regime, the drift-diffusion current can be fitted by the Shockley Equation (Eq. 6.1). Above this voltage, the current gets dominated by recombination and/or ohmic conduction and the curves show a significant dependence on the thickness of the emission layer which indicates a considerable drop of bias across this region. The measurement supports the results of a built-in voltage of 2.53 eV found by the UPS measurements and the strong level bending drop across the α -NPD:Ir(MDQ)₂acac layer.

8 Conclusion and Outlook

8.1 Conclusion

The work presented in this thesis aimed at a better understanding of the alignment between organic semiconductor layers and more complex devices, with a focus on the impact of doped layers. For most experiments, UV-photoelectron spectroscopy (UPS) and x-ray photoelectron spectroscopy (XPS) were used as powerful tools to investigate the occupied density of states of a solid under UHV conditions. The high surface sensitivity on the order of nanometers allows for interface-resolved measurements when the interface is stepwise evaporated and investigated. This gives information on the creation of dipoles, accesses the energy level barriers, and can probe the formation of depletion regions created at interfaces to doped layers.

First, the topic of the formation of metal top and bottom contacts was investigated. This was motivated by the finding that p-doped layers show symmetric injection of charge carriers, while n-doped layers in general show an increased injection from a top contact. By UPS and XPS it was found that for the p-doped system of MeO-TPD co-evaporated with F4-TCNQ, the alignment of bottom and top silver contacts is symmetric with a hole injection barrier of 1.2-1.3 eV independent on the deposition sequence. However, in the case of BPhen n-doped by Cs, a significant difference was found. For n-BPhen, the level bending at the top contact was 1.16 eV smaller compared to the bottom contact. The reason is connected to induced gap states created by a reaction of the BPhen molecules with the penetrating silver atoms. This results in a more efficient tunneling process from the top electrode, compared to the bottom one, in agreement with current voltage measurements of single carrier devices. A further observation made during these investigations was a residual organic signal for thick metal top contacts, indicating a contamination of the metal layer by molecules. Therefore, the interaction of BPhen with a silver top contact was further investigated by x-ray depth profiling. It was found that the silver considerably penetrates into the BPhen layer. This leads to a diffuse interface and a contamination of the whole Ag contact with BPhen was found. Most notably, a BPhen monolayer is present on top of the metal layer almost independent of the metal layer thickness. These effects are disadvantageous when using ultra-thin, transparent top contacts. By investigating the same interface with an 1 nm aluminum interlayer inserted between BPhen and silver a different formation was found. The aluminum binds at

the surface to the BPhen, preventing a diffusion of the subsequently deposited silver atoms. This way a pure metal layer could form on top which is advantageous for the metallic behavior and smoothness, as shown by improved device performance and SEM images.

Furthermore, the p-doping process was studied extensively on the system of MeO-TPD co-evaporated with F4-TCNQ. A moderate molar doping ratio of 0.04 already yielded a carrier concentration large enough to result in a final energetic alignment independent of the substrate. This means, Fermi level alignment between substrate and organic semiconductor is achieved and interface effects as well as the substrate work function only play a minor role for the energy alignment. By varying the amount of doping, it was found that the induced Fermi level shift exceeds the expected value of $k_B T$ by a factor of 15. The Fermi energy position within the gap could thus be controlled over 1.33 eV by the doping ratio and the conductivity of the sample could be tuned over several orders of magnitude up to a value of $\sigma = 2.3 \cdot 10^{-3} \text{ S/cm}$. At molar doping ratios larger than 0.1, the Fermi level became pinned 350 meV beyond the HOMO onset in the gap of the semiconductor. Detailed investigations of the UPS signal around the HOMO cutoff position showed an exponentially decaying tail of the DOS that extended considerably beyond the traditionally assumed HOMO onset. Consequently, we observed a DOS that reaches up to the Fermi energy upon doping ratios above 0.1. The width of this HOMO tail was found to strongly depend on the matrix material and thereby on the disorder present in the amorphous layer. By determining the depletion layer thicknesses at various doping densities, typical charge carrier concentrations in doped organic semiconductors could be deduced, ranging from $2 \cdot 10^{18}$ to $2 \cdot 10^{20} \text{ cm}^{-3}$ were found for weakly and strongly doped samples. By comparing this value to the amount of dopants present in the layer, it was found that only about 5% of the dopants are fully ionized.

Finally, the alignment between doped layers as well as doped and intrinsic layers was investigated for device relevant interfaces, ranging from a simple *pn* junction to a complete OLED device which consisted of 5 different layers placed between the metal contacts. The first interface investigated was a *pn* junction made of MeO-TPD:F4-TCNQ and C60:AOB that is applied as recombination contact in tandem solar cells. The high doping ratios lead to a large built-in voltage of $\approx 800 \text{ meV}$ across this interface. The resulting small HOMO-LUMO offset and the only 10 nm wide depletion region facilitate the efficient electron-hole recombination at this interface necessary to achieve the doubling of the open circuit voltage. In a next step, a *pin* homojunction was investigated, realized by Pentacene doped by either NDP2 and NDN1 at the interfaces and an intrinsic layer in between. The built-in voltage was found to be $eV_B = 2.1 \text{ eV}$. The measurements showed that not all of the voltage drop happens across the intrinsic layer, since considerable depletion regions form at the interfaces between the p- and n-doped layers with the intrinsic layer as well. The Pentacene layer showed a change in ionization potential upon doping due to a modified polarization screening, resulting in a 0.4 eV lower IP for n-doped layer compared to p-doped

Pentacene. This led to a different built-in voltage of the transport levels compared to the vacuum level of $eV_B^{HOMO} = 1.7$ eV. To achieve flat band conditions, it is therefore sufficient to apply this lower voltage. The validity of this last value was furthermore supported by the current-voltage and impedance spectroscopy measurements.

A similar investigation was performed on a *pin* heterojunction showing a Zener-diode behavior. The p-doped layer consisted of MeO-TPD:NDP2; for the n-side, BPhen:NDN1 was used. This time, the intrinsic layer was made of a combination of the hole conduction α -NPD and the electron conducting BAQ to ensure comparable tunneling rates for both types of charge carriers. The alignment of the molecules in the mixed layer was investigated; they exhibited vacuum level alignment. The whole device showed a large built-in voltage of $eV_B = 2.17$ eV. The intrinsic interlayer in this device is only 5 nm thick, so a considerable voltage drop of 1.14 eV takes place across the depletion regions formed in the doped layers. For this device, comparison to current-voltage and impedance spectroscopy measurements were made as well.

The device with the highest complexity under investigation was a complete red phosphorescent OLED stack consisting of the injection layers MeO-TPD:F4-TCNQ and BPhen:Cs, blocking layers of α -NPD and BPhen and an emission layer of α -NPD:Ir(MDQ)₂acac. The built-in potential created by the doped layers accounts for $eV_B = 2.53$ eV and mainly drops across the emission layer of α -NPD:Ir(MDQ)₂acac. Once more, the alignment of the two molecules in this mixed layer was investigated and found to have vacuum level alignment, which is most likely a rule for mixed layers as long as no charge transfer takes place. IV measurements supported the results of a built-in voltage of 2.53 eV found by the UPS measurements as well as the strong influence on the current by the α -NPD:Ir(MDQ)₂acac layer.

8.2 Outlook

In this thesis, I have shown that photoelectron spectroscopy is a capable tool to investigate various aspects of organic semiconductor layers ranging from fundamental properties of doped layers to material interactions and to the characterization of complete devices. However, these measurements are a small fraction of what is possible and interesting to investigate in further studies.

Most obviously, the generality of the results on the p-doping process have to be investigated. As the slope of the Fermi level change on the doping concentration was reported to be less for inorganic dopants, compared to the finding in this work for F4-TCNQ, an influence of the dopant composition and probably the size of the dopant can be assumed, as this changes the morphology of a layer and the interaction radius with the matrix. The efficiency of charge transfer, found to be rather low in this work should be checked with different matrix-dopant combinations to conclude on the individual factors governing this process. If a good dopant-matrix combination can be found that shows a considerable higher charge transfer probability, a lower doping concentration would be sufficient which is preferable for the morphology and would lead to less absorption in the transport layers. Furthermore, a comparison to

the n-doping process would be of great interest. Even though UPS is only able to observe the occupied density of states and not the LUMO of a material, the change in Fermi level position is still measurable.

An exciting topic that was observed for Pentacene and MeO-TPD in this work is the change of the ionization potential of a layer upon doping which has not been reported in literature so far. Unpublished measurements on intrinsic and doped HATCN¹, NTCDA, and Di-NPD² give additional hints for this process. Further studies should be able to reproduce and quantify this effect. If the dopants actually have such a large influence on the ionization potential, this would have to be considered since additional barriers appear between doped and undoped layers, even of similar kind, and furthermore an inhomogeneous doping concentration throughout a layer would lead to location-dependent polarization energies that probably have to be included in simulations of the transport.

An important issue for understanding organic semiconductor layers is the investigation of the tail states. It was found in this work that a considerable amount of charge carriers can be present up to 0.7 eV beyond the conventionally assumed HOMO onset in the gap of a semiconductor. This means that the ionization potentials are miscalculated and that interfaces or layers do not behave as expected from simply comparing the IP values measured by UPS. So far, the effect was only investigated for three hole transport materials. This should be expanded to different classes of molecules. Here, an investigation by synchrotron photoelectron spectroscopy would be helpful to circumvent the error-prone method of subtracting satellite lines from the non-monochromatic He excitation source. Furthermore, it can be expected that the deposition condition will play a role on the width of the tail states, as the quasi-crystalline ZnPc layer shows the shortest tail width. By performing measurements on different stages of crystallinity, e.g. by changing the deposition rate or changing the substrate temperature, the impact on the density of states should be observable.

A variety of devices have been investigated in the thesis, but for example the investigation of a solar cell has still to be done. Here, the important topic of the correlation of the offset between donor-HOMO and acceptor-LUMO and the open circuit voltage of the device should be investigated. This is challenging, as the LUMO of the acceptor material is not accessible by UPS but has to be measured by a different method like inverse photoelectron spectroscopy or cyclic voltammetry. A lot of factors will play a role for the actual value of V_{OC} , like possible interface dipoles between the organic layers, the exciton binding energy of the electron-hole pair, and the width of the previously mentioned tail states.

Finally, it has to be said that there are many methods that are suitable to be combined with PES measurements or that can support the results. It would be helpful to have inverse photoelectron spectroscopy available, that probes the LUMO of a material with a beam of electrons that couple to higher unoccupied electronic states and decay from there to lower unoccupied states under emission of a photon that

¹Hexaazatriphenylene-hexacarbonitril

²N,N'-diphenyl-N,N'-bis(4'-(N,N-bis(naphth-1-yl)-amino)-biphenyl-4-yl)-benzidine

is detected. Other capable methods are also available. With Seebeck measurements, the distance between the transport level and the Fermi energy can be investigated and related to hole injection barriers measured by UPS. Some experiments with impedance spectroscopy have been presented here, clearly the method is capable of supporting and extending results found by UPS. Especially the accessibility of depletion layer widths and barrier formations by this method is promising.

Appendix

List of important abbreviations and symbols

Å	Ångström, $1 \text{ Å} = 0.1 \text{ nm}$
AO	atomic orbital
C	capacity
CEM	channel electron multiplier
CTC	charge transfer complex
D_{is}	density of interface states
DOS	density of states
e	elementary charge ($1.602 \cdot 10^{-19} \text{ C}$)
EA	electron affinity
E	electric field
E_B	binding energy
E_{CNL}	charge neutrality level
E_{coul}	Coulomb energy, exciton binding energy
E_F	Fermi energy
E_g	transport gap
E_g^{opt}	optical gap
E_{kin}	kinetic energy
E_{pass}	pass energy of detector
E_{vac}	vacuum energy
EML	emission layer
EBL	electron blocking layer
ETL	electron transport layer
FWHM	full width of half maximum
h	Planck constant ($6.626 \cdot 10^{-34} \text{ Js}$)
HBEC	high binding energy cutoff
HOMO	highest occupied orbital
HTL	hole transport layer
HBL	hole blocking layer
I	current
ICT	integer charge transfer
IDIS	induced density of interface states

IP	ionization potential
ITO	indium tin oxide (conductive oxide)
j	current density
k_B	Boltzmann constant ($8.62 \cdot 10^{-5}$ eV/K)
LDI-TOF-MS	laser desorption/ionization-time Of flight-mass spectrometry
LUMO	lowest unoccupied orbital
LCAO	linear combination of atomic orbitals
$m_{D/M}$	mass of donor/matrix layer
$M_{D/M}$	molar mass of dopant/matrix molecule
MO	molecular orbital
mol%	molar percentage of doping
MR	molar doping ratio
N_A^-	acceptor level density
N_D^+	donor level density
N_C	conduction band density of states
N_V	valence band density of states
OLED	organic light emitting diode
$P^{+/-}$	positive and negative polarization energy
R	resistance
RSF	relative sensitivity factor
S	slope parameter
SEM	scanning electron microscopy
t	time
UHV	ultra high vacuum
UPS	ultraviolet photoelectron spectroscopy
V	voltage
V_B	built-in voltage
V_{OC}	open circuit voltage
Wf	work function
WR	doping weight ratio
wt%	weight percentage of doping
X	capacitive resistance
XPS	x-ray photoelectron spectroscopy
Z	degree of charge transfer
Δ	interface dipole
ϵ_0	dielectric constant of vacuum ($8.85 \cdot 10^{-12}$ As/Vm)
ϵ	relative dielectric constant of a material
λ	mean free path
μ	mobility
ν	frequency
ρ	charge carrier density
σ	conductivity

φ	phase of current
ϕ	hole injection barrier
ϕ_e	electron injection barrier
Ψ	molecular orbital (wave function)

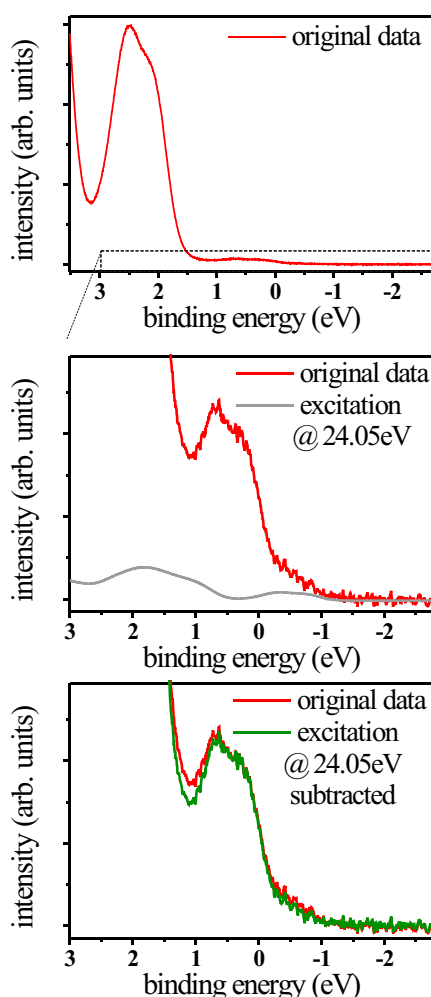
List of investigated molecules

Below a list of the molecules is given that have been investigated in the course of this work. A summary of the material properties can be found in Table 3.1 on page 58.

α -NPD	N,N'-Di(naphthalene-1-yl)-N,N'-diphenylbenzidine
AOB	3,6-bis(dimethylamino)acridine
BAIq	Aluminum(III)bis(2-methyl-8-quinolinato)-4-phenylphenolate
BPhen	4,7-diphenyl-1,10-phenanthroline
C60	Buckminster fullerene consisting of 60 Carbon atoms
C60F36	Fluorinated Buckminster fullerene
F4-TCNQ	2,3,5,6-tetrafluoro-7,7,8,8-tetracyanoquinodimethane
Ir(MDQ) ₂ acac	Iridium(III)bis(2-methyldibenzo[f,h]quinoxaline)(acetylacetonate)
MeO-TPD	N,N,N',N'-tetrakis(4-methoxyphenyl)-benzidine
NDN1	Novald Dopant N 1
NDP2	Novald Dopant P 2
NDP9	Novald Dopant P 9
PEDOT:PSS	Poly-(3,4)ethylenedioxythiophene-poly(styrenesulfonate)
PEN	Pentacene
PV-TPD	N,N'-Di(4-(2,2-diphenylethen-1-yl)phenyl)-N,N'-di(4-methylphenylphenyl)benzidine
ZnPc	Zinc-phthalocyanine

Satellite line subtraction

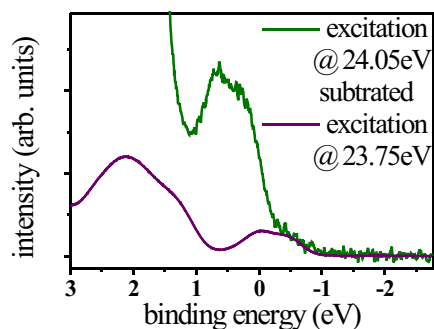
The helium discharge lamp used for the excitation during UPS measurements is not a purely monochromatic light source. Next to the main excitation of the HeI line at 21.22 eV there are three more emission lines with considerable lower intensities. These so called satellite lines have an energy of 23.09 eV (2% intensity), 23.75 eV (0.5% intensity), and 24.05 eV (0.2% intensity). The relative intensities given in the brackets are just estimates, as the exact ratio depends on the pressure of the He gas during the discharge. As mentioned in some parts of the thesis these satellite lines have to be subtracted from the spectra if weak features at the onset of the HOMO or in the gap of the semiconductor are supposed to be investigated (see Figs. 4.9, 4.12, 4.14, and 5.7). The following graphs show step by step how these three satellite lines are subtracted in a measurement performed on a layer of MeO-TPD at a helium discharge pressure of 1.1 mbar.



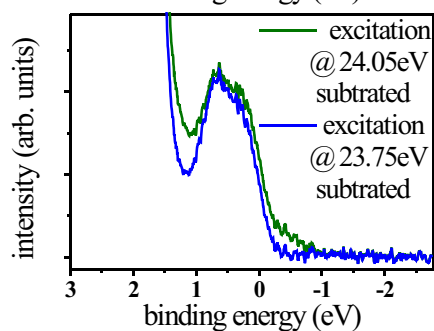
The red curve shows the original data of the valence band region of MeO-TPD as it is measured, so the satellite excitations are superimposed on the data. A close up of the gap region of this curve is shown in the next graph, the area is indicated by the box.

Obviously, additional structures appear with a shape similar to the HOMO. As the intrinsic semiconductor should have no states within the bandgap these must be from the satellite lines. The weakest of these lines with an excitation of 24.05 eV is already indicated in the graph. It is gained by shifting the original data by -2.83 eV and dividing it by a factor of 1200.

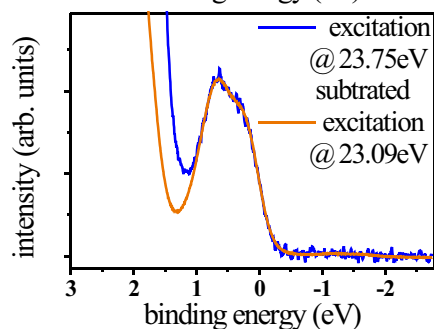
This graph shows the same close up region with the original data (red curve) and the same data when the satellite line at 24.05 eV shown before is subtracted (green curve).



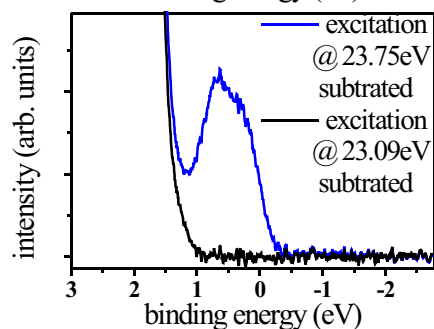
Now the second satellite line has to be subtracted, so the corrected curve from the last graph is shown (green curve) together with the excitation at 23.75 eV [original spectra shifted by -2.53 eV and divided by 330 (purple curve)].



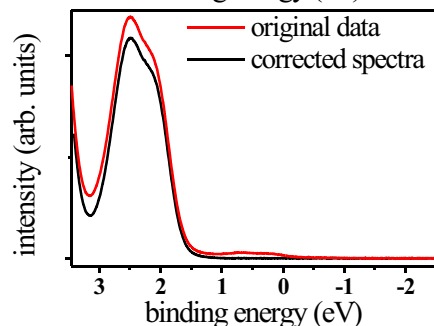
The blue curve shows the result of subtracting the 23.75 eV satellite line.



In a last step the most intense satellite line at 23.09 eV, shown as orange curve, has to be subtracted. For this, the original spectra is shifted by -1.87 eV and divided by 45.



Now the black curve shows the data from which all three satellite lines subtracted. A constant background baseline is achieved beyond the HOMO onset at 1 eV.



The result of the correction performed on the black curve is shown in comparison to the original data (red curve), zoomed out again to the same region as in the first graph.

References

- [1] M. Volmer: *Die verschiedenen lichtelektrischen Erscheinungen am Anthracen, ihre Beziehung zueinander, zur Fluoreszenz und Dianthracenbildung*. *Annalen der Physik* **40**, 775 (1913).
- [2] A. Bernanose: *Electroluminescence of organic compounds*. *British Journal of Applied Physics* **6**, 54 (1955).
- [3] C. Tang: *Two-layer organic photovoltaic cell*. *Applied Physics Letters* **48**, 183 (1986).
- [4] C. W. Tang and S. A. VanSlyke: *Organic electroluminescent diodes*. *Applied Physics Letters* **51**, 913 (1987).
- [5] J. Huang, M. Pfeiffer, A. Werner, J. Blochwitz, S. Liu, and K. Leo: *Low-voltage organic electroluminescent devices using pin structures*. *Applied Physics Letters* **80**, 139 (2002).
- [6] M. Pfeiffer, S. R. Forrest, K. Leo, and M. E. Thompson: *Electrophosphorescent p-i-n organic light emitting devices for very high efficiency flat panel displays*. *Advanced Materials* **14**, 1633 (2002).
- [7] B. Maennig, M. Pfeiffer, A. Nollau, X. Zhou, K. Leo, and P. Simon: *Controlled p-type doping of polycrystalline and amorphous organic layers: Self-consistent description of conductivity and field-effect mobility by a microscopic percolation model*. *Physical Review B* **64**, 195208 (2001).
- [8] W. Gao and A. Kahn: *Controlled p-doping of the hole-transport molecular material alpha-NPD mit tetrafluorotetracyanoquinodimethane*. *Journal of Applied Physics* **94**, 359 (2003).
- [9] M. Pfeiffer, A. Beyer, T. Fritz, and K. Leo: *Controlled doping of phthalocyanine layers by cosublimation with acceptor molecules: A systematic Seebeck and conductivity study*. *Applied Physics Letters* **73**, 3202 (1998).
- [10] J. Blochwitz, T. Fritz, M. Pfeiffer, K. Leo, D. M. Alloway, P. A. Lee, and N. R. Armstrong: *Interface electronic structures of controlled doped organic semiconductors*. *Organic Electronics* **2**, 97 (2001).

-
- [11] M. Green, K. Emery, Y. Hishikawa, and W. Wart: *Solar cell efficiency tables (version 35)*. Progress in Photovoltaics: Research and Applications **18**, 144 (2010).
- [12] H. Rabbani-Haghighi, S. Forget, S. Chenais, A. Siove, M. C. Castex, and E. Ishow: *Laser operation in nondoped thin films made of a small-molecule organic red-emitter*. Applied Physics Letters **95**, 033305 (2009).
- [13] C. Karnutsch, M. Stroisch, M. Punke, U. Lemmer, J. Wang, and T. Weimann: *Laser diode-pumped organic semiconductor lasers utilizing two-dimensional photonic crystal resonators*. IEEE Photonics Technology Letters **19**, 741 (2007).
- [14] H. Klauk, D. J. Gundlach, J. A. Nichols, and T. N. Jackson: *Pentacene organic thin-film transistors for circuit and display applications*. IEEE Transactions on Electron Devices **46**, 1258 (1999).
- [15] L. P. Ma, J. Liu, and Y. Yang: *Organic electrical bistable devices and rewritable memory cells*. Applied Physics Letters **80**, 2997 (2002).
- [16] F. Lindner, K. Walzer, and K. Leo: *Organic heterostructure device with non-volatile memory behavior using electrically doped layers*. Applied Physics Letters **93**, 233305 (2008).
- [17] K. Harada, A. G. Werner, M. Pfeiffer, C. J. Bloom, C. M. Elliott, and K. Leo: *Organic homojunction diodes with a high built-in potential: Interpretation of the current-voltage characteristics by a generalized Einstein relation*. Physical Review Letters **94**, 036601 (2005).
- [18] H. W. H. Haken: *Molecular Physics and Elements of Quantum Chemistry*. Springer-Verlag: Berlin Heidelberg New York (2004).
- [19] N. Karl: *Organic semiconductors*. Festkoerperprobleme **14**, 261 (1974).
- [20] N. Karl: *Charge carrier transport in organic semiconductors*. Synthetic Metals **133**, 649 (2003).
- [21] E. A. Silinsh: *Organic Molecular Crystals - Their Electronic States*. Springer Verlag Berlin Heidelberg New York (1980).
- [22] C. I. Wu, Y. Hirose, H. Sirringhaus, and A. Kahn: *Electron-hole interaction energy in the organic molecular semiconductor PTCDA*. Chemical Physics Letters **272**, 43 (1997).
- [23] H. Ishii, K. Sugiyama, E. Ito, and K. Seki: *Energy level alignment and interfacial electronic structures at organic metal and organic organic interfaces*. Advanced Materials **11**, 605 (1999).

-
- [24] R. Munn, A. Miniewicz, and B. E. Kuchta: *Electrical and related properties of organic solids*, vol. 24 of *Sub-Series: 3*. Proceedings of the NATO Advanced Research Workshop ERPOS-7: Electrical and Related Properties of Organic Solids, Polanica Zdrój, Poland (1997).
- [25] N. Sato, K. Seki, and H. Inokuchi: *Polarization energies of organic solids determined by ultraviolet photoelectron spectroscopy*. Journal of The Chemical Society-Faraday Transactions **77**, 1621 (1981).
- [26] P. Yu and M. Cardona: *Fundamentals of Semiconductors*. Springer-Verlag Berlin Heidelberg (1996).
- [27] H. Baessler, G. Schoenherr, M. Abkowitz, and D. M. Pai: *Hopping transport in prototypical organic glasses*. Physical Review B **26**, 3105 (1982).
- [28] J. Simon and J.-J. Andre: *Molecular Semiconductors*. Springer Verlag Berlin Heidelberg New York Tokyo (1985).
- [29] W. R. Salaneck: *Intermolecular relaxation energies in Anthracene*. Physical Review Letters **40**, 60 (1978).
- [30] P. I. Djurovich, E. I. Mayo, S. R. Forrest, and M. E. Thompson: *Measurement of the lowest unoccupied molecular orbital energies of molecular organic semiconductors*. Organic Electronics **10**, 515 (2009).
- [31] S. Krause, M. B. Casu, A. Schoell, and E. Umbach: *Determination of transport levels of organic semiconductors by UPS and IPS*. New Journal of Physics **10**, 085001 (2008).
- [32] J. Curry and E. P. Cassidy: *Effect of halogens on resistance of single crystals of Copper Phthalocyanine*. Journal of Chemical Physics **37**, 2154 (1962).
- [33] W. A. Orr and S. C. Dahlberg: *Effect of iodine incorporation on the electrical conductivity of films of Nickel Phthalocyanine*. Journal of the American Chemical Society **101**, 2875 (1979).
- [34] J. L. Petersen, C. S. Schramm, D. R. Stojakovic, B. M. Hoffman, and T. J. Marks: *New class of highly conductive molecular solids - partially oxidized Phthalocyanines*. Journal of the American Chemical Society **99**, 286 (1977).
- [35] D. R. Kearns, G. Tollin, and M. Calvin: *Electrical properties of organic solids 2: Effects of added electron acceptor on metal-free Phthalocyanine*. Journal of Chemical Physics **32**, 1020 (1960).
- [36] J. Endo, T. Matsumoto, and J. Kido: *Organic electroluminescent devices with a vacuum-deposited Lewis-acid-doped hole-injecting layer*. Japanese Journal of Applied Physics **41**, 358 (2002).

- [37] J. H. Lee, D. S. Leem, and J. J. Kim: *High performance top-emitting organic light-emitting diodes with copper iodide-doped hole injection layer*. Organic Electronics **9**, 805 (2008).
- [38] J. H. Lee, D. S. Leem, H. J. Kim, and J. J. Kim: *Effectiveness of p-dopants in an organic hole transporting material*. Applied Physics Letters **94**, 123306 (2009).
- [39] C. C. Chang, M. T. Hsieh, J. F. Chen, S. W. Hwang, and C. H. Chen: *Highly power efficient organic light-emitting diodes with a p-doping layer*. Applied Physics Letters **89**, 253504 (2006).
- [40] T. Matsushima and C. Adachi: *Enhanced hole injection and transport in molybdenum-dioxide-doped organic hole-transporting layers*. Journal of Applied Physics **103**, 034501 (2008).
- [41] M. Kroeger, S. Hamwi, J. Meyer, T. Riedl, W. Kowalsky, and A. Kahn: *P-type doping of organic wide band gap materials by transition metal oxides: A case-study on Molybdenum trioxide*. Organic Electronics **10**, 932 (2009).
- [42] D. S. Leem, H. D. Park, J. W. Kang, J. H. Lee, J. W. Kim, and J. J. Kim: *Low driving voltage and high stability organic light-emitting diodes with rhenium oxide-doped hole transporting layer*. Applied Physics Letters **91**, 011113 (2007).
- [43] M. Maitrot, G. Guillaud, B. Boudjema, J. André, and J. Simon: *Molecular material based junctions: Formation of a Schottky contact with metallophthalocyanine thin films doped by the cosublimation method*. Journal Of Applied Physics **60**, 2396 (1986).
- [44] E. J. Lous, P. W. M. Blom, L. W. Molenkamp, and D. M. Deleeuw: *Schottky contacts on a highly doped organic semiconductor*. Physical Review B **51**, 17251 (1995).
- [45] R. C. Wheland and J. L. Gillson: *Synthesis of electrically conductive organic solids*. Journal of the American Chemical Society **98**, 3916 (1976).
- [46] Z. Q. Gao, B. X. Mi, G. Z. Xu, Y. Q. Wan, M. L. Gong, K. W. Cheah, and C. H. Chen: *An organic p-type dopant with high thermal stability for an organic semiconductor*. Chemical Communications 117 (2008).
- [47] J. Blochwitz, M. Pfeiffer, T. Fritz, and K. Leo: *Low voltage organic light emitting diodes featuring doped phthalocyanine as hole transport material*. Applied Physics Letters **73**, 729 (1998).
- [48] K. Walzer, B. Maennig, M. Pfeiffer, and K. Leo: *Highly efficient organic devices based on electrically doped transport layers*. Chemical Reviews **107**, 1233 (2007).

-
- [49] W. Y. Gao and A. Kahn: *Controlled p-doping of zinc phthalocyanine by coevaporation with tetrafluorotetracyanoquinodimethane: A direct and inverse photoemission study*. Applied Physics Letters **79**, 4040 (2001).
- [50] R. C. Haddon, A. F. Hebard, M. J. Rosseinsky, D. W. Murphy, S. J. Duclos, K. B. Lyons, B. Miller, J. M. Rosamilia, R. M. Fleming, A. R. Kortan, S. H. Glarum, A. V. Makhija, A. J. Muller, R. H. Eick, S. M. Zahurak, R. Tycko, G. Dabbagh, and F. A. Thiel: *Conducting films of C60 and C70 by alkali-metal doping*. Nature **350**, 320 (1991).
- [51] G. Parthasarathy, C. Shen, A. Kahn, and S. R. Forrest: *Lithium doping of semiconducting organic charge transport materials*. Journal Of Applied Physics **89**, 4986 (2001).
- [52] L. Yan, N. J. Watkins, S. Zorba, Y. L. Gao, and C. W. Tang: *Direct observation of fermi-level pinning in Cs-doped CuPc film*. Applied Physics Letters **79**, 4148 (2001).
- [53] M. Y. Chan, S. L. Lai, K. M. Lau, C. S. Lee, and S. T. Lee: *Application of metal-doped organic layer both as exciton blocker and optical spacer for organic photovoltaic devices*. Applied Physics Letters **89**, 163515 (2006).
- [54] K. R. Choudhury, J. H. Yoon, and F. So: *LiF as an n-dopant in tris(8-hydroxyquinoline) aluminum thin films*. Advanced Materials **20**, 1456 (2008).
- [55] A. Nollau, M. Pfeiffer, T. Fritz, and K. Leo: *Controlled n-type doping of a molecular organic semiconductor: naphthalenetetracarboxylic dianhydride (NTCDA) doped with bis(ethylenedithio)-tetrathiafulvalene (BEDT-TTF)*. Journal Of Applied Physics **87**, 4340 (2000).
- [56] S. Tanaka, K. Kanai, E. Kawabe, T. Iwahashi, T. Nishi, Y. Ouchi, and K. Seki: *Doping effect of tetrathianaphthacene molecule in organic semiconductors on their interfacial electronic structures studied by UV photoemission spectroscopy*. Japanese Journal Of Applied Physics Part 1-Regular Papers Short Notes & Review Papers **44**, 3760 (2005).
- [57] J. G. Xue and S. R. Forrest: *Bipolar doping between a molecular organic donor-acceptor couple*. Physical Review B **69**, 245322 (2004).
- [58] F. H. Li, M. Pfeiffer, A. Werner, K. Harada, K. Leo, N. Hayashi, K. Seki, X. J. Liu, and X. D. Dang: *Acridine orange base as a dopant for n doping of C60 thin films*. Journal Of Applied Physics **100**, 023716 (2006).
- [59] A. G. Werner, F. Li, K. Harada, M. Pfeiffer, T. Fritz, and K. Leo: *Pyronin B as a donor for n-type doping of organic thin films*. Applied Physics Letters **82**, 4495 (2003).

- [60] C. K. Chan, E. G. Kim, J. L. Bredas, and A. Kahn: *Molecular n-type doping of 1,4,5,8-naphthalene tetracarboxylic dianhydride by pyronin B studied using direct and inverse photoelectron spectroscopies*. *Advanced Functional Materials* **16**, 831 (2006).
- [61] F. Li, A. Werner, M. Pfeiffer, K. Leo, and X. Liu: *Leuco crystal violet as a dopant for n-doping of organic thin films of Fullerene C60*. *Journal of Physical Chemistry B* **108**, 17076 (2004).
- [62] C. K. Chan, F. Amy, Q. Zhang, S. Barlow, S. Marder, and A. Kahn: *N-type doping of an electron-transport material by controlled gas-phase incorporation of cobaltocene*. *Chemical Physics Letters* **431**, 67 (2006).
- [63] C. K. Chan, A. Kahn, Q. Zhang, S. Barlow, and S. R. Marder: *Incorporation of cobaltocene as an n-dopant in organic molecular films*. *Journal Of Applied Physics* **102**, 014906 (2007).
- [64] C. K. Chan, W. Zhao, S. Barlow, S. Marder, and A. Kahn: *Decamethylcobaltocene as an efficient n-dopant in organic electronic materials and devices*. *Organic Electronics* **9**, 575 (2008).
- [65] C. K. Chan and A. Kahn: *N-doping of pentacene by decamethylcobaltocene*. *Applied Physics A - Materials Science & Processing* **95**, 7 (2009).
- [66] B. A. Gregg, S. G. Chen, and H. M. Branz: *On the superlinear increase in conductivity with dopant concentration in excitonic semiconductors*. *Applied Physics Letters* **84**, 1707 (2004).
- [67] L. Li, G. Meller, and H. Kosina: *Analytical conductivity model for doped organic semiconductors*. *Journal Of Applied Physics* **101**, 033716 (2007).
- [68] W. Y. Gao and A. Kahn: *Electronic structure and current injection in zinc phthalocyanine doped with tetrafluorotetracyanoquinodimethane: Interface versus bulk effects*. *Organic Electronics* **3**, 53 (2002).
- [69] W. Y. Gao and A. Kahn: *Controlled p doping of the hole-transport molecular material N,N'-diphenyl-N,N'-bis(1-naphthyl)-1,1'(-)-biphenyl-4,4'-diamine with tetrafluorotetracyanoquinodimethane*. *Journal Of Applied Physics* **94**, 359 (2003).
- [70] X. Zhou, J. Blochwitz, M. Pfeiffer, A. Nollau, T. Fritz, and K. Leo: *Enhanced hole injection into amorphous hole-transport layers of organic light-emitting diodes using controlled p-type doping*. *Advanced Functional Materials* **11**, 310 (2001).
- [71] M. Pfeiffer, K. Leo, X. Zhou, J. S. Huang, M. Hofmann, A. Werner, and J. Blochwitz-Nimoth: *Doped organic semiconductors: Physics and application in light emitting diodes*. *Organic Electronics* **4**, 89 (2003).

-
- [72] X. Zhou, M. Pfeiffer, J. Blochwitz, A. Werner, A. Nollau, T. Fritz, and K. Leo: *Very-low-operating-voltage organic light-emitting diodes using a p-doped amorphous hole injection layer*. Applied Physics Letters **78**, 410 (2001).
- [73] M. Pfeiffer: *Controlled doping of organic vacuum deposited dye layers: basics and applications*. Phd thesis, Institut für Angewandte Photophysik, TU Dresden, Institut für Angewandte Photophysik, TU Dresden (1999).
- [74] H. Fritzsche: *A general expression for the thermoelectric power*. Solid State Communications **9**, 1813 (1971).
- [75] M. Pfeiffer, T. Fritz, J. Blochwitz, A. Nollau, B. Ploennigs, A. Beyer, and K. Leo: *Controlled doping of molecular organic layers: Physics and device prospects*. Advances in Solid State Physics **39**, 77 (1999).
- [76] A. Kahn, N. Koch, and W. Y. Gao: *Electronic structure and electrical properties of interfaces between metals and pi-conjugated molecular films*. Journal Of Polymer Science Part B-Polymer Physics **41**, 2529 (2003).
- [77] M. Grobosch and M. Knupfer: *Charge-injection barriers at realistic metal/organic interfaces: Metals become faceless*. Advanced Materials **19**, 754 (2007).
- [78] J. Hwang, A. Wan, and A. Kahn: *Energetics of metal-organic interfaces: New experiments and assessment of the field*. Materials Science and Engineering **64**, 1 (2009).
- [79] M. G. Mason, C. W. Tang, L. S. Hung, P. Raychaudhuri, J. Madathil, D. J. Giesen, L. Yan, Q. T. Le, Y. Gao, S. T. Lee, L. S. Liao, L. F. Cheng, W. R. Salaneck, D. A. dos Santos, and J. L. Bredas: *Interfacial chemistry of Alq₃ and LiF with reactive metals*. Journal Of Applied Physics **89**, 2756 (2001).
- [80] C. Shen and A. Kahn: *The role of interface states in controlling the electronic structure of Alq₃/reactive metal contacts*. Organic Electronics **2**, 89 (2001).
- [81] C. Shen, A. Kahn, and J. Schwartz: *Chemical and electrical properties of interfaces between magnesium and aluminum and tris-(8-hydroxy quinoline) aluminum*. Journal of Applied Physics **89**, 449 (2001).
- [82] M. Fahlman, A. Crispin, X. Crispin, S. K. M. Henze, M. P. de Jong, W. Osikowicz, C. Tengstedt, and W. R. Salaneck: *Electronic structure of hybrid interfaces for polymer-based electronics*. Journal of Physics - Condensed Matter **19**, 183202 (2007).
- [83] C. Tengstedt, W. Osikowicz, W. R. Salaneck, I. D. Parker, C. H. Hsu, and M. Fahlman: *Fermi-level pinning at conjugated polymer interfaces*. Applied Physics Letters **88**, 053502 (2006).

- [84] S. Braun, W. R. Salaneck, and M. Fahlman: *Energy-level alignment at organic/metal and organic/organic interfaces*. *Advanced Materials* **21**, 1450 (2009).
- [85] J. Hwang, E. G. Kim, J. Liu, J. L. Bredas, A. Duggal, and A. Kahn: *Photoelectron spectroscopic study of the electronic band structure of polyfluorene and fluorene-arylamine copolymers at interfaces*. *Journal of Physical Chemistry C* **111**, 1378 (2007).
- [86] S. M. Sze: *Physics of Semiconductor Devices*. Wiley & Sons, New York (1981).
- [87] W. Moench: *Slope parameters of the barrier heights of metal-organic contacts*. *Applied Physics Letters* **88**, 112116 (2006).
- [88] H. Vazquez, R. Oszwaldowski, P. Pou, J. Ortega, R. Perez, F. Flores, and A. Kahn: *Dipole formation at metal/PTCDA interfaces: role of the charge neutrality level*. *Europhysics Letters* **65**, 802 (2004).
- [89] H. Vazquez, F. Flores, R. Oszwaldowski, J. Ortega, R. Perez, and A. Kahn: *Barrier formation at metal-organic interfaces: dipole formation and the charge neutrality level*. *Applied Surface Science* **234**, 107 (2004).
- [90] C. Tejedor, F. Flores, and E. Louis: *Metal-semiconductor Interface - Si (111) and Zinblend (110) Junctions*. *Journal of Physics C - Solid State Physics* **10**, 2163 (1977).
- [91] H. Vazquez, F. Flores, and A. Kahn: *Induced density of states model for weakly-interacting organic semiconductor interfaces*. *Organic Electronics* **8**, 241 (2007).
- [92] N. Hayashi, H. Ishii, Y. Ouchi, and K. Seki: *Examination of band bending at buckminsterfullerene C60/metal interfaces by the Kelvin probe method*. *Journal Of Applied Physics* **92**, 3784 (2002).
- [93] I. G. Hill, D. Milliron, J. Schwartz, and A. Kahn: *Organic semiconductor interfaces: electronic structure and transport properties*. *Applied Surface Science* **166**, 354 (2000).
- [94] I. G. Hill and A. Kahn: *Energy level alignment at interfaces of organic semiconductor heterostructures*. *Journal Of Applied Physics* **84**, 5583 (1998).
- [95] I. G. Hill and A. Kahn: *Organic semiconductor heterointerfaces containing bathocuproine*. *Journal Of Applied Physics* **86**, 4515 (1999).
- [96] I. Salzmann, S. Duhm, R. Opitz, R. L. Johnson, J. P. Rabe, and N. Koch: *Structural and electronic properties of pentacene-fullerene heterojunctions*. *Journal Of Applied Physics* **104**, 114518 (2008).

-
- [97] F. Zhang, A. Vollmer, J. Zhang, Z. Xu, J. P. Rabe, and N. Koch: *Energy level alignment and morphology of interfaces between molecular and polymeric organic semiconductors*. *Organic Electronics* **8**, 606 (2007).
- [98] R. J. Murdey and W. R. Salaneck: *Charge injection barrier heights across multilayer organic thin films*. *Japanese Journal Of Applied Physics Part 1- Regular Papers Short Notes & Review Papers* **44**, 3751 (2005).
- [99] J. X. Tang, C. S. Lee, and S. T. Lee: *Electronic structures of organic/organic heterojunctions: From vacuum level alignment to Fermi level pinning*. *Journal Of Applied Physics* **101**, 064504 (2007).
- [100] J. X. Tang, K. M. Lau, C. S. Lee, and S. T. Lee: *Substrate effects on the electronic properties of an organic/organic heterojunction*. *Applied Physics Letters* **88**, 232103 (2006).
- [101] H. Vazquez, W. Gao, F. Flores, and A. Kahn: *Energy level alignment at organic heterojunctions: Role of the charge neutrality level*. *Physical Review B* **71**, 041306 (2005).
- [102] B. Lu, H. J. Zhang, H. Y. Li, S. N. Bao, P. He, and T. L. Hao: *Photoemission study of an N,N' -bis-(1-naphthyl)- N,N' -diphenyl-1,1'-biphenyl-4,4'-diamine overlayer on Ag(111)*. *Physical Review B* **68**, 125410 (2003).
- [103] R. Schlaf, C. D. Merritt, L. A. Crisafulli, and Z. H. Kafafi: *Organic semiconductor interfaces: Discrimination between charging and band bending related shifts in frontier orbital line-up measurements with photoemission spectroscopy*. *Journal Of Applied Physics* **86**, 5678 (1999).
- [104] T. Shimada, K. Hamaguchi, A. Koma, and F. S. Ohuchi: *Electronic structures at the interfaces between copper phthalocyanine and layered materials*. *Applied Physics Letters* **72**, 1869 (1998).
- [105] R. Schlaf, P. G. Schroeder, M. W. Nelson, B. A. Parkinson, P. A. Lee, K. W. Nebesny, and N. R. Armstrong: *Observation of strong band bending in perylene tetracarboxylic dianhydride thin films grown on tin disulfide*. *Journal of Applied Physics* **86**, 1499 (1999).
- [106] C. J. Brabec: *Organic photovoltaics: technology and market*. *Solar Energy Materials and Solar Cells* **83**, 273 (2004).
- [107] J. Staudigel, M. Stoessel, F. Steuber, and J. Simmerer: *A quantitative numerical model of multilayer vapor-deposited organic light emitting diodes*. *Journal of Applied Physics* **86**, 3895 (1999).
- [108] I. G. Hill, A. J. Makinen, and Z. H. Kafafi: *Distinguishing between interface dipoles and band bending at metal/tris-(8-hydroxyquinoline) aluminum interfaces*. *Applied Physics Letters* **77**, 1825 (2000).

- [109] F. Petraki, V. Papaefthimiou, and S. Kennou: *The electronic structure of Ni-phthalocyanine/metal interfaces studied by X-ray and ultraviolet photoelectron spectroscopy*. *Organic Electronics* **8**, 522 (2007).
- [110] E. Ito, H. Oji, N. Hayashi, H. Ishii, Y. Ouchi, and K. Seki: *Electronic structures of TPD/metal interfaces studied by photoemission and Kelvin probe method*. *Applied Surface Science* **175**, 407 (2001).
- [111] H. Ishii, N. Hayashi, E. Ito, Y. Washizu, K. Sugi, Y. Kimura, M. Niwano, Y. Ouchi, and K. Seki: *Kelvin probe study of band bending at organic semiconductor/metal interfaces: examination of Fermi level alignment*. *Physica Status Solidi A* **201**, 1075 (2004).
- [112] M. Gorgoi and D. R. T. Zahn: *Band bending in copper phthalocyanine on hydrogen-passivated Si(111)*. *Organic Electronics* **6**, 168 (2005).
- [113] H. Yamane, Y. Yabuuchi, H. Fukagawa, S. Kera, K. K. Okudaira, and N. Ueno: *Does the molecular orientation induce an electric dipole in Cu-phthalocyanine thin films?* *Journal of Applied Physics* **99**, 093705 (2006).
- [114] G. Paasch, H. Peisert, M. Knupfer, J. Fink, and S. Scheinert: *Mixing of interface dipole and band bending at organic/metal interfaces in the case of exponentially distributed transport states*. *Journal of Applied Physics* **93**, 6084 (2003).
- [115] Y. Tanaka, K. Kanai, Y. Ouchi, and K. Seki: *Oxygen effect on the interfacial electronic structure of C-60 film studied by ultraviolet photoelectron spectroscopy*. *Chemical Physics Letters* **441**, 63 (2007).
- [116] S. Duhm, I. Salzmann, B. Broker, H. Glowatzki, R. L. Johnson, and N. Koch: *Interdiffusion of molecular acceptors through organic layers to metal substrates mimics doping-related energy level shifts*. *Applied Physics Letters* **95**, 093305 (2009).
- [117] K. Seki, N. Hayashi, H. Oji, E. Ito, Y. Ouchi, and H. Ishii: *Electronic structure of organic/metal interfaces studied by UPS and kelvin probe*. *Thin Solid Films* **393**, 298 (2001).
- [118] M. Popinciuc, H. T. Jonkman, and B. J. van Wees: *Energy level alignment symmetry at Co/pentacene/Co interfaces*. *Journal Of Applied Physics* **100**, 093714 (2006).
- [119] N. J. Watkins, L. Yan, and Y. L. Gao: *Electronic structure symmetry of interfaces between pentacene and metals*. *Applied Physics Letters* **80**, 4384 (2002).
- [120] Y. Hirose, A. Kahn, V. Aristov, P. Soukiassian, V. Bulovic, and S. R. Forrest: *Chemistry and electronic properties of metal-organic semiconductor interfaces: Al, Ti, In, Sn, Ag, and Au on PTCDA*. *Physical Review B* **54**, 13748 (1996).

-
- [121] V. Y. Aristov, O. V. Molodtsova, V. M. Zhilin, Y. A. Ossipyan, D. V. Vyalikh, B. P. Doyle, S. Nannarone, and M. Knupfer: *Formation of sharp metal-organic semiconductor interfaces: Ag and Sn on CuPc*. European Physical Journal B **57**, 379 (2007).
- [122] K. Ihm, H. E. Heo, S. Chung, J. R. Ahn, J. H. Kim, and T. H. Kang: *Odd characteristics of Au film on pentacene*. Applied Physics Letters **90**, 242111 (2007).
- [123] B. Jaeckel, J. B. Sambur, and B. A. Parkinson: *Ubiquitous pentacene monolayer on metals deposited onto pentacene films*. Langmuir **23**, 11366 (2007).
- [124] T. U. Kampen, A. Das, S. Park, W. Hoyer, and D. R. T. Zahn: *Relation between morphology and work function of metals deposited on organic substrates*. Applied Surface Science **234**, 333 (2004).
- [125] I. G. Hill, A. Rajagopal, and A. Kahn: *Energy-level alignment at interfaces between metals and the organic semiconductor 4,4'-N,N'-dicarbazolyl-biphenyl*. Journal Of Applied Physics **84**, 3236 (1998).
- [126] J. Park, S. I. Kang, S. P. Jang, and J. S. Choi: *Interface characteristics between Au electrode and pentacene layer in organic thin-film transistors*. Japanese Journal of Applied Physics Part 1-regular Papers Brief Communications & Review Papers **44**, 648 (2005).
- [127] S. Scholz, Q. Huang, M. Thomschke, S. Olthof, P. Sebastian, K. Walzer, K. Leo, S. Oswald, C. Corten, and D. Kuckling: *Self-doping and partial oxidation of metal-on-organic interfaces for organic semiconductor devices studied by chemical analysis techniques*. Journal of Applied Physics **104**, 104502 (2008).
- [128] A. Wan, J. Hwang, F. Amy, and A. Kahn: *Impact of electrode contamination on the alpha-NPD/Au hole injection barrier*. Organic Electronics **6**, 47 (2005).
- [129] M. Kiy, I. Biaggio, M. Koehler, and P. Gunter: *Conditions for ohmic electron injection at the Mg/Alq₃ interface*. Applied Physics Letters **80**, 4366 (2002).
- [130] C. F. Shen, I. G. Hill, and A. Kahn: *Role of electrode contamination in electron injection at Mg : Ag/Alq₃ interfaces*. Advanced Materials **11**, 1523 (1999).
- [131] C. F. Shen, A. Kahn, and J. Schwartz: *Role of metal-molecule chemistry and interdiffusion on the electrical properties of an organic interface: The Al-F16CuPc case*. Journal Of Applied Physics **90**, 6236 (2001).
- [132] T. Dobbertin, M. Kreoger, D. Schneider, E. Becker, H. H. Johannes, and W. Kowalsky: *Inverted topside-emitting organic light-emitting diodes for active-matrix OLED displays*. Organic Optoelectronics and Photonics **5464**, 145 (2004).

- [133] V. Bulovic, P. Tian, P. E. Burrows, M. R. Gokhale, S. R. Forrest, and M. E. Thompson: *A surface-emitting vacuum-deposited organic light emitting device*. Applied Physics Letters **70**, 2954 (1997).
- [134] D. B. A. Rep, A. F. Morpurgo, and T. M. Klapwijk: *Doping-dependent charge injection into regioregular poly(3-hexylthiophene)*. Organic Electronics **4**, 201 (2003).
- [135] A. Yassar, F. Demanze, and D. Fichou: *Synthesis and electrical properties of cyano-substituted oligothiophenes towards n-type organic semiconductors*. Optical Materials **12**, 379 (1999).
- [136] H. Heil, J. Steiger, S. Karg, M. Gastel, H. Ortner, H. von Seggern, and M. Stoessel: *Mechanisms of injection enhancement in organic light-emitting diodes through an Al/LiF electrode*. Journal of Applied Physics **89**, 420 (2001).
- [137] R. Meerheim, S. Scholz, S. Olthof, G. Schwartz, S. Reineke, K. Walzer, and K. Leo: *Influence of charge balance and exciton distribution on efficiency and lifetime of phosphorescent organic light-emitting devices*. Journal of Applied Physics **104**, 014510 (2008).
- [138] B. Maennig, J. Drechsel, D. Gebeyehu, P. Simon, F. Kozlowski, A. Werner, F. Li, S. Grundmann, S. Sonntag, M. Koch, K. Leo, M. Pfeiffer, H. Hoppe, D. Meissner, N. Sariciftci, I. Riedel, V. Dyakonov, and J. Parisi: *Organic p-i-n solar cells*. Applied Physics A: Materials Science & Processing **79**, 1 (2004).
- [139] J. Drechsel, B. Maennig, F. Kozlowski, D. Gebeyehu, A. Werner, M. Koch, K. Leo, and M. Pfeiffer: *High efficiency organic solar cells based on single or multiple PIN structures*. Thin Solid Films **451**, 515 (2004).
- [140] G. He, K. Walzer, M. Pfeiffer, K. Leo, R. Pudzich, and J. Salbeck: *Ultra-high efficiency electrophosphorescent p-i-n OLEDs with double emission layers*. Proceedings of SPIE **5519**, 42 (2004).
- [141] R. Meerheim, S. Scholz, G. Schwartz, S. Reineke, S. Olthof, K. Walzer, and K. Leo: *Efficiency and lifetime enhancement of phosphorescent organic devices*. Proceedings of SPIE **6999**, 699917 (2008).
- [142] S. Pfuetzner, A. Petrich, C. Malbrich, J. Meiss, M. Koch, M. K. Riede, M. Pfeiffer, and K. Leo: *Characterisation of different hole transport materials as used in organic p-i-n solar cells*. Proceedings of SPIE **6999**, 69991M (2008).
- [143] R. Meerheim, K. Walzer, M. Pfeiffer, and K. Leo: *Ultrastable and efficient red organic light emitting diodes with doped transport layers*. Applied Physics Letters **89**, 061111 (2006).

-
- [144] J. Drechsel, B. Maennig, D. Gebeyehu, M. Pfeiffer, K. Leo, and H. Hoppe: *MIP-type organic solar cells incorporating phthalocyanine/fullerene mixed layers and doped wide-gap transport layers*. *Organic Electronics* **5**, 175 (2004).
- [145] K. Schulze, C. Uhrich, R. Schueppel, K. Leo, M. Pfeiffer, E. Brier, E. Reinold, and P. Baeuerle: *Efficient vacuum-deposited organic solar cells based on a new low-bandgap oligothiophene and fullerene C60*. *Advanced Materials* **18**, 2872 (2006).
- [146] O. Solomeshch, Y. J. Yu, A. A. Goryunkov, L. N. Sidorov, R. F. Tuktarov, D. H. Choi, J. Jin, and N. Tessler: *Ground-state interaction and electrical doping of fluorinated C60 in conjugated polymers*. *Advanced Materials* **21**, 4456 (2009).
- [147] K. Fehse, K. Walzer, K. Leo, W. Loevenich, and A. Elschner: *Highly conductive polymer anodes as replacement of inorganic materials for high efficiency OLEDs*. *Advanced Materials* **19**, 441 (2007).
- [148] T. Schwieger, M. Knupfer, W. Gao, and A. Kahn: *Direct and inverse photoemission spectroscopy studies of potassium intercalated films of two organic semiconductors*. *Applied Physics Letters* **83**, 500 (2003).
- [149] J. Lee, S. S. Kim, K. Kim, J. H. Kim, and S. Im: *Correlation between photoelectric and optical absorption spectra of thermally evaporated pentacene films*. *Applied Physics Letters* **84**, 1701 (2004).
- [150] W. Zhao and A. Kahn: *Charge transfer at n-doped organic-organic heterojunctions*. *Journal of Applied Physics* **105**, 123711 (2009).
- [151] T. Y. Chu, Y. S. Wu, J. F. Chen, and C. H. Chen: *Characterization of electronic structure of aluminum (III) bis(2-methyl-8-quinolinato)-4-phenylphenolate (BALq) for phosphorescent organic light emitting devices*. *Chemical Physics Letters* **404**, 121 (2005).
- [152] C. G. Granqvist and A. Hultaker: *Transparent and conducting ITO films: new developments and applications*. *Thin Solid Films* **411**, 1 (2002).
- [153] D. Briggs and M. Seah: *Practical Surface Analysis*. John Wiley and Sons Chichester, New York, Brisbane, Toronto, Singapore (1983).
- [154] E. V. Tsiper, Z. G. Soos, W. Gao, and A. Kahn: *Electronic polarization at surfaces and thin films of organic molecular crystals: PTCDA*. *Chemical Physics Letters* **360**, 47 (2002).
- [155] M. B. Casu, Y. Zou, S. Kera, D. Batchelor, T. Schmidt, and E. Umbach: *Investigation of polarization effects in organic thin films by surface core-level shifts*. *Physical Review B* **76**, 193311 (2007).
- [156] *Specs manual for Phoibos 100/150*. www.specs.de.

- [157] J. H. Scofield: *Hartree-slater subshell photoionization cross-sections at 1254 and 1487eV*. Journal of Electron Spectroscopy and Related Phenomena **8**, 129 (1976).
- [158] H. J. Ding and Y. L. Gao: *Alkali metal doping and energy level shift in organic semiconductors*. Applied Surface Science **252**, 3943 (2006).
- [159] Q. Huang, K. Walzer, M. Pfeiffer, V. Lyssenko, G. F. He, and K. Leo: *Highly efficient top emitting organic light-emitting diodes with organic outcoupling enhancement layers*. Applied Physics Letters **88**, 113515 (2006).
- [160] X. Zhou, M. Pfeiffer, J. S. Huang, J. Blochwitz-Nimoth, D. S. Qin, A. Werner, J. Drechsel, B. Maennig, and K. Leo: *Low-voltage inverted transparent vacuum deposited organic light-emitting diodes using electrical doping*. Applied Physics Letters **81**, 922 (2002).
- [161] Y. Q. Li, J. X. Tang, Z. Y. Xie, L. S. Hung, and S. S. Lau: *An efficient organic light-emitting diode with silver electrodes*. Chemical Physics Letters **386**, 128 (2004).
- [162] J. Meiss, M. K. Riede, and K. Leo: *Towards efficient tin-doped indium oxide (ITO)-free inverted organic solar cells using metal cathodes*. Applied Physics Letters **94**, 013303 (2009).
- [163] J. Meiss, M. K. Riede, and K. Leo: *Optimizing the morphology of metal multi-layer films for indium tin oxide (ITO)-free inverted organic solar cells*. Journal of Applied Physics **105**, 063108 (2009).
- [164] T. Oyamada, Y. Sugawara, Y. Terao, H. Sasabe, and C. Adachi: *Top light-harvesting organic solar cell using ultrathin Ag/MgAg layer as anode*. Japanese Journal of Applied Physics Part 1-regular Papers Brief Communications & Review Papers **46**, 1734 (2007).
- [165] B. O'Connor, C. Haughn, K. H. An, K. P. Pipe, and M. Shtein: *Transparent and conductive electrodes based on unpatterned, thin metal films*. Applied Physics Letters **93**, 223304 (2008).
- [166] J. Meiss, N. Allinger, C. Falkenberg, K. Leo, and M. K. Riede: *Transparent conductive layers for organic solar cells - Simulation and experiment*. Proceedings of SPIE **7416**, 741603-1 (2009).
- [167] C. G. Granqvist: *Transparent conductors as solar energy materials: A panoramic review*. Solar Energy Materials and Solar Cells **91**, 1529 (2007).
- [168] S. Olthof, J. Meiss, M. Riede, B. Luessem, and K. Leo: *Photoelectron spectroscopy investigation of transparent metal top contacts for organic solar cells*. Submitted to Thin Solid Films (2010).

-
- [169] S. Reineke, F. Lindner, G. Schwartz, N. Seidler, K. Walzer, B. Luessem, and K. Leo: *White organic light-emitting diodes with fluorescent tube efficiency*. Nature **459**, 234 (2009).
- [170] *see press release at <http://heliatek.de/>* (June 2009).
- [171] Y. L. Gao and L. Yan: *Cs doping and energy level shift in CuPc*. Chemical Physics Letters **380**, 451 (2003).
- [172] V. I. Arkhipov, P. Heremans, E. V. Emelianova, and H. Baessler: *Effect of doping on the density-of-states distribution and carrier hopping in disordered organic semiconductors*. Physical Review B **71**, 045214 (2005).
- [173] M. P. Seah and W. A. Dench: *Quantitative electron spectroscopy of surfaces: A standard data base for electron inelastic mean free paths in solids*. Surface and Interface Analysis **1**, 2 (1979).
- [174] N. Koch, S. Duhm, J. P. Rabe, A. Vollmer, and R. L. Johnson: *Optimized hole injection with strong electron acceptors at organic-metal interfaces*. Physical Review Letters **95**, 237601 (2005).
- [175] K. Fehse, S. Olthof, K. Walzer, K. Leo, R. L. Johnson, H. Glowatzki, B. Broker, and N. Koch: *Energy level alignment of electrically doped hole transport layers with transparent and conductive indium tin oxide and polymer anodes*. Journal Of Applied Physics **102**, 073719 (2007).
- [176] G. M. Renger, O. T. Hofmann, L. Romaner, G. Heimel, B. Broker, R. P. Blum, R. L. Johnson, N. Koch, and E. Zojer: *F₄TCNQ on Cu, Ag, and Au as prototypical example for a strong organic acceptor on coinage metals*. Physical Review B **79**, 165306 (2009).
- [177] S. W. Tsang, Z. H. Lu, and Y. Tao: *Engineering carrier transport across organic heterojunctions by interface doping*. Applied Physics Letters **90**, 132115 (2007).
- [178] M. Ahles, R. Schmechel, and H. von Seggern: *n-type organic field-effect transistor based on interface-doped pentacene*. Applied Physics Letters **85**, 4499 (2004).
- [179] X. D. Feng, C. J. Huang, V. Lui, R. S. Khangura, and Z. H. Lu: *Ohmic cathode for low-voltage organic light-emitting diodes*. Applied Physics Letters **86**, 143511 (2005).
- [180] B. P. Rand, D. P. Burk, and S. R. Forrest: *Offset energies at organic semiconductor heterojunctions and their influence on the open-circuit voltage of thin-film solar cells*. Physical Review B **75**, 115327 (2007).
- [181] B. Minnaert and M. Burgelman: *Efficiency potential of organic bulk heterojunction solar cells*. Progress in Photovoltaics: Research and Applications **15**, 741 (2007).

- [182] M. C. Scharber, D. Wuhlbacher, M. Koppe, P. Denk, C. Waldauf, A. J. Heeger, and C. L. Brabec: *Design rules for donors in bulk-heterojunction solar cells - Towards 10% energy-conversion efficiency*. *Advanced Materials* **18**, 789 (2006).
- [183] A. Yakimov and S. R. Forrest: *High photovoltage multiple-heterojunction organic solar cells incorporating interfacial metallic nanoclusters*. *Applied Physics Letters* **80**, 1667 (2002).
- [184] M. Westphalen, U. Kreibig, J. Rostalski, H. Lüth, and D. Meissner: *Metal cluster enhanced organic solar cells*. *Solar Energy Materials & Solar Cells* **61**, 97 (2000).
- [185] A. Hadipour, B. de Boer, J. Wildeman, F. B. Kooistra, J. C. Hummelen, M. G. R. Turbiez, M. M. Wienk, R. A. J. Janssen, and P. W. M. Blom: *Solution-processed organic tandem solar cells*. *Advanced Functional Materials* **16**, 1897 (2006).
- [186] A. Hadipour, B. de Boer, and P. Blom: *Solution-processed organic tandem solar cells with embedded optical spacers*. *Journal Of Applied Physics* **10**, 074506 (2007).
- [187] K. Triyana, T. Yasuda, K. Fujita, and T. Tsutsui: *Effects of different materials used for internal floating electrode on the photovoltaic properties of tandem type organic solar cell*. *Japanese Journal Of Applied Physics Part 1-Regular Papers Short Notes & Review Papers* **43**, 2353 (2004).
- [188] G. Dennler, H. J. Prall, R. Koeppe, M. Egginger, R. Autengruber, and N. S. Sariciftci: *Enhanced spectral coverage in tandem organic solar cells*. *Applied Physics Letters* **89**, 073502 (2006).
- [189] J. Drechsel, B. Maennig, F. Kozlowski, M. Pfeiffer, K. Leo, and H. Hoppe: *Efficient organic solar cells based on a double p-i-n architecture using doped wide-gap transport layers*. *Applied Physics Letters* **86**, 244102 (2005).
- [190] K. Harada, M. Riede, K. Leo, O. R. Hild, and C. M. Elliott: *Pentacene homojunctions: Electron and hole transport properties and related photovoltaic responses*. *Physical Review B* **77**, 195212 (2008).
- [191] R. Timmreck, S. Olthof, K. Leo, and M. Riede: *Highly doped layers as efficient electron-hole recombination contacts for tandem organic solar cells*. Accepted for *Journal of Applied Physics* (2010).
- [192] N. Koch, A. Elschner, R. L. Johnson, and J. P. Rabe: *Energy level alignment at interfaces with pentacene: metals versus conducting polymers*. *Applied Surface Science* **244**, 593 (2005).
- [193] F. Amy, C. Chan, and A. Kahn: *Polarization at the gold/pentacene interface*. *Organic Electronics* **6**, 85 (2005).

- [194] S. Olthof, R. Meerheim, M. Schober, and K. Leo: *Energy level alignment at the interfaces in a multilayer organic light-emitting diode structure*. Physical Review B **79**, 245308 (2009).

Acknowledgments

I had an excellent time working at the *Institut für Angewandte Photophysik* which is due the harmonic working atmosphere and the friendly people around. For this I want to thank all the members of the institute.

In particular I want to thank my supervisor Professor Karl Leo for introducing me to the exciting topic of photoelectron spectroscopy and giving me the opportunity to work at the IAPP in the field of organic semiconductors. His reputation in this field, his extensive comprehension of organic semiconductors, his guiding skills and the excellent working conditions provided here made performing the experiments possible. And of course I am grateful for the proof reading of my manuscript.

Furthermore, I want to thank my group leaders Karsten Walzer and Björn Lüssem (Björn also did proof reading of the manuscript) of the OLED group as well as Bert Männig and Moritz Riede of my step-group (the OSOLs) for their support, the discussions and the guidance. Also, I want to thank Torsten Fritz for his willingness to review this work.

Many people helped and contributed to the thesis presented here. First of all, I want to thank Christian Urich for handing over Phoibos (i.e. the UPS machine) to me, even though it was not working at first. His experience was very helpful during my first year. I want to thank Jan Meiss for his suggestion to work together on the topic of ultra-thin top contacts and for always being open for discussions. Wolfgang Tress performed the simulations on the doping efficiency and was helpful so many times when the interpretation of some results were not clear to me. I want to thank Ronny Timmreck for supporting the UPS measurements on the recombination contacts and contributing the measurements of the solar cells. I am furthermore grateful to Hans Kleemann for the cooperation on the topic of *pin* junctions, especially the Zener diodes, for performing the IV and impedance measurements on the device stacks I investigated, for proof reading the Chapters on impedance spectroscopy and for his patience when he repeatedly had to explain his results. I want to thank Rico Meerheim, not only for the IV measurements on the OLED stack and the cooperation on the conductivity measurements, but also for the regular coffee breaks on the balcony that were always a welcoming break from work.

I furthermore want to thank Christiane Falkenberg (for patiently listening to me complaining every time my Phoibos measurement found a new way of not working. Her insight into the concept of photoelectron spectroscopy lead to many fruitful discussions), David Wynands (for constructing an UPS sample holder that allows for

temperature measurement during evaporation, and for his interest, support and discussions on UPS), Torben Menke (for the measurements that did not make it into the final version of this work and for all the non-work related topics he always came up with) and the other fellow PhD and diploma students of the OLED and OSOL group I worked with, especially Toni Müller, Matthias Schober, Gregor Schwartz, Sebastian Scholz, Thomas Rosenow, Patricia Freitag, Annette Petrich, Michael Thomschke, Martin Hermenau, Merve Anderson, Nico Seidler, Benjamin Friebe, Frank Lindner, Karsten Fehse, Kerstin Schulze, Kentaro Harada, as well as Oliver Mieth and Roman Forker and all the other ones I probably forgot now.

Furthermore, this work would not have been possible without a working measurement setup. I am very thankful for the help of the technicians Christian Kolberg and Carsten Wolf. Their patience (with me) when Phoibos or the UFO1 decided not to work again was invaluable. I owe just as much to the company of Specs, in particular Mrs. Gottschlich who gave her best to help me many times with the technical and electronic problems I had with the measurement setup. Their uncomplicated way of providing me with advice and spare parts saved me many times. Further thanks go to Kai Schmidt for being an excellent one-person-computer-task-force (and having his very own sense of humor), Eva Schmidt and Jutta Hunger for their support in administration issues, and the whole Lesker Team for their excellent work (even though I never personally submitted a sample I did benefit from the work they did for my colleagues). Also, I want to mention the Novaled AG for providing the dopants NDP2, NDP9, and NDN1.

I gratefully acknowledge the financial support by the ROLLEX project (13N8855), funded by the Bundesministerium für Bildung und Forschung (BMBF).

Last but not least, I want to thank my beloved family for their constant encouragement and support.

Erklärung

Diese Dissertation wurde am Institut für Angewandte Physik/Photophysik der Fakultät Mathematik und Naturwissenschaften an der Technischen Universität Dresden unter wissenschaftlicher Betreuung von Prof. Dr. Karl Leo angefertigt.

Hiermit versichere ich, dass ich die vorliegende Arbeit ohne unzulässige Hilfe Dritter und ohne Benutzung anderer als der angegebenen Hilfsmittel angefertigt habe; die aus fremden Quellen direkt oder indirekt übernommenen Gedanken sind als solche kenntlich gemacht. Die Arbeit wurde bisher weder im Inland noch im Ausland in gleicher oder ähnlicher Form einer anderen Prüfungsbehörde vorgelegt.

Ich versichere weiterhin, dass bislang keine Promotionsverfahren stattgefunden haben.

Ich erkenne die Promotionsordnung der Fakultät Mathematik und Naturwissenschaften an der Technischen Universität Dresden vom 20.03.2000, in der Fassung der vom Fakultätsrat am 19.06.2002 und 12.07.2002 beschlossenen und mit Erlass des Sächsischen Staatsministeriums für Wissenschaft und Kunst vom 18.03.2003 genehmigten Änderungen gemäß Satzung vom 16.04.2003 sowie gemäß der Änderungssatzung vom 17.07.2008, an.

Selina Olthof
Dresden, den 10.03.2010